Zeolite-Y Scaffolded Donor-Acceptor Systems for Nanoelectronics

A thesis submitted to Dublin City University for the award of Doctor of Philosophy

By

Gavin Sewell B.Sc. (Hons)

School of Chemical Sciences,
Dublin City University,
Glasnevin,
Dublin 9.

January 2014

Supervisor
Prof. T. E. Keyes

Declaration

I hereby certify that this material, which I now submit for assessment on the programme of study leading to the award of Doctor of Philosophy is entirely my own work, that I have exercised reasonable care to ensure that the work is original, and does not to the best of my knowledge breach any law of copyright, and has not been taken from the work of others save and to the extent that such work has been cited and acknowledged within the text of my work.

Signed: _____

ID No: _____

Date: _____

Acknowledgements

I would like to take this opportunity to sincerely thank my supervisor Professor Tia Keyes for all her guidance, time and patience over the years. I would also like to thank my internal supervisor Professor Robert Forster for the many useful discussions about my work.

I'd also like to extend my sincere gratitude to the many members of the Tia Keyes Research group, past and present that aided me in this work and with whom I so thoroughly enjoyed working and socialising with.

Big thanks is also due to the School of Chemistry technical staff, Damien, Ambrose, Vincent, Veronica, Mary, John and all the others who always did their best to help and offer support for any experiment I wished to undertake.

I wish to express my sincere gratitude to my parents, brothers and sisters for all the support they gave me over the years; I could not have done this without your help.

Finally, my biggest thanks of all, goes to my wife Ann-Marie. Your love, encouragement and patience has been truly remarkable, you'll never know how much it meant during this time.

This thesis is dedicated to the two most beautiful girls in the world.

Table of Contents

Acknowledgements iii

Table of Contents v

Abstract xii

List of Acronyms/symbols/complexes xiv

Chapter 1: General theory and introduction

1.0 Supramolecular chemistry 2
- 1.0.1 Host-Guest Chemistry 3
- 1.0.2 Clays as host materials 4
- 1.0.3 Sol-Gels 6

1.1 Zeolites 9
- 1.1.1 Zeolite Properties 11
- 1.1.2 Zeolite topology 11
- 1.1.3 Adsorption of guest molecules into zeolite materials 13
- 1.1.4 Diffusion within zeolites 18

1.2 Intrazeolitic environment 19
- 1.2.1 Confinement effects of zeolites 19
- 1.2.2 Guest interaction with exchange sites 22
- 1.2.3 Polarity and electrostatic effects 22
- 1.2.4 Guest interaction with zeolite framework 23

1.3 Charge and electron transfer within zeolites 24

1.4 Energy transfer within Zeolites 29

1.5 General Photochemistry 33
- 1.5.1 Spin 34
- 1.5.2 Electronic structure and electronic transitions 35
- 1.5.3 Photophysical pathways 36
- 1.5.4 Photophysical processes 36
  - 1.5.4.1 Internal Conversion 38
  - 1.5.4.2 Intersystem crossing 39

1.5.4.3 Fluorescence 39
1.5.4.4 Phosphorescence 39
1.6 Kinetics of photophysical processes 40
1.7 Quenching of excited states 41
1.7.1 Self quenching 42
1.7.2 Heavy-atom quenching 42
1.7.3 Electronic energy transfer 42
1.7.3.1 Förster energy transfer 43
1.7.3.2 Dexter-type mechanism 45
1.8 Excited state redox properties 46
1.9 Photoinduced electron transfer 47
1.10 Luminescence emission quenching 49
1.10.1 Stern-Volmer kinetics and dynamic quenching 49
1.10.2 Static quenching 51
1.10.3 Sphere of effective quenching 51
1.10.4 Formation of a ground state non-fluorescent complex 53
1.10.5 Deviations from simple quenching models 54
1.11 Conclusions 56
1.12 References 57

Chapter 2: Experimental approaches and Instrumentation

2.0 Chemicals 65
2.1 Electronic absorbance 65
2.2 Time resolved and steady state emission spectroscopy 65
2.2.1 Fluorescence lifetime imaging microscopy 66
2.3 Raman spectroscopy 66
2.4 General procedure for preparation of zeolite entrapped Materials 67
2.4.1 Preparation of the Zeolite encapsulated $[Ru(bpy)_3]^{2+}$ 67
2.4.2 Preparation of zeolite encapsulated $[Fe(bpy)_3]^{2+}$ and $[Fe(tpy)_2]^{2+}$ 68

2.4.3 Preparation of co-doped zeolite encapsulated Z-$[Ru(bpy)_3]^{2+}[Fe(bpy)_3]^{2+}$ and Z-$[Ru(bpy)_3]^{2+}[Fe(tpy)_2]^{2+}$ 68
2.4.4 Synthesis of Z-$[Ir(tpy)_2]^{3+}$ and Z-$[Ir(bpy)_3]^{3+}$ 69
2.5 Background theory 70
2.5.1 Time Correlated Single Photon Counting 70
2.5.1.1 Treatment of TCSPC data 71
2.5.2 Exponential decay models 72
2.5.2.1 Multiexponential decays 71
2.5.2.2 Distribution of lifetimes 73
2.5.2.3 Reconvolution and tail fitting 74
2.6 Raman Spectroscopy 76
2.6.1 Resonance-enhanced Raman spectroscopy 78
2.7 References 81

Chapter 3: Influence of Steric Confinement Within Zeolite Y on Photoinduced Energy Transfer Between $[Ru(bpy)_3]^{2+}$ and Iron Polypyridyl Complexes

3.0 Introduction 83
3.0.1 Zeolite-Y encapsulated metal polypyridyls 83
3.0.2 Zeolites as Host materials for metallic cations and complexes 82
3.0.3 Ruthenium tris-bipyridine $[Ru(bpy)_3]^{2+}$ 85
3.1 Preparation of zeolite entrapped transition metal complexes 88
3.2 Electronic absorption and photophysical properties of zeolite entrapped transition metal complexes 91
3.2.1 Effect of inhibited solvation 91
3.2.2 Effect of steric confinement 93
3.2.3 Effect of neighbouring transition metal polypyridyl species 94
3.2.4 Scope of work 99
3.3 Results and discussion 101
3.3.1 Synthesis and characterisation 101

3.3.2 Spectroscopy 104
3.3.2.1 Diffuse reflectance spectroscopy 104
3.3.2.2 $[Ru(bpy)_3]^{2+}$ diffuse reflectance spectroscopy 104
3.3.2.3 $[Fe(bpy)_3]^{2+}$ diffuse reflectance spectroscopy 105
3.3.2.4 $[Fe(tpy)_2]^{2+}$ diffuse reflectance spectroscopy 107
3.3.2.5 Diffuse reflectance spectroscopy of co-encapsulated $[Ru(bpy)_3]^{2+}$ and $[Fe(bpy)_3]^{2+}$ 111
3.3.2.6 Diffuse reflectance spectroscopy of co-encapsulated $[Ru(bpy)_3]^{2+}$ and $[Fe(tpy)_2]^{2+}$ 111
3.3.2.7 Raman spectroscopy 113
3.3.2.8 Z-$[Ru(bpy)_3]^{2+}[Fe(bpy)_3]^{2+}$ and Z-$[Ru(bpy)_3]^{2+}[Fe(tpy)_2]^{2+}$ Emission spectroscopy 120
3.3.3 Z-$[Ru(bpy)_3]^{2+}[Fe(bpy)_3]^{2+}$ and Z-$[Ru(bpy)_3]^{2+}[Fe(tpy)_2]^{2+}$ excited state lifetimes 121
3.3.4 Nature of quenching processes 129
3.4 Conclusions 136
3.5 References 137

Chapter 4: Influence of Zeolite-Y confinement on the photophysical properties of selected iridium polypyridyl complexes

4.0 Introduction 142
4.0.1 Iridium photophysics 142
4.0.1.1 Iridium bis-terpyridine $[Ir(tpy)_2]^{3+}$ 144
4.0.1.2 Iridium tris bipyridine $[Ir(bpy)_3]^{3+}$ 148
4.0.2 Iridium complexes in the solid state 149
4.0.2.1 Iridium complexes in polymers 149
4.0.2.2 Iridium complexes in zeolites 150

4.1 Experimental 153
4.1.1 Physical measurements 153
4.1.2 Synthesis of zeolite materials 154
4.2 Results and discussion 154
4.2.1 Synthesis and characterisation 154
4.2.2 Photophysical characterisation 157
4.2.2.1 Electronic absorption of zeolite entrapped iridium complexes 157
4.2.2.2 Effect of encapsulation on $[Ir(tpy)_2]^{3+}$ electronic emission 158
4.2.2.3 Concentrations effects on the extent of intercage $[Ir(tpy)_2]^{3+}$ interactions 161
4.2.2.4 Imaging of Z-Ir$[Ir(tpy)_2]^{3+}$ materials 165
4.2.2.5 Effect of encapsulation on Z-$[Ir(bpy)_3]^{3+}$ electronic emission 170
4.2.2.6 Concentrations effects on the extent of intercage $[Ir(bpy)_3]^{3+}$ interactions 172
4.2.2.7 Aggregation of iridium polypyridyl complexes 174
4.2.3 Raman spectroscopy 178
4.2.3.1 Raman spectroscopy Z-$[Ir(tpy)_2]^{3+}$ 178
4.2.3.2 Raman spectroscopy Z-$[Ir(bpy)_3]^{3+}$ 182
4.2.4 Excited state lifetimes of zeolilte entrapped complexes 184
4.2.4.1 Excited state lifetimes of Z-$[Ir(tpy)_2]^{3+}$ 184
4.2.4.2 Excited state lifetimes of Z-$[Ir(bpy)_2]^{3+}$ 185
4.3 Conclusions 189
4.4 References 190

Chapter 5: Huang-Rhys analysis of the Effect of Zeolite-Y confinement on the excited state Structure of selected ruthenium and iridium polypyridyl complexes

5.0 Introduction 194
5.0.1 Excited state distortion of complexes 195

5.0.2 Vibrational overlap and excited state distortion 196
5.0.3 Huang-Rhys analysis of emission spectra 199
5.0.3.1 Two mode Huang-Rhys Analysis 201
5.1 Experimental 202
5.1.1 Preparation $[Ir(tpy)_2][PF_6]_3$ 203
5.1.2 Preparation $[Ir(bpy)_3][PF_6]_3$ 204
5.1.3 Preparation $[Ru(tpy)_2][PF_6]_2$ 205
5.1.4 Preparation Z-$[Ru(tpy)_2][PF_6]_2$ 206
5.2 Results and discussion 206
5.2.1 Huang-Rhys analysis 77 K of ruthenium polypyridyl Complexes 207
5.2.1.1 $[Ru(bpy)_3][PF_6]_2$ and Z-$[Ru(bpy)_3]^{2+}$ 207
5.2.1.2 $[Ru(tpy)_2][PF_6]_2$ and Z-$[Ru(tpy)_2]^{2+}$ 215
5.2.2. Huang-Rhys analysis 77 K of iridium polypyridyl complexes 220
5.2.2.1 $[Ir(tpy)_2][PF_6]_3$ and Z-$[Ir(tpy)_2]^{3+}$ 220
5.2.2.2 $[Ir(bpy)_3][PF_6]_3$ and Z-$[Ir(bpy)_3]^{3+}$ 226
5.2.3 Huang-Rhys analysis 298 K 231
5.2.3.1 $[Ru(bpy)_3][PF_6]_2$ and Z-$[Ru(bpy)_3]^{2+}$ 231
5.2.3.2 Z-$[Ru(tpy)_2]^{2+}$ 234
5.2.3.3 $[Ir(bpy)_3][PF_6]_3$ and Z-$[Ir(bpy)_3]^{3+}$ 235
5.2.3.4 $[Ir(tpy)_2][PF_6]_3$ and Z-$[Ir(tpy)_2]^{3+}$ 239
5.3 Conclusions 243
5.4 References 245

Chapter 6: Interactions and energy transfer between selected Iridium polypyridyl complexes and europium bipyridine

6.0 Introduction 248
6.0.1 Lanthanide sensitisation with organic complexes 250
6.0.2 Lanthanide sensitisation with d-block complexes 253
6.0.3 Europium sensitisation with Iridium complexes 255
6.0.4 Zeolites as hosts for lanthanides 259
6.0.5 Luminescence from europium exchanged zeolites 259

6.1 Experimental 263
6.1.1 Physical measurements 263
6.1.2 Preparation of materials 263
6.2 Results and discussion 264
6.2.1 Photophysical characterisation of undoped materials 264
6.2.1.1 Z-$[Eu(bpy)_2]^{3+}$ 264
6.2.2 Photophysical Photophysical characterisation of Z-$[Ir(tpy)_2]^{3+}[Eu(bpy)_2]^{3+}$ and Z-$[Ir(bpy)_3]^{3+}[Eu(bpy)_2]^{3+}$ 265
6.2.2.1 Iridium polypyridyls luminescence 265
6.2.2.2 Excitation and phosphorescent emission 267
6.2.2.3 Excited state lifetimes 273
6.3 Conclusions 276
6.4 References 277

Chapter 7: Conclusions and further work

7.0 Conclusions and further work 280

Appendix A 284

Abstract

Gavin Sewell

Zeolites can act as hosts for supramolecular organization of molecules and complexes. A key objective in supramolecular chemistry is the development of donor acceptor systems capable of controlled photoinduced electron and energy transfer. This thesis focuses on a fundamental study of the capacity of zeolite materials to accommodate dipolar communication between metal complex guest species as well as exploring the effect of zeolite materials on the photophysical properties of guest molecules.

Chapter 1 and 2 outline the current state of zeolite host-guest chemistry and the experimental procedures and instrumentation ultilised in this work.

Chapter 3 investigates the ability of Y-zeolite to accommodate energy transfer processes between co-doped donors and acceptors. A series of $[Ru(bpy)_3]^{2+}$ (where bpy is 2,2'-bipyridine) doped Zeolite Y materials co-doped with iron polypyridyl complexes $[Fe(bpy)_3]^{2+}$ and $[Fe(tpy)_2]^{2+}$ were prepared via the 'ship in a bottle' synthesis. The co-encapsulated $[Ru(bpy)_3]^{2+}$ complex undergoes efficient energy transfer to both iron polypyridyl complexes over distances of between of 32 Å and 27 Å.

Chapter 4 examines the influence of zeolite-Y entrapment upon the photophysical properties of the Iridium (III) polypyridyl complexes $[Ir(bpy)_3]^{3+}$ and $[Ir(tpy)_2]^{3+}$. Their preparation and photophysical characterization is described. Dramatic changes in the emission spectra of the complexes were observed due to both the polarity of the zeolite interior as well as distortions caused by tight steric confinement.

Chapter 5 quantifies the extent of the excited state distortion of guest molecules entrapped within the pores of zeolite-Y by Huang-Rhys analysis. It was found that the zeolite environment impacts on the excited state geometry

of the complexes generally limiting the amount of structural distortion the complex can undergo.

In Chapter 6, iridium polypyridyl complexes in a zeolite-Y matrix were co-doped with europium bis-bipyridine. The photophysical properties of these materials were studied and indicated that sensitisation of the zeolite included europium acceptor by a co-included iridium polypyridyl energy donor complex occurred.

Chapter 7 offers conclusions on this thesis and outlines future work.

Abbreviations

A	Acceptor
BET	Back electron transfer
bpy	2,2'-bipyridine
C	Chromophore
CH_2Cl_2	Dichloromethane
CV	Cyclic voltammetry
D	Donor
DMSO	Dimethylsulfoxide
DMF	N, N-Dimethylformamide
EtOH	Ethanol
FLIM	Fluorescence lifetime imaging microscopy
G	Guest
HOMO	Highest occupied molecular orbital
HPLC	High pressure liquid chromatography
ic	Internal conversion
ILCT	Inter-ligand charge transfer
IR	Infra-red
IRF	Instrument response function
isc	Intersystem crossing
LC	Ligand centred
LC/MS	Liquid chromatography/Mass spectroscopy
$LiClO_4$	Lithium perchlorate
LUMO	Lowest unoccupied molecular orbital
LLCT	Ligand to ligand charge transfer
LMCT	Ligand to metal charge transfer
M	Multiplicity
M*	Excited molecule
MC	Metal centred
MeCN	Acetonitrile
MeOH	Methanol
MeCN	Acetonitrile

MLCT	Metal to ligand charge transfer
MW	Molecular weight
Phen	1,10-Phenanthroline
PMT	Photomultiplier tube
rR	Resonance Raman
Q	Quencher
S	Spin quantum number / Singlet state
T	Triplet state
TAC	Time-to-amplitude converter
TCSPC	Time correlated single photon counting
TLC	Thin layer chromatography
tpy	2,2';6',2''-terpyridine
Uv	Ultraviolet
Z	Zeolite
Δ	Delta
ε	Molar extinction coefficient
v	Frequency of Radiation
π	Pi Bonding Orbital
π*	Pi Anti-bonding Orbital
ϕ_f	Fluorescent Quantum Yield
ϕ_p	Phosphorescent Quantum Yield
σ	Sigma Bonding Orbital
σ*	Sigma Antibonding Orbital
τ	Lifetime
χ^2 value	Chi Squared Distribution
k_q	Quenching Rate Constant
h	Planck's Constant
N_A	Avogadro's number
ΔH	Changes in Enthalpy
ΔG	Changes in the Gibbs Free Energy
R	Gas Constant
T	Temperature in Kelvin

$[Ru(bpy)_3]^{2+}$	Ruthenium (II) tris(2,2’-bipyridine)
$[Ru(tpy)_2]^{2+}$	Ruthenium (II) bis(2,2';6',2''-terpyridine)
$[Fe(bpy)_3]^{2+}$	Iron (II) tris(2,2’-bipyridine)
$[Fe(tpy)_2]^{2+}$	Iron (II) bis(2,2';6',2''-terpyridine)
$[Ir(bpy)_3]^{3+}$	Iridium (III) tris(2,2’-bipyridine)
$[Ir(tpy)_2]^{3+}$	Iridium (III) bis(2,2';6',2''-terpyridine)
$[Eu(bpy)_2]^{3+}$	Europium (II) bis(2,2’-bipyridine)
Z-$[Ru(bpy)_3]^{2+}$	Zeolite entrapped $[Ru(bpy)_3]^{2+}$
	The Z- prefix denotes zeolite encapsulation

Chapter 1

General theory and introduction

1.0 Supramolecular chemistry

Supramolecular chemistry is the chemistry of the intermolecular bond, covering the structures and functions of the entities formed by the association of two or more chemical species.[1] Put another way, supramolecular chemistry is the area of chemistry that considers and utilises the interaction of discrete molecular entities or components bound or associated by a variety of mechanisms. Typical synthetic chemistry deals with the binding and breaking of covalent bonds in order to achieve some desired functionality, whereas supramolecular chemistry takes advantage of the particular individual properties of a minimum of two individual molecules, to work synergistically via some binding mechanism. In general subunits in supramolecular assemblies retain their individual molecular properties, but acquire a functionally that neither possesses individually. The two or more subunits of a supramolecular assembly can interact via several different non-covalent means such as hydrogen bonding, van der Waals forces, electrostatic effects and others. The advantages of some supramolecular assemblies include the capacity to construct a large complex molecule from a series of smaller molecules that arrange themselves automatically (self-assembly), making production of such materials less complex and costly than conventional methods. Other interesting examples of useful supramolecular assemblies include mechanically interlocked molecules such as rotaxanes,[2,3] which can to some degree mimic macroscale switching devices but at the molecular level and may have future applications in the quest for molecular computing devices. A further example of useful assemblies is the molecular recognition of target molecules and tailoring the sensing response of the associated target and host to best suit the proposed detection method.

1.0.1 Host-Guest Chemistry

Host-Guest Chemistry can broadly be described as the association of two molecules by a mechanism other than a non-reversible covalent interaction. An equilibrium is established between the associated constituent molecules and the isolated component species. This Host-guest complexation provides a route that facilitates the formation of supramolecular complexes.[4] A useful example of Host-guest chemistry is exemplified in inclusion complexes. These materials consist of a host molecule into which a guest molecule can be accommodated via a variety of differing non-covalent binding forces, typically on the basis of size and shape of the host or guest molecule. The host molecule is typically a large molecule, possessing a cavity large enough to fully or partially accommodate a guest molecule. The nomenclature of host-guest species is not uniform throughout the literature, generally speaking the guest molecule binds via some mechanism on its outer surface whilst the host binds via an inner site, however the relative sizes of host or guest can also determine their assignment. A well-known example is the inclusion of naphthalene into the cavity of cyclodextrin (Figure 1.1) and another is the widely studied inclusion of cations in crown ethers. [5,6,7]

There are of course many varieties of host-guest relationships, the inclusion of an individual C_{60} molecule into the cavities of cyclodextrins for example has also been demonstrated to induce double stand DNA cleavage upon visible light irradiation, useful for possible photodynamic anticancer applications.[8]

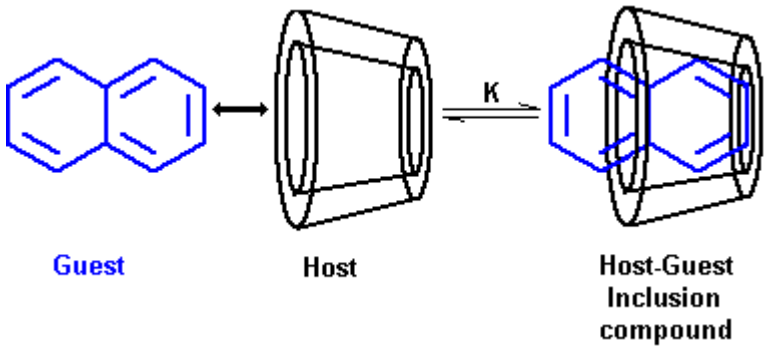

Figure 1.1: Model naphthalene-cyclodextrin supramolecular complex.

One of the key challenges of supramolecular chemistry is the confinement and strategic organisation of donor and acceptor species in three-dimensional space. This is achieved by specific bonding interactions between donor and acceptor in solution with the main interactions encountered being ionic, hydrogen bonding, hydrophobic or Van der Waals. Strategies for generating condensed phase species capable of supporting photo or electrochemically addressable functions have included production of photo and electroactive species at interfaces,[9,10] crystal engineering,[11] and the incorporation of electrochemically /optically active components into solid matrices such as sol gel,[12,13] zeolite and other mesoporous substrates. [14,15,16] Zeolites have over recent years been explored as scaffolds for molecular organisation through encapsulation of guest species and will be the central theme of this work.[17] However it is useful to consider some examples of similar host materials.

1.0.2 Clays as host materials

A wide variety of clay materials exist and are generally composed of varying stoichiometries of silicon, aluminium, iron and magnesium. These elements are found as compounds in the clay as silica, alumina and iron and magnesium hydroxides. A widely studied clay is montmorillonite, composed of two tetrahedral silica sheets linked via an octahedral alumina sheet (Figure 1.2). The macrostructure of the clay is built up as layers containing exchangeable cations such as sodium ions between these layers due to partial substitution of Al^{3+} by Mg^{2+} at the octahedral sites. The sodium ions act to neutralise the overall net negative charge.[18]

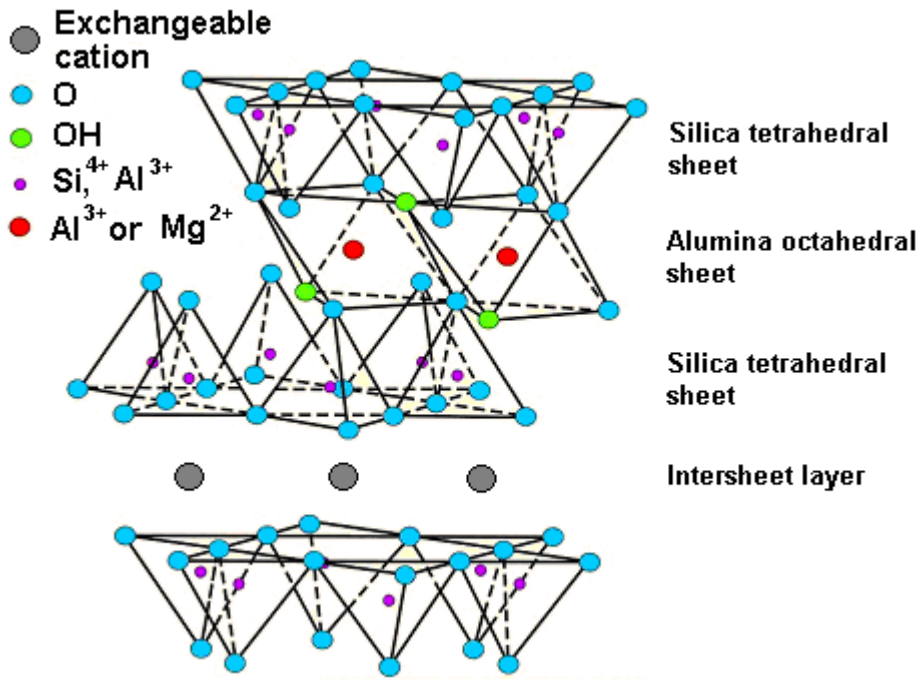

Figure 1.2: Layered structure of mortmorillonite showing location of charge balancing cations (Grimm *et al.*).[19]

The number of exchange sites as well as the nature of the species determines the extent to which clays can include guest species. Depending on the clay, anionic, cationic and neutral molecules can be intercalated into the intersheet layer. Stirring or sonicating an aqueous suspension of the clay and the guest usually accomplishes this.

Montmorillonite can act as an efficient host for the much studied ruthenium tris bipyridine.[20] Upon inclusion into the clay, the π- π * absorption peaks were found to be split due to the adsorption of the molecule at either the interlayer location or on the clay surface, allowing estimation of the extent of inclusion.

The inter-sheet layers can also be used to effect photochemical charge separation. Miyamoto *et al.* examined a methyl viologen doped hectorite (similar topology to montmorillonite) suspension to which layered niobate was added forming a double component colloid.[21] This produced a colloidal suspension that under ultraviolet irradiation, underwent electron transfer from the niobate to the methyl viologen. The methyl viologen radical was found to

be stable for many hours due to retardation of back electron transfer resulting from the spatial separation provided by the clay layer. The work demonstrated the ability of double component colloids to support long-lived charge separated species using the clay's propensity to form colloids, as well as the spatial orientation the clays interlaminar void provides.

Recently Wada *et al.* incorporated $[Ir(2\text{-phenylpyridine})_2(2,2\text{-bipyridine})]^+$ into layered silica.[22] They observed an emission blue shift with increasing concentration of the complex. This higher energy state of the iridium complex allowed for energy transfer to tetracene. This energy transfer process does not occur in solution, demonstrating the ability of clay like materials to alter the photophysical functionality of complexes.

Another property of certain clays is their capacity for adsorption of water molecules into the interlaminar void, resulting in swelling of the cavity. This allows some scope for tailoring of the void diameter. This is unlike the framework of zeolites that do not undergo swelling or shrinkage upon hydration or dehydration.

1.0.3 Sol-Gels

Sol-gels are highly cross-linked inorganic frameworks that can be created from a number of precursor materials. The process of producing sol-gels typically involves the hydrolysis and polycondensation of metal alkoxides and metal chlorides. These form colloidal particles that interconnect, eventually forming a continuous inorganic network. Much effort has been invested in the development of sol-gel materials due to their potential uses in optics, electronics, sensors and chromatography. As host materials sols provide a rigid, transparent substrate (depending on post condensation treatments) that can be spin coated yielding thin films or prepared as monoliths. The effect of encapsulation on the chemical and physical characteristics of guest molecules is due to the rigid, sterically confined cage environment in conjunction with interactions with functional groups constituting part of the guest matrix, such an example being silanol groups in the case of a silica sol-gel. Low

temperature preparation of a sol-gel generally result in a higher concentrations of active Si-OH sites whilst preparations involving densification of the material (application of heat to the sol gel resulting in decreased pore size) generally possess less Si-OH groups due to dehydroxylation of the silanol groups at higher temperatures.

The imposed rigidity on guest molecules can result in increased chemical stability, such as preventing ligand loss in ruthenium polypyridyls as well as increasing the radiative lifetime. Casalboni *et al.* studied 3,3'-diethyloxadicarbocyanine incorporated into silica gel glasses.[23] They found the emission and absorption bands of the dye blue shifted by 20 nm and the luminescence lifetime increased with higher densification temperatures. This they attributed to steric confinement, which is enhanced with the smaller cavity size induced by the higher densification temperatures.

Guest molecules entrapped within the porous network can be constrained by either physical incarceration (non-covalent binding) within the matrix or covalent bonding to the framework. The dopant is added to the precursor materials and homogenised before condensation of the sol material. A useful example of this was reported by Zhang *et al,* who described an oxygen sensor based on the luminescence quenching of ruthenium tris-bipyridine by dissolved O_2, covalently grafted to a sol gel matrix (Figure 1.3).[24]

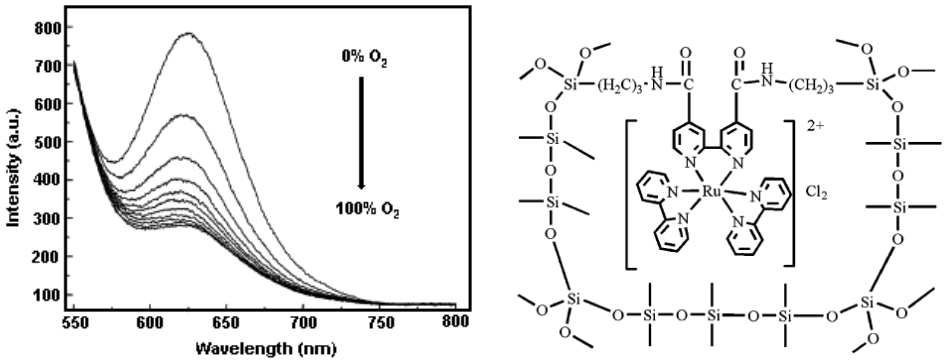

Figure 1.3: Right: Ruthenium tris bipyridine covalently grafted to sol gel host material. Left: Emisson spectra of covalently grafted $[Ru(bpy)_2(bpy\text{-}Si)]Cl_2$ thin film subjected to varying oxygen concentrations as prepared by Zhang *et al.* (*Sens. Actuators, B* **2007**, *123*, 508).[24]

The device demonstrated good sensitivity with an $I_0/I_{100} = 4.3$. I_0 and I_{100} denote the emission intensity of the doped sol gel in the presence of 100% nitrogen and 100% oxygen respectively. The grafting of the luminophore to the framework enhanced the stability of the material when compared to a physically entrapped analogue due to the absence of leaching. They also claimed a greater degree of homogeneity of the grafted material as opposed to the physically entrapped luminophore, the Stern-Volmer plot of the former showing far greater linearity. This example illustrates that the sol-gel host material's inherent chemical properties can be exploited with good effect.

Jorge *et al.* examined a system incorporating a ruthenium polypyridyl complex and CdSe-ZnS quantum dots into a sol gel material to simultaneously sense oxygen and temperature,[25] demonstrating the versatility of the material for multiplexed sensing applications. Recently Farooq *et al.* designed a sensor capable of detecting oxygen and sulphur dioxide within the same silica nanoparticle matrix based on luminescence quenching of immobilised dyes.[26] Overall sol-gels provide a rigid, if somewhat inhomogeneous environment in which to immobilise guest species.

1.1 Zeolites

Zeolites (from the Greek zein and lithos literally meaning a stone that boils) are crystalline solid aluminosilicates that possess three dimensional network structures composed of pores of molecular dimensions resulting in high surface area porous materials.[27] Their structure is based on a three dimensional network of $[AlO_4]^{5-}$ and $[SiO_4]^{4-}$ tetrahedra linked to each other via bridging oxygen atoms.[28] The presence of the aluminium atom on the zeolite network leads to an overall negative charge on the framework that is balanced by a charge compensating cation (Figure 1.4). These cations are easily exchangeable with other cations, the most important commercially of which is Proton (H^+) exchange that gives the zeolite Brönsted activity.

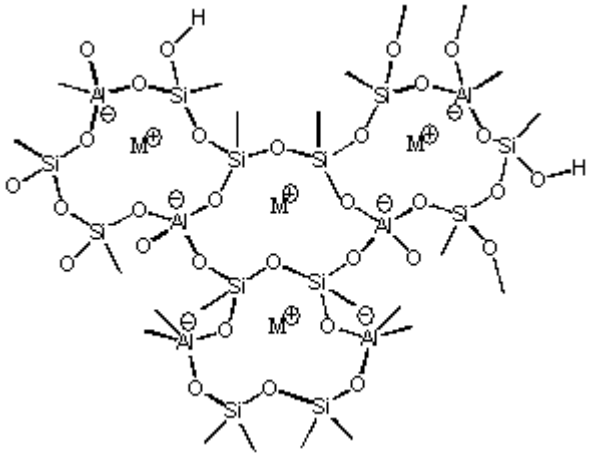

Figure 1.4: Zeolite structure, the charge compensating cation is denoted $M^{\oplus}$.

This porous structure, ion-exchange capability as well as the peculiar catalytic properties that the hydrogen form of the zeolite possesses means they have key commercial applications in fields such as water purification,[29] gas separation,[30] petrochemical industry,[31] nuclear waste sequestration[32] and many more.

Of particular interest to the present work is the faujasite zeolite-Y (Figure 1.5). These consist of a series of sodalite cages connected by six membered rings forming a supercage.[33] These supercages are arranged in a highly ordered

manner with each aperture leading to an adjacent supercage. Zeolite-Y possesses a large internal pore structure of 1.3 nm diameter and the ability to trap certain molecules within these pores by taking advantage of the fact that the apertures to the pores are only 0.74 nm. This permits the so called 'ship in a bottle synthesis', whereby each reactant with a kinetic diameter less than the aperture size is introduced into the zeolite cavity and subsequently reacted in-situ. Ideally the resulting complex is larger than the aperture and therefore permanently trapped. The zeolite material also possesses additional characteristics that can be exploited when utilising them as host molecules. They are optically transparent, relatively chemically inert and due to the dielectric properties and steric confinement the aluminosilicate cage provides have been demonstrated to provoke interesting changes in the photochemistry and photophysics of guest molecules.[14,34]

The entrapment of luminophores such as $[Ru(bpy)_3]^{2+}$ (Figure 1.6) in zeolite has attracted particular attention because of the potential importance of this species in applications such as solar energy conversion, photochemical molecular devices and sensing. For example, $[Ru(bpy)_3]^{2+}$ entrapped in zeolite Y has been extensively studied to quantitatively sense O_2.[35]

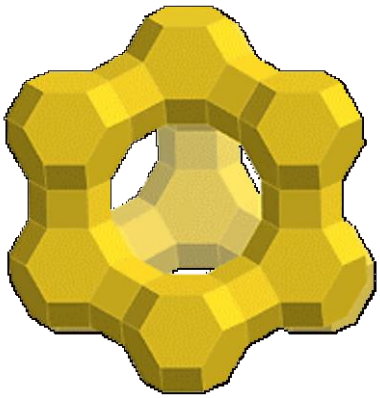

Figure 1.5: Space filling model of Faujasite zeolite (Baerlocher *et al.*, Database of Zeolite Structures: http://www.iza-structure.org/databases).[36]

1.1.1 Zeolite Properties

Zeolite materials provide not only the opportunity to organise guest molecules within their frameworks but also provide an interesting internal environment which can alter the guest molecule properties. The intrazeolitic voids and channels possess certain characteristics, which depending on the zeolite material, can influence the guests photophysics and photochemistry. The main effects imposed by the zeolite materials are a consequence of confinement, the presence of cationic sites and interaction with the zeolite framework.[14] These effects will be discussed in greater detail now, beginning with the considerations of introducing guest molecules into zeolite materials (not specifically zeolite-Y) and their diffusion properties within the porous frameworks. To better understand these processes it is first important to describe the topology of zeolite materials.

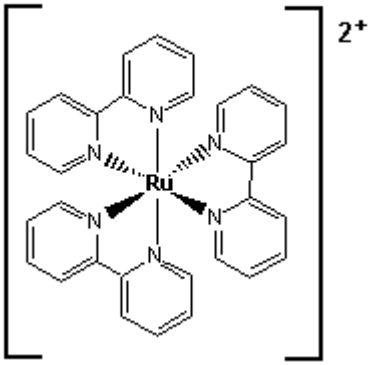

Figure 1.6: Ruthenium tris bipyridine $[Ru(bpy)_3]^{2+}$

1.1.2 Zeolite topology

The zeolite framework is anionic due to the presence of AlO_4^{5-} and has the general formula $(M+)_x[(AlO_2^-)_x(SiO_2)_y].mH_2O$. The overall negative charge of these aluminosilicates requires the presence of organic or inorganic cations to maintain the electroneutrality of the solid.[27] The faujasite family consists of X and Y zeolites, of which zeolite Y and its properties are the focus of this work.

Zeolite Y has a large roughly spherical internal supercage that is connected to four other adjacent supercages through the ‘windows' or apertures. These then build into a large network, with each supercage connected to four others building in a three dimensional fashion. Figure 1.7 shows a high-resolution transmission electron microscopy image of a zeolite Y surface.[30]

Figure 1.7: Zeolite-Y looking down [011] direction as observed by Wang *et al.* (*J. Nucl. Mater.* 2000**,** *278*, 233).[37]

Zeolite Y has an Si/Al ratio of between 3 and 1.5 whilst zeolite X has Si/Al ratios of between 1 and 1.5. Generally speaking, zeolites obey Loewenstein’s rule which states that Al atoms cannot occupy neighbouring tetrahedral sites with the result that zeolites with an Si/Al ratio of less than 1 cannot be prepared[38] (exceptions exist, such as the Linde A zeolite).[39] Zeolite Y may be prepared by mixing appropriate ratios of silica sol and aluminium solution in sodium hydroxide solution and heating at 90 ^{o}C for 24 hours.[40] The charge balancing cations are located at specific sites within the structure depending on the size and nature of the cation. A large lanthanum ion requires the application of heat to compel it to occupy sites in the sodalite cage (the smaller roughly spherical cages which form the corners of the zeolite-Y structure).[41] The nature of the charge balancing cation can have significant effects on the photophysics of guest molecules (*vide infra*).

1.1.3 Adsorption of guest molecules into zeolite materials

Both inorganic and organic guest molecules can be introduced into the zeolite framework. The capacity of guest molecules to diffuse into the pore structure is determined by a number of factors. The main considerations are size and charge. Due to the negatively charged framework, inclusion of negatively charged guests is difficult. The size of the opening to the framework will determine which molecules can enter the framework, although in some instance molecules slightly larger than the opening can enter at higher adsorption temperatures. As stated previously, guests larger than the aperture can be incorporated via the ship in a bottle synthesis and adsorption to the outer surfaces of the zeolite may also occur.

Three categories of guests can be introduced into zeolite systems. Neutral molecules of an appropriate size may be introduced by simply stirring the zeolite and guest as a slurry in a suitable solvent. The guest will diffuse in through the windows or if the guest has sufficient vapour pressure, can be introduced without any solvent.

Secondly, cationic guests can ion exchange with a present charge balancing cation. Sites within the framework are replaced with the guest cation, for instance if using Na-Y zeolite, a sodium ion is ejected into the bulk solution as the guest occupies its adsorption site. A third possibility for compound inclusion is the diffusion of reactants into the zeolite pores and subsequent reaction in-situ. This method of guest preparation has been exploited in the current study. Both inorganic compounds, such as ruthenium tris bipyridine $[Ru(bpy)_3]^{2+}$as mentioned earlier have been included, as well as organic compounds such as the 2,4,6-triphenylpyrylium ion.[42]

The adsorption process can be visualised by fluorescence microscopy. Figure 1.8 shows the adsorption of the fluorescent dye pyronin Y into the channels of a zeolite L crystal. The dye is observed to diffuse from the outer to the inner surface to with increasing time and temperature.[43]

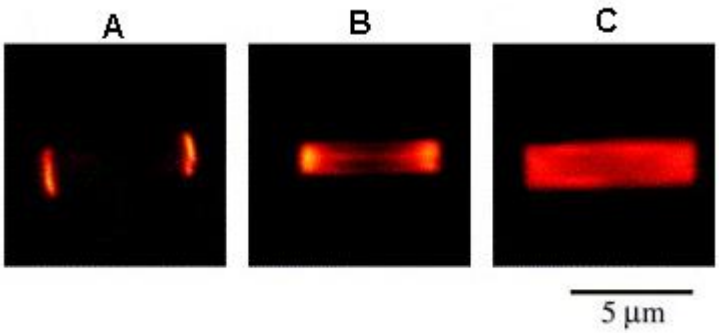

Figure 1.8: Diffusion of pyronin Y into a Zeolite L crystal with increasing time and temperature as observed by Hashimoto *et al.* (*Microporous Mesoporous Mater.* **2007**, *101*, 10). [43]

The adsorption of guest species into zeolite particles was also monitored by fluorescence spectroscopy. Hashimoto *et al.* also examined the diffusion of anthracene into sodium zeolite Y in this way.[17] The anthracene emission spectrum was initially a broad band, attributed to excimer emission, with another band present attributed to monomer emission. Over time the disappearance of the excimer band, with the simultaneous increase in monomer emission was noted. This was attributed to anthracene initially aggregating at the outer surface of the zeolite crystal and then slowly diffusing to the inner cages as a consequence of a concentration gradient. The work also demonstrated the effect of increased temperature on the rate of diffusion within particles, with enhanced rates observed with the application of heat.

Busby *et al.* demonstrated the functionalisation versatility of zeolite based systems. They bound two different dyes to the surface of zeolite L (Figure 1.9) at two distinct locations via selective functionalisation of the zeolite surface and subsequent reaction with a modified atto-425 dye molecules to covalently bind it to the zeolite wall, and secondly utilised the intrinsic adsorption properties of the host material at the channel ends to incorporate a modified atto-610 molecule at this second location.[44]

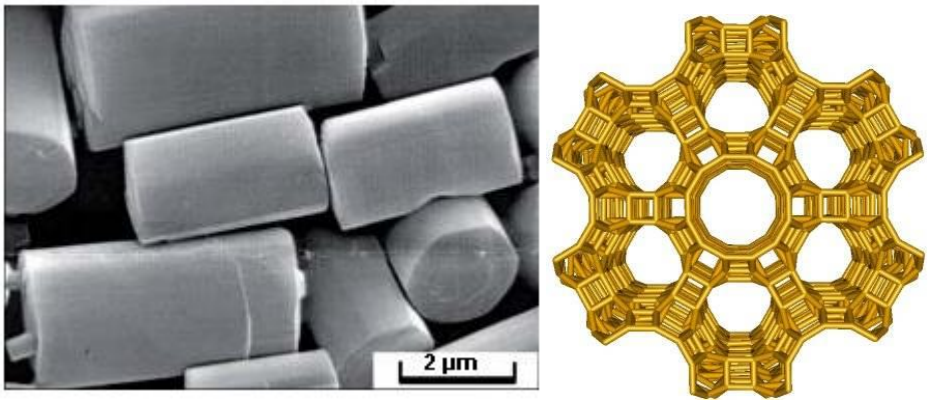

Figure 1.9: Left: Scanning electron microscopy image of Zeolite L crystals recorded by Busby *et al.* (*Adv. Mater.* **2008**, *20*, 1614–1618).[44] Right: Zeolite L structure showing parallel linear channels of 0.71nm diameter.[45]

This resulted in a covalently bound or adsorbed red emitting dye on the zeolite L crystals end channels and outer surface covered with a green emitting species.

These “orthoganally” functionalised systems demonstrate potential applications in multiplexed sensing. The system took advantage of the ability of the host material to adsorb the cationic dye into the channel structure and prevented further diffusion of the species into the crystal interior via attachment of bulky phenyl groups to the end of the dye. This effectively allows inclusion of the chromophoric portion of the molecule within the zeolite channel and blocks the crystal channels (often called a stopcock molecule) preventing any other species penetrating the end channel of the crystal. Covalent binding of a different dye via amide linkages then modified the crystals outer surface. Potential applications of these modified materials could include in-vivo optical imaging.[46] The confocal microscope image (Figure 1.10) clearly demonstrates the bifunctional nature of these materials.

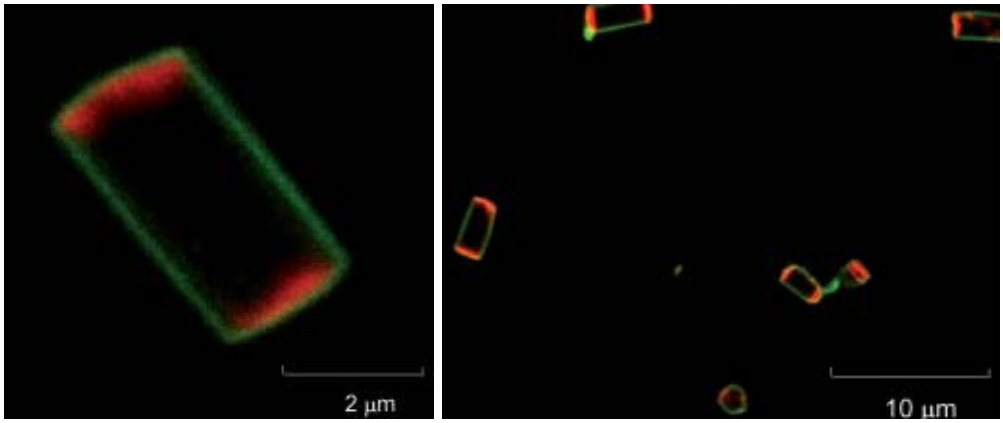

Figure 1.10: Confocal image of zeolite L crystals with attached red and green fluorescent dyes. The red portion corresponds to the zeolite channel ends (Busby *et al*., *Adv. Mater.* **2008**, *20*, 1614).[44]

Recently Beierle *et al.* looked at improving the functionalisation techniques used for zeolite L end channel modification. They produced individual zeolite L crystals with decorated with gold nanoparticles located at only the channel entrances.[47]

In another interesting study Kim *et al.* examined the aligned inclusion of dipolar dyes in the hydrophobic silicalite-1 zeolite material (Figure 1.11) for the purpose of second harmonic generation.[48,49] Adsorption of hemicyanine into the channels of silicalite-1 resulted in a rather low degrees of uniform orientation (DUO) suggesting the hydrophilic centre is located at the pyridinium portion of the molecule.

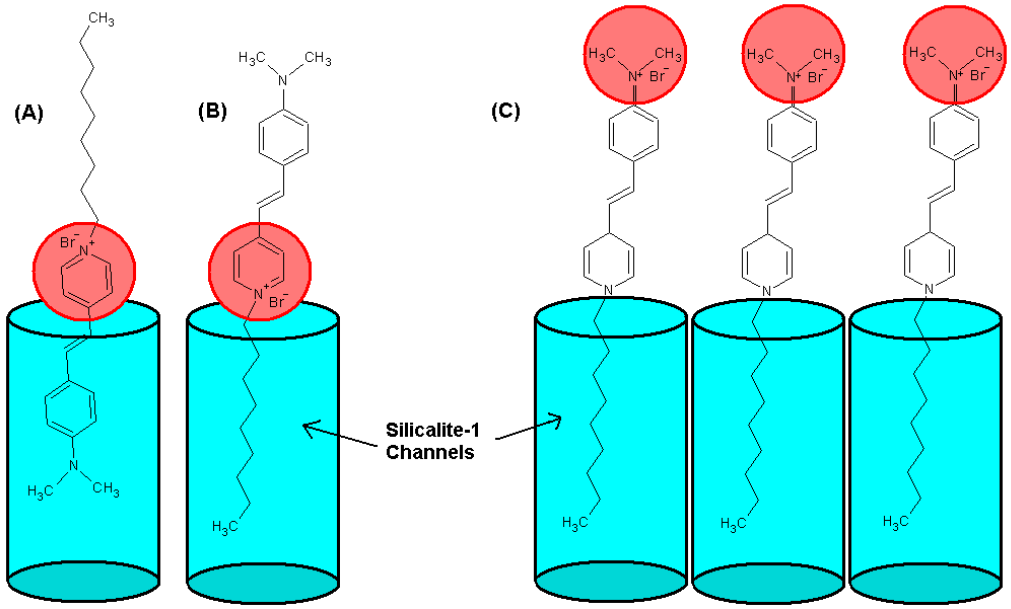

Figure 1.11: (A) Inclusion of hemicyanine into a channel of silicalite-1 dimethyl-amino group first. (B) Inclusion of hemicyanine into a channel of silicalite-1 hydrocarbon chain end first. (C) Inclusion of excited state hemicyanine into the channels of silicalite-1. The red circles are representative of charge density (Kim *et al.*, *J. Am. Chem. Soc.* **2008**, *130*, 2135).[48]

Adsorption of hemicyanine shows very little selectivity towards inclusion of the hydrocarbon or the dimethylamino-phenylenevinyl groups, resulting in a non-uniform distribution of the molecule within the channels. They concluded that both parts of the molecule are roughly similar in hydrophobicity. From theoretical studies on hemicyanine, electronic excitation results in charge density shifting from the pyridinium ring and developing at the dimethyl-amino end group essentially displacing the hydrophilic character of the species to this terminal group. The authors found that the DUO value of hemicyanine increased nearly four fold when adsorption was carried out under suitable irradiation of the dye and zeolite slurry, demonstrating that orientation controlled inclusion of excited state molecules is possible and a potentially useful technique for the creation of supramolecular entities.

1.1.4 Diffusion within zeolites

Guest species capable of adsorption into zeolite particles are free to diffuse throughout the matrix. Two separate diffusion processes are operable within zeolites with cage type structures. A molecule can move from one adsorption site to another within the same cage or 'hop' into an adjacent cage. The latter 'hop' has a higher activation barrier and is slow relative to adsorption site transport (Figure 1.12). The significance of diffusion rates is important when considering reactions between mobile guest species with long lifetimes. When reactions between guest molecules occurring on the picosecond and nanosecond timeframe, the molecule can be considered effectively static as the reaction proceeds far quicker than any diffusion take place.[14]

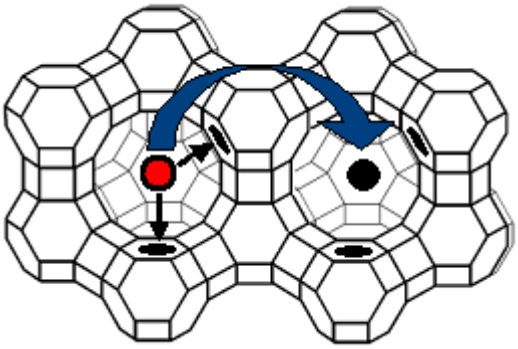

Figure 1.12: Representation of operable molecular diffusion processes within zeolite Y. Intracage diffusion (black arrows), Intercage diffusion (blue arrow), exchange sites (black spots), cation (red spot).

1.2 Intrazeolitic environment

Once a guest molecule has been included within a zeolite framework a number of different effects may be operable upon it:

1) Confinement effects.
2) Interaction with exchange sites.
3) Polarity and electrostatic effects.
4) Guest interaction with the zeolite framework.

While there is some overlap regarding these influences it is worthwhile to consider each independently.

1.2.1 Confinement effects of zeolites

For practical supramolecular applications the homogenous organization of molecules is crucial in order to avoid unfavourable effects such as molecule aggregation.[50,51] The varied types of zeolite, both natural and synthetic offer structures which range both in both size and shape, allowing approximate selections of host material to be made depending on the steric properties of the guest and nature of the spatial organization required.

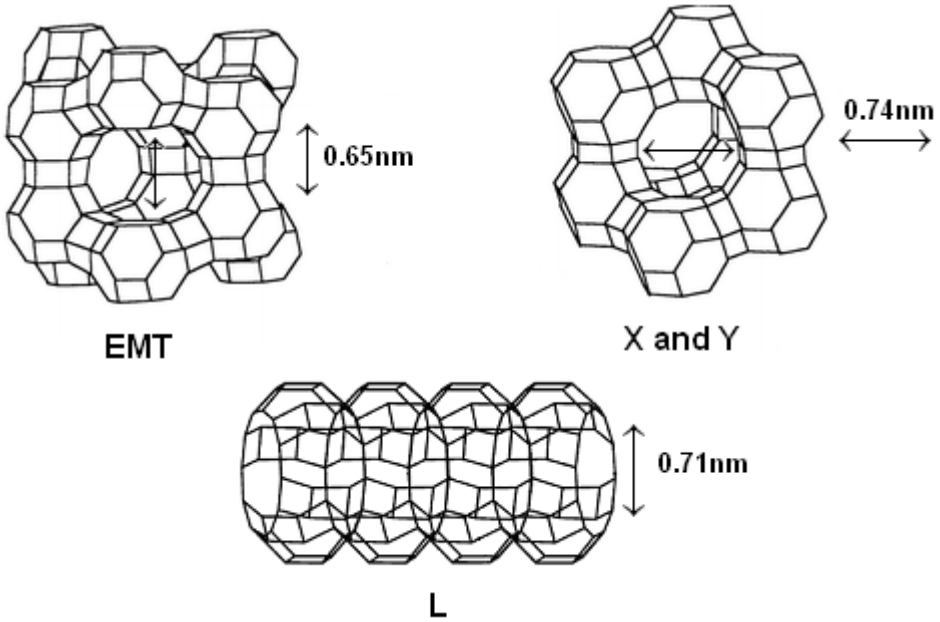

Figure 1.13: Structures of EMT, zeolite X and Yand zeolite L. (Hanif *et al.*, *Phys. Chem. Chem. Phys.* **2000**, *2*, 3349).[52]

Figure 1.13 shows three commonly used large pore zeolites. EMT and zeolite X and Y possess a cage structure whilst zeolite L has a roughly channular arrangement. The outer aperture diameter is shown, which leads to a larger cage or lobe in the zeolites displayed. This is not always the case, as some materials possess channels that are the same diameter as the opening aperture.

One of the consequences of confinement to a rigid zeolite pore or channel can be an effect on the photophysics and photochemical properties of the guest. This confinement, if severe enough is speculated to cause deformation of the guests molecular orbitals, a theory known as electronic confinement.[53] Numerous studies have been carried out on this idea of electronic confinement, involving mainly zeolite materials containing only silicon to eliminate effects due to cation sites and the charged zeolite wall (*vide infra*). Márquez *et al.* examined the effect on the photophysics of naphthalene upon inclusion in pure silica zeolites.[54] They observed a red shift in the naphthalene 0-0 transition, which they attributed to distortion of the HOMO orbital caused by the tight confines of the zeolite wall, resulting in a decreased

energy gap between HOMO and LUMO. They also noted the appearance of room temperature phosphorescence.

Another method of imposing a tight steric environment on guest molecules is the ship in a bottle synthesis. Two examples which illustrate the effect of the pore environment on molecules photophysics are the incorporation of 2,4,6,-triphenylpyrylium and ruthenium bis-terpyridine $[Ru(tpy)_2]^{2+}$.

Corma *et al.* prepared zeolite entrapped 2,4,6-triphenylpyrylium by reaction of chalcone and acetophenone in isooctane/HY (HY is the acid exchanged form of zeolite Y) slurry, yielding the entrapped molecule (Figure 1.14). [55] After extensive washing they examined the photopysical properties and found simultaneous emission of fluorescence and room temperature phosphorescence, the latter not observed in solution in ambient conditions.[56]

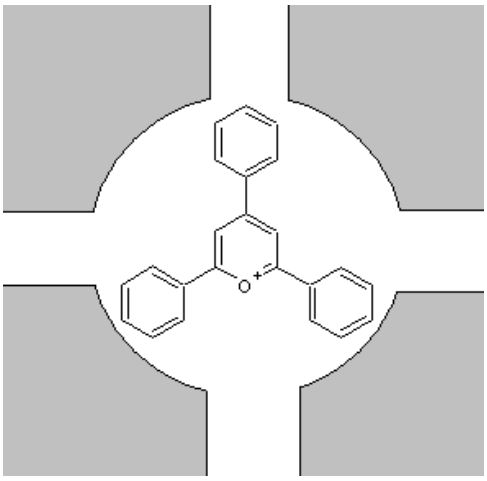

Figure 1.14: Representation of Faujasite included 2,4,6-triphenylpyrylium.[55]

The steric confinement of the transition metal complex ruthenium bis-terpyridine induces interesting effects. The complex possesses a short room temperature luminescent lifetime in solution, estimated at 250 ps but upon entrapment in zeolite Y the room temperature excited state lifetime increases to 140 ns.[57,58] It is thought that the physical constraints of the zeolite

destabilises the ligand field state (^{3}MC) resulting in a drop in the thermal population of the state and an increased lifetime.[59]

1.2.2 Guest interaction with exchange sites

The presence of cations within the framework of many zeolites can exert an influence on the properties of the guests. Ramamurthy *et al.* examined naphthalene loaded zeolites with the exchange sites substituted with cations of increasing atomic weight.[60] The cations examined were lithium, sodium, potassium, rubidium and caesium. The rate of intersystem crossing of naphthalene was noted to increase with the atomic weight of the cation and room temperature phosphorescence was observed, which is not observed in solution at ambient temperature. As expected the fluorescence emission efficiency decreased as the competing intersystem crossing rate increased. The heavy atom perturbation was found to be only operable when molecules were included in the large supercages of the faujasite, rather than surface bound to the exchanged heavy atom exchanged zeolite. The results of this work yielded similar results in terms of external heavy atom perturbation when compared with the studies carried out by Sousa *et al.* on naphathalene-crown ether derivatives exchanged with various metal cations,[61] however the magnitude of the external heavy atom effect was substantially greater in the zeolite material due to the close proximity of the cation and the higher local concentration of cations possible within intrazeolitic cavities.

1.2.3 Polarity and electrostatic effects

The interaction of the negatively charged framework and the counter balancing cations produce a dielectric comparable to that found in a highly polar salt solution.[53] The ion-exchange sites are partially shielded by the presence of a cation, however the unshielded side faces the supercage inner cavity. This results in electric field extending into the cavity that can polarise guest molecules. Studies by Uppili *et al.* suggested that the supercages of zeolite Y exchanged with Na and Li are more polar than water.[62] They studied the absorption and fluorescence properties of a number of organic probes

such as nile red and coumarin-500 adsorbed into various cation exchanged zeolite Y systems. The emission maximum of the coumarin-500 dye was progressively blue shifted with increasing cation size. They also found that the polarity of the zeolite depended not just on the size but also on the number of cations present within the supercage. Ellison *et al.* examined the degree of shielding of intrazeolitic electrostatic effects provided by various solvents.[63] Zeolite X and Y were studied using pyrene as a fluorescence probe. They found that generally the polarity is higher than experienced in bulk solution in the case of Na-X and Na-Y. These results indicated that both solvent and cation influence the polarity simultaneously and shielding effect of solvents is only partial.

1.2.4 Guest interaction with zeolite framework

Guest molecules can also interact with the anionic framework of the zeolite material. Thomas *et al.* explored the effect of the electron donating properties of zeolite X and Y in the creation of intrazeolitic pyrene anions.[64] When pyrene loaded zeolite was photolyzed, the radical cation and anion of pyrene was detected in transient absorption spectra. They concluded that electron transfer from basic oxygen sites in the zeolite framework was leading to formation of radical anions and that ionic clusters of Na_4^{4+} were behaving as lewis acid sites, accepting electrons resulting in the radical cations. They discounted the possibility of pyrene-pyrene electron transfer due to the low loading of pyrene utilised. Hashimoto *et al.* studied the electron-acceptor strength of dehydrated zeolites X and Y on the luminescence decay rate of encapsulated ruthenium tris bipyridine $[Ru(bpy)_3]^{2+}$.[65] They found that the rate of photoinduced electron transfer from excited state $[Ru(bpy)_3]^{2+}$ varies approximately linearly with Sanderson's electronegativity of alkali cation exchanged zeolites (Figure 1.15). Sanderson's electronegativities can be related to the electron accepting ability of the zeolite host based on the individual electronegativities of the component elements.

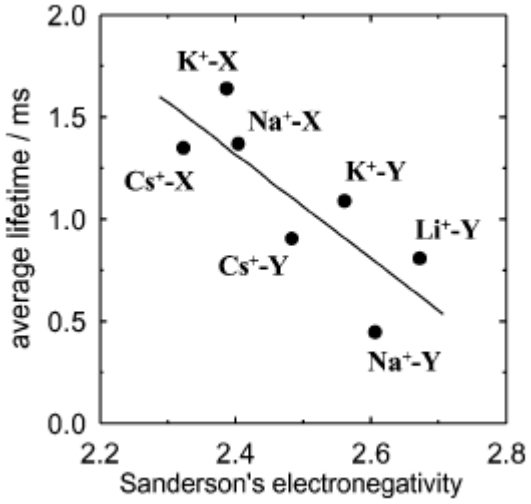

Figure 1.15: Variation of excited state lifetimes of zeolite entrapped $[Ru(bpy)_3]^{2+}$ with Sanderson's electronegativities based on ion-exchanged cation (Hashimoto *et al.*, *Photochem. Photobiol. Sci.*, **2006**, *5*, 822).[65]

1.3 Charge and electron transfer within zeolites

Electron transfer and charge transfer reactions in microheterogeneous media have been widely studied due to their potential application in solar energy conversion.[66] The zeolite as a host for such systems is interesting because of its regular framework which facilitates well defined spatial separation of interacting molecules thus mitigating the effects of energy wasting back electron transfer. This back electron process competes with the formation of the charge separated species, so control over this reverse step is crucial to the development of, for instance artificial photosynthetic systems.

Much of the research regarding charge transfer interactions in a zeolite medium has involved pyridinium derivatives as acceptor molecules and arenes as electron donors. One of the most studied acceptor compounds is methyl viologen (MV^{2+}) due its well-understood redox behaviour (Figure 1.16). The preparation of methyl-viologen exchanged zeolites is simple, typically aqueous exchange in a zeolite/$MVCl_2$ slurry is sufficient with the guest adsorption aided as the species is cationic.[67] Co-inclusion of an arene guest typically involves stirring the zeolite-MV^{2+} powder with the arene in a non-polar

solvent, usually hexane. The solvent is then evaporated and the sample hermetically sealed if dehydrated samples are required.

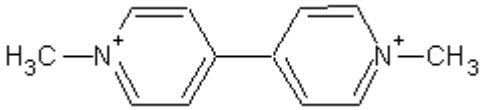

Figure 1.16: 4,4'-viologen (MV^{2+})

Yoon *et al.* examined a number of zeolite entrapped methyl viologen-arene systems.[68,69]

Figure 1.17 shows the charge transfer bands for three of the arenes studied. The transient absorption spectra of the MV^{2+}-Anthracene system showed two absorption maxima that were assigned to $MV^{+\bullet}$ (methyl viologen radical cation) and $Ant^{+\bullet}$ (anthracene radical cation) (Figure 1.18). The rate of charge recombination was ten times slower than solution phase acetonitrile studies. They proposed two possibilities for the retarded back-electron transfer rate (BET). One possibility is due to an interaction of the radical cations with the negatively charged framework wall, effectively increasing the separation between the couple and the second is that the interaction of guest species with cation adsorption sites affects their redox properties and consequently the BET. The authors surmise that the redox changes would have to be considerable to result in a ten fold BET reduction but do not rule out some possible influence.

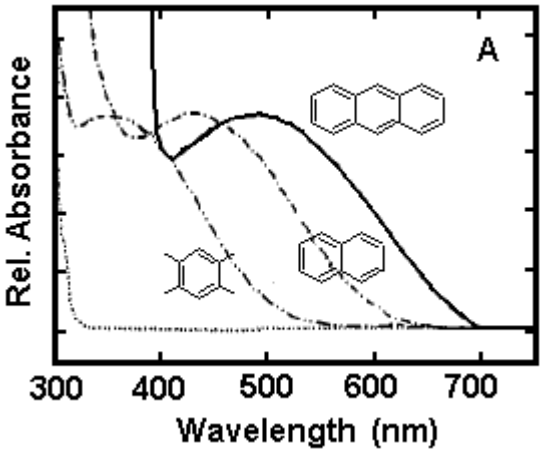

Figure 1.17: Absorption spectra of charge transfer complexes of MV^{2+} and anthracene, naphthalene and durene in dry zeolite-Y (Yoon *et al.*, *J. Phys. Chem.* **1994**, *98*, 3865).[69]

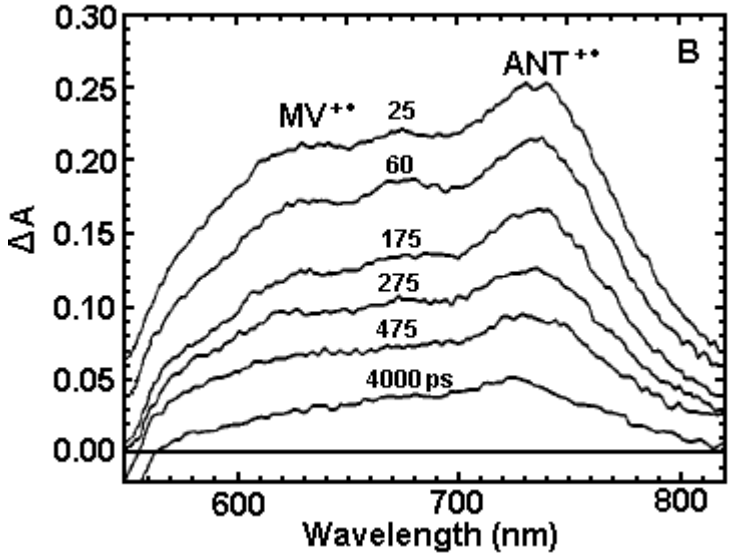

Figure 1.18: Picosecond time resolved diffuse-reflectance spectra of dry zeolite-Y entrapped charge transfer complex methyl viologen-anthracene system (Yoon *et al.*, *J. Phys. Chem.* **1994**, *98*, 3865). [69]

One widely studied electron donor-acceptor system in many heterogeneous media including zeolite Y is the $[Ru(bpy)_3]^{2+}$ -viologen system. Three common configurations for zeolite included ruthenium-viologen diad system are possible (Figure 1.19).

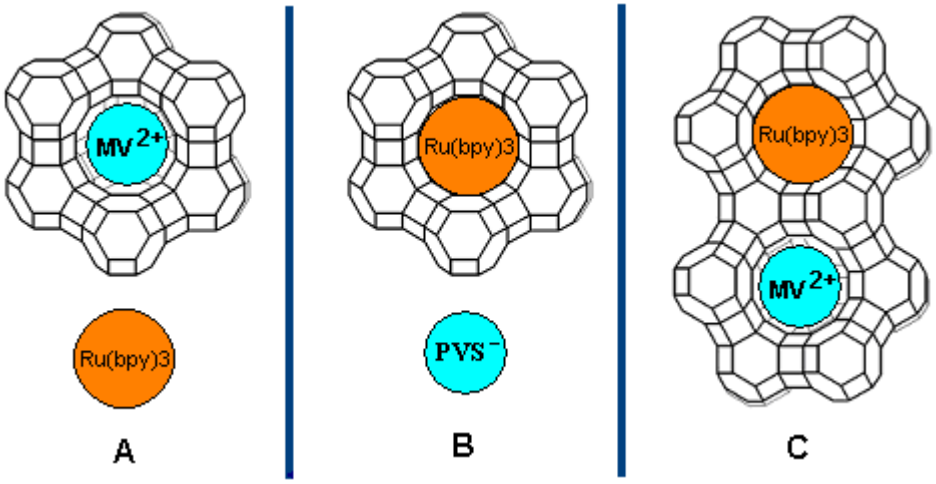

Figure 1.19: Three configurations reported in literature for zeolite based ruthenium-viologen interactions. (A) Methyl viologen resides within supercage whilst $Ru(bpy)_3^{2+}$ is sterically excluded from matrix (B) $Ru(bpy)_3^{2+}$ is entrapped and viologen is unable to diffuse from surface to inner supercages (C) Both $Ru(bpy)_3^{2+}$ and viologen are located within supercages.

Mallouk *et al.* studied a number of zeolite materials exchanged with viologen whilst a bulky sterically excluded Ruthenium donor complex (Figure 1.19 (A) configuration) was tethered to the acceptor with an aliphatic chain spacer (Figure 1.20).[70,71] The small acceptor moiety was confirmed to reside within the inner zeolite structure by solid state NMR studies and the donor remained on the solution side of the interface, too large to enter the supercages. The rate of forward electron transfer with varying spacer lengths was monitored through the decay of the MLCT excited state at 360nm. They found that the rate of forward electron transfer rate decreased with increasing spacer length. However, the quantum yield of the charge separated species increased to a maximum at five methylene spacer molecules, and then decreased rapidly with further methylene spacers. Overall, the forward and back electron transfer rates are one to two orders of magnitude slower than solution phase processes.

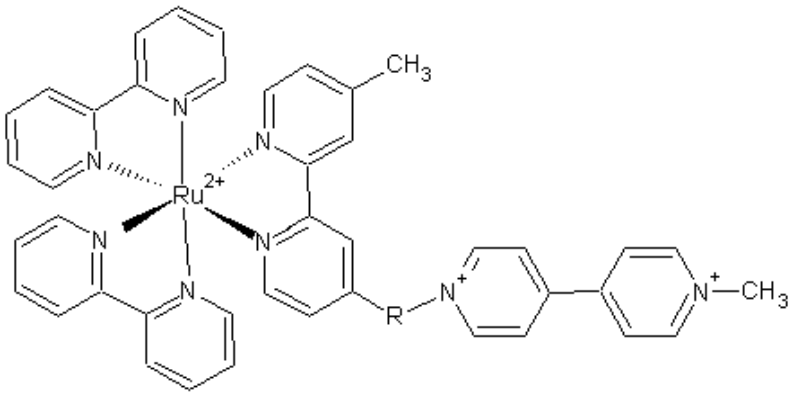

Figure 1.20: $Ru(bpy)_3^{2+}$-viologen system. R=$(CH_2)_n$ n=2-5, 7, 8.

The second situation (Figure 1.19 B) was examined by Dutta *et al.* involving $[Ru(bpy)_3]^{2+}$ entrapped within Zeolite-Y with the acceptor propylviologen sulfonate (PVS) remains outside the pore structure as the sulphonate groups are repelled by the negatively charged framework.[72] They noted that upon photolysis of a suspension of the zeolite material in PVS solution the PVS radical anion was generated in tandem with slowed back electron transfer compared to solution phase. The enhanced charge separation was attributed again to increased donor-acceptor distance resulting from the negatively charged anion interacting with the outer framework.

The third configuration (Figure 1.19 C) is the co-entrapment of both donor and acceptor within the zeolite framework. Depending on the loading of each compound, they may occupy adjacent supercages or in the case of smaller species even occupy the same supercage.

Such a system was studied by Dutta *et al.* who examined photoexcitation of zeolite entrapped $[Ru(bpy)_3]^{2+}$ adjacent to cages containing methyl viologen.[73] They found this led to the formation of the viologen radical cation ($MV^{\bullet+}$) whose appearance was monitored by UV-vis and raman spectroscopy. The radical cation was stable on the hour time scale with eventual back electron transfer to $[Ru(bpy)_3]^{3+}$ observed by monitoring the gradual increase in the

$[Ru(bpy)_3]^{2+}$ absorbance. They also noted the concomitant decay of the $MV^{+\bullet}$ absorbance, its rate of decay similar to the recovery rate of the donor dication.

1.4 Energy transfer within Zeolites

Energy transfer is a common photophysical process whereby an excited donor molecule transfers its energy to an acceptor molecule. Control over spatial arrangement is crucial to successful supramolecular compounds and as with the examples of electron transfer examined, the regular structure of zeolite material provides an interesting substrate with which to arrange species capable of energy transfer.

Energy transfer was first reported in zeolite Y in 1980 by Strome *et al*. who observed long range energy transfer between copper (I) ions and oxygen in zeolite Y.[74] Since then much work has been conducted on energy transfer between organic species adsorbed into various types of zeolite. Calzaferri *et al.* conducted extensive studies on energy migration and energy transfer in dye-doped zeolite L.[75,76,77,78,79,80] They take advantage of the confined zeolite geometry to ensure only monomers are formed thus preventing aggregation of the dyes that results in fast radiationless deactivation. Zeolite L crystals were prepared and loaded with pyronine which emits in the green (510 nm). The crystals end channels were then doped with oxonine which emits in the red (597 nm).[77] Upon irradiation of the doped crystal, fast energy migration occurs along the internal chains of pyronine and finally transfers its energy to the oxonine end molecule and where red emission is observed (Figure 1.21).

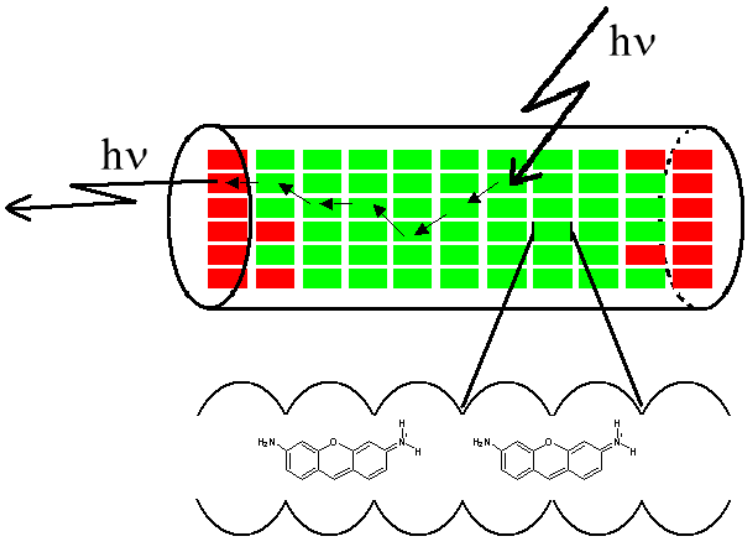

Figure 1.21: Above: Representation of energy migration (straight arrows) of pyronine (green squares) and oxonine (red squares) in zeolite L. Below: Orientation of pyronine in zeolite L channels *(*Calzaferri *et al.*, *J. Phys. Chem. B* **1999**, *103*, 1250).[77]

Due to the inherent anisotropy of the system the excitation energy migrates in a direction parallel to the cylindrical channels of zeolite L. The anisotropy is a consequence of the pyronine electronic transition moment being aligned parallel to the channel axis. The energy transfer mechanism they attributed to a Förster mechanism.

Calzaferri *et al.* reported on a similar system in which the injection of electronic excitation energy was accomplished using a ruthenium polypyridyl complex with subsequent energy transfer to the acceptor molecule oxazine.[81] The ruthenium tris bipyridine derivative complex possessed a four unit phenylene chain appended to one of the bipyrdine ligands bound electrostatically to the channel entrances. This acted as a functional 'stopcock', allowing efficient energy transfer from the donor and also preventing the leaching of the acceptor dye molecules. The phenylene chain portion was thought to reside within the zeolite channel while the bulkier ruthenium cationic portion remains on the outer surface providing the electrostatic attraction. Excitation of the ruthenium complex leads to very efficient triplet to singlet energy transfer from the Ru^{2+} complex to the oxazine 1 residing in the internal channels.

Notably, the oxazine 1 lifetime increases from between 0.5 and 1.3 ns (solvent dependant) to 3 ns when internalised in the framework. The authors attribute this to steric hindrance of the diethyl groups which prevents fast radiationless decay.

Thomas *et al.* examined energy transfer between naphthalene and anthracene co-included in zeolite Y.[82] They observed singlet-singlet energy transfer, with the fluorescence intensity quenching of naphthalene obeying Stern-Volmer kinetics. The authors also assert that because the diffusion co-efficient of the molecules is slow relative to the temporal window, the system can be treated as static rather than dynamic. The results of the Stern-Volmer plot support this view, the slopes of lifetimes and fluorescence ratios being expected to be co-linear in a purely dynamic environment (Figure 1.22).

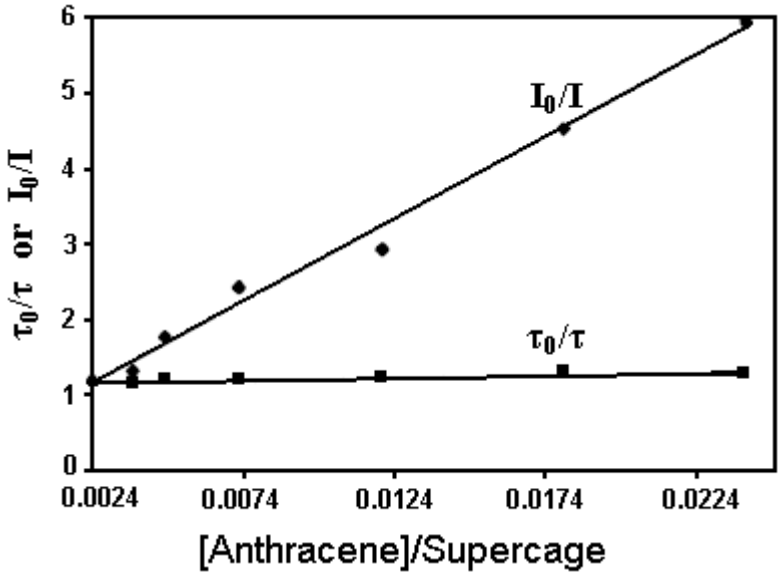

Figure 1.22: Stern-Volmer plot for quenching of naphthalene fluorescence emission and *S*1 lifetime by anthracene (Thomas *et al.*, *Langmuir,* **2000**, *16*, 4912).[82]

Hashimoto *et al.* observed energy transfer from zeolite Y included aromatic guests benzophenone and naphthalene to the rare earth cation terbium which was acting as a charge compensating cation absorbed on the internal zeolite

framework.[83] Since terbium does not complex with the donor molecules, they believe the sensitization is due to the close confinemement of the donor-acceptor pair provided by the zeolite.

The intrazeolitic cavities of zeolites have also been explored as hosts for rare earth complexes. Alvaro *et al.* prepared europium complexes within zeolite-Y with various ligands capable of different degrees of coordination.[84] Trivalent lanthanides extinction coefficients are generally too small for effective direct excitation to yield useful emission. Absorption of light by a suitable organic chromophore complexed to a lanthanide ion can lead to triplet energy transfer to the lanthanide ion's emitting level and subsequent long-lived luminescence. They found an increase in the phosphorescent yield and lifetime of the zeolite entrapped complexes compared to solution. They attributed these increases to the increased conformational rigidity of the cavity caused by the presence of large amounts of ligand and the reduction in the number of coordinating water molecules which result in deactivation of the europium excited state.

1.5 General Photochemistry

The preliminary step in any photophysical or photochemical process is absorption of a photon by a molecule or atom. If the energy of the radiation matches for instance, the energy gap between two electronic orbitals, this energy can promote the species to an electronically excited state. The mechanism of absorption is based on the interaction of the electric vector of the radiation with the electric dipole of a molecule. The oscillating electric field produces an equivalent oscillation in the electric dipole of the molecule and therefore a change in its charge distribution.[85] The probability of an absorption event occurring between a photon and an entity possessing an electric dipole is expressed in Equation 1.1.

$$P_n = \frac{4E_0(x)^2 \left|\mu_{xnm}\right|^2}{\hbar^2} \frac{\sin^2 1/2 \Delta\omega t}{\Delta\omega^2} \qquad \textbf{Equation 1.1}$$

where P_n is the probability of absorption, E_0 is the excitation energy, μ_{xnm} the transition dipole moment which is related to electron distribution in the ground and excited state coupled with electron spin and nuclear overlap integrals, $\hbar = \frac{h}{2\pi}$ and $\Delta\omega$ is the angular frequency offset i.e. the difference between the transition frequency and the radiation frequency. The probability is related to the square of the transition dipole moment and bears an inverse relationship with $\Delta\omega^2$, thus the probability of absorption increases as the incident radiation frequency coincides with the transition frequency.

Whether a transition dipole moment associated with a particular species exists is governed by a number of selection rules. If a transition is forbidden no absorption is expected to occur. However, in reality these 'rules' are frequently broken (for instance, due to instantaneous loss of symmetry in a molecule) but are still good indicators of expected magnitudes of transitions.[75]

There are two major selection rules for absorption transitions.

1. Transitions between different spin multiplicities are forbidden, i.e. singlet state to a triplet state. However, the presence of spin orbit coupling can result in relaxation of this rule. Such coupling is prevalent in molecules possessing heavy atoms such as bromine as the degree of coupling has a 4^{th} power relationship with atomic number.

2. Symmetry forbidden transitions: Transitions can be forbidden due to symmetry considerations, however vibronic coupling causes instantaneous relaxation of formal symmetry rendering the transition possible, but generally weak.

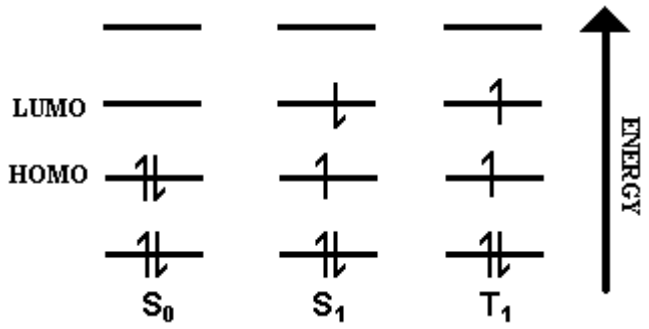

Figure 1.23: Electron configurations for singlet and triplet states. S_0 is the Ground state, electrons are paired. S_1 is the first excited singlet state and T_1 = first excited triplet state.

1.5.1 Spin

In the ground state, if the electrons in the highest occupied molecular orbital (HOMO) are paired and possess antiparallel spins, the multiplicity of the state can be calculated using the relation (M = 2S+1). If S=0 then the state is singlet in nature (Figure 1.23). If the excited state electron has a parallel spin to the HOMO electron, the same situation applies and the excited state is singlet in nature. If however the spin of the excited state electron is antiparallel the total spin quantum number will be 1 and the multiplicity will be

three, known as a triplet state. A doublet state is also possible (not shown) resulting from radical ions.

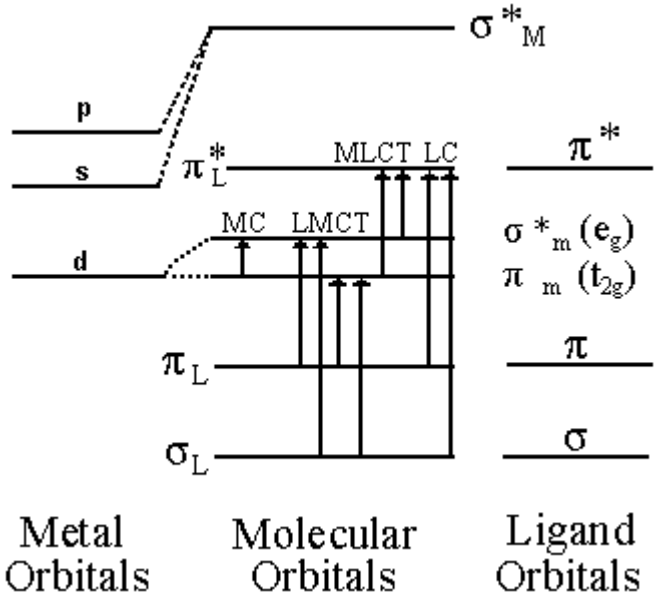

Figure 1.24: Energy-level diagram for an octahedral transition metal complex (Balzani *et al.*, *Chem. Rev.* **1996**, *96*, 759).[86]

1.5.2 Electronic structure and electronic transitions

A schematic energy-level diagram for an octahedral transition metal complex is shown in Figure 1.24. The various electronic transitions are also displayed. Ground state transition metal complexes in their typical oxidation states, have their σ_L and π_L orbitals completely filled, the π_M orbitals are either filled or partially filled and the upper orbitals are typically unoccupied.[76] Transitions localized on the metal center are known as metal centred (MC) or ligand field transitions. When transitions are localised on the ligands, they are known as ligand centred (LC) transitions. In the case where charge is transferred from a metal molecular orbital (MO) to a ligand MO or from ligand MO to metal MO, are known collectively as Charge transfer (CT) transitions. Referring to Figure 1.24, these CT transitions can be ligand to metal or metal to ligand charge transfers, LMCT or MLCT respectively. Other transitions are possible but occur less frequently such as charge transfer to solvent CTTS or between two orbitals of two different ligands residing on the same metal center LLCT.[76]

1.5.3 Photophysical pathways

The first step in a photophysical or photochemical pathway is the absorption of a photon of suitable energy by a molecule. This forms an unstable excited state molecule that typically deactivates by one of the following mechanisms shown in Figure 1.25.

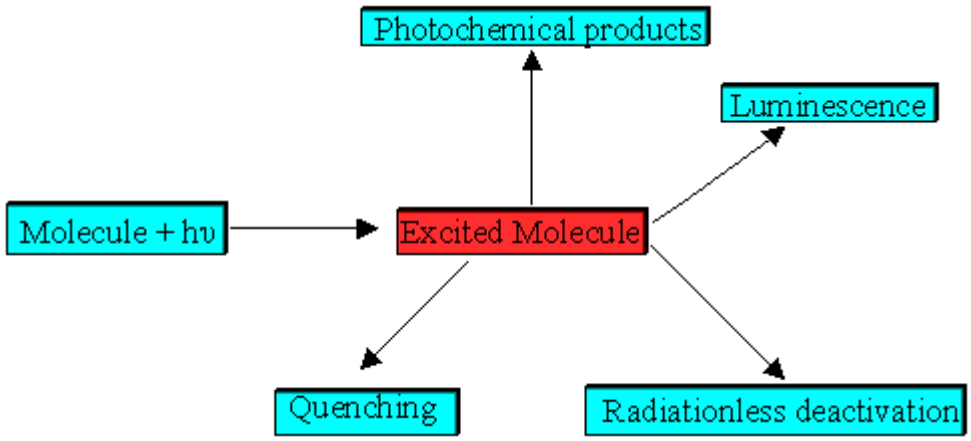

Figure 1.25: Excited state deactivation pathways.[87]

1.5.4 Photophysical processes

The Jablonski diagram (Figure 1.26) illustrates the photophysical processes involved in the deactivation of an excited state molecule.

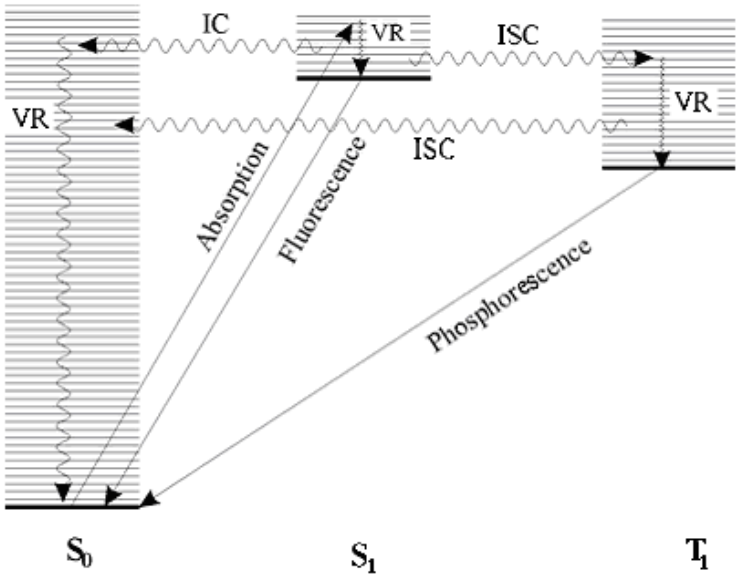

Figure 1.26: Jablonski diagram showing deactivation processes.[88]

As stated the first step in a photophysical process is the absorption of a photon of light. This process occurs in the 10^{-15} s timescale and as such no displacement of the nuclei occurs. This assertion is the basis of the Frank-Condon principle.[89] Some examples of absorption spectra with associated potential energy diagrams are shown in Figure 1.27.

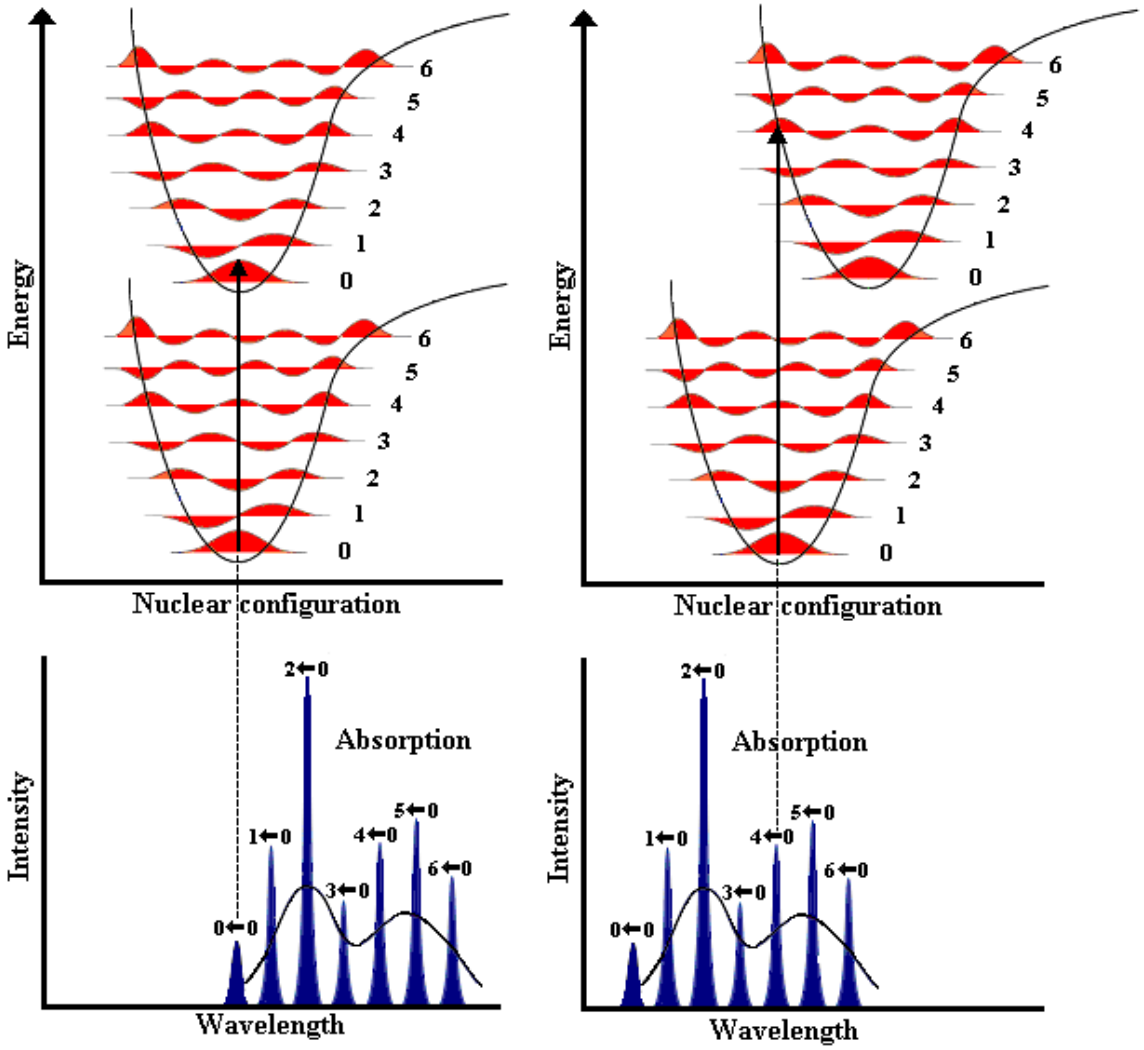

Figure 1.27: Potential energy diagrams showing vertical transitions (top) and the corresponding absorption profiles (bottom).[90]

An absorption event can result in the excitation of a molecule to an upper vibrational level of an electronic state. From this state the following processes can occur.

1.5.4.1 Internal Conversion

Internal Conversion (**IC**) is an iso-energetic transition between electronic states possessing the same multiplicity. If the transition crosses to a higher vibrational level of the electronic state, the energy can be dissipated via

vibrational relaxation (**VR**) such as collisions with solvent molecules, this process is illustrated in Figure 1.26 by the non-radiative transition $S_1 \rightarrow S_0$.

1.5.4.2 Intersystem crossing

Intersystem crossing (**ISC**) is an isoenergetic forbidden process which involves a transition between states of different multiplicity such as $S_1 \rightarrow T_1$. Spin orbit coupling can result in a relaxation of this forbidden process. As with internal conversion vibrational relaxation dissipates excess vibrational energy following crossover.

1.5.4.3 Fluorescence

Emission of a photon when relaxation from one electronic state to another of the same multiplicity occurs is known as fluorescence. In 1.26 this process is $S_1 \rightarrow S_0$, which is common in fluid solutions. The wavelength of the emission λ_{max} is longer than that of the associated absorption due to thermal losses before emission (Stokes rule), see Figure 1.28.

1.5.4.4 Phosphorescence

Phosphorescence is the emission of a photon when relaxation from one electronic state to another of a different multiplicity occurs, the process is represented by $T_1 \rightarrow S_0$ in Figure 1.26. This process is formally spin forbidden but does arise due to spin orbit coupling. The phosphorescence spectrum is observed at longer wavelengths than fluorescence as the triplet state T_1 resides at lower energy than the singlet state S_1 due to spin correlation.

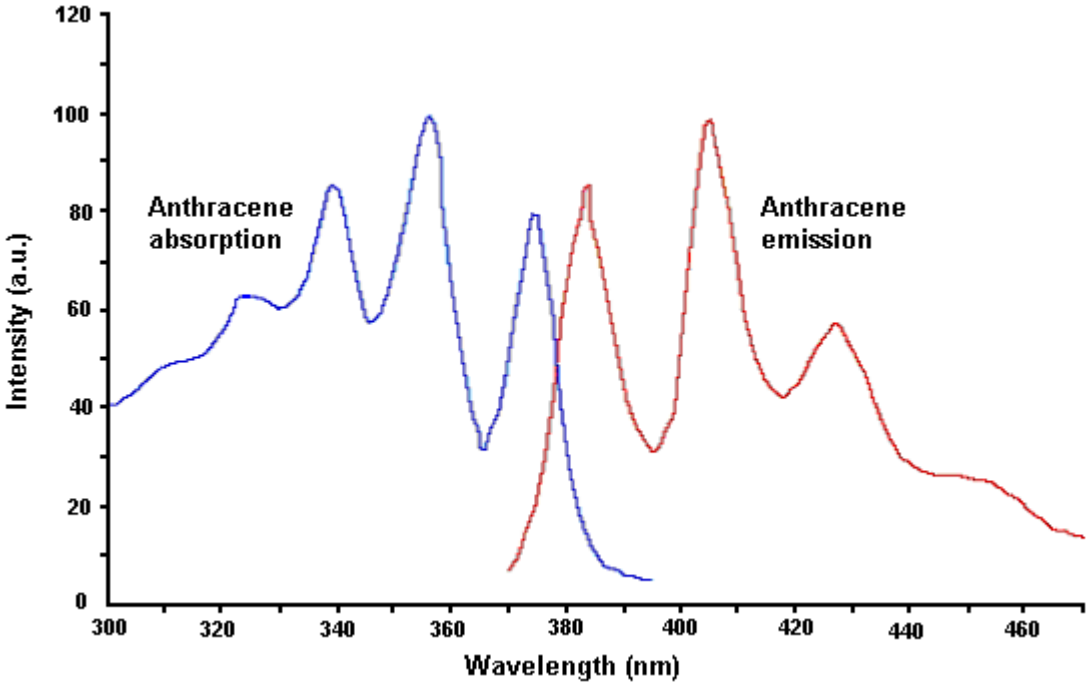

Figure 1.28: Stokes shift and spectral overlap for anthracene.[91]

1.6 Kinetics of photophysical processes

Consider a molecule M absorbing a photon hν to yield M*. If the only process of deactivation available this molecule is fluorescence, which is spontaneous, then the rate of disappearance of the excited state M* obeys first order kinetics:

$$-\frac{d}{dt}[M^*] = k_f^0[M^*] \qquad \textbf{Equation 1.2}$$

where k_f^0 is the natural fluorescence rate coefficient. Integration of the above leads to:

$$[M^*] = [M^*]_0 e^{-k_f^0 t} \qquad \textbf{Equation 1.3}$$

The natural fluorescence lifetime τ_f^0 is the reciprocal of the natural fluorescence radiative rate coefficient:

This is the time for the population of the excited state molecules to decrease to 1/eth of initial concentration. This assumes no non-radiative processes are present in the system. If for example, internal conversion was a competitive process, first order kinetics are still obeyed but with a rate coefficient k_f:

$$[M^*] = [M^*]_0 e^{-k_f t} \qquad k_f = k_f^0 + k_{IC} \qquad \textbf{Equation 1.4}$$

The fluorescence lifetime now becomes:

$$\tau_f = \frac{1}{k_f} \quad \text{or} \quad \tau_f = \frac{1}{k_f^0 + k_{IC}} \qquad \textbf{Equation 1.5}$$

The rate coefficient k_f includes other modes of decay. The fluorescence lifetime can be then calculated from the reciprocal of the summation of all the decay rate constants. The relationship between natural fluorescent lifetime and actual fluorescent lifetime is expressed as follows:

$$\tau = \tau_0 \phi_f \qquad \textbf{Equation 1.6}$$

where ϕ_f is the quantum yield of fluorescence which is the fraction of excited molecules that return to the ground state via emission of fluorescence photons.[92]

1.7 Quenching of excited states

Any species that increases the rate of decay of an electronically excited state to a lower electronic state is a quencher.[92] Some possible photophysical quenching processes are shown in Figure 1.29.

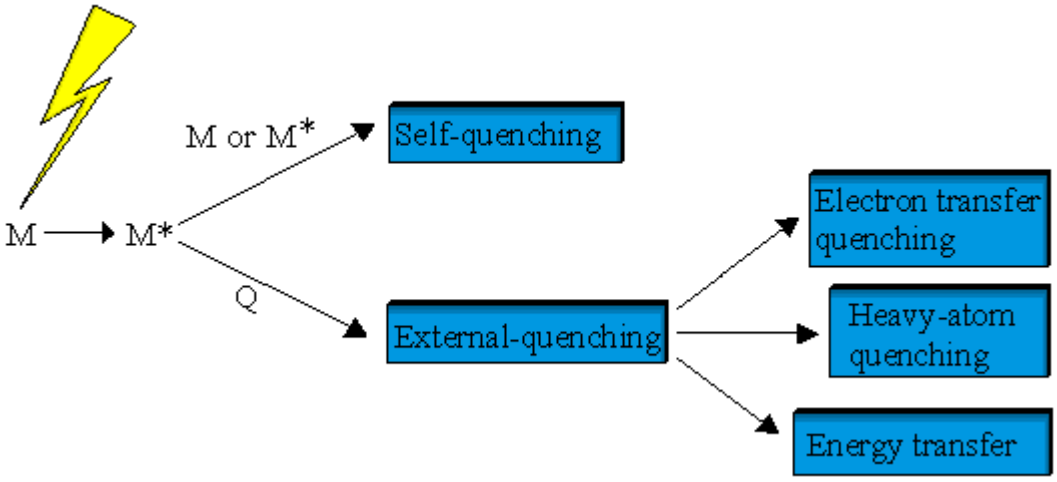

Figure 1.29: Photophysical quenching processes.[92]

1.7.1 Self quenching

This is the quenching of an excited molecule state by the same molecular species. This kind of interaction could be quenching by a ground state molecule or by an excited state molecule. The possible quenching mechanisms are the same as those for an external quencher outlined below.

1.7.2 Heavy-atom quenching

An excited state molecule having a heavy atom internally, for example a bromine substituent or externally in the form of collisions with heavy atoms in solution can increase the probability of intersystem crossing, due to an increase in spin-orbit coupling.

1.7.3 Electronic energy transfer

Electronic energy transfer at its simplest can be represented by:

$$A^* + B \rightarrow A + B^*$$

The excited state A* is quenched by B, and results in B being left in an electronically excited state. This type of energy transfer can occur by either a Förster or Dexter mechanism.

1.7.3.1 Förster energy transfer

This is a coulombic mechanism involving a dipole-dipole interaction that is operable up to 100 Å. It involves the dipole oscillation of the excited state donor coupling with the dipole oscillation of the acceptor. This increased oscillation promotes an electron in the quencher to an excited state and simultaneously de-excites the donor (Figure 1.30).

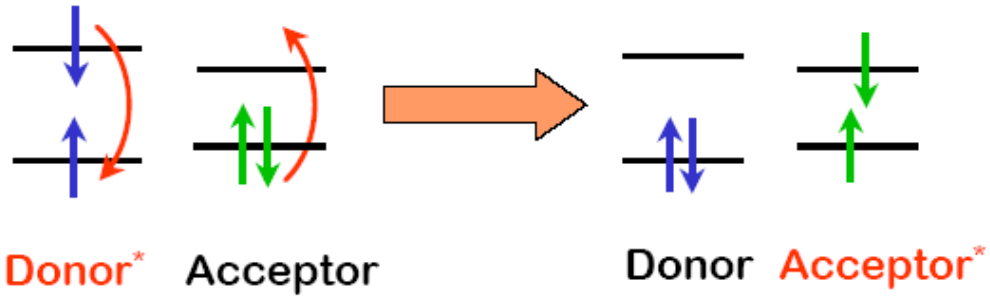

Figure 1.30: Förster energy transfer

Förster derived Equation 1.7 to evaluate the rate constant for energy transfer k_{en}:

$$k_{en} = 5.97 X 10^{-25} (\Phi_D / n^4 \tau_D r^6) \int_0^{\infty} F_D(\bar{\nu}) \varepsilon_A(\bar{\nu})\, d\bar{\nu} / \bar{\nu}^4$$

$1/r^6$ Dependance — Spectral overlap

Equation 1.7

where Φ_D is the quantum yield for the donor emission, τ_D is the lifetime of donor emission, n is the refractive index of the medium in the wavelength range of the spectral overlap, r is the distance between the two interacting species. The pre-integral displays the $1/r^6$ relationship with donor and

acceptor separation. The integral is the spectral overlap between luminophore emission and acceptor absorption and represents the thermodynamic constraints of energy transfer. Spin multiplicity of interacting molecules is conserved.

Since this work deals in particular with resonance energy transfer, the origin of Equation 1.7 is elucidated below.

The rate of coulombic energy transfer is directly related to the magnitude of the two interacting dipoles.[93] The interaction energy is related to the two dipole moments as follows:

$$E(dipole-dipole) \propto \frac{\mu_D \mu_A}{R_{DA}^3} \qquad \textbf{Equation 1.8}$$

Where μ_D and μ_A are the instantaneous dipole moments of the donor and acceptor species and R_{DA} is the distance between the two dipoles. The oscillator strength (f) of a transition produced by the interaction of light on an electric dipole is related to the square of the induced dipole moment:[94,95,96]

$$f \propto \mu_i^2 \qquad \textbf{Equation 1.9}$$

Where f is the oscillator strength and μ_i is the dipole moment induced by the electronic transition. The consequence of this is the degree of interaction between two dipoles μ_D and μ_A is related to the oscillator strengths of the donor (f_D) and acceptor species (f_A). The oscillator strengths are in turn related to the radiative lifetime and extinction coefficient associated with the transition. Förster determined the rate of coulombic energy transfer, k_{en} as:

$$k_{en} \rightarrow E^2 \propto \left(\frac{\mu_D \mu_A}{R_{DA}^3} \right)^2 = \frac{\mu_D^2 \mu_A^2}{R_{DA}^6} \qquad \textbf{Equation 1.10}$$

The relationship between transition moments and measurable quantities can be described by the following:

$$\mu_D^2(D^* \Leftrightarrow D) \rightarrow \int \varepsilon_D \text{ or } k_D^0$$
$$\mu_A^2(A^* \Leftrightarrow A) \rightarrow \int \varepsilon_A \text{ or } k_A^0$$

Equation 1.11

Where $\int \varepsilon$ is the integrated extinction coefficient of an absorption band and k^0 is the natural radiative rate. Replacing the transition moments with these experimental quantities yields:

$$k_{en} \rightarrow \frac{k_D^0 \int \varepsilon_A}{R_{DA}^6}$$

Equation 1.12

Coulombic energy transfer also requires that the spectral overlap of the donor emission and acceptor absorption spectra to be considered. This is result of the requirement for resonance between the donor and acceptor oscillating dipoles. Considering this requirement as well as various experimental parameters yields the more familiar version expressed in Equation 1.13:

$$k_{en} = k \frac{\kappa^2 k_D^0}{R_{DA}^6} J\left(\varepsilon_A\right)$$

Equation 1.13

The term k is constant and can be determined by experimental set-up and κ^2 is the orientation of the dipoles in space, generally taken to be ⅔ if the dipoles are randomly orientated. For systems with non-random orientations which might occur in rigid glasses and polymer systems, a different value must be assigned. The term $J(\varepsilon_A)$ is the spectral overlap integral which includes the extinction coefficient of the acceptor species.

1.7.3.2 Dexter-type mechanism

The Dexter mechanism is an electron exchange operable over much shorter distances than the Forster mechanism due to the requirement for orbital overlap of acceptor and donor molecules. In electronic interactions it involves

the transfer of an electron from the HOMO of the excited state molecule to the LUMO of an acceptor and the simultaneous transfer of a ground state electron from the acceptor HOMO to the donor HOMO (Figure 1.31).[97] The distance relationship is exponential with donor-acceptor separation, with efficiency of energy transfer falling rapidly at distances greater than 10Å. The rate of Dexter energy transfer is expressed as follows:

$$k_{en} = \left(\frac{2 \mid H_{AB} \mid^2}{h}\right)\left(\frac{\pi^3}{\lambda RT}\right)\exp\left(-\frac{\Delta G^{\neq}}{RT}\right) \quad \textbf{Equation 1.14}$$

where $|H_{AB}|$ is the electronic coupling matrix, h is Plancks constant, λ is the reorganisational energy, R is the gas constant, T the absolute temperature and $\Delta G^{\neq}$ is the Gibbs free energy of activation.

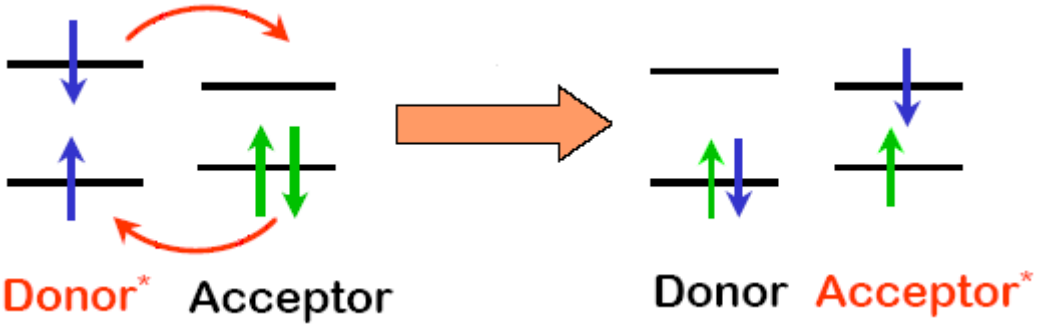

Figure 1.31: Dexter energy transfer

1.8 Excited state redox properties

The excited states of diamagnetic species with closed shell ground states are better oxidising and reducing agents than their associated ground states.[94] When an electron is excited to a higher orbital, it is easier to remove that electron because it now has a lower ionisation potential. The vacancy created by the excited state also increases the species electron affinity. Figure 1.32 illustrates these processes.

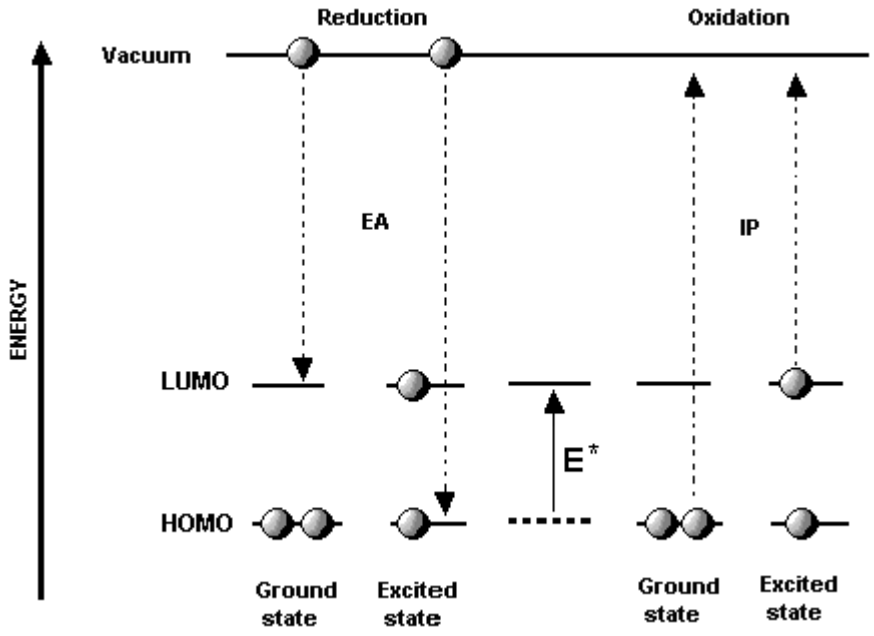

Figure 1.32: Orbital representation of reduction and oxidation processes in the ground and excited state (Balzani *et al.*, 'Photosensitization and photocatalysis using inorganic and organometallic compounds', Kluwer Academic Publishers, 1993).[98]

1.9 Photoinduced electron transfer

Photoinduced electron transfer is often responsible for fluorescence quenching.[78] Photoinduced electron transfer occurs when an electron is transferred from an excited donor LUMO to a ground state molecule. This is represented schematically in Figure 1.33.

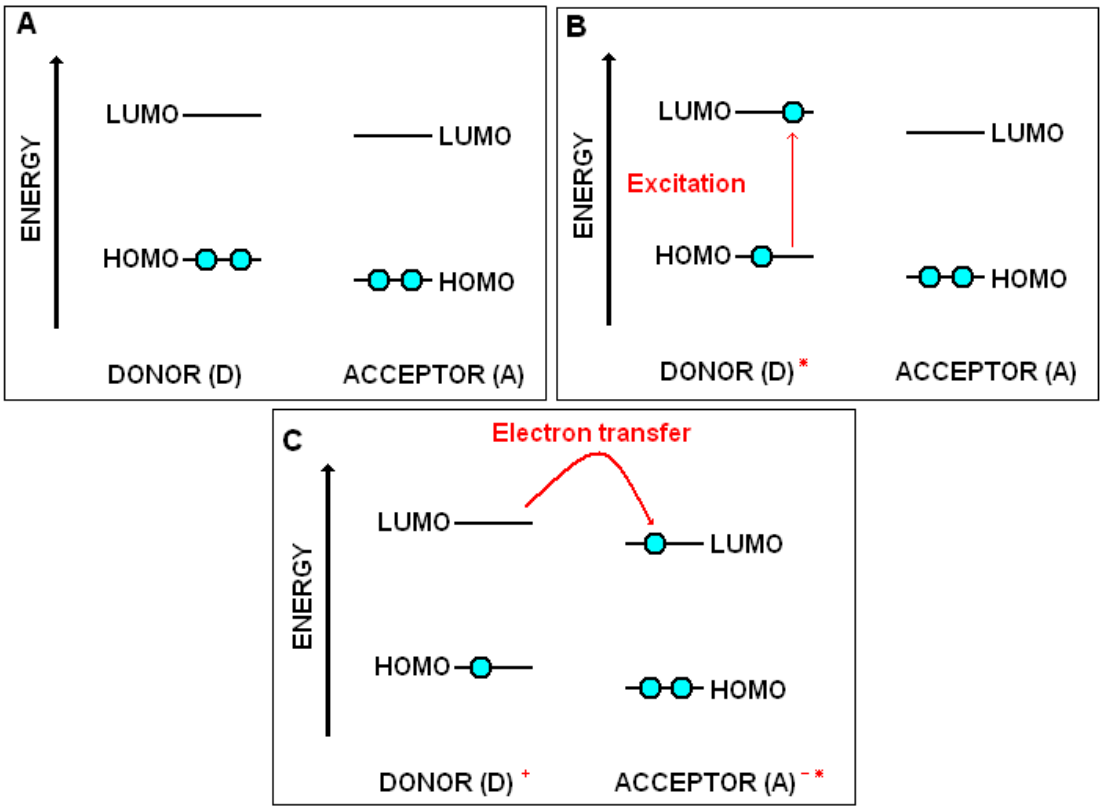

Figure 1.33: Molecular orbital schematic for photoinduced electron transfer. A) Initial states of donor and acceptor, B) donor is electronically excited by photon and C) Electron transfer to acceptor occurs yielding charge-transfer complex $[D^{+}A^{-}]^{*}$.

The overall change in free energy for an electron transfer is determined from redox potentials and excitation energies, expressed by the Rehm-Weller equations (Equation 1.14). Two additional terms are included if measurements are made in solution to include solvation effects and coulombic energy of ion pairs formed:[97]

$$\Delta G^{0} = E^{0}_{D^{\bullet+}/D} - E^{0}_{A/A^{\bullet-}} - \Delta E_{00}(D) - \Delta H_{solv} - \frac{e^{2}}{4\pi\varepsilon r}$$

Equation 1.14

where $E^{0}_{D^{\bullet+}/D}$ and $E^{0}_{A/A^{\bullet-}}$ are the standard ground-state oxidation and reduction potentials of donor D and acceptor A, ΔE_{00} is the zero-zero spectroscopic energy for the acceptor and donor species, e is the electron

charge, ε is the dielectric constant of the solvent and r is the distance between the two ions and ΔH_{solv} the enthalpy term for solvation.

1.10 Luminescence emission quenching

The kinetic aspects of an encounter between a quencher molecule Q and an excited state molecule M* in solution or in a solid matrix will be considered now. Measuring the steady state decrease in emission intensity or the rate of excited state emission decay, whilst varying the quencher concentration allows for the monitoring of quenching processes.[98]

There exist two kinetic possibilities involving the intermolecular interaction of an excited state molecule with a quencher molecule. The interaction can be of a static or dynamic nature.[94]

1.10.1 Stern-Volmer kinetics and dynamic quenching

The decay of an excited state molecule M* obeys Equation 1.15:

$$\frac{d[M^*]}{dt} = -(k_{TOTAL} + k_q[Q])[M^*] \qquad \textbf{Equation 1.15}$$

where k_{TOTAL} is $k_r + k_{nr}$ = $1/\tau_0$ and τ_0 is the lifetime in the absence of any any quenching:

$$= -(1/\tau_0 + k_q[Q])[M^*] \qquad \textbf{Equation 1.16}$$

Integration of which gives:

$$[M^*] = [M^*]_0 \exp\{-(1/\tau_0 + k_q[Q])t\} \qquad \textbf{Equation 1.17}$$

Fluorescence intensity is proportional to the concentration of M* and is given by:

$$i(t) = k_r[M^*] \qquad \textbf{Equation 1.18}$$

where k_r is the radiative rate constant of M*, substitution yields:

$$i(t) = k_r[M^*]_0 \exp\{-(1/\tau_0 + k_q[Q])t\} \qquad \textbf{Equation 1.19}$$

$$= i(0) \exp\{-(1/\tau_0 + k_q[Q])t\} \qquad \textbf{Equation 1.20}$$

The lifetime decay according to single exponential kinetics whose is given by:

$$\tau = \frac{1}{\frac{1}{\tau_0} + k_q[Q]} = \frac{\tau_0}{1 + k_q\tau_0[Q]} \qquad \textbf{Equation 1.21}$$

Therefore:

$$\frac{\tau_0}{\tau} = 1 + k_q\tau_0[Q] \qquad \textbf{Equation 1.22}$$

The fluorescence quantum yield in the presence of quencher is:

$$\Phi = \frac{k_r}{k_r + k_{nr} + k_q[Q]} = \frac{k_r}{1/\tau_0 + k_q[Q]} \qquad \textbf{Equation 1.23}$$

The fluorescence quantum yield without quencher is:

$$\Phi_0 = k_r\tau_0 \qquad \textbf{Equation 1.24}$$

Combining Equations 1.23 and 1.24 above gives:

$$\frac{\Phi_0}{\Phi} = \frac{I_0}{I} = 1 + k_q \tau_0 [Q] = 1 + K_{SV}[Q] \qquad \textbf{Equation 1.25}$$

Since $\frac{I_0}{I} \propto \frac{\Phi_0}{\Phi}$ a plot of $\frac{I_0}{I}$ against various quencher concentrations should yield a linear plot if the quenching is dynamic with a slope equal to $k_q \tau_0$.

If the process is diffusion limited, then the rate k_q is equal to the diffusional rate constant k_{diff}. The Smoluchowski equation describes this:

$$k_{diff} = 4\pi N_A^{'} R_c D \qquad \textbf{Equation 1.26}$$

where $N_A^{'}$ is equal to $N_A / 1000$, R_c is the distance of closest approach, which is the sum of the radii of the quencher and emitter and D is the mutual diffusion coefficients of the two species. The diffusion rate sets an upper limit for the rate of bimolecular reaction in solution phase of approximately 1 X 10^{10} $mol^{-1}s^{-1}$. For example the dynamic quenching of excited state $[Ru(bpy)_3]^{2+}$ by $[Fe(bpy)_3]^{2+}$ in water was determined by Creutz *et al.* ultilising the Stern-Volmer formulation.[99] They attributed the mechanism to energy transfer and determined the rate constant to be 1.0 X 10^9 $mol^{-1}s^{-1}$.

1.10.2 Static quenching

Static quenching can apply to a situation where a donor and acceptor species are immobilised such as in a sol-gel or zeolite system. The donor-acceptor pair effectively form a ground state non-fluorescent complex.

1.10.3 Sphere of effective quenching

When the excited state molecule and quenching species remain stationary for duration of the excited state lifetime, the Perrin model can be utilised. This model proposes that a volume exists around the emitter whereby inclusion of a quencher molecule within this volume results in complete quenching of its

luminescence.[78] The model assumes that if the quencher molecule is outside of this critical radius then its fluorescence remains unaffected. This is represented in Figure 1.38.

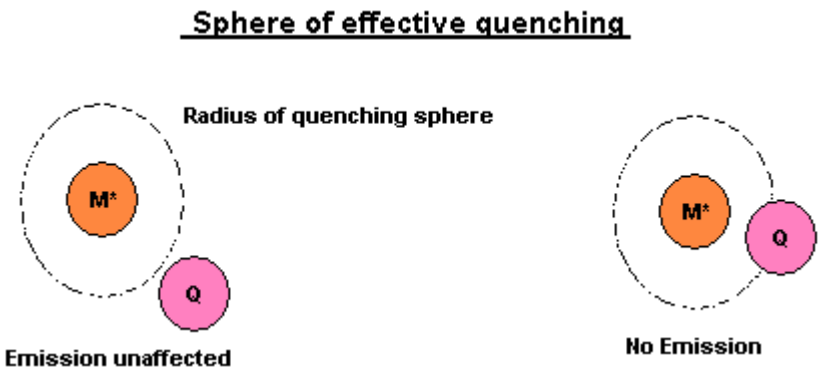

Figure 1.38: Perrin Model of Static quenching

No change is expected for the excited state lifetimes within this model as quenching is either total or unaffected. The luminescence intensity however is expected to decrease exponentially with quencher concentration. The derivation of the Perrin model is as follows:

The probability that n quenchers reside within the quenching volume V_q obey a Poisson distribution:

$$P_n = \frac{\langle n \rangle^n}{n!} \exp(-\langle n \rangle) \qquad \textbf{Equation 1.27}$$

where $\langle n \rangle$ is the mean number of quenchers in the volume V_q and $\langle n \rangle = V_q N_a [Q]$, then the probability that there is no quencher within V_q is:

$$P_0 = \exp(-\langle n \rangle) = \exp(-V_q N_a [Q]) \qquad \textbf{Equation 1.28}$$

Since emission intensity is proportional to P_0, then:

$$\frac{I_0}{I} = \exp(V_q N_a [Q]) \qquad \textbf{Equation 1.29}$$

A plot of $\ln\left(\frac{I_0}{I}\right)$ versus quencher concentration will yield a linear plot, from which V_q may be calculated.

1.10.4 Formation of a ground state non-fluorescent complex

A simple non-fluorescent 1:1 complex exists in equilibrium with its individual elements:

$$M + Q \rightleftharpoons MQ \qquad \textbf{Equation 1.30}$$

The stability constant for this is:

$$K_S = \frac{[MQ]}{[M][Q]} \qquad \textbf{Equation 1.31}$$

Combing this with the mass conservation law $[M_0] = [M] + [MQ]$, the following is true:

$$\frac{[M]}{[M]_0} = \frac{1}{1 + K_S[Q]} \qquad \textbf{Equation 1.32}$$

At low concentrations fluorescence intensities are proportional to the concentrations, then this can be rewritten as:

$$\frac{I_0}{I} = 1 + K_S[Q] \qquad \textbf{Equation 1.33}$$

The excited state lifetime is expected to remain unchanged whilst the fluorescence intensity decreases linearily. A study carried out by Seery *et al.* on the interactions of between [$Ru(bpy)_3^{2+}$] and the polyoxotungstate anion $[S_2W_{18}O_{62}]^{4-}$ showed such behaviour.[100] They observed a large drop in emission intensity as the ion clusters formed. The ion cluster

$[Ru(bpy)_3]_2[S_2W_{18}O_{62}]$ had a lifetime substantially shorter than free $[Ru(bpy)_3^{2+}]$ and was found to be independant of tungstate concentration, indicative of static quenching.

1.10.5 Deviations from simple quenching models

In systems where partial diffusion of the quencher, donor or both is possible, there is a mixture of static and dynamic quenching. Any plots using standard Stern-Volmer or Perrin formulations will result in deviations from linearity usually (but not always) in the form of upward curvatures. There are a number of modified formulations which will estimate both the dynamic and static components contributions in systems where there is mixing of the two mechanisms (Figure 1.40).

Abe and co-workers studied photoinduced electron transfer between $[Ru(bpy)_3]^{2+}$ and MV^{2+} (methyl viologen) dispersed in poly(ethylene oxide).[101] They determined that electron transfer occurs by both a dynamic and static mechanism. The Stern-Volmer plot showed upward curvature and the change in the τ_0/τ slope typical (Figure 1.39) of a mixed dynamic/static quenching system.

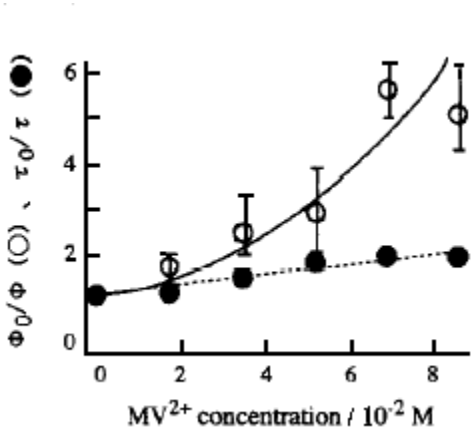

Figure 1.39: Stern-Volmer plot based on $[Ru(bpy)_3]^{2+}$ emission and lifetime with increasing concentration of MV^{2+} co-dispersed in ploy(ethylene oxide). (Abe *et al.*, *React. Funct. Polym.* **1998**, *37*, 133).[101]

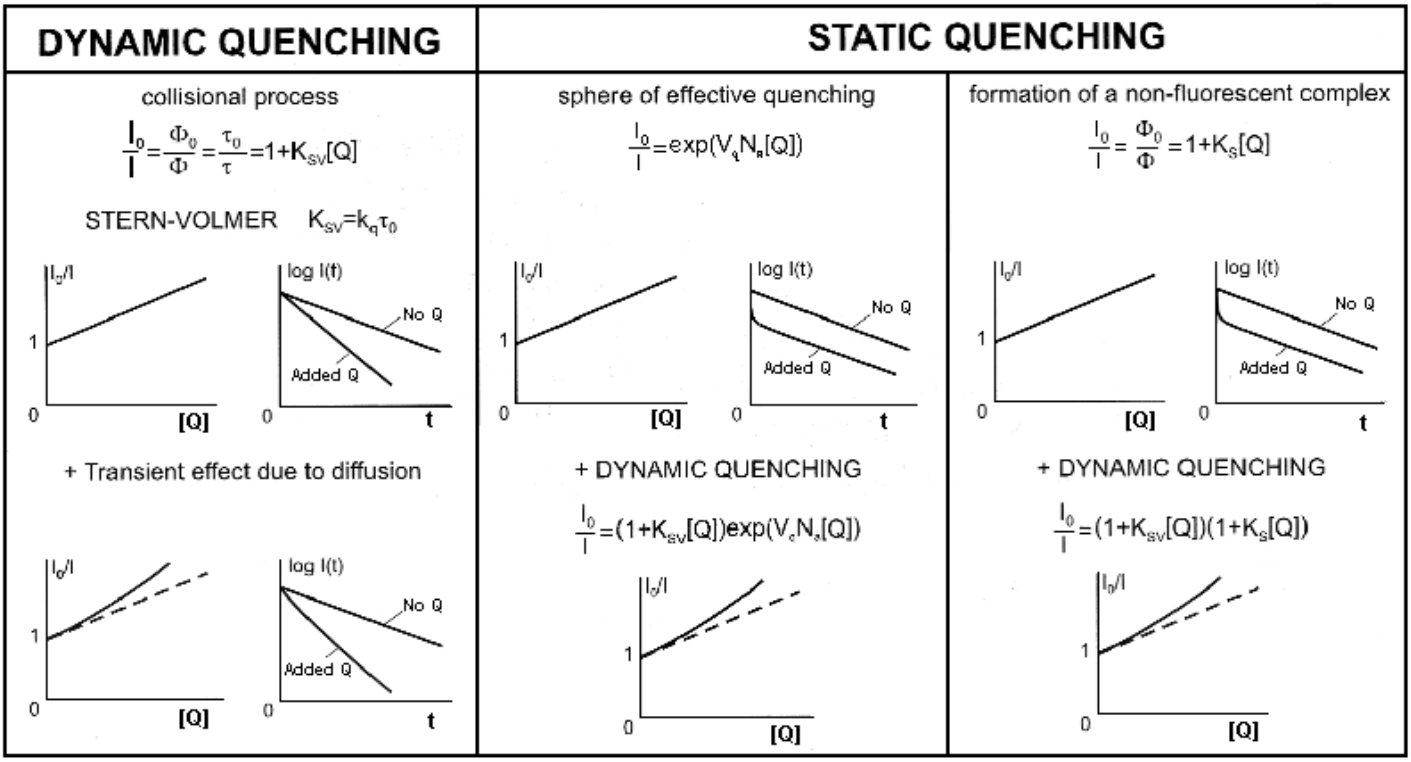

Figure 1.40: Influence of Dynamic and static quenching on Stern-Volmer plots (Valeur, B. *'Molecular Fluorescence – Principles and Applications'* Wiley-Vch publishers, Weinheim, 2002).[102]

1.11 Conclusions

The chapter demonstrated the large variety of host-guest interactions that can occur between zeolite and guest species in terms of the confinement imposed on guest species by the rigid zeolite framework, the polarity of the internal pore and guest interactions with intrazeolitic ion-exchange sites.

The current strategies utilised for the introduction and arrangement of guest molecules into the zeolite matrix were also outlined as well as a detailed description of zeolite topology. Finally, examples of photophysical interaction between a variety of co-entrapped species such as energy and electron transfer were examined in detail.

In summary, the combination of the rigid framework, large accessible channels and the non-innocent internal cage environment provided by zeolite materials present an interesting matrix within which to assemble and study supramolecular entities.

1.12 References

[1] Lehn J.M. "Supramolecular chemistry" *Science,* **1993,** *260*, 1762-1763.

[2] Hubin TJ, Busch D.H. *Coordination Chemistry Reviews* **2000**, *200*, 5.

[3] Chhun, C.; Richard-Daniel, J.; Kempf, J.; Schmitzer, A.R. *Org. Biomol. Chem.* **2013**,*11*, 6023.

[4] Ciba Foundation Symposium No. 158, Host-Guest molecular interactions: From Chemistry to Biology, Wiley-Interscience, **1991**.

[5] Jiang, H.M.; Sun H.J.; Zhang S.B.; Hua R.N.; Xu Y.M.; Jin S.B.; Gong H.Y.; Li, L. *J. Inclusion Phenom. Macrocyclic Chem.* **2007,** *58*, 133-138.

[6] Izait, R.M.; Pawlak, K.; Bradshaw , J.S. *Chem. Rev.* **1991**, *91*, 1721-2085 and references therein.

[7] Takeuchi, T ; Tokunaga, K ; Lim, LW *Anal. Sci.* **2013**, *4*, 423.

[8] D, Wang , L . Weiliu , W. Chang , X . G ao , Z. Wang *Environ. Sci. Technol.* **2009,** *43,* 5825–5829

[9] Walsh, D. A.; Keyes, T. E.; Forster, R. J. *J. Phys. Chem. B* **2004**, 108, 2631.

[10] Hjelm, J.; Handel, R. W.; Hagfeldt, A.; Constable, E. C.; Housecroft, C. E.; Forster, R. J. *J. Phys. Chem. B* **2003**, *107*, 10431.

[11] Brammer, L. *Chem. Soc. Rev.* **2004**, *33*, 476.

[12] Hiruta, Y.; Yoshizawa, N.; Suzuki, K. *Anal. Chem.* **2012,** *84***,** 10650.

[13] Watton, S. P.; Taylor C. M.; Kloster G. M.; Bowman, S. C. *Prog. Inorg. Chem.* **2003**, *51*, 333.

[14] Dutta, P. K.; Ledney, M. *Prog. Inorg. Chem.* **1997**, *44*, 209.

[15] Bruhwiler, D.; Calzaferri, G. *Microporous Mesoporous Mater.* **2004**, *72*, 1.

[16] Diskin-Posner, Y.; Dahal, S.; Goldberg I. *Angew. Chem. Int. Ed.* **2000**, *39*, 1288.

[17] Hashimoto, S. *J. Photochem. Photobiol. C* **2003**, *4*, 19.

[18] Takagi, K.; Shichi, T. Molecular and Supramolecular photochemistry, Volume 5, ‘Solid State and Surface Photochemistry’, 31, Marcel Dekker, Inc. 2000.

[19] http://pubs.usgs.gov/of/2001/of01-041/htmldocs/images/monstru.jpg (date accessed 20th April 2007)

[20] Schoonheydt, R. A.; De Pauw, P.; Vliers, D.; De Schrijver, F. C. *J. Phys. Chem.* **1984**, *88*, 5113 – 5118.

[21] Miyamoto, N.; Yamada, Y.; Koizumi, S.; Nakato, T. *Angew. Chem., Int. Ed.* **2007**, *46*, 4123-4127.

[22] Mochizuki, D.; Sugiyama, M.; Maitani, M.M.p; Wada, J. *Eur. J. Inorg. Chem.* **2013**, 2324–2329

[23] (a) Casalboni, M.; Senesi, R.; Prosposito, P.; De Matteis, F.; Pizzoferrato, R. *Appl. Phys. Lett.* **1997**, *70*, 2969.

(b) Casalboni, M.; De Matteis, F.; Ferone, V.; Prosposito, P.;Senesi, R.; Pizzoferrato, R.; Bianco, A.; De Mico, A. *Chemical Physics Letters* **1998,** *291* 167–172.

[24] Zhang, H.; Lei, B.L.B.; Li, W.; Lu, S. *Sens. Actuators, B* **2007**, *123*, 508-515.

[25] Jorge, P.A.S.; Maule, C.; Silva, A.J.; Benrashid, R.; Santos, J.L.; Farahi, F. *Anal. Chim. Acta* **2008**, *606*, 223–229.

[26] Farooq, A.; Al-Jowder, R.; Narayanaswamy, R.; Azzawi, M.; Roche, P.J.R.; Whitehead, D.E.; *Sensors and Actuators B* **2013**, *183*, 230–238.

[27] Rabo, J.A. Ed. 'Zeolite Chemistry and Catalysis', ACS Mono, Ser. 176, Washington D.C. **1975**.

[28] Yoon, K.B., 'Charge and Electron Transfer Reactions in Zeolites', 'Molecular and Supramolecular Photochemistry', volume 5, Marcel Dekker Inc., **2000**.

[29] Chen, J.; Kong, H.; Wu, D.; Hu, Z.; Wang, Z.; Wang, Y. *J. Colloid Interface Sci.* **2006**, 300, 491-497.

[30] De Baerdemaeker, T.D.; De Vos, D. *Nature Chemistry* **2013**, *5*, 89.

[31] Heinemann, H. *Catal. Reviews Sci. Eng.* **1981**, 23.

[32] Dyer, A.; Mikhail, K.Y. *Mineral Mag.* **1985**, *49*, 203.

[33] Suib, S.L., 'Luminesence as a probe of porous solids, Photochemistry and Photophysics', Volume 3, CRC Press, **1991**.

[34] Corma, A.; Garcia, H. *Eur. J. Inorg. Chem.* **2004**, *6*, 1143 and references therein.

[35] Meier, B.; Werner, T.; Klimant, I.; Wolfbeis, O. S. *Sens. Actuators B* **1995**, *29*, 240.

[36] Baerlocher, Ch.; McCusker, L.B. Database of Zeolite Structures: http://www.iza-structure.org/databases/ (accessed 26th April 2007)

[37] Wang, S. X.; Wang, L. M.; Ewing. R. C. *J. Nucl. Mater.* **2000**, *278*, 233-241.

[38] Loewenstein, W. *Am. Miner.***1954**, *39*, 92.

[39] Bursill, L.A.; Lodge, E.A.; Thomas J.M.; Cheetham A.K. *J. Phys. Chem.* **1981**, *85*, 2409-2421.

[40] Dutta, P.K.; Shieh, D.C.; Puri, M. *J. Phys. Chem.* **1987**, *91*, 2332 – 2336.

[41] Lee, E.F.T.; Rees, L.V.C. *Zeolites* 1987, *7*, 143.

[42] Corma, A.; Fornes, V.; Garcia, H.; Miranda, M.A.; Primo, J.; Sabater, M.J. *J. Am. Chem. Soc.* **1994**, *116*, 2276.

[43] Hashimoto,S.; Moon, H.R.; Yoon, K.B. *Microporous Mesoporous Mater.* **2007**, *101*, 10-18.

[44] Busby, M.; Kerschbaumer, H.; Calzaferri, G.; De Cola, L. *Adv. Mater.* **2008**, *20*, 1614–1618.

[45] http://zeolites.cqe.northwestern.edu/Music/electrostatic/zeolite.jpg (accessed 29th July 2008)

[46] Ndiege, N.; Raidoo, R.; Schultz, M.K.; Larsen, S. *Langmuir,* **2011**, *27*, 2904.

[47] Beierle, J.M. Roswanda, R.; Erne, P.M.; Coleman, A.C. Browne, W.R.; Feringa, B.L. *Part. Part. Syst. Charact.* **2013**, *30*, 273–279.

[48] Kim, H.S.; Pham, T.T.; Yoon K.B*. J. Am. Chem. Soc.* **2008**, *130*, 2135.

[49] Min, H.; Jeon, Y.; Sung, J.; Seok, S.; Kim, D.; Kim, H.; Yoon, K.B. J*. Phys. Chem. C* **2007**, *111*, 18159-18163.

[50] Kasha, M.; Rawls, H.R.; El-Bayoumi, M.A. *Pure Appl. Chem.* **1965**, *11*, 371.

[51] Valdes-Aguilera, O.; Neckers, D.C. *Acc. Chem. Res.* **1989**, *22*, 171.

[52] Hanif, N.; Anderson, M.W.; Alfredsson, V.; Terasaki, O. *Phys. Chem. Chem. Phys.* **2000**, *2*, 3349-3357.

[53] Marquez, F. Garcıa, H.; Palomares, E.; Fernandez, L.; Corma A. *J. Am. Chem. Soc.* **2000**, *122*, 6520.

[54] Márquez, F.; Zicovich-Wilson, C.M.; Corma, A.; Palomares, E.; García H. *J. Phys. Chem. B* **2001**, *105*, 9973-9979.

[55] Corma, A.; Fornés, V.; García, H.; Miranda, M. A.; Primo, J.; Sabater, M. J. *J. Am. Chem. Soc.* **1994**, *116*, 2276.

[56] Cano, M.L.; Cozens, F.L.; García, H.; Martí, V.; Scaiano, J.C. *J. Phys. Chem.* **1996**, *100*, 18152-18157.

[57] Winkler, J.R.; Netzel, T.L.; Creutz, C.; Sutin, N. *J.Am Chem. Soc.* **1987**,*109*, 2381.

[58] Bhuiyan, A.A.; Kincaid, J.R. *Inorg. Chem.* **1998**, *37*, 2525.

[59] Maruszewski, K.; Strommen, D. P.; Kincaid, J.R. *J. Am. Chem.Soc.* **1993**, *115*, 8345.

[60] Ramamurthy, V.; Caspar, J.V.; Eaton, D.F.; Kuo, E.W.; Corbin, D.R. *J. Am Chem. Soc.* **1992**, *114*, 3882.

[61] Larson, J.M.; Sousa, L.R. *J. Am. Chem. Soc.* **1978**, *100*, 1942.

[62] Uppili, S.; Thomas, K.J.; Crompton, E.M.; Ramamurthy, V. *Langmuir* **2000**, *16*, 265.

[63] Ellison, E.H.; Moodley, D.; Hime, J. *J. Phys. Chem. B* **2006**, *110*, 4772.

[64] Liu, X.; Lu, K.K.; Thomas, J.K. *J. Phys. Chem.* **1994**, *98*, 7877.

[65] Taira, N.; Saitoh, M.; Hashimoto, S.; Moon, H.R.; Yoon, K.B. *Photochem. Photobiol. Sci.*, **2006**, *5*, 822.

[66] Grätzel, M.; Kalyanasundaram, K.; Eds. 'Kinetics and Catalysis in microheterogeneous systems', Marcel Dekker: New York, **1991**.

[67] Yoon, K.B.; Kochi, J.K. *J. Am. Chem. Soc.* **1989**, *111*, 1128.

[68] Sankararaman, S.; Yoon, K.B.; Yabe, T.; Kochi, J.K. *J. Am. Chem. Soc.* **1991**, *113*, 1419.

[69] Yoon, K.B.; Hubig, S.M.; Kochi, J.K. *J. Phys. Chem.* **1994**, *98*, 3865.

[70] Krueger, J. S.; Mayer, J. E.; Mallouk, T. E. J. Am. Chem. Soc **1988**, 110, 8232.

[71] Yonemoto, E.H.; Kim, Y.I.; Schmehl, R.H.; Wallin, J.O.; Shoulders B.A.; Richardson, B.R.; Haw, J.F.; Mallouk, T.E. *J. Am. Chem. Soc.* **1994**, *116*, 10557.

[72] Borja, M.; Dutta, P.K. *Nature* **1993**, *362*, 43.

[73] Dutta, P.K.; Incavo, J.A. *J. Phys. Chem.* **1987**, *91*, 4443.

[74] Strome, D.H.; Klier, K., 'Adsorption and ion exchange with synthetic zeolites', Flank, W.H. Ed.; American Chemical Society: Washington DC, ACS Symp. Ser. No. 135, p155, **1980**.

[75] Gfeller, N.; Calzaferri, G. *J. Phys. Chem. B* **1997**, *101*, 1396.

[76] Gfeller, N.; Megelski, S.; Calzaferri, G. *J. Phys. Chem. B* **1998**, *102*, 2433.

[77] Gfeller, N.; Megelski, S.; Calzaferri, G. *J. Phys. Chem. B* **1999**, *103*, 1250.

[78] Megelski, S.; Lieb, A.; Pauchard, M.; Drechsler, A.; Glaus, S.; Debus, C.; Meixner, A.J.; Calzaferri, G. *J. Phys. Chem. B* **2001**, *105*, 25.

[79] Huber, S.; Ruiz, A.Z.; Li, H.; Patrinoiu, G.; Botta, C.; Calzaferri, G. *Inorg. Chim. Acta* **2007**, *360*, 869-875.

[80] Wang, Y.; Li, H.; Feng, Y.; Zhang, H.; Calzaferri, G.; Ren, T. *Angew. Chem. Int. Ed.* **2010**, *49*, 1434.

[81] Bossart, O.; De Cola, L.; Welter, S.; Calzaferri, G. *Chem. Eur. J.* **2004**, *10*, 5771.

[82] Thomas, K.J.; Sunoj, R.B.; Chandrasekhar, J.; Ramamurthy, V. *Langmuir,* **2000**, *16*, 4912.

[83] Hashimoto, S.; Kirikae. S.; Tobita, S. *Phys. Chem. Chem. Phys.* **2002**, *4*, 5856.

[84] Alvaro, M.; Fornes, V.; Garcia, S.; Garcia, H.; Scaiano, J.C. *J. Phys. Chem. B* **1998**, *102*, 8744-8750.

[85] Gilbert, A.; Baggott, J. 'Essentials of Molecular Photochemistry', Blackwell Scientific Publications, **1991**.

[86] Balzani, V.; Juris, M.; Campagna, S.; Serroni, S. *Chem. Rev.* **1996**, *96*, 759.

[87] Balzani, V.; Juris, A.; Barigelletti, F.; Campagna, S.; Belser, P.; Zelewsky, A.V. *Coord. Chem. Rev.* **1988**, *84*, 85-277.

[88] http://www.pci.uni-heidelberg.de/pci/d_index.html?http://www.pci.uni-heidelberg.de/pci/cschulz/d_spectro_tracer.html (accessed 4th October 2012)

[89] Valeur, B. 'Molecular Fluorescence, Principles and applications', Wiley-VCH, **2002**.

[90] http://www.answers.com/topic/franck-condon-principle?cat=technology (accessed September 8th 2007)

[91] http://www.optiglass.com/ukhome/d_ref/f_ref/No1C.gif (accessed September 8th 2007)

[92] Principles of Photochemistry, J.A. Barltrop and J.D. CoyleWiley, **1975**.

[93] Förster, T. 'Fluorenzenz Organische Verbindungen', Gottingen, Vandenhoech and Ruprech, **1951**.

[94] Turro, T.J. 'Modern Molecular Photochemistry', University Science Books, p.87, **1991**.

[95] (a) Robinson, G.W., Experimental Methods of Physics, Vol 3, Eds. Marton, L. Williams, D., New York: Academic Press, p. 155, **1962**.
(b) Heitler, W. Quantum Theory of Radiation, Oxford: Clarendon Press, **1944**.
(c) Lewis, G.N.; Calvin, M. *Chem Rev.* **1939**, *25*, 273.

[96] (a) Bowen, E.J.; Chemical Aspects of Light, Oxford: Clarendon Press, **1946**.
(b) Maccoll, A. *Quart. Rev.* **1947**, *1*, 16.
(c) McMillin, D. R. *J. Chem. Ed.* **1978**, *55*, 7.

[97] Vos J. G.; Forster, R. J.; Keyes T. E. 'Interfacial supramolecular assemblies', Chichester : Wiley, **2003**.

[98] Balzani, V.; Maestri, M. 'Intermolecular energy and electron transfer processes', 'Photosensitization and photocatalysis using inorganic and organometallic compounds', Kluwer Academic Publishers, **1993**.

[99] Creutz, C.; Chou, M.; Netzel, T.L.; Okumura, M.; Sutin, N. *J. Am. Chem. Soc.* **1980**, *102*, 1315.

[100] Seery, M.K.; Guerin, L.; Forster, R.J.; Gicquel, E.; Hultgren, V.; Bond, A.M.; Wedd, A.G.; Keyes, T.E. *J. Phys. Chem. A* **2004**, *108*, 7399.

[101] Abi, T.; Ohshima, T.; Nagai, K.; Ishikawa, S.; Kaneko, M. *React. Funct. Polym.* **1998**, *37*, 133.

[102] Valeur, B. *'Molecular Fluorescence – Principles and Applications'* Wiley-Vch publishers, Weinheim, **2002**.

Chapter 2

Experimental approaches and Instrumentation

2.0 Chemicals

All synthesis reagents used were obtained from Sigma Aldrich and were analytical grade. All solvents used for photophysical measurements were spectroscopic grade. Water was purified to greater than 18 MΩ.cm utilising a 'MilliQ' water purification system. Hexaammineruthenium(III) chloride, Iridium(III) chloride hydrate, 2,2'-bipyridine, 2,2':6',2"-terpyridine, Iron(II) chloride-4-hydrate, ammonium iron(II) sulphate-6-hydrate, potassium hexafluorophosphate, hydrofluoric acid, hydrochloric acid and all solvents were purchased from Sigma Aldrich and used without further purification. Sodium Zeolite-Y was purchased from Sigma Aldrich and calcined in air at 600 °C for six hours, extensively washed with 10% NaCl solution and finally washed with deionised water until no chloride could be detected with silver nitrate solution (0.1 M).

2.1 Electronic absorption

Diffuse reflectance UV-Vis experiments were conducted using either an ocean optics UV-vis spectrometer with diffuse reflectance angled fibre attachment or a Perkin Elmer UV-vis NIR 900 spectrometer with a Spectralon coated integrating sphere for solid samples. Na-Y zeolite was used as a blank and spectra were recorded in absorbance mode.

2.2 Time resolved and steady state emission spectroscopy

Luminescence Spectra were collected using the Varian Cary Eclipse spectrofluorimeter employing a solid sample attachment for zeolite samples, undoped calcined Na-Y zeolite was used as a blank. Solid samples were sonicated in acetone and drop coated onto glass slides until an even layer was achieved. Luminescence spectra were recorded a minimum of four times and the results averaged. The variability between individual measurements on different areas of the drop cast powder was typically less than 2%. Some degree of variability in luminescence intensity was anticipated given the difficulty in casting a homogeneous layer of zeolite material, so

measurements were confined to areas of material presenting a smooth surface to the excitation source.

Luminescent lifetimes were determined by time-correlated single-photon-counting (TCSPC) using two different instruments. 1) For chapter 3 an Edinburgh Analytical instruments system (nF900 flash lamp and S900 detection system). The excitation pulse was generated by nitrogen discharge, pulsing at 40 KHz and monochromated to 337 nm. The temporal measurement window was extended to ten times the longest-lived component. For the lifetime measurements a small quantity of the zeolite material was dispersed in dimethyl-sulfoxide. Low temperature measurements were collected using an OptistatDn cryostat coupled to an Oxford Instruments 'Intelligent' Temperature Controller. For low temperature measurements a degassed ethanol/methanol (4:1) or butyronitrile liquid nitrogen cooled glass was used. The remainder of the lifetimes were recorded using a Picoquant Fluotime 100 TCSPC system exciting at 450 nm and using a 510 nm narrow band pass dielectric filter. The instrument response function was determined by using ludox colloidal silica solution (Aldrich).

2.2.1 Fluorescence lifetime imaging microscopy

Luminescence images were recorded using with a Zeiss LSM510 Meta confocal microscope using a 64x oil immersion objective lens. The 458 nm argon ion laser excitation was used for the iridium materials. Optical density filters were reduced to 0.1% transmission in order to mitigate any effects of photobleaching. The luminescence signal was collected was collected using 420/490 nm long pass filters.

2.3 Raman spectroscopy

Raman spectroscopy was conducted using a confocal High Resolution Horiba Labram system. The exciting Ar ion laser (514 nm, 488 nm or 457. 9 nm) or diode laser (785 nm) was focused into the solution cell or onto a solid sample

using a 10x objective lens. A spectral resolution of 0.5 cm^{-1} per pixel was achieved using a grating of 600 lines/mm, and the x-axes was calibrated against acetonitrile and silicon. A typical Raman instruments schematic is shown in Figure 2.1.

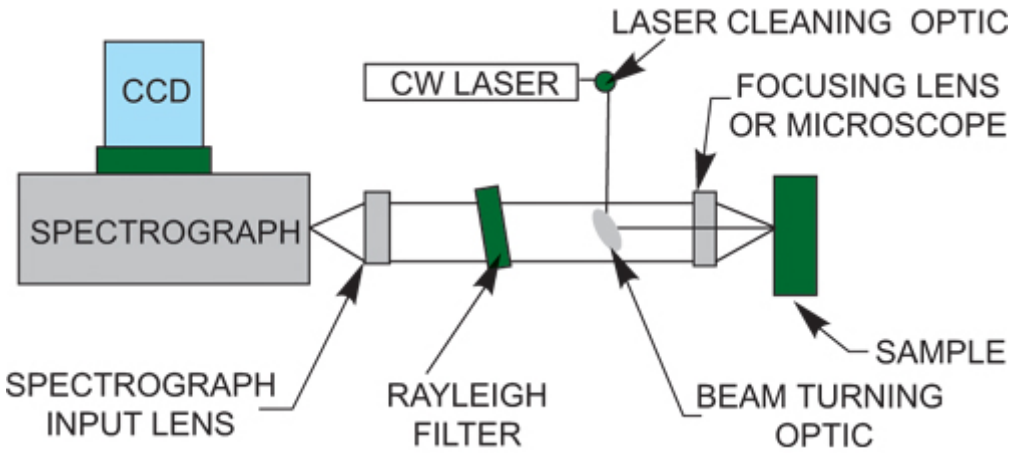

Figure 2.1: Raman instrument schematic.[1]

2.4 General procedure for preparation of zeolite entrapped materials

2.4.1 Preparation of the Zeolite encapsulated $[Ru(bpy)_3]^{2+}$

Z-$[Ru(bpy)_3]^{2+}$ was prepared using a method adapted from the work of Lundsford *et al.* and Bossmann *et al.* employing $[Ru(NH_3)_6]^{3+}$ as the precurser.[23] All solutions and suspensions were degassed with nitrogen and all procedures were performed under a nitrogen atmosphere in order to prevent formation of ruthenium red. Calcined Na-Y zeolite (11.91 g) was suspended in cold degassed deionised water (500mls) at room temperature. The pH of this suspension was adjusted to pH 5.4 ±0.1 using HCl (0.1 M). For an occupation of one ruthenium complex per 20 supercages $[Ru(NH_3)_6]Cl_3$ (0.0851 g, 2.748 X 10^{-4} moles) was added to the solution and this was stirred for eight hours at 4 °C. The resulting Z-$[Ru(NH_3)_6]^{3+}$ was filtered and washed with deionised water until no Cl^- could be detected using silver nitrate solution (0.1 M). The Z-$[Ru(NH_3)_6]^{3+}$ was then dried in vacuo and

dispersed in degassed ethylene glycol (150 mL), dimethylsulfoxide (1 mL) and H_2O (1 mL). 2,2'-bipyridine (0.154 g, 9.871 X 10^{-4} moles, which represented approximately a 20% excess) was added and the slurry brought to reflux with stirring under nitrogen for four hours. The resulting orange product was filtered and sonicated with copious amounts of hot ethanol, then dispersed in NaCl (10% w/v, 500 mL) and stirred for 1 hour in order to remove superficially or surface bound ruthenium species. Finally the doped zeolite was washed extensively with deionised water until no chloride could be detected in the filtrate using silver nitrate (0.1 M). Finally, excess 2,2'-bipyridine was removed by Soxhlet extraction into ethanol.

2.4.2 Preparation of zeolite encapsulated $[Fe(bpy)_3]^{2+}$ and $[Fe(tpy)_2]^{2+}$

Calcined Na-Y zeolite (5.001g) was suspended in cold degassed (N_2) deionised water (100 mL). The pH of this suspension was then adjusted to pH 5.3 $\pm$0.1 using HCl (0.1 M). For an occupation of one iron species per 20 supercages, $FeCl_2.4H_2O$ (0.0229 g, 1.151 X 10^{-4} moles) was added to the suspension. The solution was then left for eight hours at 4 °C with stirring. The Z-Fe^{2+} was filtered and washed with deionised water until no Cl^- could be detected using silver nitrate solution (0.1 M). These materials were dispersed in ethanol and the ligands added with an additional 20% excess in a 3:1 and 2:1 ligand to metal molar ratio of 2,2'-bipyridine (0.0649 g, 4.16 X 10^{-4} moles) and 2,2':6',2"-terpyridine (0.0646 g, 2.77 X 10^{-4} moles) respectively. These suspensions were brought to reflux with stirring for four hours. The products were filtered and washed with copious amounts of hot ethanol. The Z-$[Fe(bpy)_3]^{2+}$ or Z-$[Fe(tpy)_2]^{2+}$ was dispersed in NaCl (10% w/v, 500 mL) and stirred for 30 minutes in order to remove superficially surface bound iron species. Finally the doped zeolites were washed with deionised water until no chloride could be detected using silver nitrate solution (0.1 M). Excess 2,2'-bipyridine and 2,2':6',2"-terpyridine was removed by further washing in hot ethanol. The corresponding parent iron compounds $[Fe(bpy)_3][PF_6]_2$ and

$[Fe(tpy)_2][PF_6]_2$ were prepared from ammonium iron(II) sulfate-6-hydrate and the appropriate ligands according to standard procedures.

2.4.3 Preparation of co-doped zeolite encapsulated Z-$[Ru(bpy)_3]^{2+}[Fe(bpy)_3]^{2+}$ and Z-$[Ru(bpy)_3]^{2+}[Fe(tpy)_2]^{2+}$

The co-doped zeolites were prepared in a similar manner to the iron doped zeolites, expect the Z-$[Ru(bpy)_3]^{2+}$ was employed instead of Na-Y zeolite. The reaction with 2,2'-bipyridine or 2,2':6',2"-terpyridine was carried out by refluxing in ethanol with no addition of dimethylsulfoxide and H_2O as performed for the Z-$[Ru(bpy)_3]^{2+}$ material. The products were filtered and washed with copious amounts of hot ethanol. The co-doped materials were then dispersed in NaCl (10% w/v, 500 mL) and stirred for 30 minutes in order to remove superficially surface bound iron species then washed with deionised water until no chloride could be detected using silver nitrate solution (0.1 M). These materials were dispersed in ethanol, warmed, and filtered twice and then extensively washed with ethanol in order to remove excess unreacted ligand.

Iridium(III) chloride hydrate, 2,2':6',2"-terpyridine, 2,2'-bipyridine, iron(II) chloride-4-hydrate, potassium hexafluorophosphate, hydrofluoric acid, hydrochloric acid and all solvents were purchased from Sigma Aldrich and used without further purification. Sodium Zeolite Y was purchased from Sigma Aldrich and calcined in air at 600 °C for six hours, extensively washed with 10% NaCl solution and finally washed with deionised water until no chloride could be detected upon treatment with silver nitrate solution (0.1 M).

2.4.4 Synthesis of Z-$[Ir(tpy)_2]^{3+}$ and Z-$[Ir(bpy)_3]^{3+}$

Sodium Zeolite-Y was dispersed in deionised water and the appropriate amount of Iridium(III) chloride hydrate added and the suspension brought to reflux under nitrogen overnight resulting in a light grey powder. This resulting Z-Ir^{3+} was washed with deionised water until no free Cl^- could be detected using silver nitrate solution (0.1 M). This was then dispersed in ethylene

glycol and the appropriate amount of 2,2':6',2"-terpyridine added and the suspension brought to reflux under nitrogen with stirring for two days. This was then filtered and washed with copious amounts of hot ethanol and then dispersed in NaCl (10% w/v, 500 mL) and stirred for 1 hour in order to remove superficially or surface bound iridium species. Finally the doped zeolite was washed extensively with deionised water until no chloride could be detected in the wash using silver nitrate solution (0.1 M). These materials were dispersed in ethanol, warmed, and filtered twice and then extensively washed with ethanol in order to remove excess unreacted ligand. Z-$[Ir(bpy)_3]^{3+}$ was prepared and purified in a similar fashion using 2,2'-bipyridine as opposed to 2,2':6',2"-terpyridine .$[Ir(tpy)_2][PF_6]_3$ and $[Ir(bpy)_3][PF_6]_3$ were prepared according to literature procedures.[4,5,6]

2.5 Background theory

2.5.1 Time Correlated Single Photon counting

Time correlated single photon counting (TCSPC) is a widely used tool for the evaluation of excited state lifetimes. The basic principle is the difference in time taken for a photon emitted from an excitation source to reach a detector in the absence of a sample (reference light pulse) compared to the time taken for a photon absorbed and re-emitted from a luminescent sample to be detected (Figure 2.2).

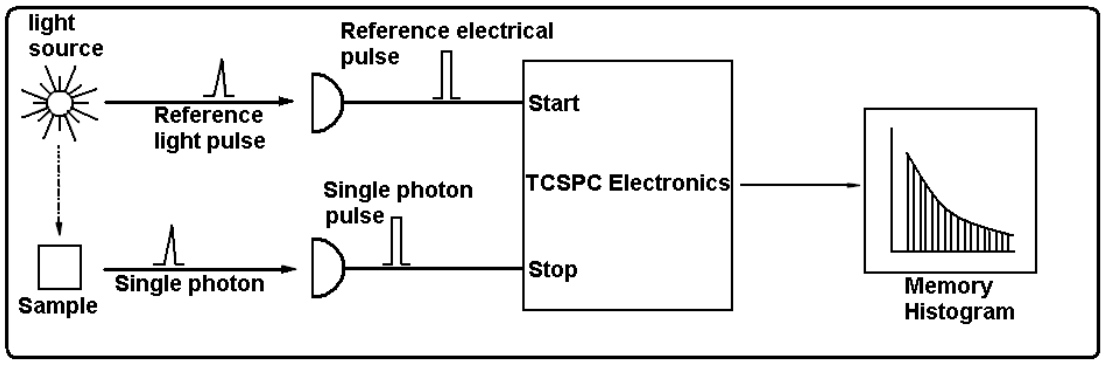

Figure 2.2: Instrument schematic for general TCSPC system.[7]

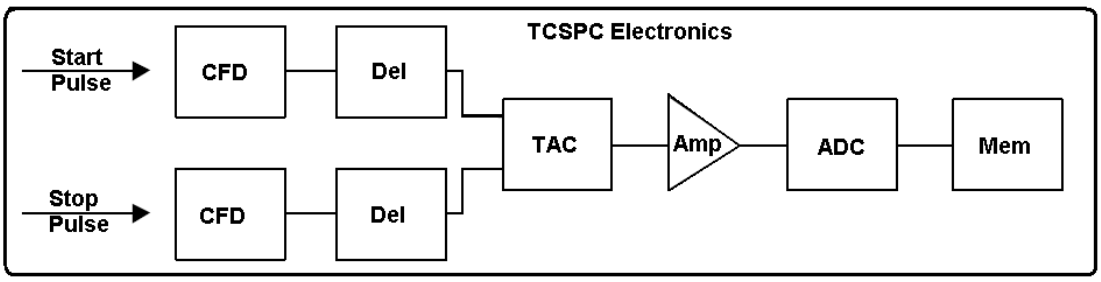

Figure 2.3: TCSPC electronics schematic.[7]

The method is statistically based and requires the use of a high repetition excitation source. This excitation source is split, the reference light pulse starting a time to amplitude converter (TAC) and the emitted luminescence photon stopping the TAC. The constant fraction discriminator (CFD) measures the temporal position of the incoming light pulses based on the slope of the incoming pulse as opposed to absolute amplitude comparison. When triggered by an electrical pulse the TAC begins a linear voltage ramp until stopped by the arrival of the emission photon. The output pulse from the TAC is then amplified and arrives at a pulse height measuring device, an analogue to digital converter (ADC). The varieties of different amplitudes arising from the excited state decay are counted in separate time bins. A histogram of these events can then be constructed yielding a decay curve. Since a high repetition source is used, many millions of events can be recorded every second. The electronic components of a TCSPC are illustrated in Figure 2.3.

2.5.1.1 Treatment of TCSPC data

TCSPC data can be analysed via a number of different methods, including method-of-moments, maximum entropy method, Laplace transformations and others.[8] The one selected for the following work utilises non-linear least squares (NLLS) analysis. The initial step in a decay analysis is the fitting to a mathematical model describing the slope and the subsequent application of NLLS to the model and the experimental data is order to establish to what degree the model agrees with the experimental data points. This yields a reduced chi squared value that, along with other considerations such as residual plots (a visual representation of experimental data distribution around

the model decay over the entire temporal range) allows the analyst to assign the correct exponential model within certain confidence limits. The materials under examination in this work typically yield multi-exponential decay profiles due to the various environments the luminophore encounters. The most significant one being the differing distances between emitter and quencher complexes, resulting in a variety of decay times.

2.5.2 Exponential decay models

2.5.2.1 Multi-exponential decays

As stated above, the initial experimental data obtained from TCSPC measurement require fitting to a suitable mathematical model in order to determine the intrinsic lifetime or lifetimes relating to a particular decay process. A cartoon exponential decay process is shown in Figure 2.4. This fitting is typically achieved by use of a suitable exponential decay using a single or the summation of multiple exponential decays as shown in Equation 2.1, (typically not more than the summation of three exponentials, since the validity of the information extracted from decays becomes doubtful after that number). If there is a suspicion that the decay is represented by more than three exponential decays, a stretched exponential model may be employed which fits the data assuming a statistical distribution of multiple lifetimes (vide infra).

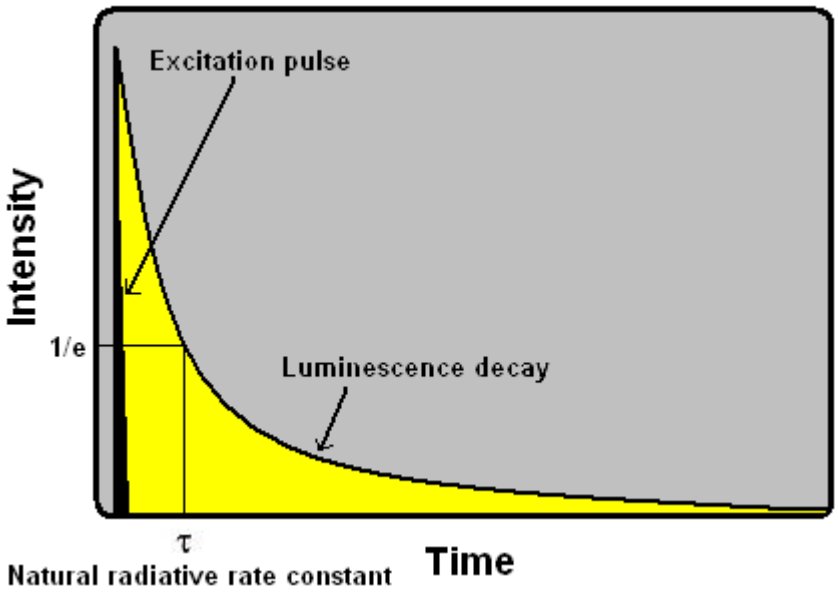

Figure 2.4: Sample exponential decay showing non-ideal excitation pulse.

Equation 2.1 outlines a triexponential decay mathematically. The term A is included when the slope of the decay reaches zero while intensity or count remains at some constant value, representing the effective dark counts of the instruments.

$$R(t) = A + \sum_{i=1}^{3} B_i \, e^{-\frac{t}{\tau_i}} \qquad \textbf{Equation 2.1}$$

The pre-exponential term B_i includes both sample and instrument information but since instrumental parameters remain constant over the course of an experiment, these values can be used to estimate the relative contribution of each exponential component.

2.5.2.2 Distribution of lifetimes

Not all lifetime decays can be accurately or appropriately described with the use of a single, double or treble exponential model. A luminophore in an inhomogenous environment can display a large range of lifetimes rather than just one or two which may be encountered for example in the case of

association quenching of a luminophore. The presence of a mixed solvent system can lead to lifetime distributions rather than discrete decay times.[8] In such cases it is necessary to introduce a property known as a distribution function. The pre-exponential term B_i above becomes a distribution function $B(\tau)$ where each constituent lifetime of the distribution is described by:

$$I(\tau,t) = B(\tau)\, e^{-\frac{t}{\tau}} \qquad \textbf{Equation 2.2}$$

The summation of all these constituent lifetimes describes the overall decay:

$$I(t) = \int_{\tau=0}^{\infty} B(\tau)\, e^{-\frac{t}{\tau}} d\tau \qquad \textbf{Equation 2.3}$$

where $I(t) = \int B(\tau) d\tau = 1$.[8] The parameters used for the lifetime distribution function $B(\tau)$ are typically Gaussian or Lorentzian functions. A less complicated method for assessing a decay with a distribution of lifetimes is the use of a stretched exponential:

$$I(t) = I_0 \exp[(-t/\tau)^{\beta}] \qquad \textbf{Equation 2.4}$$

The expression β, yields information relating to the decay time distribution. More detailed explanations of the decay models selected for data interpretation will be presented in the relevant results chapters.

2.5.2.3 Reconvolution and tail fitting

Another complication associated with the modelling of the decay data is the non-ideal excitation pulse of the flashlamp or laser, resulting in loss of temporal information about the analyte during the early portion of its decay (Figure 2.4). The ideal excitation pulse would of course be infinitely short in duration and modern instrumentation can achieve very short pulse widths of 1 picosecond. However routine picosecond measurements can still present

experimental challenges and most routine TSCPC measurements are in nanosecond time range. Fortunately extraction of nanosecond experimental data from much longer excitation pulse durations is relatively straightforward. The instrument response function (IRF) of a TCSPC system includes the approximately lorentzian excitation pulse as well as interferences from instrument detection electronics. The IRF is readily acquired by use of a scattering solution and is then compared to the decay of the sample, an example IRF and decay is shown in Figure 2.5. The sample decay is convoluted as it includes elements of the IRF.

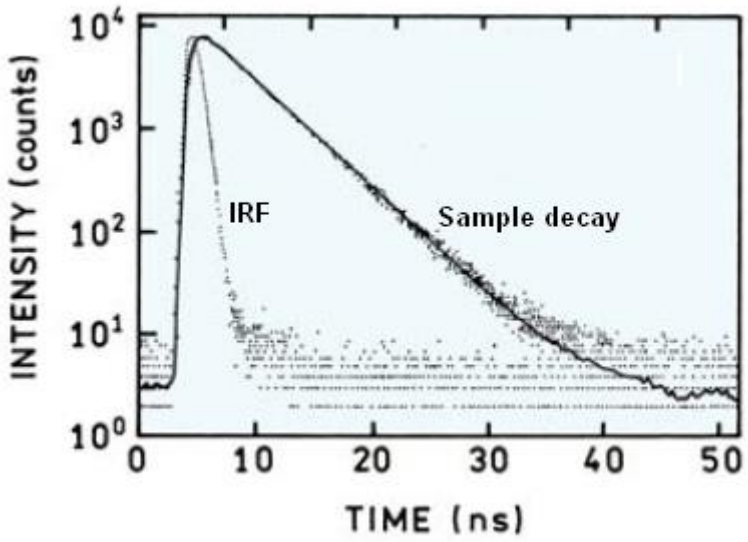

Figure 2.5: TCSPC decay, exponential fit and IRF for a fluorescein sample in water (Lakowicz, J.R., Principles of Fluorescence spectroscopy, Kluwer Acad./Plenum Publ. 1999).[8]

A mathematical operation known as a convolution integal is employed in order to deconvolute the decay and extract the true lifetime data. Commercially available fitting software allows for the routine deconvolution of decay data.

Another option for fitting decay data is known as a tail fit. A tail fit only includes data after the initial rise of the decay data and neglects any contribution from that early portion of the data (it essentially ignores any IRF contribution). It is useful when considering long lifetimes and closer examination of the long-lived elements of an excited state decay. The

difference between the data selection for reconvolution and tail fits is illustrated in Figure 2.6.

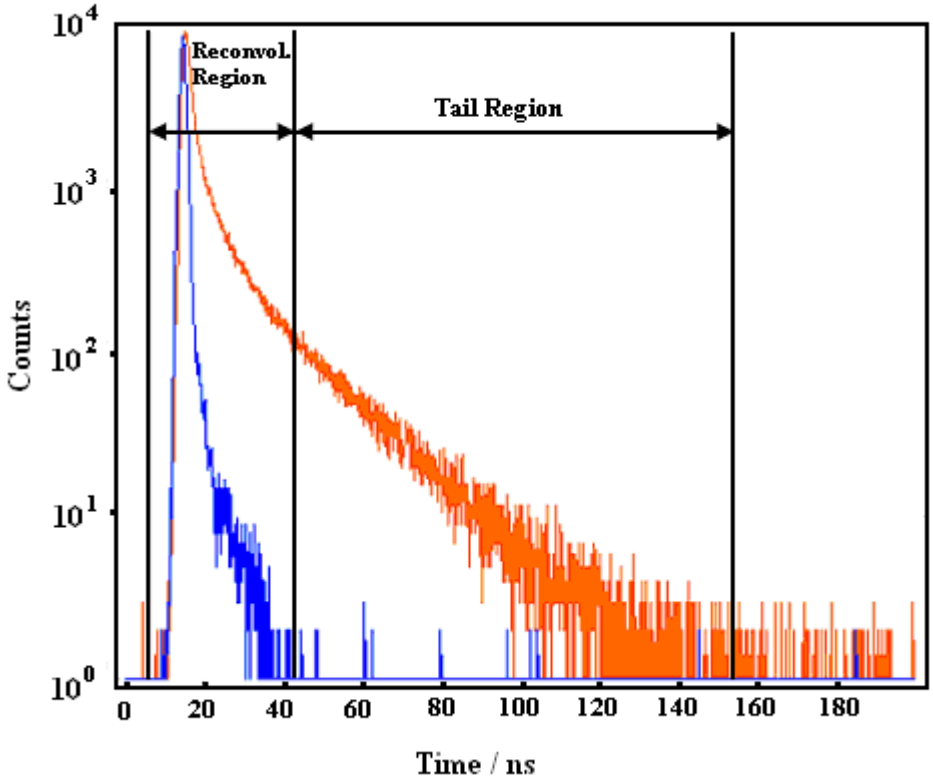

Figure 2.6: Regions of data utilised for reconvolution and tail fits.[9]

2.6 Raman Spectroscopy

A photon interacting with a molecule is either scattered or absorbed. Absorption of a photon requires the photon to be of equal energy as the two energy states of the molecule and induces a change in the dipole moment of the molecule. When scattered a photon can polarize the electron cloud within a molecule, the polarization resulting in a change of shape of the electron cloud due to the electric vector of the incident photon interacting with the electron cloud. This distorted electron cloud is known as a virtual state and is extremely short lived. System equilibrium is restored with a photon being ejected, which possesses the same energy as the incident photon (Rayleigh Scattering), more energy (anti-Stoke Scattering) or less energy (Stokes Scattering). Figure 2.7 demonstrates these processes in the presence of two

initial vibrational states and two corresponding virtual states. Rayleigh scattering occurs when there is no change in the nuclear displacement of the molecule during the short lifetime of the virtual excited state, the incident photon is emitted at the same frequency (elastic scattering). However, if nuclear displacement occurs during the polarization event, a quantum of vibrational energy can be transferred to the re-emitted photon yielding a higher energy photon (Anti-Stokes scattering). The opposite can also occur and result in a photon of lower energy than the initial incident radiation (Stokes scattering). Both Stokes and anti-Stokes are known as inelastic scattering as some energy is either lost or gained by the incident photon. Since nuclear displacement occurs extremely slowly in comparison to electronic events, Rayleigh scattering is more prevalent by about six orders of magnitude. Another feature to note from Figure 2.7 is the anti-Stokes scattering originates from an upper initial excited state and being a temperature dependent process, the more dominant inelastic scattering process will be Stokes in nature. As a consequence of the weak intensities of Stokes scattering, experimental set-ups require laser excitation.

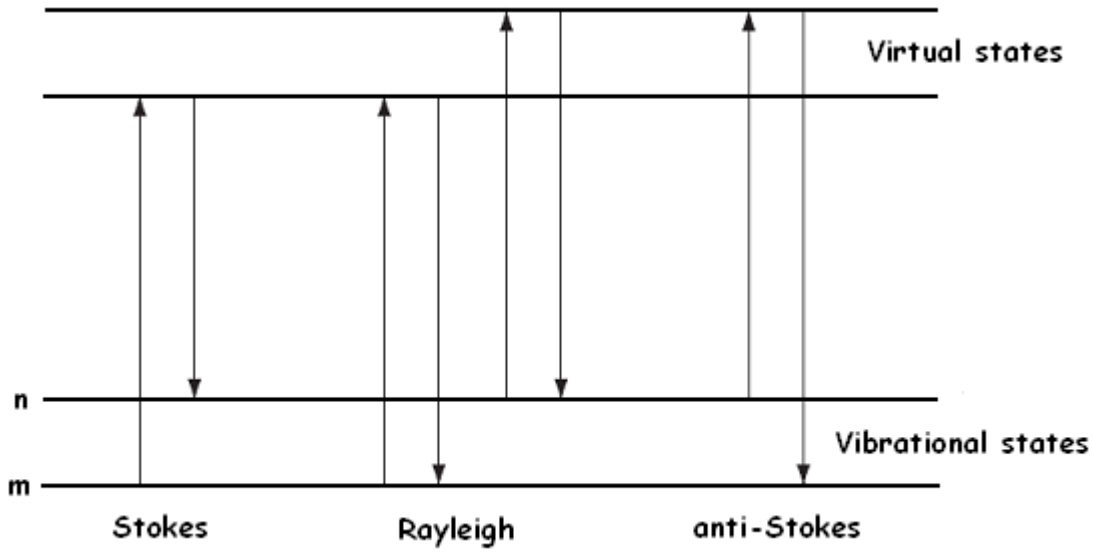

Figure 2.7: Energy level diagram for Raman and Rayleigh scattering showing the upper and lower initial vibrational states as well as the virtual excited state (Smith *et al.* Modern Raman Spectroscopy - A Practical Approach, Wiley, 2005).[10]

The energy difference between the incident and scattered photon yields information about the associated vibrational modes. Figure 2.8 shows the Raman Spectrum of cyclohexane.

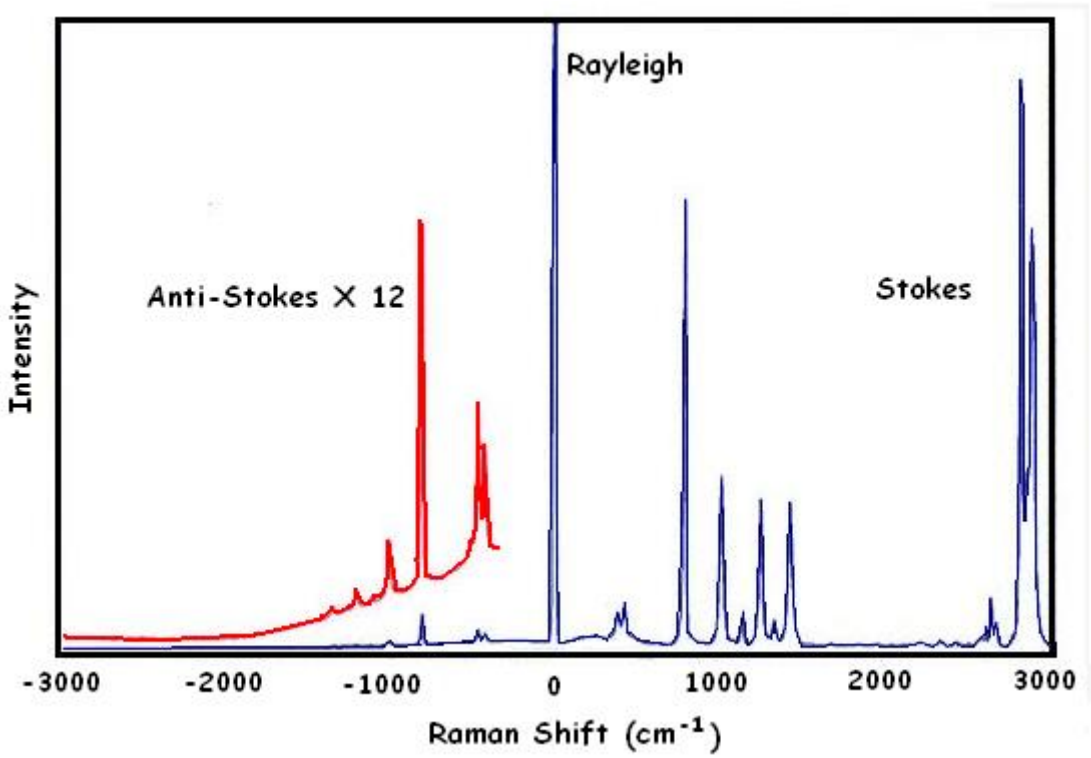

Figure 2.8: Raman spectrum of cyclohexane showing elastic and both inelastic scattering processes.[11]

2.6.1 Resonance-enhanced Raman spectroscopy

Resonance Raman scattering can occur when a laser excitation line used is co-incident with an electronic absorption band of a molecule. Typically the intensities of resonance Raman are enhanced by 10^2 to 10^6. The resonant Raman spectra are usually considerably less congested than their Raman counterparts, as the intensity enhancements are associated mostly with the vibrations involved in the electronic transition. An energy level diagram for a resonance Raman transition is shown in Figure 2.9.

The source of this enhanced scattering intensity can be explained by considering the Equations 2.5 and 2.6 and by reference to Figure 2.9.

The theoretical intensity of a Raman band (I_{mn}) is described by Equation 2.5:[12]

$$I_{mn} = c.I_0.(\nu_0 - \nu_{mn})^4 \sum_{\rho\sigma} \left|(\alpha_{\rho\sigma})_{mn}\right|^2 \qquad \textbf{Equation 2.5}$$

where I_0 is the intensity of the incident laser of frequency ν_0, $(\nu_0 - \nu_{mn})$ is the difference in energy between the incident laser light and the Raman transition and the term $\sum_{\rho\sigma} \left|(\alpha_{\rho\sigma})_{mn}\right|^2$ is related to the change in the polarizability α caused by the transition, with the various related polarizabilty tensors (x-y-z tensor coordinates) described by the $\rho\sigma$ summation. Equation 2 above can be rewritten as:

$$(\alpha_{\rho\sigma})_{mn} = \frac{1}{h} \sum_e \left(\frac{M_{me} M_{en}}{\nu_{em} - \nu_0 + i\Gamma_e} + \frac{M_{me} M_{en}}{\nu_{en} + \nu_0 + i\Gamma_e}\right) \qquad \textbf{Equation 2.6}$$

where M_{me} and M_{en} are the electric transition moments, the relevant transitions are shown in Figure 2.9, h is Plancks constant, $i\Gamma_e$ term is the damping constant. As stated above the intensity of a Raman band is related to second power of $(\alpha_{\rho\sigma})_{mn}$. With using non-resonance Raman spectroscopy the value of ν_0 is selected so that its value is substantially less than that of an electronic transition ($\nu_0 << \nu_{em}$) and hence $(\nu_0 - \nu_{mn})$ is relatively large, since Raman intensity is proportional to $(\nu_0 - \nu_{mn})^4$. With resonant conditions ν_0 approaches ν_{em}, the value of the $(\nu_0 - \nu_{mn})$ term decreases and results in a very large increase the overall band intensity.[13]

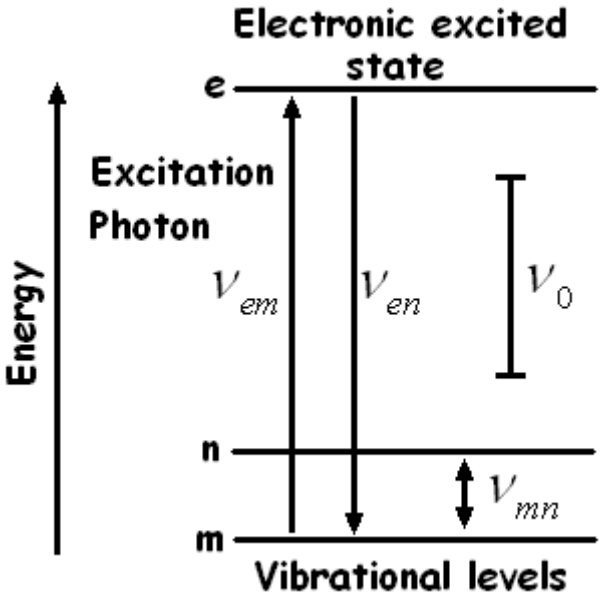

Figure 2.9: Energy level diagram for a resonance Raman transition (Ferraro *et al.*, Introductory Raman Spectroscopy, Academic Press, Inc. 1994).[13]

2.8 References

[1] http://www.andor.com/learn/applications/?docid=64 (accessed 25th June 2009)

[2] DeWilde, W.; Peeters, G.; Lunsford, J. H. *J. Phys. Chem.* **1980**, *84*, 2306.

[3] Bossmann, S. H.; Turro, C.; Schnabel, C.; Pokhrel, M. R.; Payawan, L. M.; Baumeister, B.; Wörner, M. *J. Phys. Chem. B* **2001**, *105*, 5374.

[4] Collin, J.P.; Dixon, I.M.; Sauvage, J.P.; Williams, J.A.G.; Barigelletti, F.; Flamigni, L. *J.Am. Chem. Soc.* **1999**, *121*, 5009-5016.

[5] Watts, R.J.; Harrington, J.S.; Houten, J.V. *J. Am. Chem. Soc.* **1976**, *99*, 2179.

[6] Sullivan, B.P.; Meyer, T.J. *J. Chem. Soc., Chem. Commun.* **1984**, *7*, 401.

[7] http://www.picoquant.com/_instrumentation.htm (accessed 26th June 2009)

[8] Principles of Fluorescence spectroscopy, Kluwer Acad./Plenum Publ. **1999**.

[9] Edinburgh Instruments F900 Analysis of Lifetime Data Manual, issue 1, December **2000**.

[10] W.E. Smith and G. Dent, Modern Raman Spectroscopy - A Practical Approach, Wiley, **2005**.

[11] Avaloninstruments.com /images/Raman%20Stokes%20Antistokes (accessed 26th June 2009)

[12] J. Tang, A.C. Albrecht, “Developments in the theories of vibrational Raman intensities”, Raman Spectroscopy, (H.A. Szymanski, Ed.), Vol 2, Plenum Press, New York, **1970**.

[13] J. R. Ferraro, K. Nakamoto, Introductory Raman Spectroscopy, Academic Press, Inc. **1994**.

Chapter 3

Influence of Steric Confinement Within Zeolite Y on Photoinduced Energy Transfer Between $[Ru(bpy)_3]^{2+}$ and Iron Polypyridyl Complexes

3.0 Introduction

3.0.1 Zeolite-Y encapsulated transition metal complexes

The application of zeolite's well-ordered topology for creating molecular level organisation continues to be an attractive field of research.[1,2] The well defined spatial arrangement provides opportunities for well defined distances between guest molecules, as well as apertures or windows leading from supercages that allow small molecules access to the inner molecules. Zeolite-Y is also relatively chemically inert, but can induce changes to the local environment due to the steric constraint of the cage, interesting solvating conditions encountered within the zeolite framework and more factors that were discussed in earlier chapters.[3] These attributes can be exploited for applications necessitating long-lived charge separation.[4] Zeolite encapsulation also offers opportunities for sensing devices such as oxygen sensors, with oxygen sensed quantitatively by entrapped ruthenium tris bipyridine.[5,6] Energy and electron transfer processes, many again involving ruthenium complexes as donor and viologens as model acceptor species [7,8,9,10] or organic dye based energy donor-acceptor systems also take advantage of the zeolite hosts inherent structural properties.[11,12,13] This introduction outline how transition metal complexes are incorporated into zeolite frameworks and how the cavity microenvironment affects their photophysical properties.

3.0.2 Zeolites as Host materials for metallic cations and complexes

The ion exchange properties of zeolite materials have been known and exploited for many decades. The ready incorporation of transition metal cations into the zeolite frameworks prompted experimentation on the reactions of such species within the pore structure of zeolites by various ligand types. The first wide scale studies of transition metal complexes within the pores of zeolite-Y began in the late seventies. Lunsford *et al.*[14] studied ethylene diamine copper complexes, describing the effects of hydration and reaction conditions on the degree of ethylene diamine coordination. They

also examined the stability of copper ethylene diamine complexes on Montmorrillonite clay as a continuation of this study and explored the effects of microenvironment on the photophysical properties of the complex.[15]

In 1980, Lunsford *et al.* also carried out the first studies on the luminescent ruthenium tris bipyridine located within the cages of zeolite-Y.[16] Their initial reasoning for the study was to investigate the ability of the zeolite cage to prevent excited state collisional deactivation whilst still allowing gas phase oxygen and water molecules access to the complex. They found the encased luminophore to be quenched effectively, like the free complex, by both oxygen and water. Further to this study Quayle and Lunsford examined the feasibility of photocatalytic splitting of water using encapsulated ruthenium polypyridyls.[17] They converted Z-$[Ru(bpy)_3]^{2+}$ to Z-$[Ru(bpy)_3]^{3+}$ using chlorine gas and assessed its reduction by intrazeolite water. They found that subsequent electron transfer processes necessary for O_2 production were hindered by the zeolite microenvironment. Quayle *et al.* concurrently examined Z-$[Fe(bpy)_3]^{2+}$ and Z-$[Fe(bpy)_3]^{3+}$ in order to access any changes in the spectroscopic behaviour of the species resulting from the local zeolite microenvironment.[18] The observed spectroscopic changes were comparable to divalent or trivalent iron tris bipyridine in other matrices. They did however notice the effect of high complex loading on the ability of chlorine gas to access complexes deeper within the zeolite particle, noting only partial oxidation of the complexes present. Calzaferri *et al.* also later commented on this phenomenon with regard to actual formation of tris ligated complexes at higher cation loading (*vide infra*). It would appear at high loadings the entrance to the zeolite interior is blocked by materials already deposited at the exterior of the particles.

Further studies queried the ability of ruthenium metal to support catalytic reactions in zeolite-Y, the interest owing to the porous nature of the material and its ion exchange capability, however these catalytic properties are not important to this work and are not discussed further.[19,20]

3.0.3 Ruthenium tris bipyridine $[Ru(bpy)_3]^{2+}$

Prior to discussing the effects of encapsulation on the properties of transition metal complexes, the main photophysical properties of the complexes are outlined below.

Ruthenium tris bipyridine (Figure 3.1) and its analogues been the subject of scrutiny for many years and consequently the major photophysical and photochemical characteristics of the compounds are well known. The reason for such intense study is the interesting and useful properties that these transition metal complexes offer in terms of stability, excited state redox properties and relatively long luminescent lifetimes which make them useful in practical systems such as oxygen sensors, artificial photosynthetic systems and many more.

$[Ru(bpy)_3]^{2+}$ is a d_6 metal complex possessing an octahedral geometry. Photoexcitation of the molecule at 240 nm and 450 nm results in the promotion of an electron from a π_M metal orbital to the π_L^* ligand orbitals collectively know as metal to ligand charge transfer (MLCT). The d-orbitals are split due to the octahedral configuration into three lower energy t_{2g} and two e_g orbitals. The two bands at 185 nm and 285 nm are assigned to ligand centred (LC) $\pi \rightarrow \pi^*$ transitions. The two weak shoulders at 322 nm and 344 nm have been attributed to Laporte forbidden d-d transitions, also know as metal centred (MC) transitions. The nature of the chelating ligands can also be tailored to alter the energy level of the LUMO of the complex leading to shifts in the MLCT and MC states and subsequent changes to the emissive characteristics of the complex. $[Ru(bpy)_3]^{2+}$ and analogous complexes has been widely studied for its properties as a photosensitiser due to the absorbance in both the UV and visible region leading to long lived luminescence. Excitation of any of the absorption bands of $[Ru(bpy)_3]^{2+}$ results in a luminescent emission.[21] Excitation of $[Ru(bpy)_3]^{2+}$ promotes an electron into the singlet excited state (^{1}MLCT), this is followed by fast intersystem crossing, thought to be approximately 110 fs into the lowest triplet

excited state (^{3}MLCT).[22] The intersystem crossing has a quantum efficiency of near unity.[23] The major radiative (k_r) and non-radiative decay (k_{nr}) pathways for excited state ruthenium tris bipyridine are outlined in Figure 3.2. The luminescence emission λ_{max} for ruthenium polypyridyl complexes is around 620 nm depending of course on the coordinating ligands properties. The triplet excited state lifetime of $[Ru(bpy)_3]^{2+}$ in de-aerated acetonitrile at 293 K is approximately 850 ns.[24] In rigid glasses at 77 K the excited state lifetime is ~5 μs with an emission quantum yield of ~0.4.[25] This increased lifetime is a result of the absence of previously allowed vibrational relaxation pathways due to the rigidity of the frozen glass.

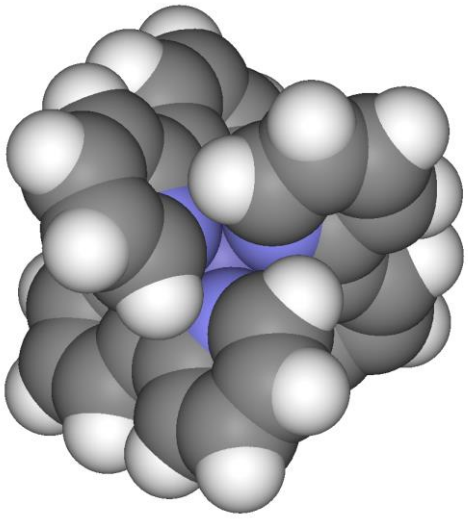

Figure 3.1: Space filling model of Ruthenium tris-bipyridine $[Ru(bpy)_3]^{2+}$.[26]

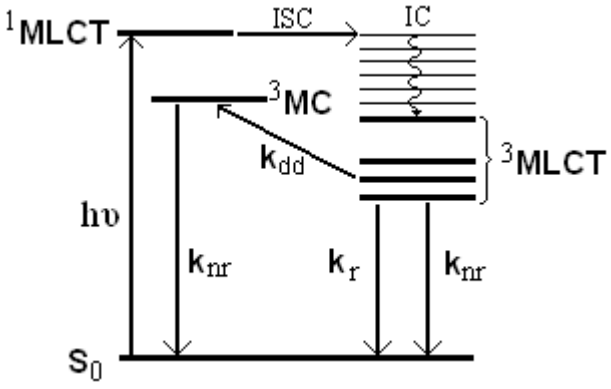

Figure 3.2: Simplified Jablonski diagram for $[Ru(bpy)_3]^{2+}$, showing the possible transitions after excitation and the energy states involved.

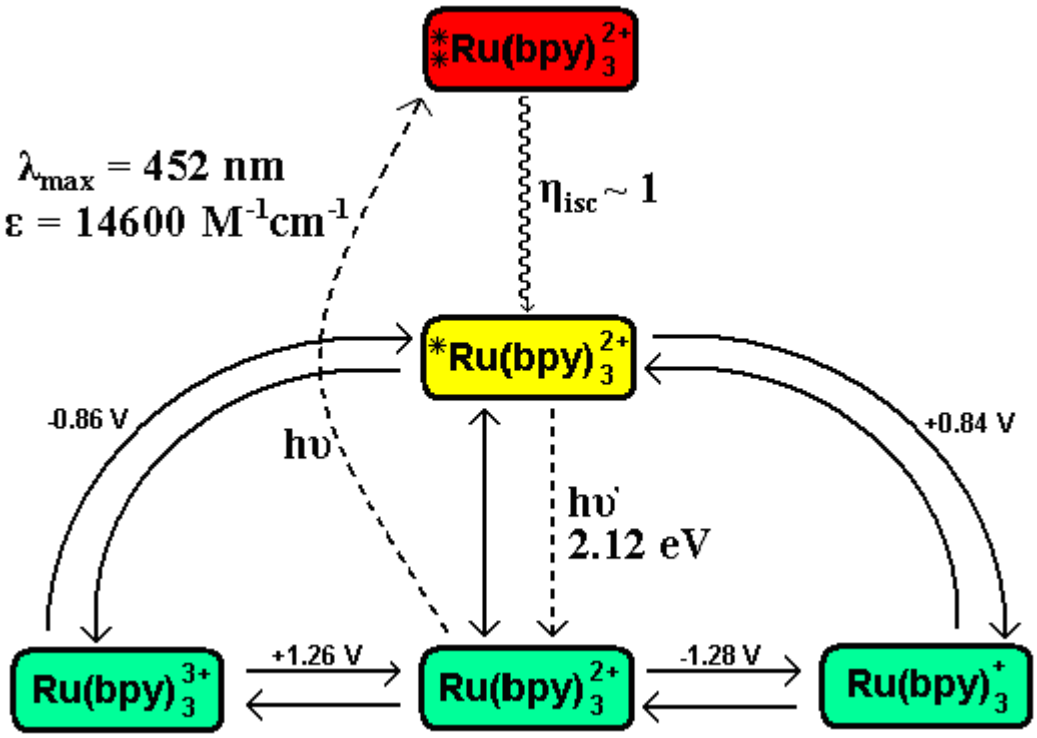

Figure 3.3: Diagram showing molecular quantities for Ruthenium tris bipyridine $[Ru(bpy)_3]^{2+}$ ** Represents higher energy spin allowed excited states whilst * indicates the lowest energy spin forbidden excited state, in this case a ^{3}MLCT state (Campagna, *et al.*, *Top. Curr. Chem.* **2007**, *280*, 117-214).[27]

Figure 3.3 shows some of the molecular quantities for $[Ru(bpy)_3]^{2+}$. The redox potentials can be determined from cyclic voltammetry and hence the excited state redox potentials (*vide supra*). One electron oxidation of $Ru(bpy)_3^{2+}$ results in removal of a metal centred electron whilst reduction is based at the bipyridine moieties, three increasing reduction potentials resulting from the sequential reduction of the three bipyridine ligands. In the excited state, $Ru(bpy)_3^{2+}$ is a stronger oxidant and reductant than in the ground state as a consequence of the lowering of the ionisation potential and enhancement of the excited state molecules electron affinity (*vide supra*). The triplet excited state is sufficiently long lived to interact with solute molecules, which can

result in energy or electron transfer processes occurring, the most obvious experimental consequence is the effective quenching of the triplet-excited state by dissolved atmospheric oxygen.

3.1 Preparation of zeolite entrapped transition metal complexes

The preparation of zeolite-Y entrapped transition metal complexes involves broadly two steps. Firstly, the metal centre is ion exchanged into the zeolite, replacing an ion present in the starting zeolite. The exchange is performed with a cationic salt of the transition metal, and can be performed in aqueous or non-aqueous solvent depending on the solubility of the salt. It's also possible to ion exchange by volatilisation of a suitable metal cation that has been mixed thoroughly with the zeolite material, ammonium hexachloroosmate for example, sublimes at 170 ^{0}C. In terms of the success of this approach the most important requirements are the size of the metal ion species relative to the zeolite pore window and its charge (since the aluminosilicate framework is negatively charged, this makes anionic exchange impractical). The cation species must be sufficiently small to allow entry via the zeolite aperture. The slurry is left stirring for a prolonged period, usually around eight hours to ensure that the ion exchange process is complete and that the salt has time to distribute itself evenly throughout the zeolite particles internal pore structure. Insufficient ion exchange time would result in much of the cations remaining close to the external surfaces, leading to an uneven distribution of cations.

The rate of ion exchange can be increased by the application of heat since interpore and intra-pore cationic site hopping is a thermally activated process.[28] The rate of migration of compounds within zeolites has been estimated previously, and can be used to determine the optimal ion exchange period.[29] Another possibility to increase the rate of ion exchange is the use of smaller zeolite particles.[30] In the case of ruthenium cation exchange, the process is carried out at reduced temperature with ruthenium hexammine dichloride to prevent the formation of undesirable ammoniated ruthenium oxychloride (ruthenium-red). The exchange is carried out at 4 ^{0}C to inhibit

such formation, as any ruthenium red formed is unavailable for subsequent ligation/reaction and then acts as a contaminant. This lower temperature necessitates an 8-hour exchange whereas a water based iron cation exchange under reflux conditions could accomplish a similar degree of cation exchange within approximately two hours. When ion exchange is complete, the slurry of zeolite and metal cation is filtered and the zeolite material washed thoroughly with the cation solvent. This ensures that any surface adsorbed metal salt is removed and only ion exchanged metal remains, conserving the homogeneity of the cation within the framework. This is desirable as the possibility exists that physical absorption could occur on outer surfaces during exchange, since the outer edge of the particles are in intimate contact with relatively concentrated bulk solution. Ideally metallic ion concentrations will be lower than the effective maximum exchange capacity of a given quantity of zeolite to ensure an even distribution.

The next synthetic step is reaction of the cation-exchanged zeolite with the required ligand. This can be carried out in a similar fashion as the cation exchange by exposure of the ligand to the zeolite, either as a melt, sublimination of pure ligand or in a suitable solvent with stirring. As before, the rate of diffusion of ligand can be enhanced with the application of heat, which in many cases the reaction also necessitates. The same criteria apply with regard to ligand size and charge, however this does not preclude two or three ligands reacting with a single metal centre within a large pore. In the case of ruthenium tris bipyridine, three bipyridine ligands react with one ruthenium ion resulting in a complex residing in the large zeolite cage too large to escape through the small apertures. This process has been termed the flexible ligand method or “ship-in-a-bottle” synthesis (Figure 3.4).[31] The reaction slurry is left stirring for the appropriate time and filtered. At this point it is generally treated with a concentrated sodium chloride solution, if for instance the sodium form of zeolite-Y was used. This removes any cationic complex that may have located itself on the zeolite particle surface and not in an internal cage. The washings can be monitored for the presence of the species until none is detected. After the salt wash, the transition metal doped zeolite material is subjected to prolonged solvent extraction (typically Soxhlet

extraction) in order to eliminate any unreacted ligand still residing in the internal zeolite structure. The progress of this can be monitored by UV-vis absorbance measurements of the extraction solvent.

The inclusion of the complex within the pore structure can then be confirmed with a host of spectroscopic techniques by reference to the pure complex. Shifts in emission maxima and broadening of Raman bands relative to the pure complex are typical of incarceration.

Entrapped complexes can only be removed from the zeolite cage by the dissolution of the zeolite host. This can be accomplished by the use of concentrated sulphuric acid, generally undesirable due to possible decomposition of complexes or dilute hydrofluoric acid, a much milder substitute. The removal of the complex from the zeolite cage is usually carried out in order to confirm the identity of the guest and for quantification of complex present per quantity of zeolite material.

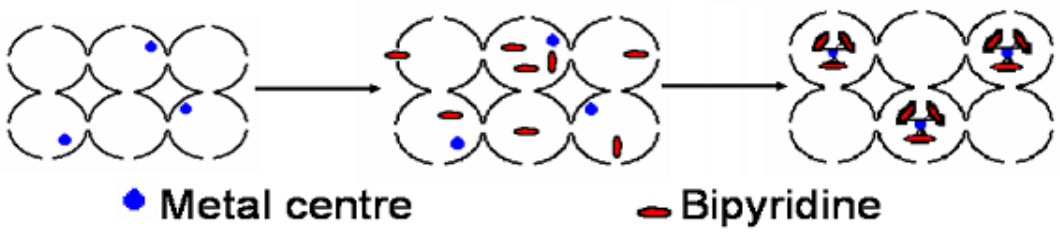

Figure 3.4: Schematic of a "Ship-in-a-bottle" synthesis incorporating a d_6 metal cation and bipyridine ligand

The degree to which the pore structure of a zeolite particle can be filled is also an important consideration. Calzafferi *et al.* found that at very high loading of ruthenium cations, reaction with bipyridine ligand was retarded for the cations exchanged further into the particle.[32] They found that a 50% (1 complex per two supercages) occupancy of available supercages by $[Ru(bpy)_3]^{2+}$ led to pure product and practically complete reaction with the available ligand. At 65% occupancy, multiple attempts at ligation were required for complete reaction and above that occupation, the reaction failed to go to completion. In

order to explain this behaviour they studied the concentration of complex at varying depths into the zeolite particles by partial dissolution of the zeolite framework with dilute hydrofluoric acid. It was suspected that initial reaction of bipyridine at the surface of the zeolite particle led to complex formation that effectively blocked access to further bipyridine entering the inner cavities, leaving the internal ruthenium cations inaccessible and unreacted.

The procedure for the preparation of heteroleptic entrapped complexes is slightly different depending on the required species. For example, preparation of Z-Ru[$(bpy)_2$(dmb)]$^{2+}$ (dmb=4,4'-dimethyl-2,2'-bipyridine) proceeds via a low temperature initial preparation of the bis-bipyridine complex, followed by extensive washing to remove excess ligand.[33] The dmb is than added and the reaction completed.

3.2 Electronic absorption and photophysical properties of zeolite entrapped transition metal complexes

3.2.1 Effect of inhibited solvation

Incavo *et al.* carried out a detailed examination of the optical properties of zeolite entrapped $[Ru(bpy)_3]^{2+}$, which included for the first time time resolved optical measurements.[34] They examined the effect of varying levels of hydration and the influence of non-polar solvent inclusion within the pores on the steady state luminescence and excited state characteristics of $[Ru(bpy)_3]^{2+}$ doped zeolite. An unoccupied zeolite-Y unit cell is estimated to hold up to 235 water molecules which are more ordered than solution phase water, resulting in increased apparent solvent viscosity.[35] On inclusion of a $[Ru(bpy)_3]^{2+}$ molecule, it's estimated that around two to three water molecules remain local to each bipyridine as well as other water molecules located in the surrounding sodalite cages.[36] The electronic absorption spectra of the hydrated zeolite material are very similar to solution phase studies. However, upon dehydration of the zeolite material there is a shift to higher energy $\pi \rightarrow \pi^*$ transitions. The lack of water could result in an enhanced interaction between the ruthenium cation and the negatively charged zeolite framework due to the

absence of the mediating effect of included water molecules.[34] This results in distortion of the molecule and a possible decrease in the degree of delocalisation within the bipyridine ligand, thereby increasing the electronic transition energy. The absence of a solvation sphere surrounding the excited state luminophore would also be expected to cause excited state destabilisation resulting in blue shifted emission due to the polar nature of the excited state species. The same study also found similar blue shifts in the presence of zeolite incorporated non-polar hexane. These effects are comparable to studies on $[Ru(bpy)_3]^{2+}$ in cellulose carried out by Thomas *et al.*[37] They found a 15 nm blue shift of $[Ru(bpy)_3]^{2+}$ in cellulose upon dehydration whilst Incavo *et al*. found a sizable 30 nm blue shift with dehydrated zeolite samples.

The excited state lifetimes of the hydrated and dehydrated ruthenium polypyridine doped zeolites are also markedly different, with the dehydrated samples possessing a biexponential lifetime considerably shorter than the single exponential decay of the hydrated sample. The biexponential nature of the decay the authors attributed to incomplete dehydration of the zeolite, with the shorter lifetime due to completely dehydrated cages and the longer component to partially hydrated cages, although they admit this finding was unexpected. Later work carried out Sykora *et al*. (*vide infra*) posited that adjacent cage interactions (at concentrations of $[Ru(bpy)_3]^{2+}$ considered by Incavo to be insignificant with regard to the possibility of substantial intercage interactions) could indeed lead to multi-exponential decays suggesting the extent of hydration was not the only factor resulting in the fast deactivation observed by Incavo as noted in the preceding paragraph.[38]

A further study by Dutta *et al*. provided more insight into the effect of zeolite hydration on the properties of $[Ru(bpy)_3]^{2+}$.[3] They examined Z-$[Ru(bpy)_3]^{2+}$ co-entrapped with tetraethyl ammonium (TEA). The purpose of the TEA was to mimic the size and (roughly) the steric influence of a bipyridinium ion. TEA was used since it does not quench $[Ru(bpy)_3]^{2+}$ excited state, whereas bipyridinium is a commonly used quencher molecule for studying rates of forward and back electron transfer in zeolite systems. This approach

effectively isolated the steric effect of a large organic molecules residing close to the ruthenium complex without the complexity of quenching, thus yielding information on the excited state perturbation due to steric hindrance. They found that the presence of TEA in close proximity to the luminophore resulted in a blue shifted emission, longer excited state lifetime and increased emission intensity. They suspected this arose due to the absence of water molecules that had been displaced by ion-exchanged TEA. They postulated that the $[Ru(bpy)_3]^{2+}$ excited state resides on a bipyridine ring facing an aperture (since the anionic bipyridine is unlikely to reside directly beside the anionic framework wall), which in the absence of TEA can hold water molecules that can re-orientate to stabilise the polar excited state. When water is absent the emission is blue shifted. The increase in lifetime was attributed to the increased energy gap and the decrease of available O-H moieties to effect non-radiative decay.

3.2.2 Effect of steric confinement

The kinetic diameter of $[Ru(bpy)_3]^{2+}$ is about 1 nm smaller than the internal diameter of a 1.3 nm zeolite-Y supercage. This tight fit has some potentially useful consequences. The supercage imparts added chemical stability to complexes, for example, entrapped $[Ru(bpy)_3]^{2+}$ is stable up to 400 ^{0}C due to prevention of permanent ligand loss (the distinct possibility exists that ligand-metal bonds are being broken and reformed before loss of ligand from the cage can occur).[34] The steric confinement also influences photophysical relaxation pathways and therefore can directly interfere with the photophysical properties of a species depending on the degree of steric hindrance imposed by the framework, as well as the highly electrostatic cavity environment. These combined factors and their impact on entrapped species has been termed electronic confinement.[39] In order to assess the extent of this effect, Kincaid *et al*. examined the temperature dependence of a number of ruthenium polypyridyls in zeolite-Y.[40] They found that compared to solution phase studies, the ligand field state was raised in energy to such an extent so as to eliminate it as a deactivation pathway. This increase in ^{3}dd energy they attributed to inhibited Ru-N bond elongation, thus preventing population of the

state and subsequent decomposition through ligand loss. The low energy resonance Raman modes show shifts suggestive of changes to Ru-N modes.

A later study by Bhuiyan and Kincaid demonstrated very nicely the potential for photophysical manipulation by entrapment within a zeolite pore structure.[41] Ruthenium bis-terpyridine was synthesised within zeolite-Y with the knowledge that the solution phase complex is non-emissive at room temperature. Up until then there was speculation as to reason for the lack of emission and its short 250 ps lifetime.[42] Upon entrapment, room temperature emission was observed with a lifetime of 140 ns. As before, temperature dependence studies were performed on the material and an increase of nearly 1200 cm^{-1} in the ^{3}dd state was recorded. This increase in energy of the ligand field state was attributed by the author to a similar distortion of the Ru-N bond elongation mode as observed for the ruthenium tris bipyridine. A similar study involving a tris-ligated ruthenium polypyridyl yielded similar results “turning on” a previously non-emissive complex.[43]

3.2.3 Effect of neighbouring transition metal polypyridyl species

The first study conducted on $[Ru(bpy)_3]^{2+}$ loaded zeolite-Y described excited state quenching at high complex loading. Lunsford *et al*. examined the effect of increasing complex concentration on the emission properties of the zeolite material.[16] They attributed a fall in emission intensity with increased complex loading to concentration quenching, and tentatively assigned the mechanism as resonance energy transfer, since they correlated the reciprocal intensity to the square of concentration which is proportional to the effective reciprocal distances between species. They also noted a drop in the excited state lifetime with increasing complex concentration eliminating the possibility of merely radiative energy transfer, however no attempt was made to quantify the extent of these interpore interactions.

Dutta *et al*. carried out the first detailed examination of the interactions between host $[Ru(bpy)_3]^{2+}$ complexes in zeolite-Y.[44] They prepared zeolite samples with a wide range of complex loadings. In this manner, the

behaviour of individual "isolated" $[Ru(bpy)_3]^{2+}$ complexes, becoming progressively surrounded by adjacent cage $[Ru(bpy)_3]^{2+}$ was examined. They looked at concentrations ranging from 1 complex per 60 supercages to 1 complex per supercage. However, the results at this high loading must be tempered by reference to later articles casting doubt on the overall purity of complexes at such high zeolite loadings.[32] They found that at the highest loading, nominally 1 complex residing in each supercage (that is to say each $[Ru(bpy)_3]^{2+}$ is totally surrounded by four other $[Ru(bpy)_3]^{2+}$ complexes in adjacent cages) the MLCT absorbance band was red shifted by ~40 nm, from 453 nm to ~490 nm. The red shift was attributed to the presence of the other guest molecules since it was absent at lower loadings. The emission wavelength was unchanged but the intensity was diminished and the excited state lifetimes also decrease with increased loading. Later studies carried out by Calzaferri *et al*. demonstrated that large amounts of impurities are introduced at such high loadings (*vide supra*) casting doubt on the extent of shifts observed in the absorbance spectra. Later work by Sykora *et al.* failed to reproduce these shifts and reported only modest blue shifts of 5 nm.[38]

Yamashita *et al.* examined the influence of different alkali earth metals on the spectroscopic properties of encapsulated $[Ru(bpy)_3]^{2+}$.[45] Extended X-ray absorption fine structure data revealed that the average Ru-N bond length and emission intensity decreased with increasing cation size, indicative of charge balancing cation distortion of the guest complex.

Kincaid *et al.* carried out an interesting study on interactions between adjacent cage species.[46] Earlier studies had utilised a purely statistical distribution of complexes within the zeolite framework, adjacent cage interaction becoming more predominant at higher complex loadings. The group was interested in locating all the complexes in adjacent cages eliminating any influences from isolated species. They achieved this by initial introduction of $[Ru(bpy)_2(bpz)]^{2+}$ (where bpz is 2,2'-bipyrazine) and subsequent reaction with $[Ru(NH_3)_5(H_2O)]^{2+}$ yielding $Ru(bpy)_2(bpz)\text{-}Ru(NH_3)_5$. Purification of this material removed excess $[Ru(NH_3)_5(H_2O)]^{2+}$. Reaction of the zeolite bound dimetallic species

with 5-methyl-2,2'-bipyridine (mmb) yielded Z-$[Ru(bpy)_2(bpz)]^{2+}$ with adjacent Z-$[Ru(mmb)_3]^{2+}$ complexes (Figure 3.5).

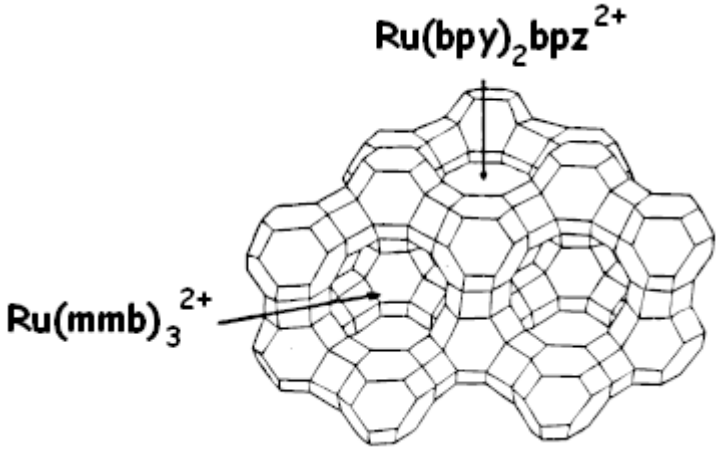

Figure 3.5: Adjacent cage Ruthenium polypyridyl complexes prepared by Kincaid *et al* (*J. Am. Chem. Soc.* **1998**, *120,* 3490-3498).[46]

They observed a dramatic 2.5 to 4-fold reduction in emission intensity when compared to samples containing a random distribution or a mechanical mixture of particles containing only one type of the complexes in each particle. This was not unexpected considering previous studies used only differing loadings of $[Ru(bpy)_3]^{2+}$ (*vide supra*).[44]

The authors considered the nature of the quenching processes, however the lack of definitive intrazeolitic excited state redox potentials for the complexes studied meant only general conclusions could be drawn. They compared solution phase redox potentials, showing electron transfer between two ^{3}MLCT state complexes to be energetically feasible, but ruled this possibility unlikely for the zeolite samples due to the low light intensity of the laser excitation. They suggest that quenching may be possible between an excited state complex located next to a ground state species if the intrazeolitic redox potentials are affected by inclusion, since this process is slightly unfavourable in solution (ΔG^0 = 0.03 eV for the oxidative quenching of $[Ru(mmb)_3]^{2+}$). Ultimately, the most energetically feasible process is energy transfer from excited state $[Ru(mmb)_3]^{2+}$ to $[Ru(bpy)_2(bpz)]^{2+}$ (ΔG^0 = -0.12 eV) but

contribution from electron transfer processes are not ruled out due to possible local changes in excited state redox potentials.

Sykora *et al.* investigated the effects of intercage interactions of $[Ru(bpy)_3]^{2+}$ loaded zeolite in order to quantify the extent of interaction with loading as well as provide information as to the nature of the quenching process.[38] $[Ru(bpy)_3]^{2+}$ loaded Zeolite-Y samples were prepared with a wide range of concentrations ensuring that the lowest loading had relatively few adjacent cage complexes and the highest loading had many. They modelled the intercage distribution of complexes based on mean occupation of supercages as the average distance between complexes decreases with increased loading.

Distribution of $Ru(bpy)_3^{2+}$ in Y-Zeolite as a Function of $Ru(bpy)_3^{2+}$ load

load (Ru/no. cages)	shell (no. cages/shell)						
	b (4)	c (12)	d (12)	e (6)	f (12)	g (24)	h (12)
1/66.7	5.86%	15.61%	13.02%	5.68%	9.92%	15.18%	5.76%
1/29.7	12.80%	29.39%	19.48%	7.12%	10.52%	11.60%	3.06%

Figure 3.6: Distribution of complex within zeolite as a function of loading (Sykora *et al., J. Phys. Chem. B* **1999** *103*, 309-320).[38]

A random 100 $[Ru(bpy)_3]^{2+}$ molecules at a loading of 1 complex per ~30 supercages (Figure 3.6) will have the following arrangement. 12-13 molecules will have an adjacent complex (shell B), 29-30 complexes will have separation of at least one supercage from its nearest neighbouring complex and 19-20 molecules will have at least two empty supercages between it and another complex. The shell refers to the distance from a random complex to its nearest neighbouring cage, shell b being closer to a random complex than shell c and so on (Figure 3.7). They calculated these distributions as follows:

Taking the loading as 1/30, the probability of a randomly selected cage containing a complex is 1/30 = 0.033. Therefore the probability of selecting an unoccupied cage is 1-0.033 = 0.967. If a random occupied cage containing a complex is selected than the probability of finding an unoccupied

cage adjacent to the complex is 0.967. If each cage is surrounded by four other cages (Figure 3.7), then the probability that every surrounding cage is empty is calculated by: $0.967^4 = 0.874$. Therefore the probability that an adjacent cage contains at the least one other complex is 1-0.874 = 0.126 (i.e one of the four possible locations around a 'lone' complex is occupied). Another way of considering this probability is to consider shell to be ~13% occupied. Therefore, at this concentration, 87% of complexes are calculated to be isolated from any adjacent $[Ru(bpy)_3]^{2+}$.

They observed that the excited state lifetime of isolated $[Ru(bpy)_3]^{2+}$ to be comparable to aqueous studies, but adjacent cage species could interact in two ways. Firstly via a ground state-excited state interaction (GS-ES), one molecule in a ^{3}MLCT state in a cage adjacent to a ground state molecule. This results in deactivation of the excited state and a much reduced excited state lifetime. This quenching is attributed tentatively to an external heavy atom effect, whereby the close proximity of the adjacent GS complex induces fast relaxation in the ES molecule.

The other possibility explored was an excited state-excited state (ES-ES) interaction. The appearance of a new shorter lifetime than observed with a GS-ES with increased laser power prompted an extensive study on the effect of laser power on lifetimes. They found that the contribution from the shortest component increased with increasing excitation power. They speculated that interacting ^{3}MLCT molecules resulted in triplet-triplet annihilation. At low light intensities the likelihood of two adjacent cage excited state complexes is low but increases with higher light intensities.

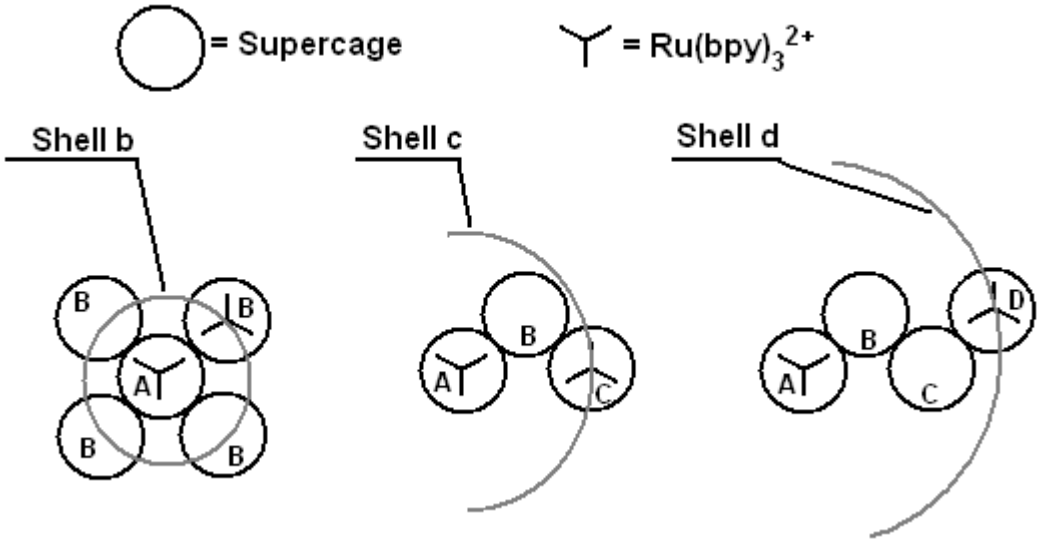

Figure 3.7: Schematic of shell nomenclature for zeolite-Y system (Sykora *et al., J. Phys. Chem. B* **1999** *103*, 309-320).[38]

3.2.4 Scope of work

This introduction was aimed at outlining the main contributions that highlight the important effects zeolite entrapment has on the behaviour of transition metal polypyridyl species, both isolated within the zeolite host material as well as with other guest molecules present.

The following chapter explores, for the first time the interaction of the model luminophore entrapped within zeolite-Y with co-included iron polypyridyl complexes that are expected to effectively quench the excited state emission. Interestingly it was found that unlike the quenching observed with pure $[Ru(bpy)_3]^{2+}$ loaded material, which appears to be between adjacent cages in nature only, the iron polypyridyls effectively quench the emission over relatively large distances, up to three supercage separation distance apart. This indicates that long-range energy transfer between transition metal complexes is possible through the zeolite media.

In addition to the intermolecular communication, this chapter examines the effect of the zeolite environment on the excited state acceptor properties of an

entrapped iron polypyridyl complex. Distortion of the iron complex caused by the rigid framework “turns on” excited state acceptor properties of the complex. Quenching behaviour by the same solution phase complex is not observed in solution.

These novel effects must be considered when designing the format of any complex zeolite systems based on donor-acceptor supramolecular entities. These findings have implications for any future applications employing luminescent complexes entrapped within zeolite systems, especially when considering any multiplexed application requiring multiple co-entrapped species.

3.3 Results and discussion

3.3.1 Synthesis and characterization

The full experimental procedure is described in detail in chapter 2.To encapsulate $[Ru(bpy)_3]^{2+}$ and $[Fe(L\text{-}L)_n]^{2+}$ within the 13 Å supercage of zeolite Y ,'ship in a bottle' synthesis was employed. Metal precursors and ligand were ion exchanged or diffused into the zeolite and reacted in-situ. Once formed, the complexes are physically trapped and cannot leach out of the zeolite since the molecular diameter of the product exceeds the size of the pore entrance. The resulting powders were washed and ion exchanged extensively to eliminate encapsulated reagent or any surface bound complex. Soxhlet extraction was used to eliminate any unreacted ligand. The initial progress of the reaction was easily followed by the obvious colour changes occurring in the materials. The slurries were kept rapidly stirred via a magnetic stir bar in order to keep local ligand concentration with regard to each zeolite particle as homogeneous as possible during the reaction as well as to ensure that the zeolite particles were fully dispersed.

For the purposes of discussing the loading of metal complexes into zeolite Y we use the number of supercages per metal complex or percentage occupancy, for example 1 metal complex per 20 supercages, represents a five percent occupancy of zeolite supercages, or the concentration expressed in mol dm^{-3} based on Y-zeolite having a density 1.92 g/cm^{-3} and the volume of a unit cell equal to 15,000 $Å^3$. Using these values Y-zeolite is calculated to contain 2.778 X 10^{20} supercages per 1 g of material.[47,48] The concentrations for the purposes of synthesis and quantitation were calculated as follows. For instance, the preparation of 1 g of 1 $[Ru(bpy)_3]^{2+}$ per 20 supercages. 1 $[Ru(bpy)_3]^{2+}$ per 20 supercages represents 5% supercage occupancy. Therefore 5% of 2.778 X 10^{20} are occupied or 1.380 X 10^{19} $[Ru(bpy)_3]^{2+}$ complexes are present in 1 g of material. Division of this number by Avogardro's number yields the required number of moles of metal cation required for 5% pore occupancy.

On the basis of the solution phase extinction coefficient and electronic absorbance spectroscopy (*vide infra*) the Z-$[Ru(bpy)_3]^{2+}$ prepared for these studies contained 1 $[Ru(bpy)_3]^{2+}$ per 22 supercages. This material was subsequently doped with the desired loading of either $[Fe(bpy)_3]^{2+}$ or $[Fe(tpy)_2]^{2+}$ to yield the co-doped materials. A single synthetic batch of Z-$[Ru(bpy)_3]^{2+}$ was used for all iron encapsulation reactions. The concentrations of metal complex within the zeolite was confirmed by dissolving 50 mg of the zeolite material in hydrofluoric acid (1 mL, 10% V/V) and the concentrations of $[Ru(bpy)_3]^{2+}$, $[Fe(bpy)_3]^{2+}$ and $[Fe(tpy)_2]^{2+}$ were then estimated from the visible absorbance.[49] The electronic absorbance was measured in HF solution directly after dissolution. In separate experiments, we confirmed that $[Ru(bpy)_3]^{2+}$, $[Fe(bpy)_3]^{2+}$ and $[Fe(tpy)_2]^{2+}$ were all stable in 10% V/V HF over periods at least twice as long as those required for the zeolite analysis. The concentrations of the co-doped materials are shown in Table 3.1.

TABLE 3.1: Concentrations of transition metal co-doped materials presented in this thesis.

Conc $[Fe(bpy)_3]^{2+}$ [a] within Z-$[Ru(bpy)_3]^{2+}$ [b]		Total loading[c]	Conc $[Fe(tpy)_2]^{2+}$ [a] within Z-$[Ru(bpy)_3]^{2+}$ [b]		Total loading[c]
Mol dm^{-3}	S/cages per $[Fe(bpy)_3]^{2+}$	S/cages per $M(LL)_n$	Mol dm^{-3}	S/cages per $[Fe(tpy)_2]^{2+}$	S/cages per $M(LL)_n$
0.0334	26.5	12.1	0.119	7.4	5.6
0.0187	47.4	15.2	0.056	15.8	9.3
0.0162	54.7	15.9	0.038	23.3	11.4
0.0127	69.8	16.9	0.027	32.8	13.3
0.0120	73.8	17.2	0.024	36.9	13.9
0.0090	98.4	18.2	0.019	46.6	15.1
0.0080	110.7	18.6	0.016	55.4	15.9
			0.015	59.1	16.2
			0.009	92.4	18.0

[a]Based on Y-zeolite with density 1.92 g/cm^{-3} and 1 g Y-zeolite containing 2.778 X 10^{20} supercages (S/cages).[47,48] [b]Concentration of Z-$[Ru(bpy)_3]^{2+}$ remained constant at 0.0396 Mol dm^{-3}, corresponding to 1 $[Ru(bpy)_3]^{2+}$ per 22 supercages. [c]Represents combined loading of donor and acceptor complexes.

In order to ensure that no uncomplexed iron persisted in the zeolite, additional 2,2'-bipyridine and ascorbic acid were added to the extracted supernatant solution. This did not alter the absorption spectrum, indicating that any uncomplexed iron remaining after reaction had been removed via the extraction procedures described. The lack of residual iron is not unexpected, since the material is ion exchanged with a relatively concentrated sodium chloride solution during the purification procedure.

Separate experiments confirmed that iron polypyridyl complexation occurs in low pH solutions, precluding the possibility that the low pH of the HF solution could affect the quantitation of the uncomplexed iron. The diffuse reflectance spectrum of Z-$[Ru(bpy)_3]^{2+}$ in the absence of added iron shows a small shoulder at ~545 nm. This is attributed to a small amount of an iron impurity within the zeolite material. In spite of extensive washing of the zeolite with sodium chloride solution the iron persisted. The actual quantity of the iron impurity is estimated to be less than 1 iron complex impurity per 135 supercages.

3.3.2 Spectroscopy

3.3.2.1 Diffuse reflectance Spectroscopy

Both $[Ru(bpy)_3]^{2+}$ and $[Fe(bpy)_3]^{2+}$ have been included separately in zeolite-Y and the electronic spectroscopy reported.[50,51,52,53] The electronic spectroscopy of our products agreed closely with these reports.

3.3.2.2 $[Ru(bpy)_3]^{2+}$ diffuse reflectance spectroscopy

The diffuse reflectance spectroscopy of Z-$[Ru(bpy)_3]^{2+}$ (Figure 3.8) broadly mirrors that of solution phase absorbance measurements as described in section 3.0.3. Lunsford *et al.* who first prepared the zeolite entrapped $[Ru(bpy)_3]^{2+}$ noted that the diffuse reflectance is characterised by its similarity to the solution phase with only modest shifts in the absorption maximum (458 nm) observed at high loadings of $[Ru(bpy)_3]^{2+}$.[50] However there is a significant decrease in the relative intensities of the $\pi \rightarrow \pi^*$ transition compared to the MLCT transition after zeolite entrapment. The effects of the degree of hydration on the electronic absorption of Z-$[Ru(bpy)_3]^{2+}$ is discussed in section 3.2.1. They also noted the appearance of the band at ~545 nm and attributed it to an $[Fe(bpy)_3]^{2+}$ impurity.

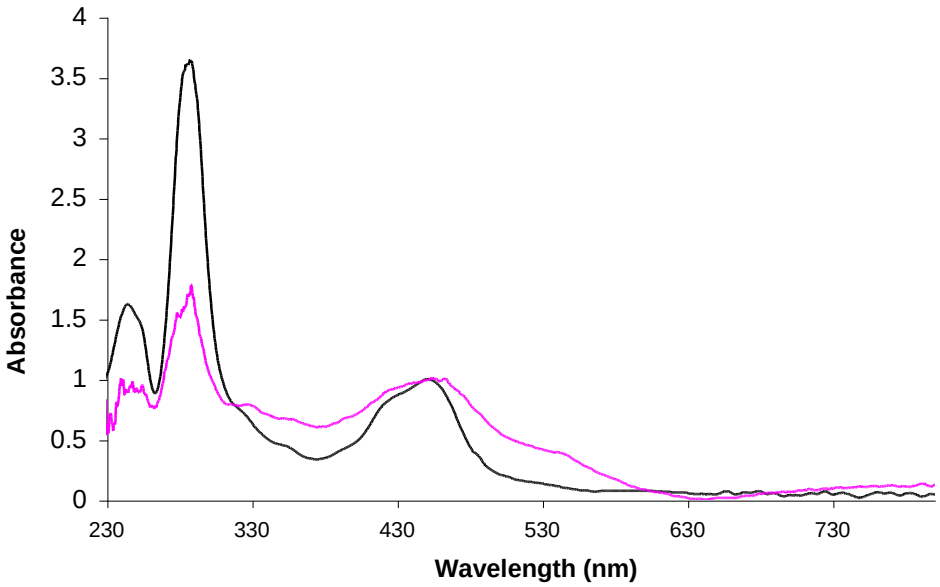

Figure 3.8: Absorption spectrum of $[Ru(bpy)_3][PF_6]_2$ (5.05×10^{-5} M in acetonitrile) black trace and diffuse reflectance spectrum of Z-$[Ru(bpy)_3]^{2+}$ (1 $[Ru(bpy)_3]^{2+}$ per 22 supercages), pink trace. Spectra were normalised based on the complexes absorption MLCT maxima for comparison purposes.

3.3.2.3 $[Fe(bpy)_3]^{2+}$ diffuse reflectance spectroscopy

A comparison of the diffuse reflectance spectrum of Z-$[Fe(bpy)_3]^{2+}$ and solution phase $[Fe(bpy)_3]^{2+}$ is shown in Figure 3.9.

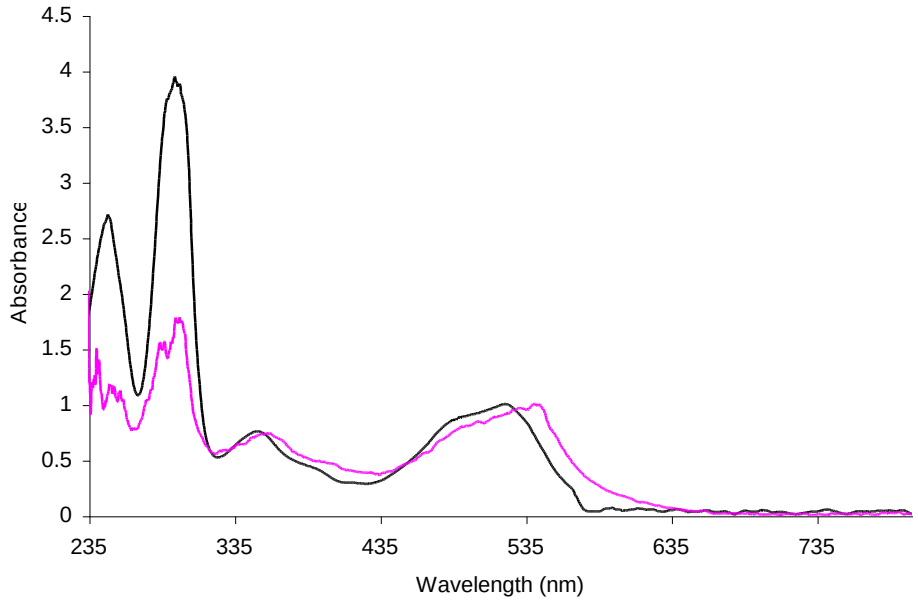

Figure 3.9: Absorption spectrum of $[Fe(bpy)_3][PF_6]_2$ (6.75 x 10^{-5} M in DMSO) black trace and diffuse reflectance spectrum of Z-$[Fe(bpy)_3]^{2+}$ (1 $[Fe(bpy)_3]^{2+}$ per 20 supercages), pink trace. Spectra were normalised based on the complexes MLCT absorption maxima for comparison purposes.

The UV-vis spectra of $[Fe(bpy)_3][PF_6]_2$ and Z-$[Fe(bpy)_3]^{2+}$ are compared in Figure 3.9. The high-energy absorption at 300 nm is associated with π→π* transitions of the coordinated ligand.[54] The intense visible absorption at 522 nm for the $[Fe(bpy)_3][PF_6]_2$ and 544 nm for the Z-$[Fe(bpy)_3]^{2+}$ material have been assigned to MLCT transitions.[55] The significant shifts associated with the MLCT bands are attributed to interactions of the complex with the framework wall. Mössbauer spectroscopy carried out by Vijayalakshmi *et al.* on both Z-$[Fe(bpy)_3]^{2+}$ and $[Fe(bpy)_3][ClO_4]_2$ indicates that the entrapped complex experiences significant structural distortion.[56] As noted for the Z-$[Ru(bpy)_3]^{2+}$ material there are substantial changes in the relative intensities of the π→π* and MLCT absorption bands upon zeolite incarceration of the complex.

3.3.2.4 $[Fe(tpy)_2]^{2+}$ diffuse reflectance spectroscopy

In contrast to the Z-$[Fe(bpy)]_3^{2+}$ system, there is significant broadening of the visible bands of encapsulated $[Fe(tpy)_2]^{2+}$ with concomitant shifts in the absorbance maxima compared to the complex in solution (Figure 3.10). These absorbance changes have a profound impact on the photophysical properties of this complex (*vide infra*).

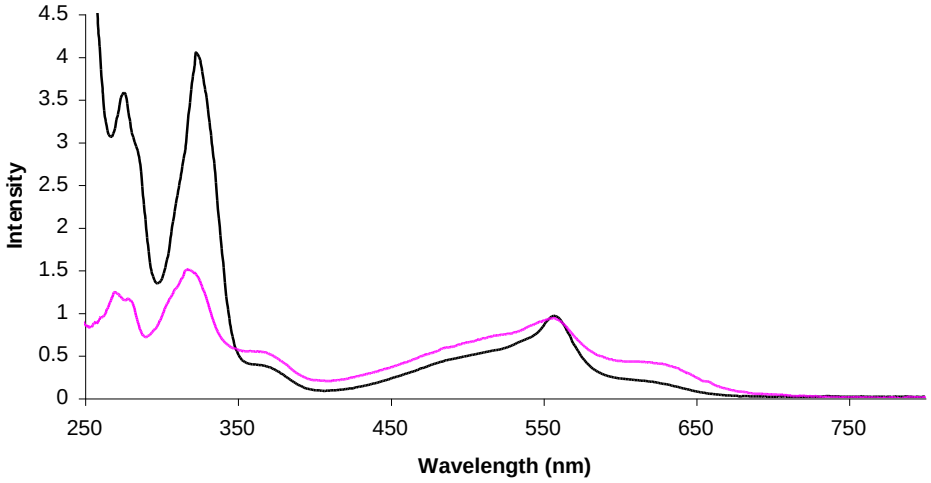

Figure 3.10: Absorption spectrum of $[Fe(tpy)_2][PF_6]_2$ (4.97×10^{-5} M in DMSO) black trace and diffuse reflectance spectrum of Z-$[Fe(tpy)_2]^{2+}$ (1 $[Fe(tpy)_2]^{2+}$ per 20 supercages), pink trace. Spectra were normalised based on the complexes MLCT absorption maxima for comparison purposes.

In order to quantify the extent of absorption band broadening of $[Fe(tpy)_2]^{2+}$ after entrapment, spectral fitting was performed (Figure 3.11 and Figure 3.12) in order to deconvolute the absorption and diffuse reflectance spectra and examine individual absorbance envelopes. The details of the experimental conditions and software utilised to perform this are described in chapter 5.

For $[Fe(tpy)_2]^{2+}$ in DMSO, spectral fitting shows that the $[Fe(tpy)_2]^{2+}$ metal to ligand charge transfer Fe (t_2g $d\pi$) to tpy (π^*) transition,[57] can be deconvoluted into three contributions, centered at 558, 536 and 521 nm (Figure 3.11). The wavelength of the sharp feature at 558 nm, remains unchanged in zeolite,

although its relative intensity is significantly reduced (Figure 3.12). The features at 536 and 521 nm have been assigned to the Fe (t_2g $d\pi$) to terpy (π^*) transition corresponding to excitation into higher lying levels within the π^* manifold.[57,58] These features undergo substantial changes, shifting to 525 nm and 504 nm respectively upon inclusion in zeolite. In addition, the 525 nm band is considerably broadened and its intensity enhanced in zeolite.

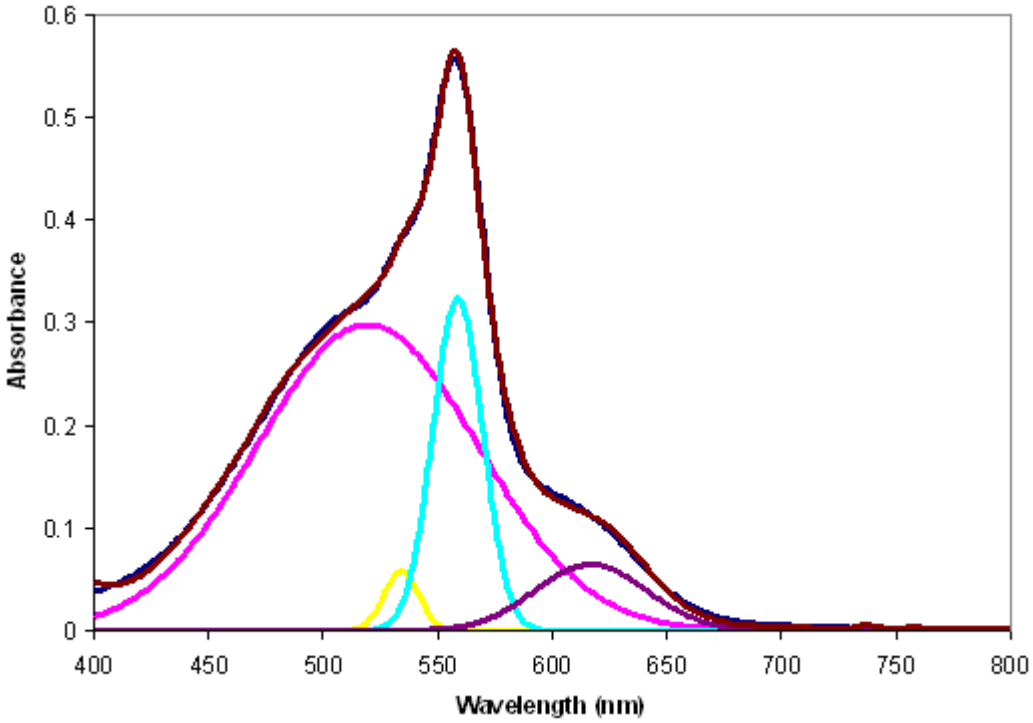

Figure 3.11: Deconvoluted absorbance spectrum of $[Fe(tpy)_2][PF_6]_2$ (4.97×10^{-5} M in DMSO). Recorded $[Fe(tpy)_2][PF_6]_2$ spectrum (wine red trace), calculated deconvolution fit (dark blue trace), Individual absorbance envelope contributions (magenta, yellow, cyan and purple).

The low energy tail to the MLCT envelope for $[Fe(tpy)_2]^{2+}$ centered at 625 nm is assigned to an allowed $^1T_2 \leftarrow {}^1A_1$ ligand field transition.[59] This feature is also strongly influenced by inclusion within the zeolite. This transition is weakly allowed in iron complexes of tridentate imines because the formal octahedral symmetry is reduced toward D_{4h} symmetry. In zeolite, this band is broadened and the relative intensity (as a percentage of the overall visible absorption envelope) of this feature increased by a factor of approximately three. This

observation suggests that the deviation away from octahedral geometry increases on encapsulation presumably due to the spatially restrictive zeolite environment. The impact of the zeolite on the geometry of $[Fe(tpy)_2]^{2+}$ complexes is consistent with the very large increases in luminescence intensity and lifetime observed for the analogous ruthenium complex when incorporated in zeolite, although there is some debate as to the origin of the photophysical changes.[41] Such structural changes are furthermore reflected in changes to Raman spectroscopy (*vide infra*) when $[Fe(tpy)_2]^{2+}$ is encapsulated. Bhuiyan *et al.* however noted no substantial alteration in $[Ru(tpy)_2]^{2+}$ absorption bands upon entrapment.[41] Further discussion of the distortion of complexes within zeolite-Y is contained in chapter 5.

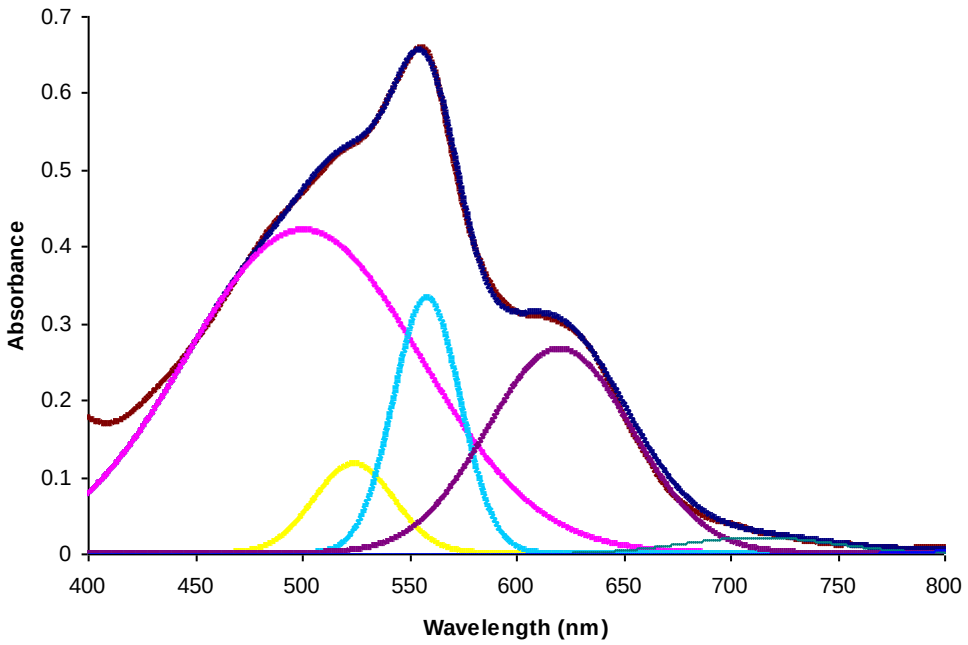

Figure 3.12: Deconvoluted diffuse reflectance spectrum of Z-$[Fe(tpy)_2]^{2+}$ (1 $[Fe(tpy)_2]^{2+}$ per 20 supercages). Recorded Z-$[Fe(tpy)_2]^{2+}$ spectrum (wine red trace), calculated deconvolution fit (dark blue trace), Individual absorbance envelope contributions (magenta, yellow, cyan and purple).

3.3.2.5 Diffuse reflectance spectroscopy of co-encapsulated $[Ru(bpy)_3]^{2+}$ and $[Fe(bpy)_3]^{2+}$

In order to assess if there were any changes to the respective spectra of Z-$[Ru(bpy)_3]^{2+}$ and Z-$[Fe(bpy)_3]^{2+}$ when co-doped, we compared the electronic spectroscopy of the individual complexes in zeolite Y with those in which the metal complexes are combined. Figure 3.13(A) shows the diffuse reflectance spectra of approximately 1:20 metal to pore loadings (5% total pore occupation) of (i) Z-$[Ru(bpy)_3]^{2+}$ and (ii) Z-$[Fe(bpy)_3]^{2+}$ in Zeolite Y. Figure 3.13 (A) (iii) shows the linear addition of these two component spectra. Figure 3.13 (B) shows the diffuse reflectance spectrum of 5% Z-$[Ru(bpy)_3]^{2+}$ with increasing loadings of $[Fe(bpy)_3]^{2+}$.

The diffuse reflectance for the co-doped samples show only minor changes to the main MLCT band, where for example there is a slight red shift in the ruthenium absorbance at the highest concentration of $[Fe(bpy)_3]^{2+}$.

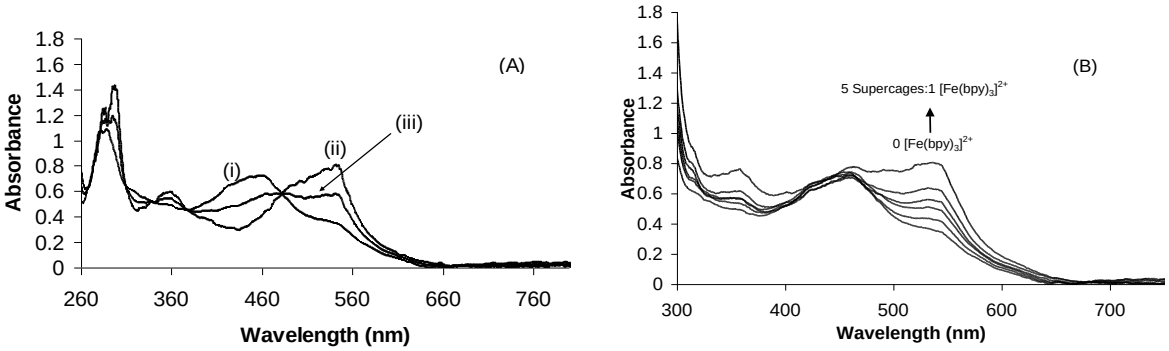

Figure 3.13: Diffuse Reflectance Spectra of (i) 1:22 pore Z-$[Ru(bpy)_3]^{2+}$ (ii) 1:20 pore Z-$[Fe(bpy)_3]^{2+}$ and (iii) the averaged combined spectra of the two (b) Diffuse reflectance spectra 1:22 Z-$[Ru(bpy)_3]^{2+}$ with increasing concentration of encapsulated Z-$[Fe(bpy)_3]^{2+}$.

Overall, however, comparison of the spectrum for 1:22 metal : supercage loadings of Z-$[Ru(bpy)_3]^{2+}$ co-doped with less than 1: 20 metal : supercage loadings of Z-$[Fe(bpy)_3]^{2+}$ shows little evidence for ground state intermolecular

interactions between the iron and ruthenium bpy complexes when co-incorporated. Assuming an even distribution of the complexes throughout the zeolite matrix, the probability that adjacent cages contain a ruthenium and an iron centre is low. For example at the highest loading of $[Fe(bpy)_3]^{2+}$ used here, 1 in 26.5 supercages, the probability of adjacent cages containing a Ru-Fe pair is approximately 14%. Therefore, it is not surprising that electronic spectroscopy indicates no interaction between the co-immobilized complexes.

3.3.2.6 Diffuse reflectance spectroscopy of co-encapsulated $[Ru(bpy)_3]^{2+}$ and $[Fe(tpy)_2]^{2+}$

The diffuse reflectance spectra for the Z-$[Fe(tpy)_2]^{2+}$ co-doped system (Figure 3.14) also shows no strong indications of any ground state interactions at low complex loading. However at the highest iron complex loadings, a red shift of 3 nm in the $[Ru(bpy)_3]^{2+}$ was noted. This red shift appears similar in nature to the intercage $[Ru(bpy)_3]^{2+}$ interactions observed by Dutta *et al.* at high complex loadings (*vide supra*).[34]

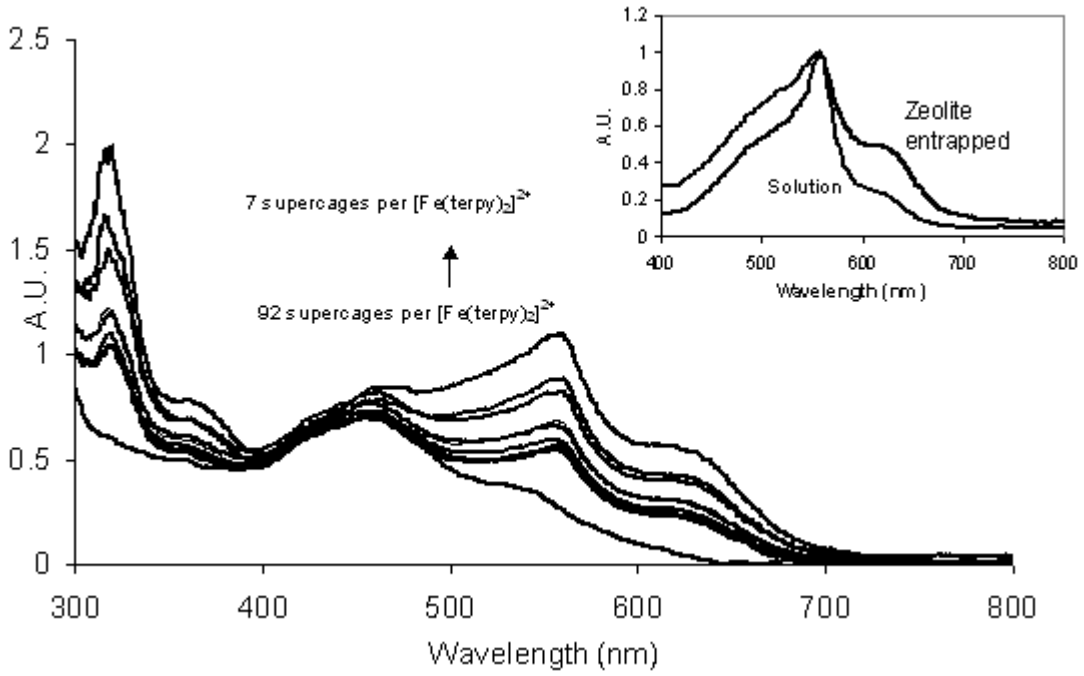

Figure 3.14: The diffuse reflectance spectrum of 1 : 22 loading of Z-$[Ru(bpy)_3]^{2+}$ with increasing loadings of $[Fe(tpy)_2]^{2+}$. The inset compares the normalised diffuse reflectance spectrum of Z-$[Fe(tpy)_2]^{2+}$ (1:20) in the absence of ruthenium and the solution phase absorbance spectrum of $[Fe(tpy)_2][PF_6]_2$ in dimethylsulfoxide (DMSO).

Diffuse reflectance spectra of co-encapsulated $[Ru(bpy)_3]^{2+}$ and $[Fe(tpy)_2]^{2+}$ exhibit MLCT absorptions arising from each guest complex, the former at 458 nm and the latter at 559 nm. Although, like co-doped $[Fe(bpy)_3]^{2+}$ and $[Ru(bpy)_3]^{2+}$ there are no new features to suggest strong ground state communication. At the highest loading of $[Fe(tpy)_2]^{2+}$, the Z-$[Ru(bpy)_3]^{2+}$ MLCT is slightly red shifted by 4 nm to 462 nm whilst the Z-$[Fe(tpy)_2]^{2+}$ MLCT formerly at 559 nm undergoes a red shift of 3 nm. These shifts are comparable to those attributed to adjacent cage interactions of $[Ru(bpy)_3]^{2+}$ in zeolite Y and likely to originate from similar inter-cage interactions at high co-loadings.[51] This is not unexpected since the combined loading of both ruthenium and iron complexes results in a loading of ~1 complex per 6 supercages. Additional high load $[Fe(tpy)_2]^{2+}$ co-doped materials were prepared in order to better assess the unexpected photophysical changes that occurred within the co-doped material, hence the difference between the highest concentrations of the $[Fe(tpy)_2]^{2+}$ and $[Fe(bpy)_3]^{2+}$ co-doped materials

in Table 3.1. The number of adjacent cage complexes at this loading is expected to be significant.

3.3.2.7 Raman Spectroscopy

Raman spectroscopy of the doped materials was studied in order to gain insight into structural changes accompanying co-encapsulation. Raman spectroscopy of $[Fe(bpy)_3]^{2+}$ and $[Ru(bpy)_3]^{2+}$ separately encapsulated in zeolite have been reported previously.[60,61] However, as mentioned, to our knowledge this is the first report of $[Fe(tpy)_2]^{2+}$ in zeolite and therefore this material is focused on here.

Figure 3.15 (a) shows the resonance Raman spectrum of solid $[Fe(tpy)_2][PF_6]_2$ excited at 457.9 nm and Figure 3.15 (b) shows the spectrum for Z-$[Fe(tpy)_2]^{2+}$ under the same conditions. This excitation wavelength is pre-resonant with the MLCT transition, and therefore modes associated with chromophores involved with this transition are enhanced.

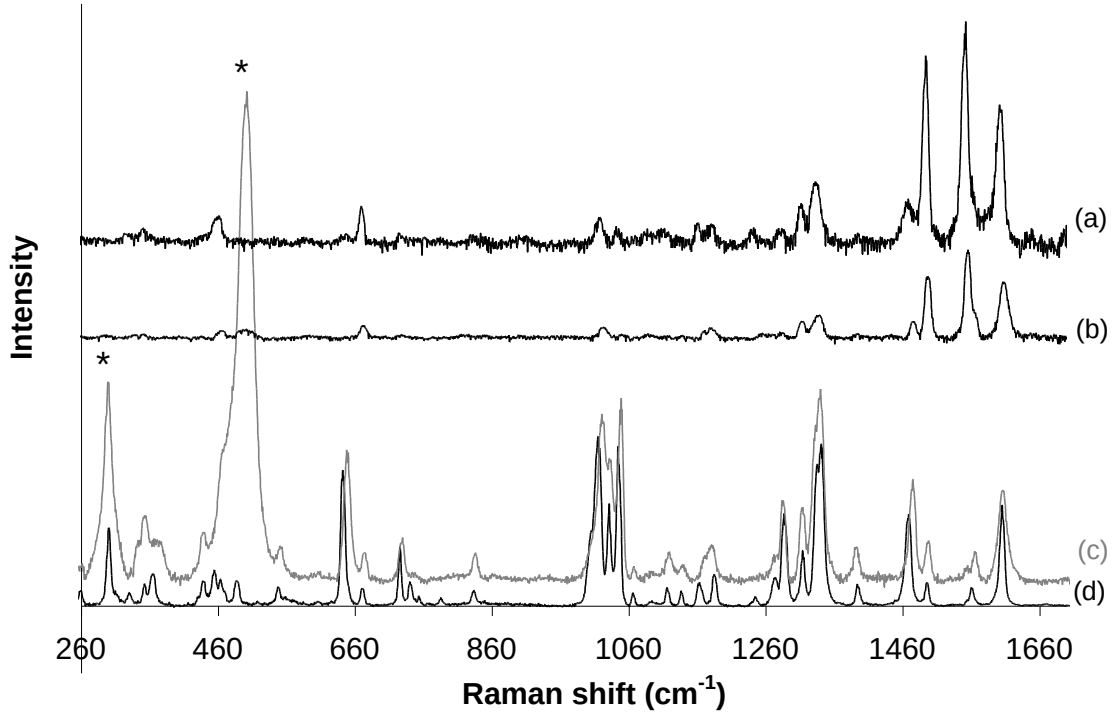

Figure 3.15: Raman Spectroscopy of (a) $[Fe(tpy)_2][PF_6]_2$ powder excited at 458 nm (b) 1:20 $[Fe(tpy)_2]^{2+}$ encapsulated in zeolite-Y, excited at 458 nm (c) 1:20 $[Fe(tpy)_2]^{2+}$ encapsulated in zeolite-Y, excited at 785 nm (d) solid $[Fe(tpy)_2][PF_6]_2$ powder excited at 785 nm. * Indicates zeolite modes.

Comparing the two spectra, it is evident that the zeolite Y framework imposes geometric constraints on $[Fe(tpy)_2]^{2+}$ reflected in spectral shifts of Raman modes. In addition, the Raman features are somewhat broadened in the zeolite attributed to the microenvironmental heterogeneity experienced by individual Z-$[Fe(tpy)_2]^{2+}$ complexes.

Complete normal coordinate analysis have been reported for both $[Fe(tpy)_2]^{2+}$ and the analogous $[Ru(tpy)_2]^{2+}$ complex and these analysis were exploited here in band assignments.[62,63] From Figure 3.15 (a) and (b), there is a general trend toward the higher vibrational frequencies for the complex in zeolite compared with solid or solution (Resonance Raman spectra of the complexes in solid and solution phase showed no noticeable shifts and so comparisons

are made interchangeably). For example, the mode at 671 cm^{-1} (+/- 0.5 cm^{-1} resolution was achieved for all Raman shifts), which is assigned to a ring deformation mode, largely confined to the middle tpy ring, is shifted by approximately 4 cm^{-1} to 675 cm^{-1} when the complex is encapsulated in zeolite. The weaker mode, centered at 726 cm^{-1}, attributed to ring deformation modes of the external rings is shifted to a comparable extent. This trend continues for the higher frequency modes between approximately 1450 and 1700 cm^{-1} that possess mostly ring stretch character, where blue shifts of between 5 and 8 cm^{-1} are observed for the zeolite encased complex. Large shifts are observed for the coupled C-H bend ring stretch mode at 1470 cm^{-1} which shifts to 1477 cm^{-1} on encapsulation and the C-H bend at 1163 cm^{-1} shifts to 1177 cm^{-1} in zeolite. The most perturbed mode is the ring stretch at 1245 cm^{-1} that shifts by 16 cm^{-1} to 1261 cm^{-1} in zeolite. The mode at 356 cm^{-1}, which contains mostly Fe-N character, is largely unperturbed by the zeolite matrix. Similar insensitivity in the metal ligand stretch mode toward encapsulation was previously reported for $[Ru(bpy)_3]^{2+}$.[60] The resonant Raman was then compared with the non-resonant Raman (λ_{ex} 785 nm) spectra of solid and zeolite encapsulated $[Fe(tpy)_2]^{2+}$, the latter are shown in Figure 3.15 (c) and (d) respectively. Again, there is substantial broadening of many bands, by comparison with solid or solution due to the microenvironmental heterogeneity of the intrazeolite pore, but more importantly, significant shifts in certain vibrational modes which were not resonantly enhanced were observed, for example, the ring bend mode at 642.5 cm^{-1} shifts by approximately 8 cm^{-1} to 651 cm^{-1} when the $[Fe(tpy)_2]^{2+}$ is encapsulated. There are, in particular, substantial changes to the cluster of ring stretch modes between 1006 cm^{-1} and 1049 cm^{-1}, to the extent that the shoulder at 1006 cm^{-1} and a ring stretch mode at 1248 cm^{-1} in solid $[Fe(tpy)_2]^{2+}$ are lost on encapsulation. A third unassigned feature at 791 cm^{-1} is also lost on encapsulation. Overall, therefore, Raman spectroscopy suggests that the supercage has a significant impact on the on the peripheral structure of the complex consistent with the steric confinement implied by the electronic spectroscopy. Raman spectral shifts of up to 16 cm^{-1} are observed between solid and encapsulated complex and the magnitude of these shifts are considerably greater than those previously reported for $[Ru(bpy)_3]^{2+}$ or $[Fe(bpy)_3]^{2+}$, suggesting greater

perturbation to the $[Fe(tpy)_2]^{2+}$ structure. Comparison to the observed Raman shifts of zeolite entrapped $[Ru(tpy)_2]^{2+}$ also supports this conclusion. Bhuiyan *et al.* examined the resonance Raman of Z-$Ru(tpy)_2]^{2+}$ and noted the same general trends as outlined above.[41] They observed some of the largest shifts (shifts after complex encapsulation in parenthesis) at modes associated with the center pyridine fragment of the tpy ligand at 1551 cm^{-1} (+3 cm^{-1}) and 1166 cm^{-1} (+1 cm^{-1}).[64,65] We observed larger shifts for zeolite entrapped $[Fe(tpy)_2]^{2+}$ at 1551 cm^{-1} (+7 cm^{-1}) and 1163 cm^{-1} (+14 cm^{-1}), suggestive of greater perturbation than the ruthenium analogue. Furthermore, changes to the number of vibrational modes observed may imply changes to the symmetry of the encapsulated complex.

Finally, Figure 3.16 shows the resonance Raman spectra of the mixed loadings of iron and ruthenium polypyridyl complexes, providing further confirmation that both species were present within the co-doped materials. The ruthenium content across the materials is constant. The effect of increasing the concentration of iron complex on the ruthenium signature was negligible for most of the materials examined.

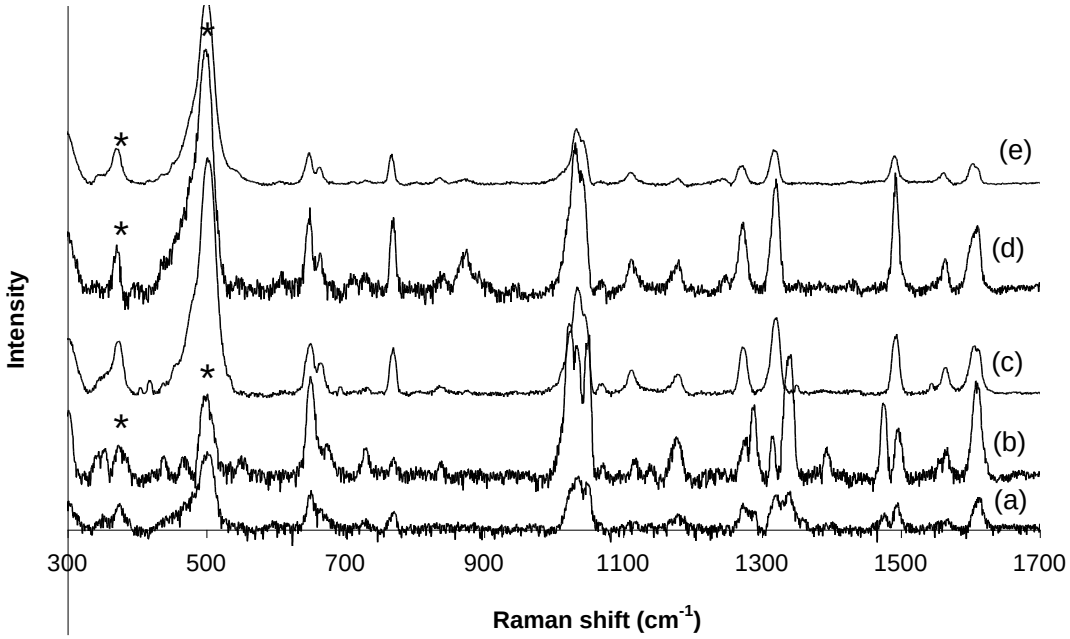

Figure 3.16: Raman Spectroscopy of 1:22 Z-$[Ru(bpy)_3]^{2+}$ doped with (a) $[Fe(tpy)_2]^{2+}$ 1:37 pore (b) $[Fe(tpy)_2]^{2+}$ in zeolite Y 1:7 pore (c) $[Fe(bpy)_3]^{2+}$ in zeolite Y 1:74 pore (d) $[Fe(bpy)_3]^{2+}$ in zeolite Y 1:26 pore and (e) 1:22 Z-$[Ru(bpy)_3]^{2+}$ alone. $\lambda_{excitation}$ 785 nm. * indicates zeolite modes.

As reported previously, the Z-$[Ru(bpy)_3]^{2+}$ material exhibits an intense emission at 617 nm with a long lived excited state that decays according to biexponential kinetics. Unsurprisingly, neither Z-$[Fe(bpy)_3]^{2+}$ nor Z-$[Fe(tpy)_2]^{2+}$ exhibited luminescence under any conditions of temperature or oxygenation explored. For photophysical measurement, we focused on metal loadings up to 1:12 for Z-$[Ru(bpy)_3]^{2+}[Fe(bpy)_3]^{2+}$ and to 1:11 for Z-$[Ru(bpy)_3]^{2+}[Fe(tpy)_2]^{2+}$. The ruthenium concentration remained constant at 1:22 $[Ru(bpy)_3]^{2+}$ per supercage throughout. This loading was chosen as it provided sufficient luminescence intensity with relatively low probability of adjacent cage interactions between centers.

Prior to discussing quenching of the encapsulated complexes, it is useful to consider the quenching of $[Ru(bpy)_3]^{2+}$ by $[Fe(tpy)_2]^{2+}$ and $[Fe(bpy)_3]^{2+}$ in solution. Creutz *et al.* first reported the latter where the bimolecular

quenching rate constant was reported as 1 x 10^9 mol s^{-1} in aqueous media and was attributed to a photoinduced energy transfer.[66] Quenching of $[Ru(bpy)_3]^{2+}$ by $[Fe(tpy)_2]^{2+}$ has not been reported. The effect of titrating increasing aliquots of $[Fe(tpy)_2]^{2+}$ into a solution of 5 x 10^{-5} mol dm^{-3} $[Ru(bpy)_3]^{2+}$ was therefore studied. This resulted in a decrease in $[Ru(bpy)_3]^{2+}$ luminescence intensity due to absorption by the $[Fe(tpy)_2][PF_6]_2$ and was accompanied by distortion of the emission spectral band indicative of radiative energy transfer or trivial quenching of the $[Ru(bpy)_3]^{2+}$ emission. Figure 3.17 demonstrates the observed distortion of the $[Ru(bpy)_3]^{2+}$ emission band at the highest concentration of $[Fe(tpy)_2][PF_6]_2$.

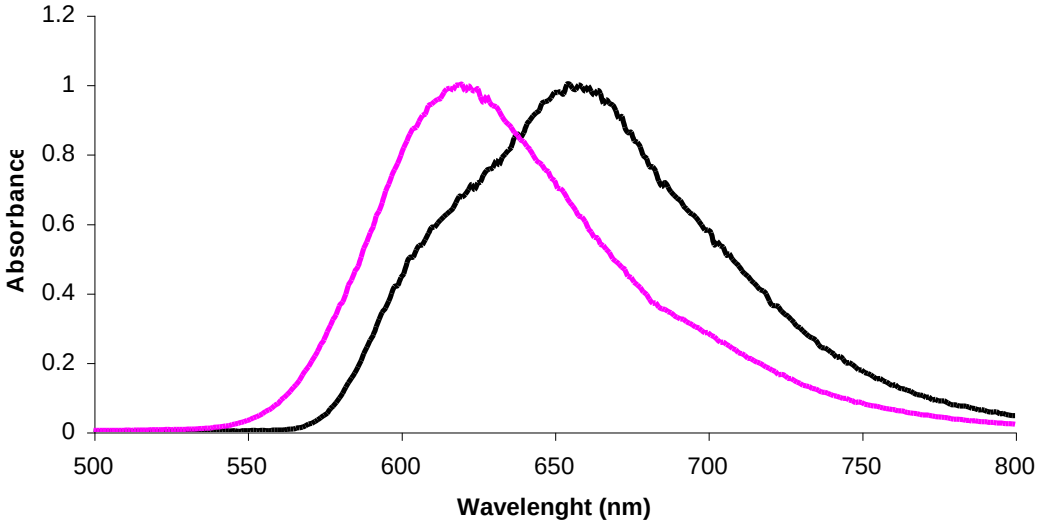

Figure 3.17: Normalised emission spectra of $[Ru(bpy)_3][PF_6]_2$ (1 x 10^{-5} in DMSO, slit width 5 nm, excitation 452 nm) pink trace and $[Ru(bpy)_3][PF_6]_2$ after addition of $[Fe(tpy)_2][PF_6]_2$ ($[Ru(bpy)_3][PF_6]_2$ 1 x 10^{-5} and $[Fe(tpy)_2][PF_6]_2$ 1.85 x 10^{-4} M, both in DMSO, slit width 5 nm, excitation 452 nm) black trace.

The absence of significant non-radiative energy or electron transfer quenching was confirmed by luminescence lifetime studies, which confirmed that within experimental error, $[Ru(bpy)_3]^{2+}$ lifetimes did not change over the range of $[Fe(tpy)_2][PF_6]_2$ concentrations investigated. Table 3.2 shows the lifetime of $[Ru(bpy)_3][PF_6]_3$ in de-aerated DMSO with no $[Fe(tpy)_2][PF_6]_2$ present and also the lifetime of $[Ru(bpy)_3][PF_6]_3$ at the highest concentration of

$[Fe(tpy)_2][PF_6]_2$. As there is no reason to believe that these two cationic complexes would associate static quenching could be ruled out.

$[Fe(tpy)_2][PF_6]_2$ Concentration (mols dm-3)	0 mol dm^{-3}	1.85 x 10^{-4} M
$[Ru(bpy)_3][PF_6]_3$ τ (ns)	952 ns $\pm$ 8 %	940 ns $\pm$ 8%

Table 3.2: Excited state lifetimes of de-aerated $[Ru(bpy)_3][PF_6]_3$ (1.2 x 10^{-5} M in DMSO) in the absence and presence of $[Fe(tpy)_2][PF_6]_2$.

Z-$[Fe(tpy)_2]^{2+}$ concentration within mechanical mixture of Z-$[Fe(tpy)_2]^{2+}$ and Z-$[Ru(bpy)_3]^{2+}$	0 mol dm^{-3}	0.035 M
Z-$[Ru(bpy)_3]^{2+}$ τ (ns)	771$\pm$ 9 ns 390 $\pm$ 18 ns	759 $\pm$ 7 ns 384 $\pm$ 15 ns

Table 3.3: Excited state lifetimes of Z-$[Ru(bpy)_3]^{2+}$ (1 $[Ru(bpy)_3]^{2+}$ per 22 supercages) in the absence and presence of mechanically mixed Z-$[Fe(tpy)_2]^{2+}$. Lifetimes recorded in air equilibrated deionised water.

3.3.3 Z-$[Ru(bpy)_3]^{2+}[Fe(bpy)_3]^{2+}$ and Z-$Ru(bpy)_3]^{2+}[Fe(tpy)_2]^{2+}$ Emission Spectroscopy

Figures 3.18 (a) and (b) show that the emission intensity of Z-$[Ru(bpy)_3]^{2+}$ decreases with increasing concentration of both co-entrapped iron complexes. The behavior of the $[Fe(tpy)_2]^{2+}$ complex in zeolite contrasted markedly with that in solution where only trivial quenching had been observed. Co-entrapped $[Fe(tpy)_2]^{2+}$ elicited a decrease in the Z-$[Ru(bpy)_3]^{2+}$ lifetime whereas mechanically mixing Z-$[Ru(bpy)_3]^{2+}$ and Z-$[Fe(tpy)_2]^{2+}$ resulted in excited state lifetime behavior reminiscent of that in solution (Table 3.3). The mechanical mixture was prepared by addition of Z-$[Fe(tpy)_2]^{2+}$ and Z-$[Ru(bpy)_3]^{2}$ into acetone and dispersion by sonication to ensure intimate mixing of the two materials.

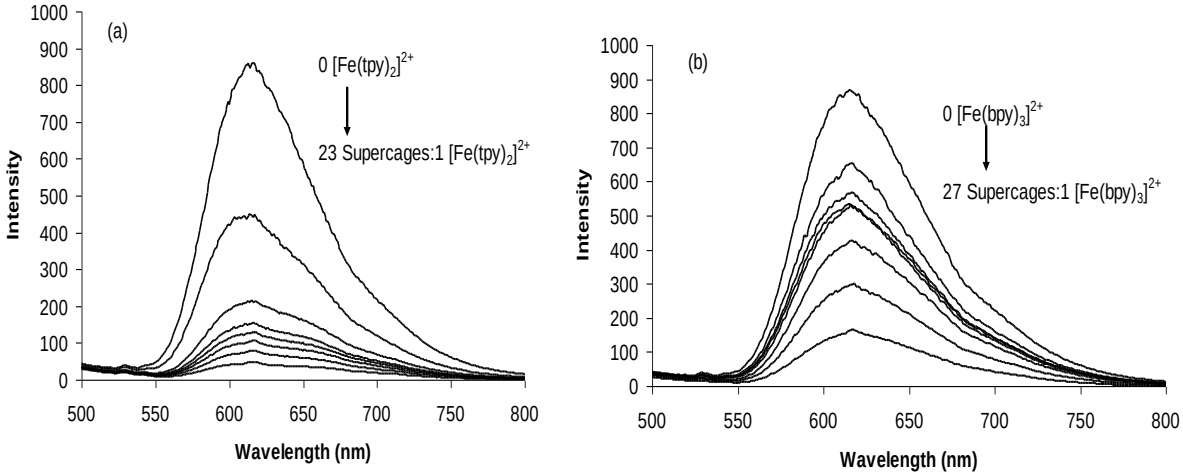

Figure 3.18: Luminescence spectra of 1:22 Z-$[Ru(bpy)_3]^{2+}$ in the presence of increasing concentrations of co-encapsulated iron polypyridyl complex (a) $[Fe(tpy)_2]^{2+}$ in zeolite Y 1:92, 1:59, 1:55, 1:47, 1:37, 1:33, 1:23, pore, (b) $[Fe(bpy)_3]^{2+}$ in zeolite Y 1:110, 1:98, 1:74, 1:70, 1:55, 1:47, 1:27 pore. Experiments performed in air with $\lambda_{excitation}$ of 452 nm.

Indeed, when encapsulated within the zeolite, $[Fe(tpy)_2]^{2+}$ becomes a more efficient quencher of $[Ru(bpy)_3]^{2+}$ excited state than $[Fe(bpy)_3]^{2+}$. For

example, for Z-$[Ru(bpy)_3]^{2+}$ co-encapsulated with 1:55 $[Fe(tpy)_2]^{2+}$:supercages, the ruthenium luminescence is decreased by approximately 82%, compared with a 52% reduction of emission intensity for a 1:55 loading of $[Fe(bpy)_3]^{2+}$ under identical conditions.

3.3.4 Z-$[Ru(bpy)_3]^{2+}[Fe(bpy)_3]^{2+}$ and Z-$[Ru(bpy)_3]^{2+}[Fe(tpy)_2]^{2+}$ excited state lifetimes

Table 3.4 and Table 3.5 show the lifetimes of 1:22 Z- $[Ru(bpy)_3]^{2+}$ when co-doped with increasing concentrations of $[Fe(bpy)_3]^{2+}$ and $[Fe(tpy)_2]^{2+}$ respectively. Figures 3.19 (a) and (b) show plots of Fe loading vs. $[Ru(bpy)_3]^{2+}$ lifetime for $[Fe(bpy)_3]^{2+}$ and $[Fe(tpy)_2]^{2+}$ respectively to highlight trends in the data and the Figure 3.20 shows the effect of increased loading of $[Fe(tpy)_2]^{2+}$ on the luminescent decay of Z- $[Ru(bpy)_3]^{2+}$.

Table 3.4: Emission lifetimes of $[Ru(bpy)_3]^{2+}$ in Zeolite Y with various concentrations of co-encapsulated $[Fe(bpy)_3]^{2+}$

Conc $[Fe(bpy)_3]^{2+}$ (Mol dm^{-3})[a]	τ_1/ns	A[b]	τ_2/ns	B[b]
0	771±9	62	390±18	38
0.008	638±5	67	300±3	33
0.009	588±5	70	256±6	30
0.012	616±4	50	308±8	50
0.0127	689±5	35	385±17	65
0.0162	627±5	39	288±11	61
0.0187	555±4	37	236±15	63
0.0334	520±4	23	177±16	77

[a]Concentration of co-encapsulated $[Fe(bpy)_3]^{2+}$ within Z-$[Ru(bpy)_3]^{2+}$ doped zeolite Y. [b]Percent contribution of each individual lifetime decay fit to appropriate exponential model. Lifetimes measured in air equilibrated deionised water.

Table 3.5: Emission lifetimes of $[Ru(bpy)_3]^{2+}$ in Zeolite Y with various concentrations of co-encapsulated $[Fe(tpy)_2]^{2+}$

Conc $[Fe(tpy)_2]^{2+}$ (Mol dm^{-3})[a]	τ_1/ns	A[b]	τ_2/ns	B[b]
0	771±9	62	390±18	38
0.0096	653±7	58	153±15	42
0.015	487±6	54	152±11	46
0.016	410±9	45	116±7	55
0.019	386±7	41	109±10	59
0.024	357±13	37	98±41	63
0.027	336±7	29	92±39	17
0.038	308±7	22	77±38	78
0.056	386±3	11	62±3	89
0.119	447±3	16	38±5	84

[a]Concentration of co-encapsulated $[Fe(tpy)_2]^{2+}$ within Z-$[Ru(bpy)_3]^{2+}$ doped zeolite Y. [b]Percent contribution of each individual lifetime decay fit to the appropriate exponential model. Lifetimes measured in air equilibrated deionised water

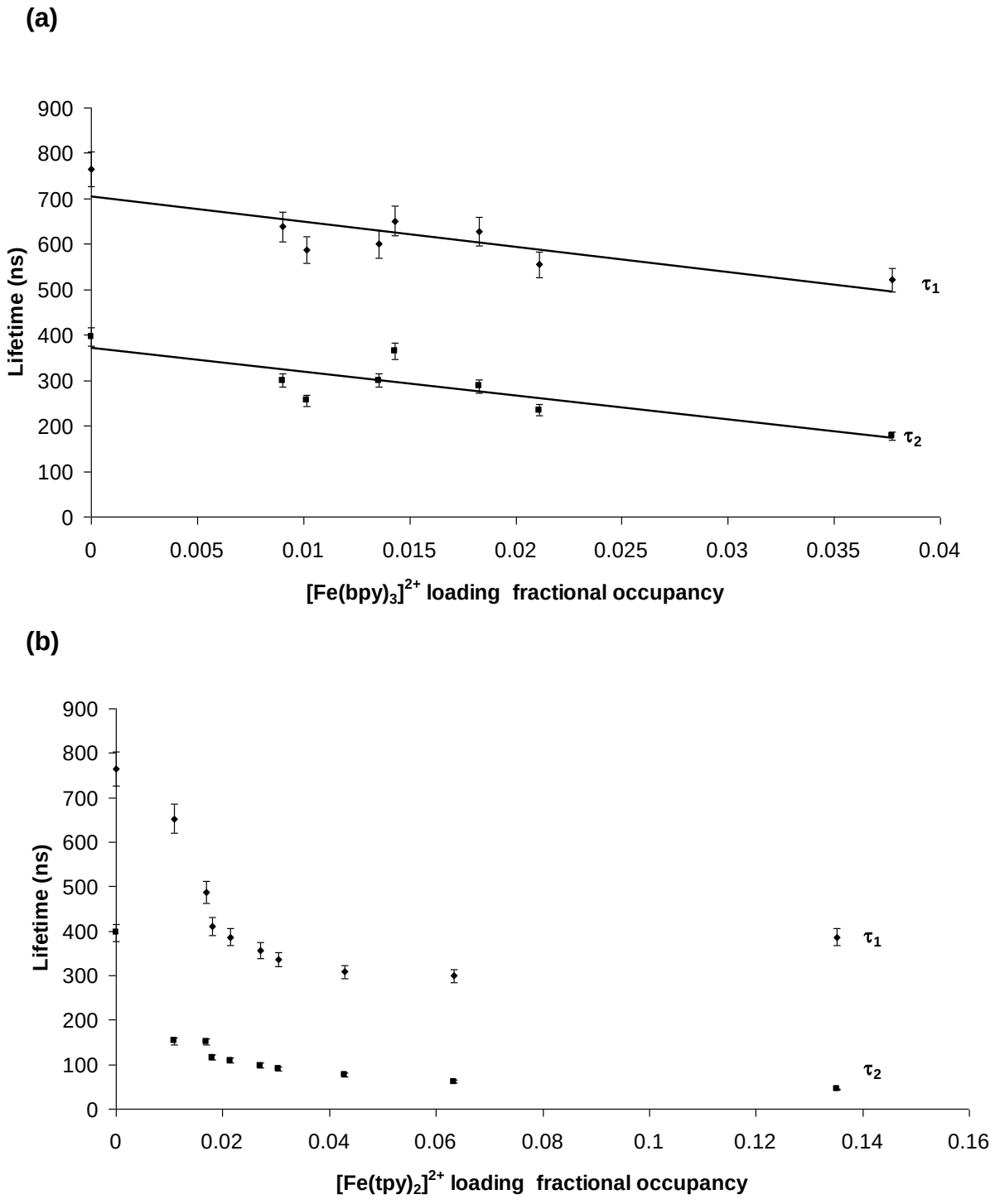

Figure 3.19: (a) Plots of lifetime of both long (τ_1) and short components (τ_2) of luminescent decay of 1:22 Z-$[Ru(bpy)_3]^{2+}$ versus loading of $[Fe(bpy)_3]^{2+}$ (b) Plots of lifetime of both long (τ_1) and short components (τ_2) of luminescent decay of 1:22 Z-$[Ru(bpy)_3]^{2+}$ versus loading of $[Fe(tpy)_2]^{2+}$. Lifetimes recorded in air equilibrated deionised water suspensions.

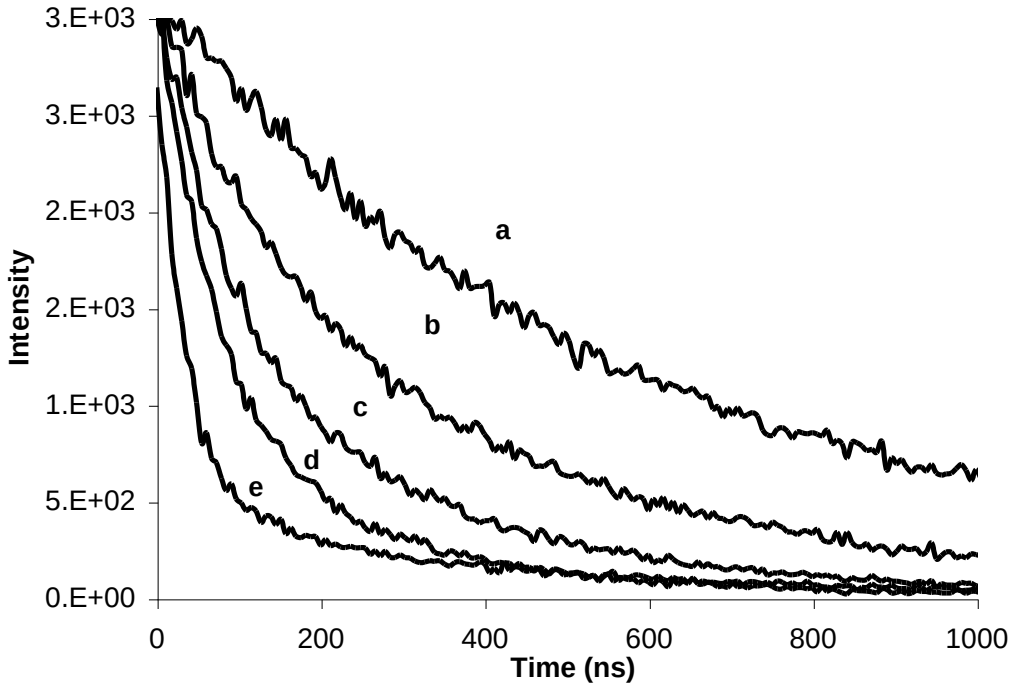

Figure 3.20: Luminescent decays for (a)1:22 Z-$[Ru(bpy)_3]^{2+}$ and 1:22 Z-$[Ru(bpy)_3]^{2+}$ doped with $[Fe(tpy)_2]^{2+}$ at the following pore ratios 1:59 (b), 1:37 (c), 1:23 (d), 1:7 (e) corresponding to concentrations of entrapped $[Fe(tpy)_2]^{2+}$ of 0.015 M, 0.024 M, 0.038 M and 0.119 M. Lifetimes recorded in air equilibrated deionised water suspensions.

Lifetimes were collected from suspensions of the doped zeolite in air equilibrated deionised water. The water, when filtered, showed no residual emission and the lifetimes recorded were independent of the amount of material suspended. Z-$[Ru(bpy)_3]^{2+}$ alone exhibited a luminescence decay which fitted best to a dual exponential model, to yield τ_1 of 772 ns (69%) and τ_2 of 391 ns (31%).

The lifetime of both the short and long components of the Z-$[Ru(bpy)_3]^{2+}$ decay changed upon co-inclusion of iron polypyridyl complex. Crucially, when Z-$[Fe(tpy)_2]^{2+}$ or Z-$[Fe(bpy)_3]^{2+}$ were mechanically mixed with Z- $[Ru(bpy)_3]^{2+}$ the lifetime of Z- $[Ru(bpy)_3]^{2+}$ in the mixture did not change (Table 3.3). In the case of the Z-$[Ru(bpy)_3]^{2+}$- Z-$[Fe(tpy)_2]^{2+}$ mixture, decreases in intensity and distortion of emission spectra of Z-$[Ru(bpy)_3]^{2+}$ reminiscent of that observed in

solution were observed consistent with radiative energy transfer (Figure 3.21). Figure 3.22 shows the source of the distortion with the mechanical mixture. The intensities of the two peaks in the spectrum reflect the relative amount of pure $[Ru(bpy)_3]^{2+}$ emission and $[Ru(bpy)_3]^{2+}$ emission which has encountered a $[Fe(tpy)_2]^{2+}$ doped particle and lost intensity due to absorption by the iron complex. It is important to note however, that the reduction in intensity was considerably less than observed for the co-encapsulated complex and as described, there was no significant change in lifetime (Table 3.3). There was an approximately 80% greater decrease in intensity for the co-encapsulated Z-$[Ru(bpy)_3]^{2+}$ $[Fe(tpy)_2]^{2+}$ complexes compared with the same relative concentrations in the mechanical mixtures.

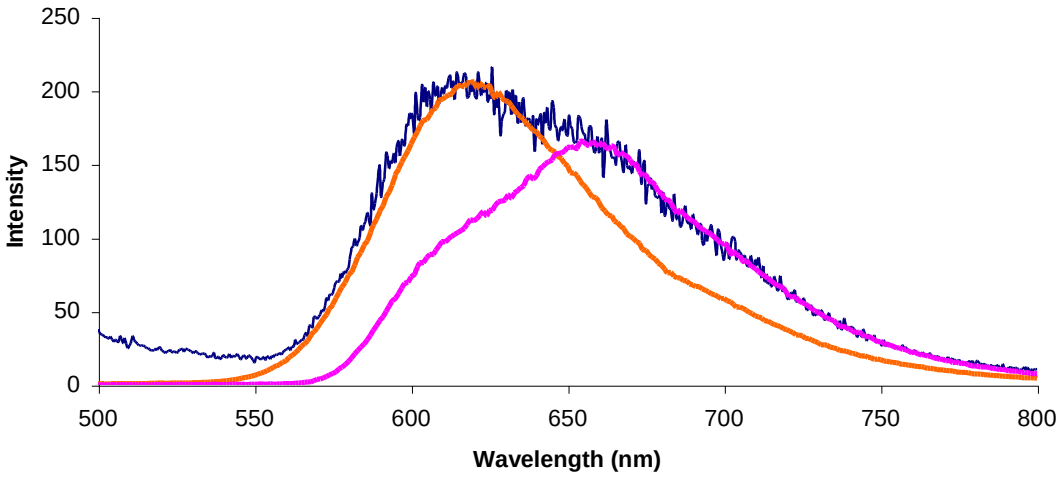

Figure 3.21: Emission spectrum of mechanical mixture of Z-$[Ru(bpy)_3]^{2+}$ and Z-$[Fe(tpy)_2]^{2+}$ (Approx. concentration of $[Fe(tpy)_2]^{2+}$ was 0.035 M, excitation 452 nm, slit width 5 nm) blue trace. For illustration purposes only, are shown $[Ru(bpy)_3]^{2+}$ emission (orange trace) and the distorted $[Ru(bpy)_3]^{2+}$ emission in presence of $[Fe(tpy)_2]^{2+}$ (purple trace, *vide supra*). The intensities of these spectra were adjusted to match the mechanical emission spectrum for clarity of presentation only.

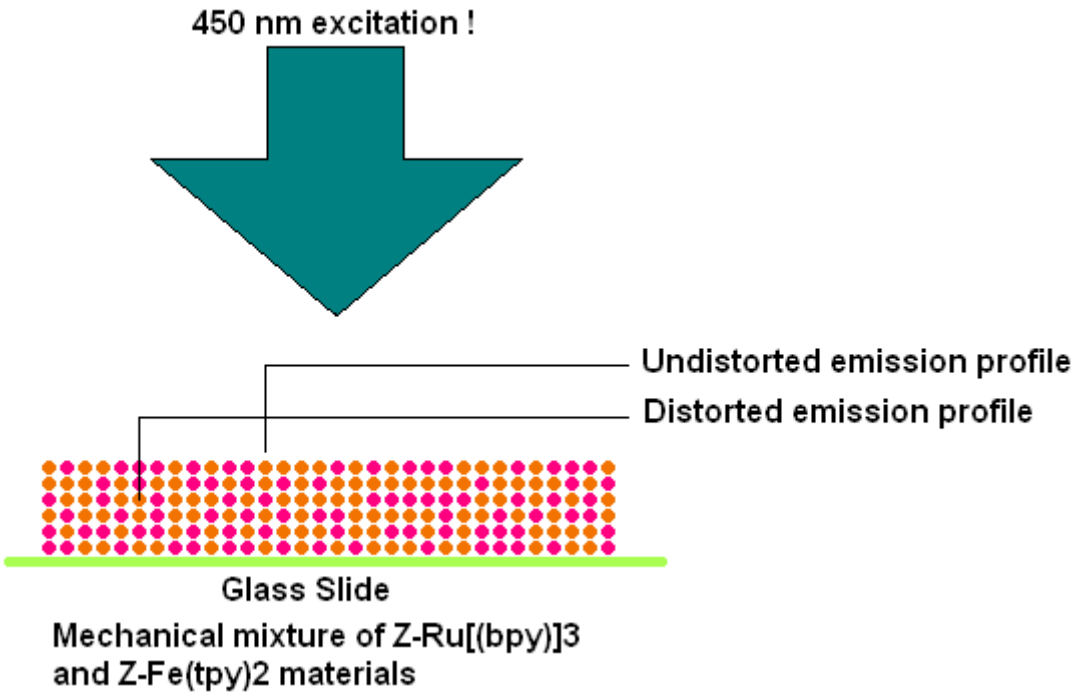

Figure 3.22: Diagram showing source of emission distortion from mechanical mixture of Z-$[Ru(bpy)_3]^{2+}$ and Z-$[Fe(tpy)_2]^{2+}$. Zeolite particles on the surface emit normally while emission from particles deeper into the layer encounter $[Fe(tpy)_2]^{2+}$ and lose intensity due to absorption.

Systematic decreases in both lifetime components of Z-$[Ru(bpy)_3]^{2+}$ were observed with increasing Z-$[Fe(bpy)_3]^{2+}$ concentration. For example, the long-lived component decreased from 771 ns to 505 ns with a loading of 1 $[Fe(bpy)_3]^{2+}$ per 27 supercages and the short lived component decreased from 390 to 177 ns. The % contribution also changed with increasing loading, the short component dominating at higher iron loadings. For example, for $[Fe(bpy)_3]^{2+}$ at 1 Fe in 27 supercages, the short component represents 77% of the decay contribution.

Interestingly, consistent with the luminescence intensity studies, the impact of Z- $[Fe(tpy)_2]^{2+}$ on the lifetime of Z-$[Ru(bpy)_3]^{2+}$ is greater than for $[Fe(bpy)_3]^{2+}$. Again, a biexponential model adequately fits the decay of Z- $[Ru(bpy)_3]^{2+}$ over the range of $[Fe(tpy)_2]^{2+}$ loadings explored. However, for example, whereas the lifetime of $[Ru(bpy)_3]^{2+}$ decreases to 236 and 555 ns respectively for τ_2

and τ_1, at $[Fe(bpy)_3]^{2+}$ loadings of 1 per 47 supercages, in the presence of equivalent concentrations of Z-$[Fe(tpy)_2]^{2+}$ the decay of $[Ru(bpy)_3]^{2+}$ had reduced to 109 ns and 386 ns respectively. As Table 3.5 shows, the lifetimes of $[Fe(tpy)_2]^{2+}$ doped Z-$[Ru(bpy)_3]^{2+}$ material increase at the two highest concentrations of the iron complex. This we attribute to pore blocking of the outer surface of the zeolite particle at higher iron loadings preventing ready penetration of the terpyridine ligands deep into the zeolite during the iron polypyridyl inclusion reaction. Essentially the formation of the iron complexes at the outer surface prevents further terpyridine penetration into the particle leaving the interior available iron cations unreacted. This would increase the number of isolated $[Ru(bpy)_3]^{2+}$ molecules in the interior of the zeolite particle, which would reside at a greater average distance from a quencher molecule than those donors closer to the exterior.

Interestingly, whereas the lifetime of $[Ru(bpy)_3]^{2+}$ decreases approximately linearly with Z-$[Fe(bpy)_3]^{2+}$ concentration, it decreases exponentially with $[Fe(tpy)_2]^{2+}$ loading. This is remarkable, given that $[Fe(tpy)_2]^{2+}$ does not quench Z-$[Ru(bpy)_3]^{2+}$ in solution except through trivial/radiative energy transfer, and strongly suggests that a new quenching process occurs in zeolite. Currently, the origin of the difference in loading-lifetime dependence between the two types of iron complex is unclear, but since mechanically mixed Z- $[Fe(tpy)_2]^{2+}$ and Z- $[Ru(bpy)_3]^{2+}$ do not exhibit lifetime changes, it is unlikely to arise simply from a mixture of radiative and non-radiative energy transfer pathways for Z- $[Fe(tpy)_2]^{2+}$.

Finally, it was necessary to ensure that the distribution of complexes was homogeneous throughout the particle to rule out the possibility of high concentrations of complexes near the exterior surface of the particles and lower concentrations towards the centre of individual particles (Figure 3.23). To access this, a sample of zeolite powder was ground repeatedly in a mortar and pestle. The application of large pressures is known to result in partial destruction of the outer zeolite framework. The excited state lifetime of the sample was recorded before grinding and compared to the lifetime of the

sample after grinding and sodium chloride washing (to remove any surface bound complexes which may leach into the suspension in which the lifetime determination is carried out). Within experimental error the lifetimes were the same, demonstrating that distributions are similar throughout the zeolite except at the highest loading as evidenced by other results (*vide supra*).

To confirm that partial destruction of the zeolite framework was achieved, the UV-vis spectra of the salt washings were examined and indicated that release of the complexes from the matrix had occurred.

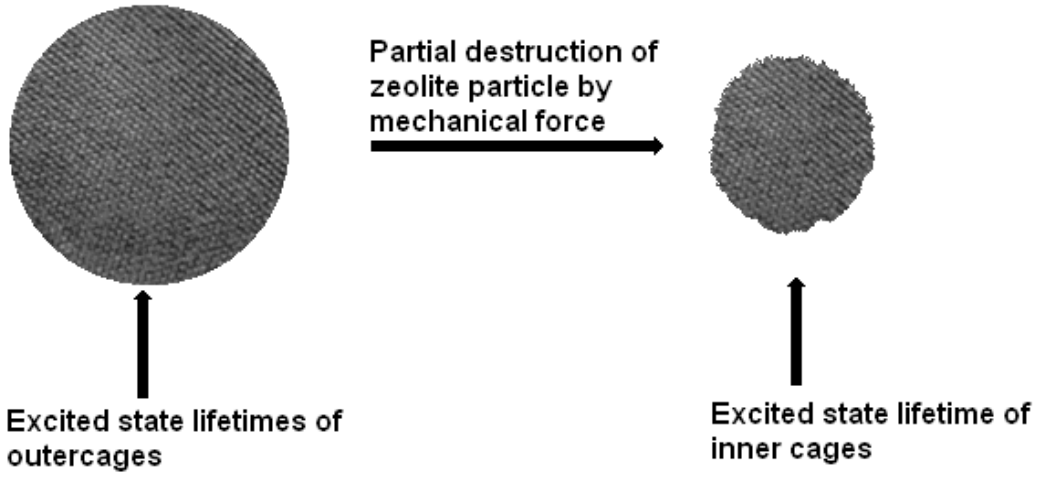

Figure 3.23: Diagram describing excited state lifetime sampling of zeolite exterior and zeolite interior. Spheres represent individual zeolite particles before and after mechanical force has been applied to them.

3.3.4 Nature of quenching processes

The luminescent lifetime behavior of Z-$[Ru(bpy)_3]^{2+}$ was reported by Sykora et *al.* who studied the effect of exciting laser power density and concentration of $[Ru(bpy)_3]^{2+}$ in zeolite Y.[38] Two components of the decay, were similarly observed, the long time component was attributed to isolated $[Ru(bpy)_3]^{2+}$ units within the zeolite, and the shorter component to adjacent cage interactions originating, potentially from a variety of mechanisms.

The combined concentration of luminophore and quencher in this study was maintained sufficiently low to limit the probability of adjacent cage interactions

between two rutheniums to at most 17% and between a ruthenium and iron to approximately 13% at 1:12 supercages of Iron. A ruthenium-iron adjacent cage interaction at the lowest loading of $[Fe(tpy)_2]^{2+}$ is around 4%, given the significant impact of co-doping on the emission intensity and lifetime even at this loading, this implies that adjacent cage interactions are not required for quenching. This result is consistent with the absorption spectra of the materials which show no significant perturbation of the MLCT or $\pi \rightarrow \pi^*$ transitions of $[Ru(bpy)_3]^{2+}$ except at the highest loading of Z-$[Fe(tpy)_2]^{2+}$. However, we must consider the possibility that the iron quenching behaviour is like the self-quenching observed by Sykora *et al.* for $[Ru(bpy)_3]^{2+}$ at high loadings. Overall, the decrease in luminescence intensity with increasing iron loading observed here is considerably greater than that found for ruthenium self-quenching.[38,51] Any adjacent cage triplet-triplet annihilation within the present system resulting in a short-lived component can be excluded for two reasons. Firstly, time correlated single photon counting was employed for luminescent lifetimes, using diode lasers whose maximum power would be insufficient to generate two adjacent excited states. Secondly, the $[Fe(L\text{-}L)_n]^{2+}$ complex is unlikely to participate in triplet-triplet annihilation. Electron transfer from $[Fe(bpy)_3]^{2+}$ to $[Ru(bpy)_3]^{2+}$ can be excluded on thermodynamic grounds (*vide infra*).[66] In addition, electron transfer and Dexter energy transfer, require direct orbital interactions between the donor and acceptor, requiring adjacent cage interactions between $[Fe(bpy)_3]^{2+}$ and $[Ru(bpy)_3]^{2+}$. At low iron loadings, the probability of adjacent cage interactions between $[Ru(bpy)_3]^{2+}$ and $[Fe(L\text{-}L)_n]^{2+}$ pairs (based on the structural model outlined earlier) is not sufficiently high to generate the magnitude of quenching observed.

The overall change in free energy for an electron transfer can be estimated from the modified Rehm-Weller Equation 3.1:

$$\Delta G^0 = E^0_{D^{\bullet+}/D} - E^0_{A/A^{\bullet-}} - \Delta E_{00}(D) \qquad \textbf{Equation 3.1}$$

where $E^{\circ}_{D^{\bullet+}/D}$ and $E_{A/A^{\bullet-}}$ are the standard ground-state oxidation and reduction potentials of donor D and acceptor A, ΔE_{00} is the zero-zero spectroscopic energy for the acceptor and donor species. The ΔG^0 for electron transfer from $[Ru(bpy)_3]^{2+}$ to $[Fe(bpy)_3]^{2+}$ is estimated to be 0.40 eV and from $[Fe(bpy)_3]^{2+}$ to $[Ru(bpy)_3]^{2+}$ to be 0.17 eV. The ΔG^0 for electron transfer from $[Ru(bpy)_3]^{2+}$ to $[Fe(tpy)_2]^{2+}$ is estimated to be 0.31 eV and from $[Fe(tpy)_2]^{2+}$ to $[Ru(bpy)_3]^{2+}$ to be 0.44 eV.

For energy transfer processes, the standard free energy change between the reactant and product can be estimated by:

$$\Delta G_0 = E^{0-0}(A^*/A) - E^{0-0}(D^*/D) \qquad \textbf{Equation 3.2}$$

Where E^{0-0} are the zero-zero energies of the donor and acceptor excited states that are estimated from the emission and absorption spectra of the donor and acceptor. On this basis, the ΔG^0 for energy transfer from Z-$[Ru(bpy)_3]^{2+}$ to Z-$[Fe(bpy)_3]^{2+}$ is –0.15 eV and for Z-$[Ru(bpy)_3]^{2+}$ to Z-$[Fe(tpy)_2]^{2+}$ is –0.33 eV. Considering the calculated ΔG^0 values for electron and energy transfer, energy transfer between both iron complexes and ruthenium is exergonic, and likely to be the origin of the quenching, so application of Förster energy transfer model is appropriate.

The Perrin model, Equation 3.3, is commonly applied to excited state quenching interactions in systems where the donor and acceptor are immobilized, i.e. where no diffusion is possible.

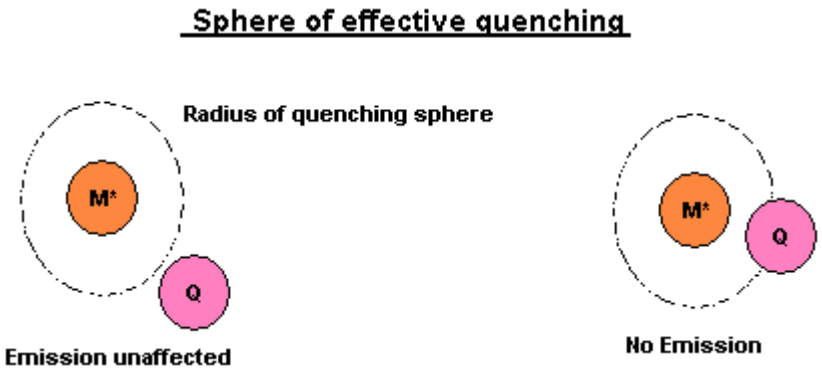

Figure 3.24: Perrin Model of Static quenching.

When the quencher molecule is outside the sphere of effective quenching the emission is unaffected (left). When the quencher molecule is inside the sphere, the emission is completely quenched (right).

$$\ln(I_0/I)=V_q N_a[Q] \text{ X } 10^{-24} \qquad \textbf{Equation 3.3}$$

Where I_0 and I are the luminescence intensity in absence and presence of quencher respectively, V_q the quenching volume, N_a Avogadro's number and [Q] the quencher concentration. The model makes no mechanistic assumptions about the quenching process but proposes a "quenching sphere" centered about the excited molecule. Should a quencher occupy this sphere, the model assumes complete quenching efficiency with zero quenching efficiency outside and assumes a homogeneous distribution of luminophore and quencher within the zeolite (Figure 3.24).

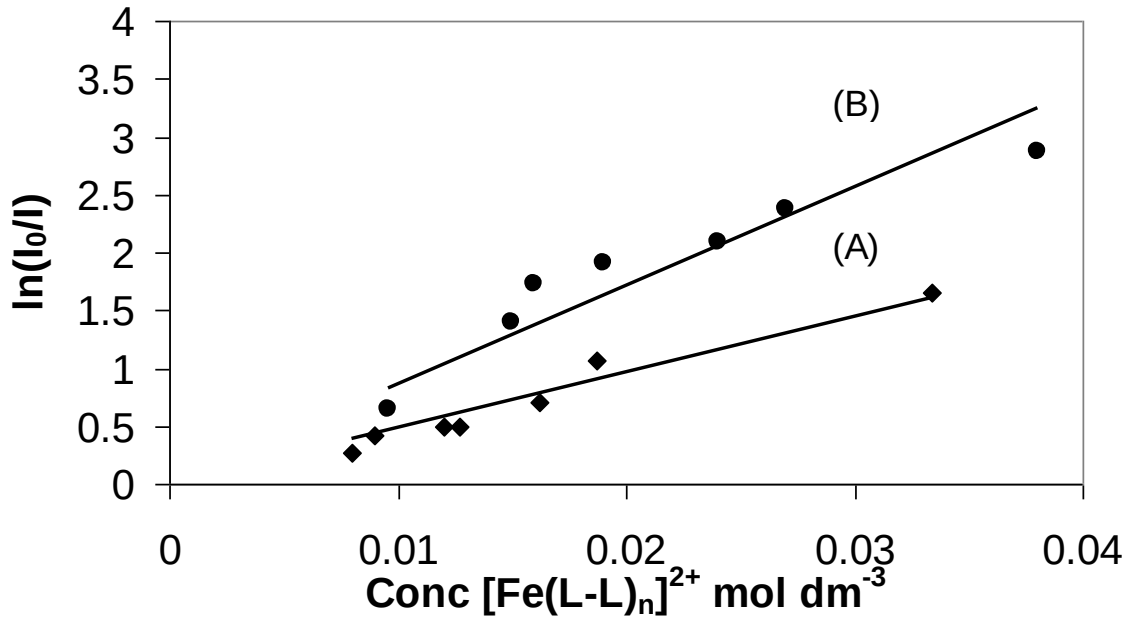

Figure 3.25: Perrin Plots for 1:22 Z-$[Ru(bpy)_3]^{2+}$ quenched by co-encapsulated (a) $[Fe(bpy)_3]^{2+}$ and (b) $[Fe(tpy)_2]^{2+}$. Measurements were performed in air.

Figure 3.25 (a) and (b) shows Perrin Plots for quenching of Z-$[Ru(bpy)_3]^{2+}$ by $[Fe(bpy)_3]^{2+}$ and $[Fe(tpy)_2]^{2+}$. While not shown here, the curves plateau at high iron loadings presumably because inter-cage interactions play a role. The linear portion of the Perrin plots yield quenching sphere radii for the iron terpyridine and iron bipyridine doped samples of 32Å and 27Å, respectively. These values are comparable with the calculated geometrical distances between approximately five and three cages.[38] The important conclusion of the Perrin fit is that the quenching distances substantially exceed that expected for adjacent inter-pore interactions. For example, Dutta *et al.* applied the Perrin Model to self-quenching occurring in high concentrations of $[Ru(bpy)_3]^{2+}$ in zeolite Y and obtained a quenching radius of 12 Å, leading to the conclusion that adjacent cage interactions were primarily responsible for the luminescence quenching observed. The long-range quenching observed here is consistent with Förster energy, rather than electron, transfer. A significant assumption of the Perrin model is that complete quenching occurs once donor/acceptor lie within the reaction volume whereas the rate of Förster energy transfer varies with donor-acceptor distance.[67,68]

Therefore, the Förster model has been applied. The Förster radius, which is the distance at which energy transfer or spontaneous decay is equally likely, can be calculated from Equation 3.4:

$$R_0^6 = \frac{9000(\ln 10)\kappa^2 \Phi_D^0}{128\pi^5 N_A n^4} \int_0^\infty I_D(\lambda)\varepsilon_A(\lambda)\lambda^4 d\lambda \qquad \textbf{Equation 3.4}$$

where R_0 is the Förster radius, κ^2 is the orientational factor which was taken to be 1, Φ_D^0 is the fluorescence quantum yield in the absence of transfer which was taken as 0.042,[69] n is the refractive index of the medium taken to be 1.5,[70] and $\int_0^\infty I_D(\lambda)\varepsilon_A(\lambda)\lambda^4 d\lambda$ is the spectral overlap between donor emission and acceptor absorbance. The spectral overlap was calculated from spectral data for Z-$[Ru(bpy)_3]^{2+}$, $[Fe(bpy)_3]^{2+}$ and $[Fe(tpy)_2]^{2+}$, and found to be 1.3959 X 10^{-14} and 6.1882 X 10^{-14} cm^3M^{-1} for the intrazeolitic $[Fe(bpy)_3]^{2+}$ and $[Fe(tpy)_2]^{2+}$ acceptors respectively. Figure 3.26 shows a representation of the spectral overlap between donor and acceptor emission and absorption. The Förster radii calculated using Equation 3.4 were 22 Å and 28 Å for Z-$[Ru(bpy)_3]^{2+}$ doped with $[Fe(bpy)_3]^{2+}$ and $[Fe(tpy)_2]^{2+}$ respectively. The values calculated from the Perrin model of 27 Å and 32 Å for the Z-$[Ru(bpy)_3]^{2+}$ doped with $[Fe(bpy)_3]^{2+}$ and $[Fe(tpy)_2]^{2+}$ compare well with these values. The slight over estimation of the quenching sphere radii likely arises from small contributions from radiative energy transfer processes to the overall decrease in emission intensity of the Z-$[Ru(bpy)_3]^{2+}$.

The apparent switch from trivial energy transfer between $[Ru(bpy)_3]^{2+}$ and $[Fe(tpy)_2]^{2+}$ in solution to non-radiative energy transfer within the zeolite matrix is attributed to enhanced spectral overlap of the donor emission and the acceptor absorption spectra induced by structural distortion of the $[Fe(tpy)_2]^{2+}$ when in the zeolite matrix. As described above, there is a very large increase in absorbance cross section of the low energy tail of the $[Fe(tpy)_2]^{2+}$ in zeolite Y which represents the acceptor states in Förster energy transfer.

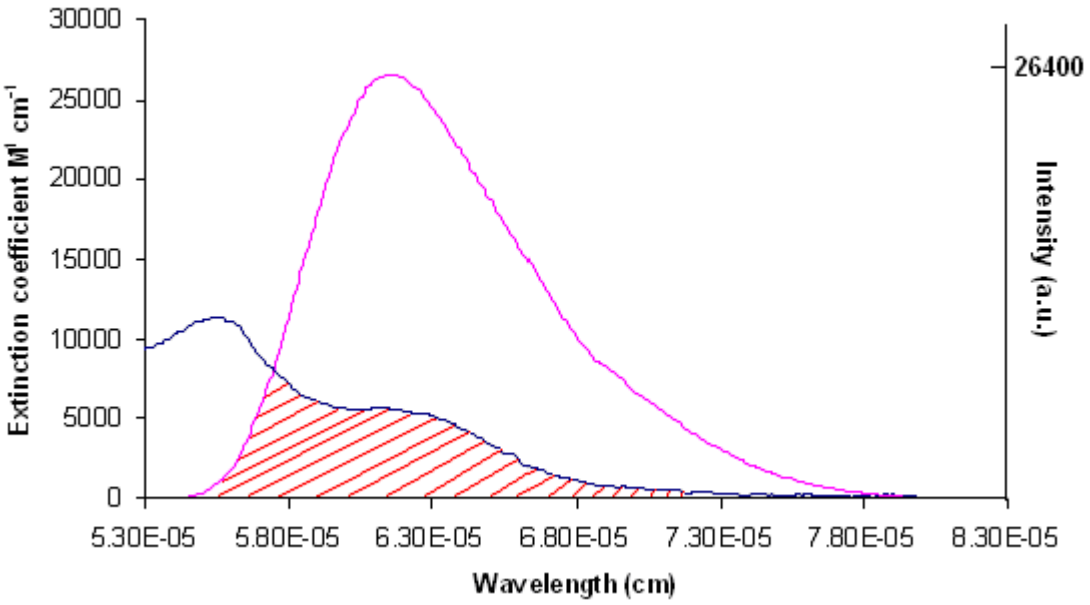

Figure 3.26: Representative spectral overlap (shaded region) between the absorption spectrum of Z-$[Fe(tpy)_2]^{2+}$ (blue trace) and the emission spectrum of $[Ru(bpy)_3]^{2+}$ with area normalized to 1 (intensity reduced by a factor of 4 for illustration purposes only, magenta trace)

3.4 Conclusions

$[Ru(bpy)_3]^{2+}$ co-encapsulated in zeolite Y with varying concentrations of $[Fe(bpy)_3]^{2+}$ or $[Fe(tpy)_2]^{2+}$ were prepared. The zeolite encased iron complexes were found to quench both intensity and lifetime of the $[Ru(bpy)_3]^{2+}$ complex and this behavior was compared to that found in solution. In solution, $[Fe(bpy)_3]^{2+}$ has been shown to dynamically quench $[Ru(bpy)_3]^{2+}$ through non-radiative energy transfer whereas $[Fe(tpy)_2]^{2+}$ appears to quench only through a radiative or trivial energy transfer mechanism, which exerts no influence on the luminescent lifetime of $[Ru(bpy)_3]^{2+}$. In zeolite, therefore, it appears that for $[Fe(tpy)_2]^{2+}$ the behaviour changes and a non-radiative mechanism occurs. The $[Fe(tpy)_2]^{2+}$ exhibits significant structural distortion in the zeolite supercage, which is reflected in Raman and resonance Raman spectroscopy. This reduces the symmetry about the iron coordination sphere, and enhances a $^1T_2 \leftarrow {}^1A_1$ ligand field transition in the complex, enhancing the spectral overlap between $[Ru(bpy)_3]^{2+}$ and $[Fe(tpy)_2]^{2+}$. Therefore, zeolite-Y support and indeed enhances non-radiative energy transfer. The Förster radii were calculated to be 22 Å and 28 Å for $[Fe(bpy)_3]^{2+}$ and $[Fe(tpy)_2]^{2+}$ respectively within the zeolite structure, which corresponds to energy transfer across an approximately three-cage separation.

3.5 References

[1] Vohra V.; Bolognesi A.; Calzaferri G.; Bota, C**.** *Langmuir* **2009**, *25* **,** 20**,** 12019-12023.

[2] Cucinotta, F.; Popovic, Z.; Weiss, EA.; Whitesides, G.M.; De Cola, L**.** *Advanced Materials* **2009**, *21*,1142-1145.

[3] Coutant, M.A.; Le, T.; Castagnola, N.B.; Dutta, P.K. *J. Phys. Chem. B* **2000**, *104,* 10783-10788.

[4] Vitale, M.; Castagnola, N. B.; Ortins, N. J.; Brooke, J. A.; Vaidyalingam, A.; Dutta, P. K. *J. Phys. Chem. B* **1999**, *103*, 2408.

[5] Borja, M.; Dutta, P.K. *Nature* **1993**, *362*, 43–45.

[6] Meier, B.; Werner, T.; Klimant, I.; Wolfbeis, O. S. *Sens. Actuators B* **1995**, *29*, 240.

[7] Krueger, J. S.; Mayer, J. E.; Mallouk, T. E. *J. Am. Chem. Soc* **1988**, *110*, 8232.

[8] Brigham, E. S.; Snowden, P. T.; Kim, Y. I.; Mallouk,T.E. *J. Phys. Chem.* **1993**, *97*, 8650.

[9] Das, S. K.; Dutta P. K. *Langmuir* **1998**, *14*, 5121.

[10] Coutant, M. A.; Sachleben, J. R.; Dutta, P. K. *J. Phys. Chem. B* **2003**, *107*, 11000.

[11] Lutkouskaya K.; Calzaferri, G. *J. Phys. Chem. B* **2006**, *110*, 5633.

[12] Ruiz, A.Z.; Li, H.R.; Calzaferri, G. *Angewandte Chem.-Intern Ed.* **2006**, *45*, 5282.

[13] Bossart, O.; de Cola, L.; Welter, S.; Calzaferri, *Chem. Eur. J.* **2004**, *10*, 5771.

[14] Lunsford, J.H.; Peigneur, P.; De Wilde, W.; Schoonheydt, R.A. *J. Phys. Chem.* **1977**, *81*, 1179.

[15] Lunsford, J.H.; Peigneur, P.; Velghe, F.; Schoonheydt, R.A.; Uytterhoeven, J.B. *J. Phys Chem.* **1977**, *81*, 1187.

[16] DeWilde, W.; Peeters, G.; Lunsford, J.H. *J. Phys. Chem.* **1980**, *84*, 2306-2310.

[17] Quayle W.H.; Lunsford, J.H. *Inorg. Chem.* **1982**, *21*, 97-103.

[18] Quayle, W.H.; Peeters, G.; De Roy, G.L.; Vansant, E.F.; Lunsford, J.H. *Inorg. Chem.* **1982**, *21,* 2226-2231.

[19] Leith, I. *J. Chem. Soc., Chem. Commun.* **1983**, *2*, 93-94.

[20] Gustafson B.L.; Lunsford, J.H. *Journal of Catalysis*, **1982**, *74,* 393-404.

[21] Balzani, V.; Juris, A.; Barigelletti, F.; Campagna, S.; Belser, P.; Zelewsky, A.V. *Coordination Chemistry Reviews*, **1988**, *84*, 85-277.

[22] Yoon, S.; Kukura, P.; Stuart, C.M.; Mathies, R.A. *Mol. Phys.* **2006**, *104*, 1275–1282.

[23] (a) Lytle, F. E.; Hercules, D. M. *J. Am. Chem. Soc.* **1969**, *91*, 253.
(b) Demas, J. N.; Crosby, G. A. *J. Am. Chem. Soc.* **1971**, *93*, 2841.

[24] Young, R.C.; Meyer, T.J.; Whitten D.G. *J. Am. Chem Soc.* **1976**, *98*, 286.

[25] (a) Campagna, S, Puntoriero, F.; Nastasi, F.; Bergamini, G.; Balzani, V. *Top. Curr. Chem.* **2007**, *280*, 117-214.
(b) Juris, A.; Balzani, V.; Barigelletti, F.; Campagna, S.; Belser, P.; von Zelewsky, A. *Coord. Chem. Rev.* **1998**, *84*, 85-227.
(c) Crosby, G.A. *Acc. Chem. Res.* **1975**, *8*, 231.
(d) Chen, Y.; Meyer T.J. *Chem. Rev.* **1998**, *98*, 1439.

[26] Ref: http://www.answers.com/topic/fe-bipy-3-png-1 (accessed 9th September 2007)

[27] Campagna, S.; Puntoriero, F.; Nastasi, F.; Bergamini, G.; Balzani, V. *Top. Curr. Chem.* **2007**, *280*, 117-214.

[28] Auerbach S.M.; Henson N.J.; Cheetham A.K.; Metiu H.I. *J. Phys. Chem.* **1995**, *99*, 10600-10608.

[29] Riekert, L. *AIChE J.,* **2004**, *17*, 446.

[30] Castagnola N.B.; Dutta P.K. *J. Phys. Chem. B.* **1998**, *102*, 1696-1702.

[31] Balkus, K.I.; Gabrielov, A.G. Phenomena and molecular recognition in chemistry. *J. Inclusion Phenom.* **1995**, *21*, 159.

[32] Laine, P.; Lanz, M.; Calzaferri, G. *Inorg. Chem.* **1996**, *35,* 3514-3518.

[33] Maruszewski, K.; Strommen, D.P.; Handrich, K.; Kincaid, J.R. *Inorg. Chem.* **1991**, *30*, 4519-4582

[34] Incavo, J.; Dutta, P.K. .*J. Phys. Chem.* **1990**, *94,* 3075-3081.

[35] Resing, H. A.; Thompson, J. K. *Adv. Chem. Ser.* **1971**, *101*, 473.

[36] Jensen, A.; Basolo, F.; Neuman, H. M. *J. Am. Chem. Soc.* **1958**, *80*, 2354.

[37] Milosavljevic, B. H.; Thomas, J. K. *Chem. Phys. lett.* **1985**, *114,* 133.

[38] Sykora M, Kincaid JR, Dutta PK, Castagnola N.B. *J. Phys. Chem. B* **1999** *103*, 309-320.

[39] Marquez, F. Garcıa, H.; Palomares, E.; Fernandez, L.; Corma A. *J. Am. Chem. Soc.* **2000**, *122*, 6520.

[40] Maruszewski, K.; Strommen, D.P.; Kincaid, J. R. J. Am. Chem. Soc. **1993**, *115*, 8345-8350.

[41] Bhuiyan, A.A.; Kincaid, J.R. *Inorg. Chem.* **1998**, *37,* 2525-2530.

[42] Winkler, J. R.; Netzel, T. L.; Creutz, C.; Sutin, N. *J. Am. Chem. Soc*. **1987**, *109*, 2381.

[43] Maruszewski, K.; Kincaid, J.R. *Inorg. Chem.* **1995**, *34,* 2002-2006.

[44] Turbeville, W.; Robins, D.S.; Dutta, P.K. *J. Phys. Chem.* **1992**, *96*, 5024.

[45] Mori, K.; Kawashima, M.; Kagohara, K.; Yamashita, H. *J. Phys. Chem. C* **2008**, *112,* 19449–19455.

[46] Sykora, M.; Maruszewski, K.; Shelly M. Treffert-Ziemelis,; Kincaid, J.R. *J. Am. Chem. Soc.* **1998**, *120,* 3490-3498.

[47] Breck, D. W. *Zeolite Molecular Sieves: Structure Chemistry and Use*; John Wiley and sons: New York, 1974.

[48] Weitcamp, J.; Karge, H. G.; Pfeifer, H.; Holderich, W. Eds. *Zeolites and Related Materials*: State of the Art; Elsevier: Amsterdam, 1994.

[49] Maruszewski, K.; Strommen, D. P.; Handrich, K.; Kincaid, J. R. *Inorg. Chem*. **1991**, *30*, 4579.

[50] DeWilde, W.; Peeters, G.; Lundsford, J.H. *J. Phys. Chem.* **1980**, *84*, 2306.

[51] Turbeville, W.; Robins, D. S.; Dutta, P. K. *J. Phys. Chem.* **1992**, *96*, 5024.

[52] Quayle, W. H.; Peeters, G.; De Roy, G. L.; Vansant, E. F.; Lunsford, J. H. *Inorg. Chem.* **1982**, *21*, 2226.

[53] Bossmann, S. H.; Shahin, N.; Le Thanh, H.; Bonfill, A.; Wörner, M.; Braun, A. M. *Chemphyschem* **2002**, *3*, 401.

[54] Braterman P.S.; Song, J.I.; Peacock R.D. *Inorg. Chem.* **1992**, *31*, 555.

[55] Palmer, R. A.; Piper, T. S. *Inorg. Chem.* **1966**, *5*, 864.

[56] Vijayalakshmi, R.; Kulshreshtha, S.K. *Microporous Mesoporous Mater.* **2008**, *111*, 449.

[57] Krumholz, P. *Inorg. Chem*., **1965**, *4*, 612.

[58] Baggio-Saitovitch, E.; De Paoli, M. A*. Inorg. Chim. Acta* **1978**, *27*, 15.

[59] Spence, T. G.; Trotter, B. T.; Posey, L. A*. J. Phys.Chem. A* **1998**, *102*, 7779.

[60] Dutta, P. K.; Incavo, J. A. *J. Phys.Chem.* **1987**, *91*, 4443.

[61] Incavo, J. A.; Dutta, P. K. *J. Phys.Chem.* **1990**, *94*, 3075.

[62] Jensen, P. W.; Jørgensen, L. B. J. Mol. Struct. **1982**, *79*, 87.

[63] Hansen, P. W.; Jensen, P. W. *Spectrochim.Acta Part A* **1994**, *50*, 169.

[64] Schneider, S.; Brehm, G.; Prenzel, C.; Jager, W.; Silva, M.; Burrows, H.; Formosinho, S. J. Raman Spectrosc. 1996, 28, 163.

[65] Coe, B. J.; Thompson, D. W.; Culbertson, C. D.; Schoonover, J. R.; Meyer, T. J. Inorg. Chem. 1995, 34, 3385.

[66] Creutz, C.; Chou, M.; Netzel, T. L.; Okumura, M.; Sutin, N. *J. Am. Chem. Soc.* **1980**, *102*, 1309.

[66] Constable, E. C.; Thompson, A. M. W. C *J. Chem. Soc. Dalton Trans.* **1992**, *20*, 2947.

[67] Roller, R. S.; Winnik, M. A*. J. Phys. Chem. B* **2005**, *109*, 12261.

[68] Inokuti, M.; Hirayama, F. *J. Chem. Phys.* **1965**, *43*, 1978.

[69] Van Houten, J.; Watts, R. J. *J. Am. Chem, Soc.* **1976**, *98*, 4853.

[70] Suárez, S.; Devaux, A.; Bañuelos, J.; Bossart, O.; Kunzmann, A.; Calzaferri G. *Adv. Funct. Mater.* **2007**, *17*, 2298.

Chapter 4

Influence of Zeolite-Y confinement on the photophysical properties of selected Iridium polypyridyl complexes

4.0 Introduction

Iridium polypyridyl complexes have recently attracted considerable attention owing to their long-lived luminescent excited state time-range, intense emission and tuneable emission wavelengths from blue to red.[1] Early problems with iridium polyimine coordination chemistry associated with harsh reaction conditions have been addressed over the years, leading to increased yields and purer products.[2] These early synthetic obstacles were due in part to the inertness of third row transition metals coordination sphere. The required reaction conditions, utilising temperatures up to 230 ^{0}C yielded many side products that proved difficult to separate. However, advances in synthetic techniques for iridium complexes by for example Meyer *et al.* in the mid eighties, led to easily synthesised precursors (the most important being the use of triflate as a leaving group, *vide infra*) and a host of new Iridium polypyridyl complexes.[3]

This presented possibilities for iridium complexes in the field of organic light emitting device (OLED), solar energy harvesting as well as sensor applications due to various iridium polypyridyl complexes insensitivity and sensitivity to dissolved oxygen depending on the appended ligand.[4,5,6] The major initial drawbacks for applications concerned the UV or near UV excitation required. Recently however, new ligand designs have attempted to address this problem yielding some success.[7] In applications of iridium across optics and sensing a key barrier is their inclusion in a solid matrix to ensure their stability. The current study focuses on iridium complexes in the solid state, so a review of the iridium polypyridyl photophysics is outlined below, followed by an examination of iridium complexes in solid-state matrices.

4.0.1 Iridium photophysics

Iridium tris bipyridine and iridium bis terpyridine are d_6 complexes possessing an octahedral geometry (Figures 4.2 and 4.3). When coordinated to polypyridyl ligands the crystal field splitting energy is quite large compared to

ruthenium complexes, rendering the upper d-orbitals sufficiently high in energy to make metal centered transitions unlikely and hence increases their photostability and lifetime.

Many Ir (III) polypyridyl complexes are luminescent, the emission originating from charge-transfer or ligand centred emissive states, depending on the coordinated ligands.[1] The luminescent emission from the iridium complexes examined in the following chapter are primarily ligand based in nature, the nature of contributions from MLCT transitions in extended polypyridyl ligands is still the matter of on-going debate, however comparison of low temperature studies (77 K) of $[Zn(bpy)_3]^{2+}$ and $[Ir(bpy)_3]^{3+}$ phosphorescent emission profiles suggest the emitting state is $^3\pi\pi^*$ rather than MLCT based and studies on $[Ir(tpy)_2]^{3+}$ also suggests purely ligand based transitions.[8,9,10]

The reason for the predominantly ligand centred excited states of purely nitrogen Ir(III) bonded complexes compared to analogous Ru(II) species is due to the high oxidation potential of the iridium centre. The higher energy required for MLCT states puts them above the lower energy ligand-based transitions.[8] On this basis, the emission observed with zeolite included species is assumed to be ligand based phosphorescence, as it seems unlikely that the zeolite environment could sufficiently alter the oxidation potential of the included iridium (III) metal centre. MLCT transitions are possible when strong σ-donating ligands such as cyclometalating ligands are coordinated to the iridium centre due to their added charge density.

A large proportion of current research involves cyclometallated Iridium(III) complexes, which occurs where bonding of the iridium is through via a carbon atom rather than through more typical nitrogen atoms of ruthenium and osmium complexes (Figure 4.1).

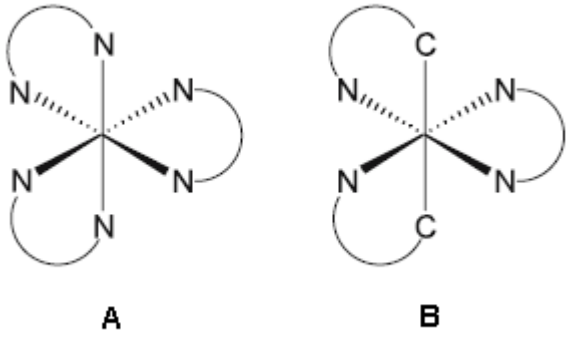

Figure 4.1: Representations of (A) $Ir(bpy)_3^{3+}$ and (B) Cyclometallated complex $Ir(bpy\text{-}C\text{^}N)_2(bpy\text{-}N\text{^}N)^+$ (bpy-N^N and bpy-C^N represent bonding to the metal ion through either the two nitrogen's of the ligand or one nitrogen and one carbon of the ligand), (Flamigni *et al. Top Curr. Chem*. **2007**, 281, 143).[1]

The photophysical properties of organic ligands bound to metals such as Ir(III) and Pt(II) are altered due to the heavy atom effect which enhances intersystem crossing from singlet excited states to triplet excited states (compare the spin-orbit coupling constant of Ruthenium ζ = 1042 cm^{-1} and iridium ζ = 3909 cm^{-1}) resulting in phosphorescent lifetimes (usually around 1 µs) substantially greater than unperturbed ligand fluorescence lifetimes (~1-10 ns). These enhanced lifetimes offer more scope for sensor development as well as light to chemical energy conversion applications involving energy or electron transfer processes.[4]

4.0.1.1 Iridium bis-terpyridine $[Ir(tpy)_2]^{3+}$

$[Ir(tpy)_2]^{3+}$ (Figure 4.2) was first synthesised by Ayala *et al.* who described the preparation and purification of the complex as time consuming and difficult.[11] Collin *et al.* re-examined the synthetic routes and managed to develop a milder synthetic route as well as offering strategies for the design of Ir(III) complexes with modified terpyridine based ligands via the $Ir(tpy)Cl_3$ precursor and synthesized the complexes in Figure 4.3.[8]

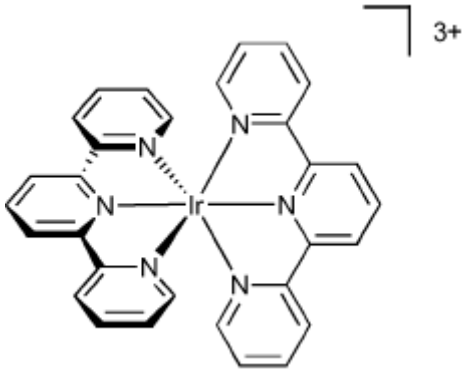

Figure 4.2: Structure of $[Ir(tpy)_2]^{3+}$ (Leslie *et al., Dalton Trans.* **2004**, 623).[9]

Based on their photophysical studies Collin *et al.* proposed that in the case of complex 1 (Figure 4.3) the emission was mostly ligand centered (^{3}LC) in nature due to the similarity of the 77 K emission spectrum of $[Zn(tpy)_2]^{2+}$ and $[Ir(tpy)_2]^{3+}$. This was attributed to the high oxidation potential of the iridium metal center of 2.7 eV, making MLCT transitions unlikely since the ^{3}LC level is estimated at 2.5 eV based on low temperature spectroscopic studies.[10] The emission spectrum of the complex under near UV excitation yields a structured profile with vibrational spacings of ~1400 cm^{-1} (Figure 4.4).

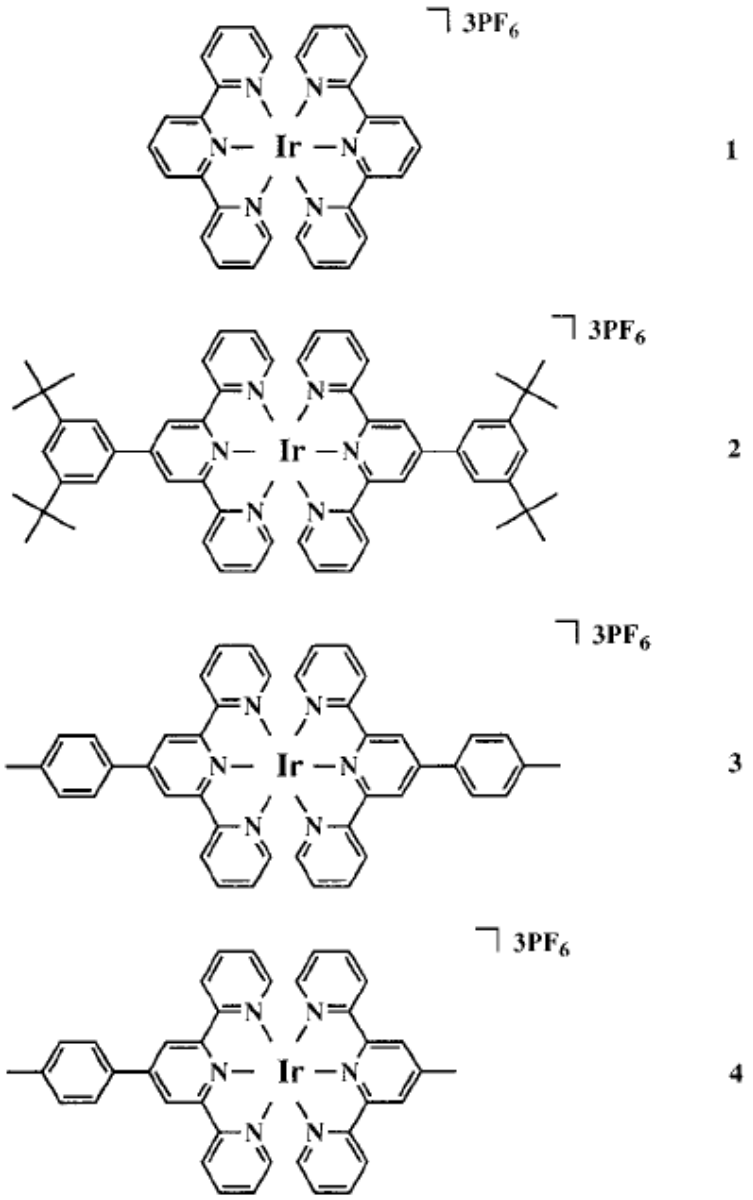

Figure 4.3: Iridium bis-terpyridine and bis-terpyridine derivatives prepared and studied by Collin *et al.* (*J. Am. Chem. Soc.* **1999**, *121*, 5009).[8]

These spacing are generally associated with coupling with aromatic C=C stretching modes and are also typical of ligand-centered emission.[4]

They further noted that the 77 K spectra of the Zn bis terpyridine derivatives did not match the analogous spectra of Ir complexes 2,3 and 4, inferring that in the case of the 4'-aryl substituted complexes, there may be a contribution from MLCT states as well as ligand centered ones.

The excited state lifetime of $[Ir(tpy)_2]^{3+}$ in degassed aqueous solution is 1.2 μs with a quantum yield of 0.03.[8] Leslie *et al.* demonstrated that choosing ligands with extended aromatic systems such as $[Ir(tpy)(tpy\text{-}\Phi Ph)]^{3+}$ (Figure 4.5) led to excited state lifetimes in the order of 100 μs.[12] The long lifetimes were attributed to stabilization and lowering of the energy of the of the ^{3}LC state due to the extended conjugation.

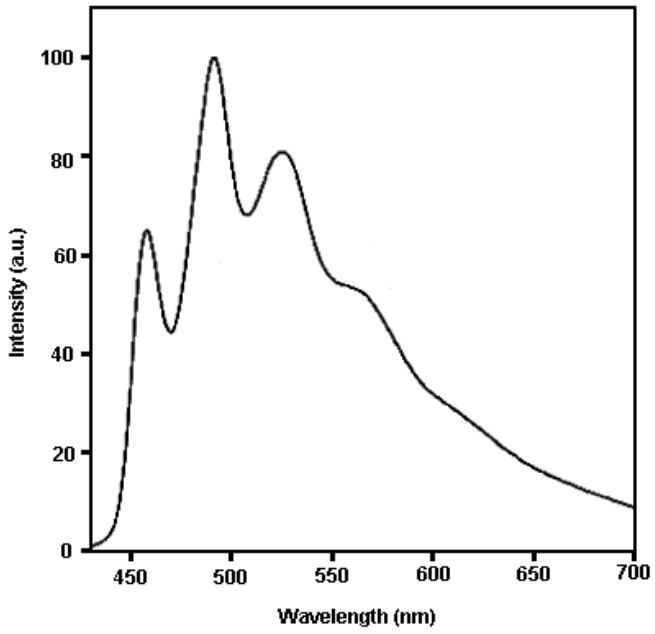

Figure 4.4: Luminescence spectrum of $[Ir(tpy)_2]^{3+}$ in degassed acetonitrile at 293 K exciting at 360 nm (Collin *et al., J. Am. Chem. Soc.* **1999**, *121*, 5009).[8]

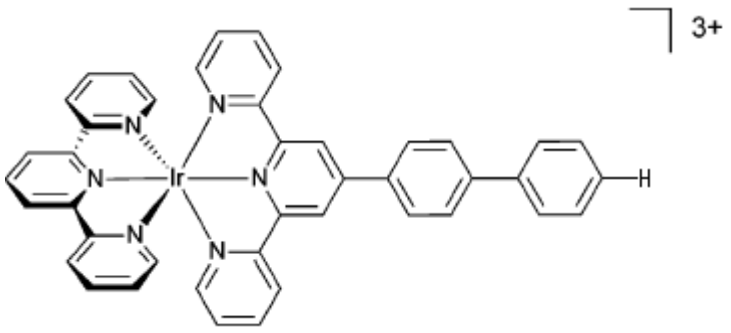

Figure 4.5: Structure of $[Ir(tpy)(tpy\text{-}\Phi Ph)]^{3+}$ (Leslie *et al.*, *Dalton Trans.* **2004**, *4*, 623).[12]

4.0.1.2 Iridium tris bipyridine $[Ir(bpy)_3]^{3+}$

One of the most widely studied iridium polypyridyl complex is $[Ir(bpy)_3]^{3+}$.[13] Martin *et al.* first reported it in 1958 employing a prolonged melt of K_3IrCl_6 and bipyridine.[14] Demas *et al.* further refined the melt synthetic technique but still described the work-ups for the melt procedure as arduous.[15] The difficultly in obtaining good yields and pure product prompted Meyer *et al.* to re-examine the synthesis.[16] They dispensed with the melt altogether, instead utilising a step wise synthesis with triflate leaving groups, resulting in much enhanced yields and greatly improved purity (scheme 1).

$IrCl_3.3H_2O + 2\ bpy \rightarrow [Ir(bpy)_2Cl_2]Cl$

$Ir(bpy)_2Cl_3 + CF_3SO_3H \rightarrow [Ir(bpy)_2Cl_2][CF_3SO_3] + HCl$

$[Ir(bpy)_2Cl_2][CF_3SO_3] + 2\ CF_3SO_3H \rightarrow [Ir(bpy)_2(OSO_2CF_3)_2] + 2HCl$

$[Ir(bpy)_2(OSO_2CF_3)_2][CF_3SO_3] + bpy \rightarrow [Ir(bpy)_3][CF_3SO_3]_3$

Scheme 1: Reaction scheme for synthesis of $[Ir(bpy)_3][CF_3SO_3]_3$
(Trifluoromethane sulphonic acid-CF_3SO_3H)

The luminescent emission from $[Ir(bpy)_3]^{3+}$ is thought to be ligand centred in nature for the same reasons as outlined for the $[Ir(tpy)_2]^{3+}$ complex however, there is speculation that the excited state may also contain MCLT character.[17,18] It has a room temperature excited state lifetime of 2.4 μs and around 80 μs at 77 K.[18] Figure 4.6 shows a summary of $[Ir(bpy)_3]^{3+}$ energetics indicating that $*[Ir(bpy)_3]^{3+}$ is a good oxidising agent but a relatively poor reducing one.

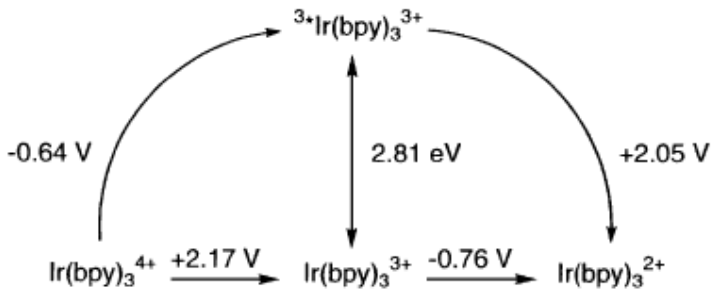

Figure 4.6: Reduction potentials (vs. SHE) of ground and excited state $[Ir(bpy)_3]^{3+}$ (Dixon *et al., Chem. Soc. Rev.,* **2000**, *29*, 385).[13]

4.0.2 Iridium complexes in the solid state

4.0.2.1 Iridium complexes in polymers

The largest range of solid-state studies involving iridium polypyridyl complexes has been polymers containing Iridium polypyridyl units. The inclusion of iridium compounds into polymer materials has also been examined in the quest for cheap flexible display material. The predominant use of iridium complex polymers has been in the field of organic light emitting diodes.

The use of heavy metal ions is attractive in their design owing to the induced spin-orbit coupling resulting in the potential for full utilisation of the generated excited singlet and triplet states as well as their synthetic versatility.[19]

Various synthetic strategies can be employed for their production, but in the main, has involved derivatization of one constituent polypyridine ligand with an ether linkage to a silane polymer or indeed many of the same polymer systems utilised in myriad ruthenium polypyridyl studies.[20] In general, polymers with appended iridium complexes are used to avoid phase separation problems when manufacturing OLED devices, the polymer environment does not in itself impact heavily on the independent photophysics of the complex. The polymerisation also acts to prevent aggregation of individual complexes to maximise device efficiency.

One study took advantage of the intermolecular heavy atom effect of iridium complex dopants on the host polymer material. Most luminescent polymers have very low inter-system crossing efficiencies due to their low atomic mass constituents. An iridium guest complex substantially enhanced the intersystem crossing in the host polymer material increasing the polymer triplet population 10 to 20 fold.[21] The mechanism of enhancement was attributed to resonant intermolecular heavy atom effect.

4.0.2.2 Iridium in zeolites

The present study focuses on the effects of separate encapsulation of the two iridium complexes $[Ir(tpy)_2]^{3+}$ and $[Ir(bpy)_3]^{2+}$ within the supercages of zeolite-Y (Figures 4.7 and 4.8).

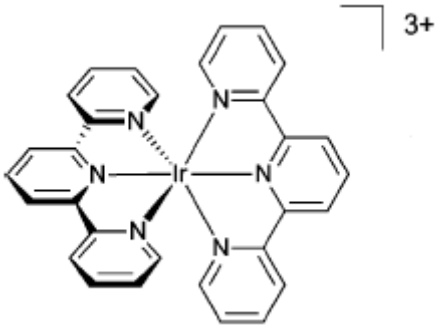

Figure 4.7: Iridium bis-terpyridine structure (Williams *et al. Dalton Trans.*, **2008**, 2081).[4]

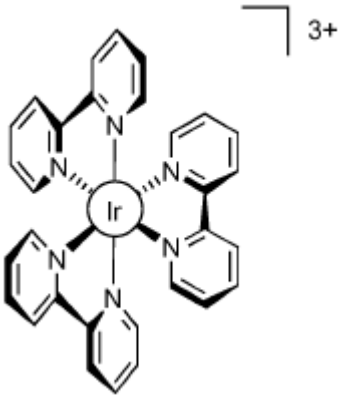

Figure 4.8: Iridium tris bipyridine structure (Williams *et al. Dalton Trans.*, **2008**, 2081).[4]

Only a relatively small body of work concerns the inclusion of iridium complexes into zeolite pores and with nearly all of these, the complexes are metal carbonyls or composed of small organic ligands with the focus being on catalytic performance rather then the photophysical properties of the complexes.[22,23] The encapsulation of any iridium polypyridyl complexes into zeolite structures has only recently been examined by Xu *et al.*[24] They studied the encapsulation of a cyclometallated species within zeolite-X (zeolite-X is topologically alike to zeolite-Y but has a greater ratio of alumina to silica rendering the intrazeolitic cavity more polar).[25] They prepared via a 'ship in a bottle' methodology tris-2-phenylpyridine (ppy) and tris 2-(2,4-di-fluorophenyl)pyridine (dfppy) based iridium complexes (Figure 4.9) within zeolite-X.

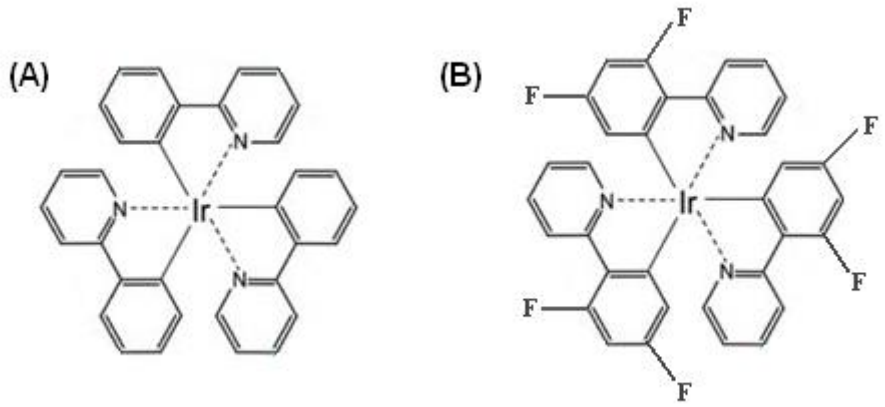

Figure 4.9: (A) $[Ir(ppy)_3]^{3+}$ and (B) $[Ir(dfppy)_3]^{3+}$ (Xu *et al., Eur. J. Inorg.* **2012**, 3113).[24]

They successfully synthesized the two complexes within the zeolite framework ultilising both the classical heating in ethylene glycol (12 hours at 473 K) and via an additional microwave synthesis step (10 minutes at 453 K). Disappointingly, the actual efficacy of the microwave step in enhancing ligand complexation with the ion-exchanged iridium cations was not investigated. An earlier experiment they performed using only microwave-assisted synthesis resulted in the complex forming outside of the cage structure rather than in the porous framework hence the use of extended heating periods, presumably to allow the ligand sufficient time to diffuse throughout the zeolite crystals.

They examined the absorption spectra of the materials and found by deconvolution of the spectra and comparison to solution phase that geometrical isomers for both complexes had formed within the zeolite. They also found a biexponential decay was required in order to fit lifetime data and attributed the two lifetimes to facial and meridional isomers. An estimation of the ratio of the two isomers was assessed based on the % contribution of each lifetime component coupled with their respective quantum yields. This estimate was predicated on no formation of intrazeolite side products that could interfere with the photophysical characteristics of the species under study. Given the scale of literature describing the difficult synthesis and purification of iridium complexes, this seems a somewhat risky assumption.

Mixtures of two complexes within the same zeolite crystals were also examined. This involved initial reaction of iridium exchanged zeolite with equimolar quantities of the two ligands and subsequent reaction with a larger quantity of only one of the ligands in order to produce a mixed complex material.

These were characterized by deconvolution of their emission spectra and comparison of the deconvoluted peak positions to the various expected components. The altered emission profile of the material demonstrated that indeed new emissive species had formed but they did not evaluate the number of different species present. Perhaps a better strategy would have been reaction to completion of one quantity of iridium-exchanged zeolite with the appropriate ligand followed by further ion exchange and reaction with the second ligand with the temperature controlled with regard to solution phase reaction temperatures.

The following chapter reports, for the first time, the effect of inclusion of iridium nitrogen bonded polypyridyl complexes into the rigid pore structure of zeolite-Y in order to assess the impact of the sterically confined environment on the photophysics of the complexes and also to examine the extent of interactions between co-entrapped complexes.

4.1 Experimental

4.1.1 Physical measurements

Luminescence, excited state lifetimes and Raman spectroscopic measurements were carried out in the same fashion as previous experiments. The electronic emission spectra represent the average of four separate emission intensity measurements.

Quantitation of Iridium complex loadings was carried out in a similar fashion to the previous chapter. Samples of sodium zeolite-Y used in the preparation of the samples were reacted with the ligands either terpyridine or bipyridine and the level of iron purity assessed. The iridium containing zeolite samples were then dissolved in hydrofluoric acid (10% v/v) and the absorbance measured and corrected for any iron impurities present. Experiments confirmed the stability of both iridium complexes in the hydrofluoric acid solvent for at least 30 minutes (*vide infra*). Typically the measurements were carried out directly after dissolution of the zeolite framework, usually ten minutes or less was taken to measure the absorbance. The extinction coefficients for the relevant iron complexes were calculated by preparation of standard solutions.

Nomenclature for zeolite guest concentration: Once again the concentrations of complex in zeolite will mostly be expressed with regard to the number of empty supercages, e.g. 5 % occupation of available supercages by a complex means that 1 in 20 is occupied. So the concentration would be expressed as 1:20 $[M(LL)_x]^{y+}$ (read 1 complex per 20 empty supercages). This method makes interpretation of results a little more intuitive when considering adjacent cage interactions.

4.1.2 Synthesis of zeolite materials

The synthesis of both Z-$[Ir(tpy)_2]^{3+}$ and Z-$[Ir(bpy)_3]^{3+}$ is described in detail in the beginning of chapter 2, experimental approaches and instrumentation.

4.2 Results and discussion

4.2.1 Synthesis and characterisation

Preparation of the iridium-based materials was carried out in broadly similar steps to the previous iron and ruthenium polypyridyl based materials. There were a number of changes however. The initial purification of the starting zeolite material remained the same with the exception that ion exchange with the iridium metal salt was conducted at reflux in water. The same washing procedures were employed to remove any un-exchanged iridium cations residing on the surface or inner cavities of the zeolite material, again using hot deionised water to aid the salt dissolution and removal. After reaction with the required ligand, the compounds were again washed in concentrated salt solution (10% w/v) to remove any surface bound extraneous material.

In order to ensure that the parent complexes are stable in the HF solution used to dissolve the zeolite framework, solutions of the complexes were prepared in HF (10%) and the absorbance recorded at several time points. Figures 4.10 and 4.11 show the absorption spectra of $[Ir(bpy)_3][PF_6]_3$ and $[Ir(tpy)_2][PF_6]_3$ dissolved in HF (10%) at time zero and 35 and 30 minutes respectively after acid addition. In each case no change in the absorption spectrum was noted. The concentration measurements were actually carried out in less than ten minutes, with the analyte only actually exposed to HF at a 10 % concentration for 2-3 minutes, the remainder of the 10 minutes maximum exposure was to a 4 % HF solution.

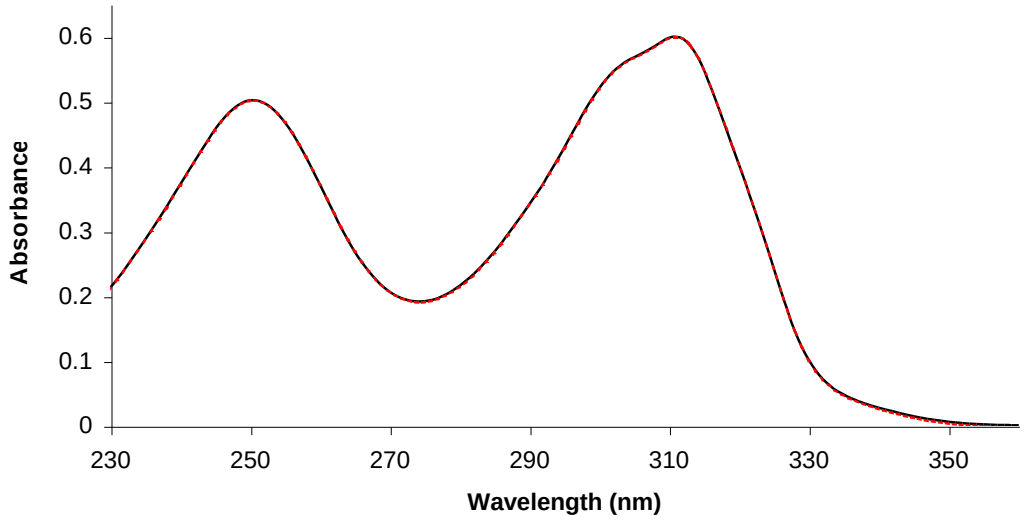

Figure 4.10: Absorption spectra of $[Ir(bpy)_3][PF_6]_3$ (1.3×10^{-5} M) dissolved in hydrofluoric acid (10% w/w). Slit width 5 nm. Absorption spectra immediately after acid addition(—) and 35 minutes after HF addition (---).

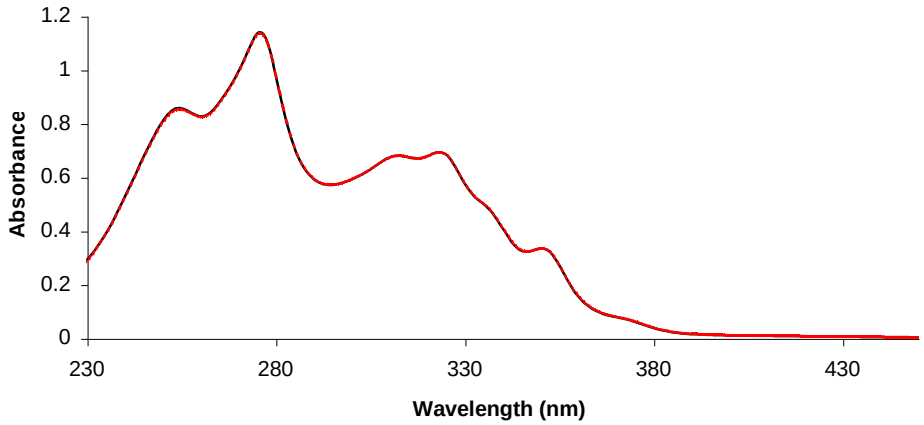

Figure 4.11: Absorption spectra of $[Ir(tpy)_2][PF_6]_3$ (6.4×10^{-5} M) dissolved in hydrofluoric acid (10% w/w). Slit width 5 nm. Absorption spectra immediately after acid addition(—) and 30 minutes after HF addition (---).

Physical entrapment of the complexes within the zeolite matrix was confirmed by reference to their Raman and emission spectra. Upon entrapment, broadening of Raman shifts were observed, typical of encapsulated species as well as substantial differences in the observed emission profile compared to solution phase measurements (*vide infra*).

The concentrations of the complexes within the zeolite are shown in table 4.1. A photo showing some of the zeolite materials used in this study coated on glass slides is shown in Figure 4.12.

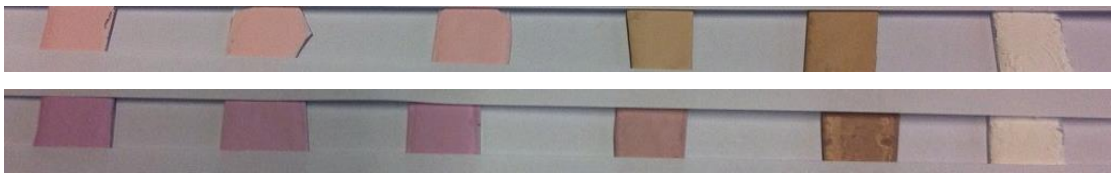

Figure 4.12: Photo showing samples of zeolite-complex materials drop coated onto glass slides. The top shows Z-$[Ir(bpy)_3]^{3+}$ samples with increasing complex concentration. The bottom photo shows Z-$[Ir(bpy)_3]^{3+}$ with increasing concentration. In each case the slide at the far right is zeolite-Y with no entrapped species.

As can be noted from the samples of low iridium complex concentration the iron impurity persists with the batch of zeolite material purchased (pink and purple impurities which are $[Fe(bpy)_3]^{2+}$ and $[Fe(tpy)_2]^{2+}$ respectively). The large extinction coefficients associated with the MLCT transitions of these impurities ensure a strongly coloured material even at very low concentrations. Despite rigorous and prolonged ion exchange with concentrated sodium chloride solution it could not be removed. As stated in chapter three, the actual concentration of iron complexes is estimated at approximately 1 complex per 135 supercages, making their influence negligible.

Table 4.1: Concentrations of zeolite included complexes

Concentration $[Ir(tpy)_2]^{3+}$ within Na-Y [a]		**Concentration $[Ir(bpy)_3]^{3+}$ within Na-Y [a]**	
Mol dm^{-3}	**Supercages per $[Ir(tpy)_2]^{3+}$**	**Mol dm^{-3}**	**Supercages per $[Ir(bpy)_3]^{3+}$**
0.178	5	0.116	8
0.126	7	0.048	18
0.029	30	0.017	51
0.025	36	0.011	81
0.018	49	0.006	147
0.016	69	0.002	390

[a]Based on Y-zeolite with density 1.92 g/cm^{-3} and 1 g Y-zeolite containing 2.778 X 10^{20} supercages.[26,27]

4.2.2 Photophysical Characterisation

4.2.2.1 Electronic absorption of zeolite entrapped iridium complexes

The diffuse reflectance spectra of the zeolite-encapsulated species as shown in Figure 4.12 were recorded as a powder coated onto the glass slides. Unfortunately, the persistent iron contaminant present within the zeolite masked the spectral region of interest and interfered with the measurement of the materials electronic absorption characteristics. This was due to the formation of iron polypyridyl analogues iron tris-bipyridine $[Fe(bpy)_3]^{2+}$ and iron bis-terpyridine $[Fe(tpy)_2]^{2+}$ that possess substantially larger molar absorptivities than the corresponding iridium complexes. Spectroscopic information about the included species therefore was gleaned from emission and Raman studies.

4.2.2.2 Effect of encapsulation on $[Ir(tpy)_2]^{3+}$ electronic emission

The emission spectra of the series of iridium terpyridine samples are shown in Figure 4.15. Three vibrationally resolved maxima are present at 458, 488 and 522 nm. At the highest concentration of complex within the zeolite the lowest energy maximum emission intensity is strongly enhanced, while the λ_{max} remains relatively unaffected. Comparison of the emission spectra of the medium loading (1 complex per 36 supercages) of complex to the parent solution phase complex reveals a small blue shift in the entrapped species (Figure 4.16).

This is not unexpected considering the confined and highly polar intrazeolite pore environment and that both $[Ir(tpy)_2][PF_6]_3$ and $[Ir(bpy)_3][PF_6]_3$ display negative solvatochromism. Figures 4.13 and 4.14 shows normalised emission spectra of both in solutions of either acetone (dielectric constant 20.7) or 90 % water 10% acetonitrile (dielectric constant 76.80 at room temperature).[28] The emission of $[Ir(tpy)_2][PF_6]_3$ red shifts ~ 5 nm going from the 90 % water solution to the lower dielectric solvent acetone while $[Ir(bpy)_3][PF_6]_3$ red shifts 9 nm from its highest emission band under the same conditions. This solvatochromism results from the extensive delocalisation of the excited state that is expected from an excited state with large ligand character. Entrapment of the complex in the zeolite is therefore expected to yield a blue shift in response to the high local polarity of the pore as well as some degree of rigidochromism stemming from the confined environment. The nature of these shifts is also considered in more detail in chapter 5.

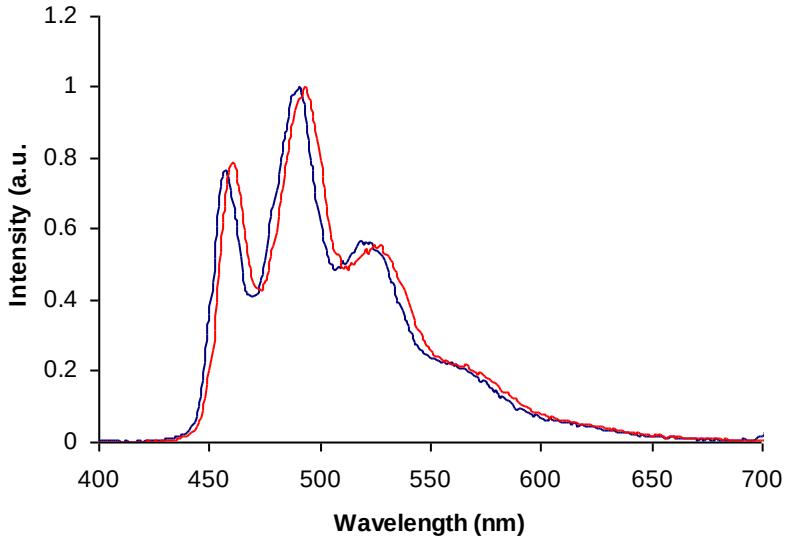

Figure 4.13: Comparison of normalised electronic emission of $[Ir(tpy)_2][PF_6]_3$ (1.15×10^{-5} M) in 90 % deionised water 10 % acetonitrile (blue trace) and $[Ir(tpy)_2][PF_6]_3$ (1.2×10^{-5} M) in acetone. Excitation 350 nm and slit width 5 nm.

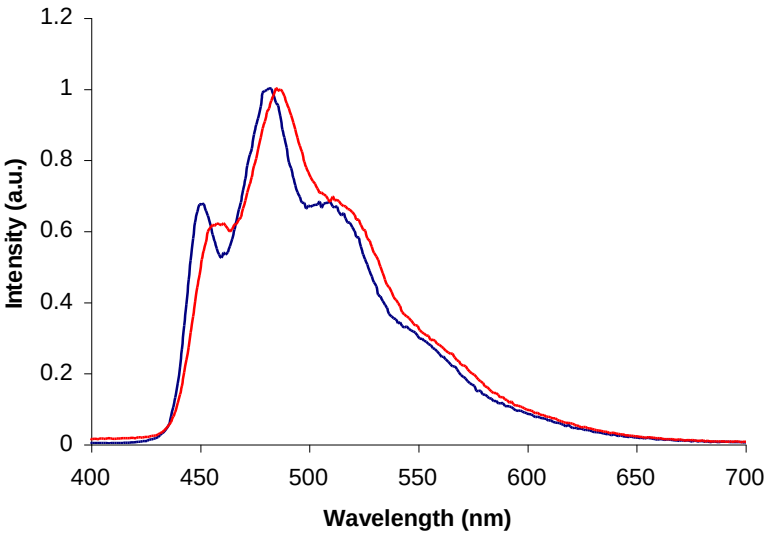

Figure 4.14: Comparison of normalised electronic emission of $[Ir(bpy)_3][PF_6]_3$ (1.1×10^{-5} M) in 90 % deionised water 10 % acetonitrile (blue trace) and $[Ir(bpy)_3][PF_6]_3$ (1.0×10^{-5} M) in acetone. Excitation 319 nm and slit width 5 nm.

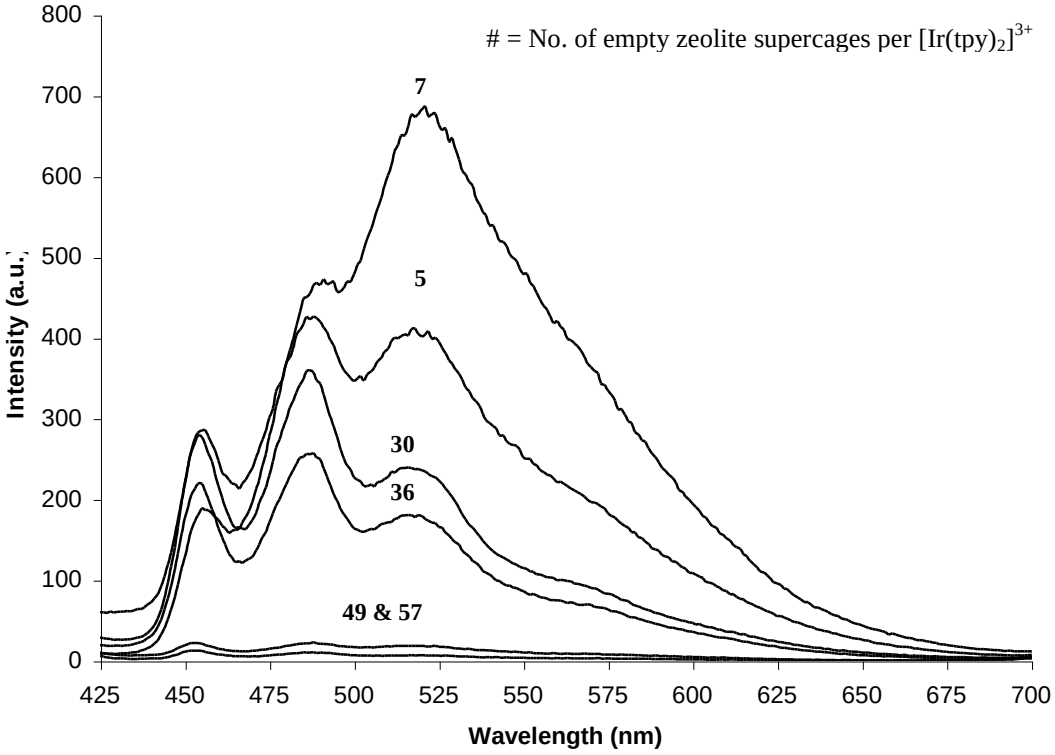

Figure 4.15: Luminescence spectra of Zeolite entrapped $[Ir(tpy)_2]^{3+}$ coated on glass slides. Samples excited at 330 nm, slit width 5 nm.

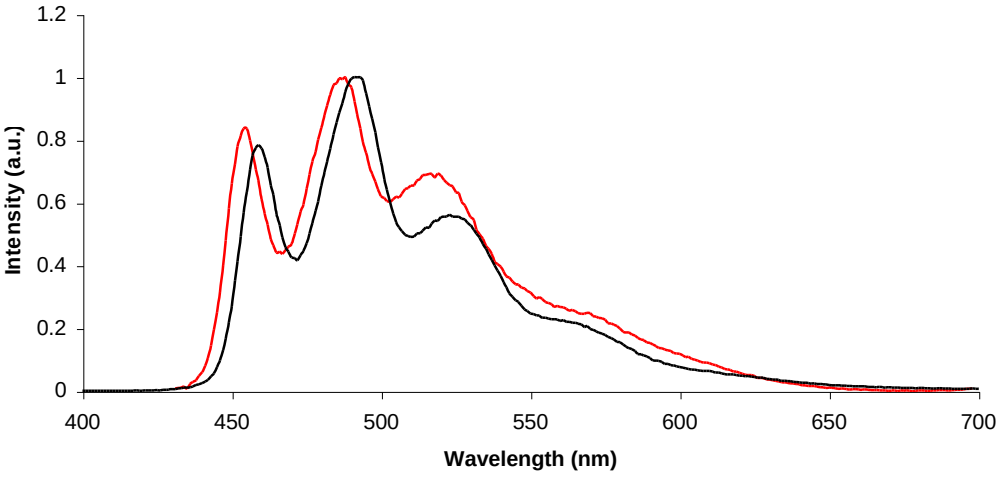

Figure 4.16: Comparison of normalised electronic emission spectra of $[Ir(tpy)_2][PF_6]_3$ (1.4×10^{-5} M) in butyronitrile exciting at 350 nm and slit width of 5 nm black trace) and Z- $[Ir(tpy)_2]^{3+}$ (1 complex per 36 supercages), exciting at 330 nm and slit width 5 nm (red trace).

4.2.2.3 Concentrations effects on the extent of intercage $[Ir(tpy)_2]^{3+}$ interactions

The luminescence intensity of the doped materials increases with increasing concentration. A plot of luminescent intensity at the three major emission wavelengths versus concentration is shown in Figure 4.17.

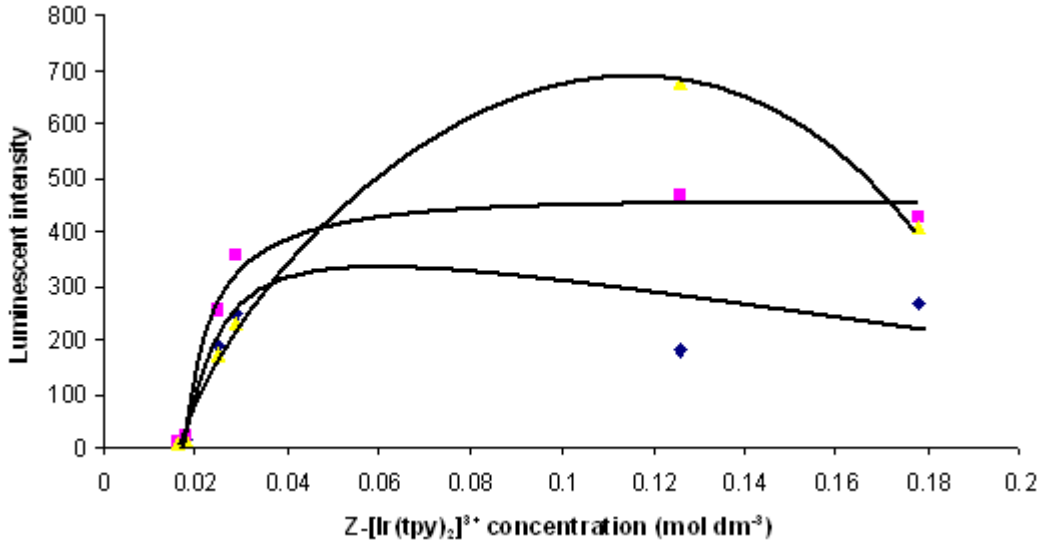

Figure 4.17: Emission intensity at 458 nm (blue dots), 488 nm (purple dots), 522 nm (yellow dots) vs. concentration (mols dm^{-3}). Excitation at 330 nm and slit widths 5 nm. Data extracted from Figure 15. Included trend lines are for clarity of data presentation only.

What is apparent from the plot is the deviation from linearity as the concentration goes beyond 0.03 mol dm^{-3}. This is attributed to a self-absorption process that becomes more obvious at the higher concentrations of complex. This process is not often seen in transition metal complexes but has been noted with other luminescent compounds.[29,30]

In order to confirm that self-absorption was occurring, a dilute $[Ir(tpy)_2][PF_6]_3$ solution (1.4×10^{-5} M in acetonitrile) was excited at 458 nm (exciting into the highest energy emission band wavelength) and the emission monitored

(Figure 4.18). The solution displayed the same emission profile confirming the large overlap of the absorption and emission spectra.

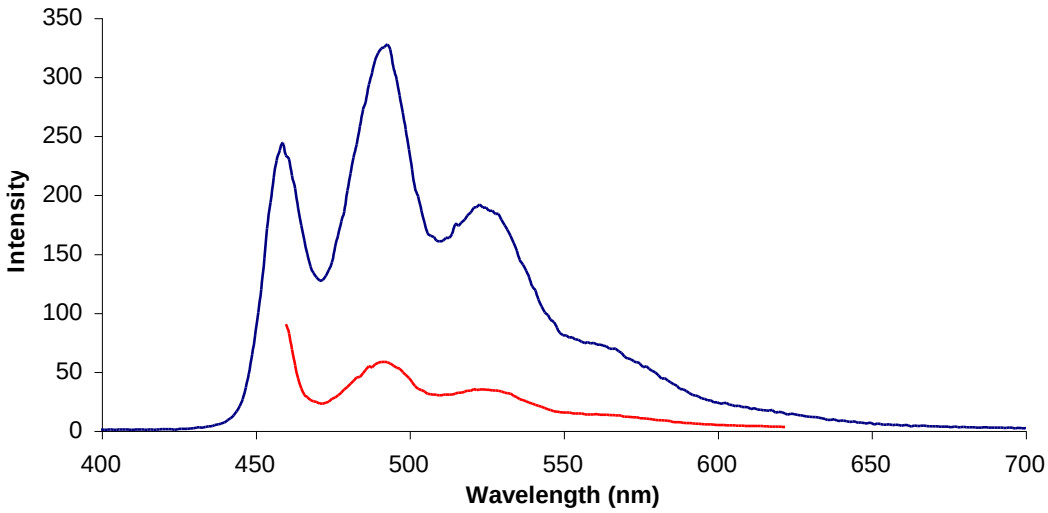

Figure 4.18: Emission spectrum of $[Ir(tpy)_2][PF_6]_3$ (1.4 x 10^{-5} M in acetonitrile), excitation at 350 nm (blue trace) and excitation at 458 nm (red trace). Slit width 5 nm for both experiments.

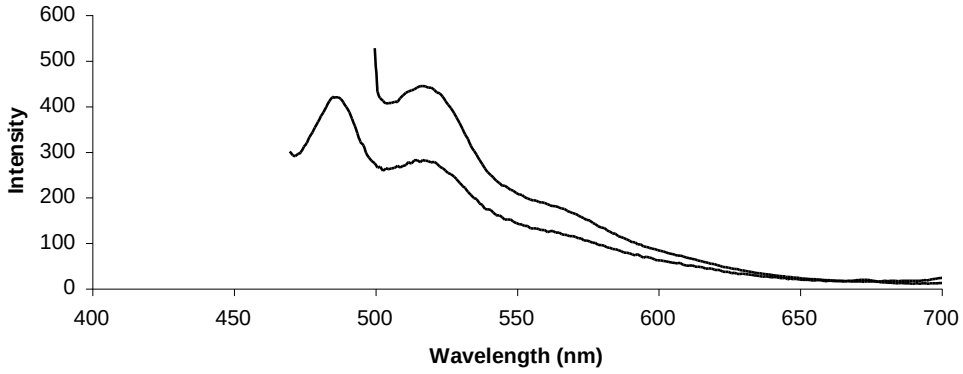

Figure 4.19: Emission spectra of Z-$[Ir(tpy)_2]^{3+}$ (1:30). Emission spectrum of Z-$[Ir(tpy)_2]^{3+}$ (1:30) exciting at 458 nm (bottom trace) and emission spectrum Z-$[Ir(tpy)_2]^{3+}$ (1:30) exciting at 492 nm (top trace). Slit widths 5 nm for all measurements.

The increase in relative intensity of the low energy component appears only at higher zeolite loadings, so therefore is attributed to an increased degree of

self-absorption. The increase in the apparent intensity observed at the 522 nm band is reflective of an increased local concentration of complex. The apparent increase in the intensity of this band actually reflects a diminished intensity for the two higher energy components due to this self-absorption phenomenon. To ensure that this behaviour was replicated with the zeolite entrapped material, Z-$[Ir(tpy)_2]^{3+}$ (1:30) was excited at both 458 nm and 492 nm and the emission monitored. As before, structured emission is observed, confirming the process is operable in zeolite as well as solution (Figure 4.19).

The origin of the long wavelength absorption is tentatively assigned to direct triplet state excitation, analogous to that observed for similar osmium polypyridyl complexes.[31] This is not unreasonable considering the spin-orbit coupling constant of iridium (ξ = 3909 cm^{-1})[32] compared to osmium (ξ ~ 3000 cm^{-1}).[33]

An emission with an anomalous intensity was noted in Figure 4.15. Considering only the two higher concentration samples, the lower concentration sample 1:7 Z-$[Ir(tpy)_2]^{3+}$ has the higher 522 nm luminescent intensity compared with the 1:5 Z-$[Ir(tpy)_2]^{3+}$ sample. The prominence of this spectral feature with the lower concentration sample over its more concentrated counterpart may lie with its method of preparation.

The source of this is likely to be the initial heating step during the materials preparation. The reaction between the ligand and the ion-exchanged zeolite may have been carried out faster (i.e. the reaction solution was brought to reflux very quickly) for the lower concentration sample (1:7 Z-$[Ir(tpy)_2]^{3+}$). This could result in less time for ligand diffusion to the core of the zeolite crystal before the ship in a bottle synthesis is complete resulting in a preponderance of complexes near the outer surface of the zeolite particle due to initially higher temperatures and greater concentration of available ligand (Figures 4.20, 4.21 and 4.23). The formation of these complexes on the outer edge may inhibit further ligand infiltration to the core and hence the lower than expected concentration but the higher than expected luminescent intensity at

the crystal edge. This phenomenon would only apply to the samples with rather large concentrations of ions so any effect on the remainder of the samples is negligible. This does however indicate that caution is required concerning intrazeolitic reactions that proceed rapidly. Although the production of $[Ir(bpy)_3]^{3+}$ is sluggish, the formation of the bis-complex $[Ir(bpy)_2]^{3+}$ is rapid and is of sufficient molecular volume to remain entrapped within a pore and effectively block or slow further diffusion of other guest species. The formation of the $[Ir(tpy)_2]^{3+}$ also proceeds rapidly at high temperatures highlighting the need for sufficient time and moderate temperatures to ensure uniform dispersion of reagents throughout the crystal.

The actual yield of complexes per prepared sample was somewhat difficult to control. Synthesis of the analogous zeolite entrapped ruthenium polypyridyl complexes proceded in excellent yield with respect to the moles of ion-exchanged metal centre before ligation, and the concentration of actual complex as determined by HF dissolution after. The yield of iridium polypyridyl complexes encapsulated within zeolite-Y was substantially less than the quantity of metal exchanged, with yields on average around 40% of expected for the Z-$[Ir(tpy)_2]^{3+}$ materials and approximately 20% of the total expected for the Z-$[Ir(bpy)_3]^{3+}$ materials. These low yields are attributed to the inertness of the Iridium ion as outlined above in conjunction with the likely sterically hindered environment encountered by reacting ligands.

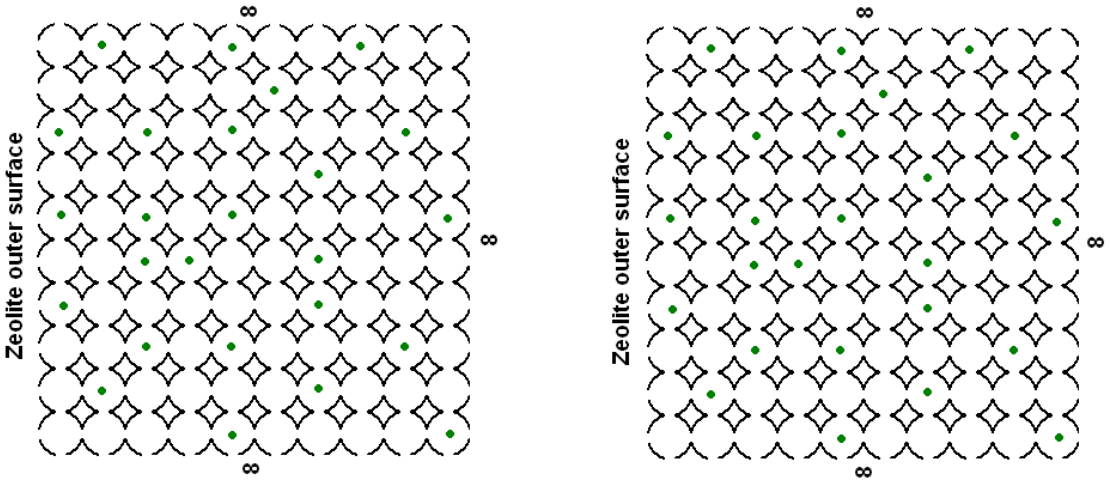

Figure 4.20: Ion-exchanged zeolite Y (Metal ions-green dots) and the zeolite crystal extending to infinity in a particular direction (∞).

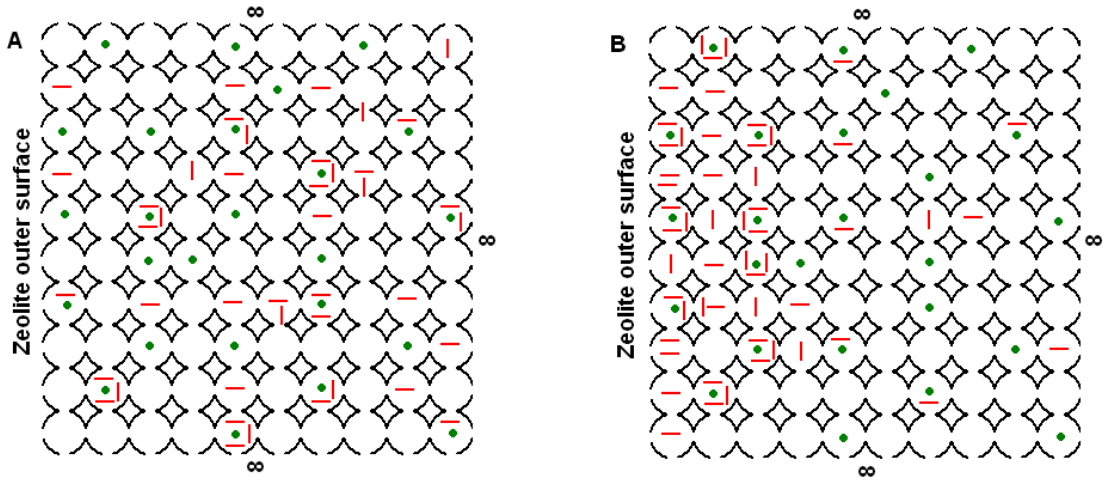

Figure 4.21: Model proposed for edge reactions in ion-exchanged zeolite-Y with unreacted ligands (red lines) under two possible conditions. (A) Normal initial heating, ligands have time to diffuse throughout zeolite crystal. (B) Rapid heating, ligands have less time to diffuse and congregate around outer surfaces

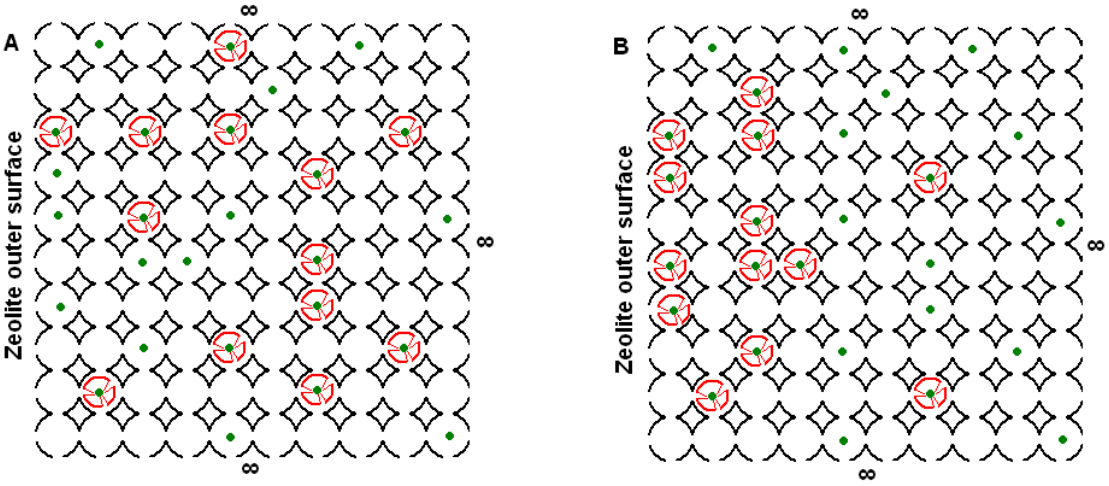

Figure 4.22: Following reaction and excess ligand removal a greater number of adjacent complexes have formed at the surface of (B) due to initial higher local ligand concentration.

4.2.2.4 Imaging of Z-$[Ir(tpy)_2]^{3+}$ materials

The full experimental set-up is described in chapter two, experimental approaches and instrumentation. The Z-$[Ir(tpy)_2]^{3+}$ materials were imaged

using a fluorescence lifetime imaging microscope (experimental details in chapter 2). The imaging was carried out in order to determine the size and homogeneity of the zeolite crystals as well as examine the uniformity of the luminescence and lifetime at the level of individual crystals.

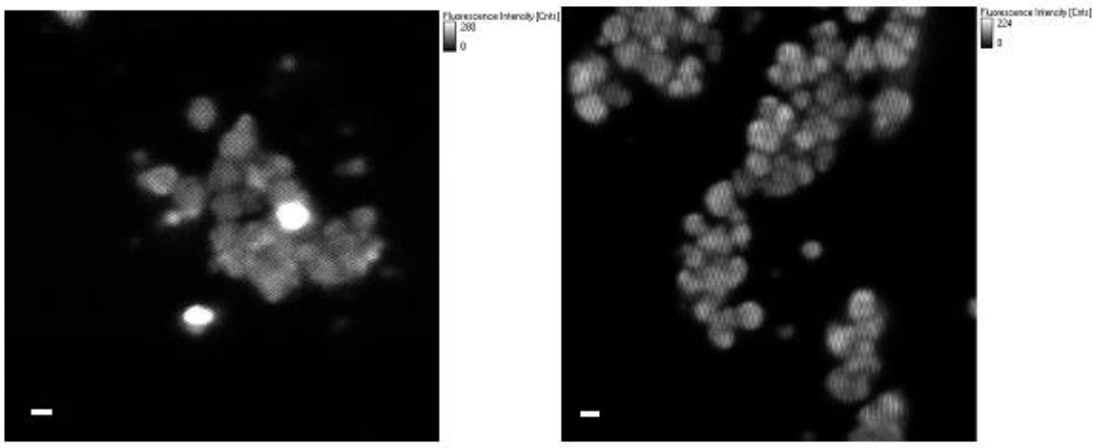

Figure 4.23: Left: Luminescence intensity map of 1:30 Z-$[Ir(tpy)_2]^{3+}$ and right: 1:7 Z-$[Ir(tpy)_2]^{3+}$. Excitation at 448 nm and Scale bars are 1 μm.

Figure 4.23 shows luminescence intensity maps for 1:30 Z-$[Ir(tpy)_2]^{3+}$ and 1:7 Z-$[Ir(tpy)_2]^{3+}$ samples. The particles are approximately 1 μm in size and display reasonable size homogeneity. The luminescence intensity appears to be slightly more uniform for the lower concentration 1:30 Z-$[Ir(tpy)_2]^{3+}$ samples compared to the higher concentration 1:7 Z-$[Ir(tpy)_2]^{3+}$ samples. There appears to be more variance in luminescent intensity across individual particles at the higher loading, which may account for the anomaly in the samples luminescent intensity mentioned in the previous section. However, the resolution is at the limits of the instrument so definitive determinations based on the images obtained are not possible. The source of the bright spots observed on the 1:30 Z-$[Ir(tpy)_2]^{3+}$ intensity map are unclear, it may be possible that insoluble impurities from the iridium trichloride material may still be present, and would account for the bright reflectance observed.

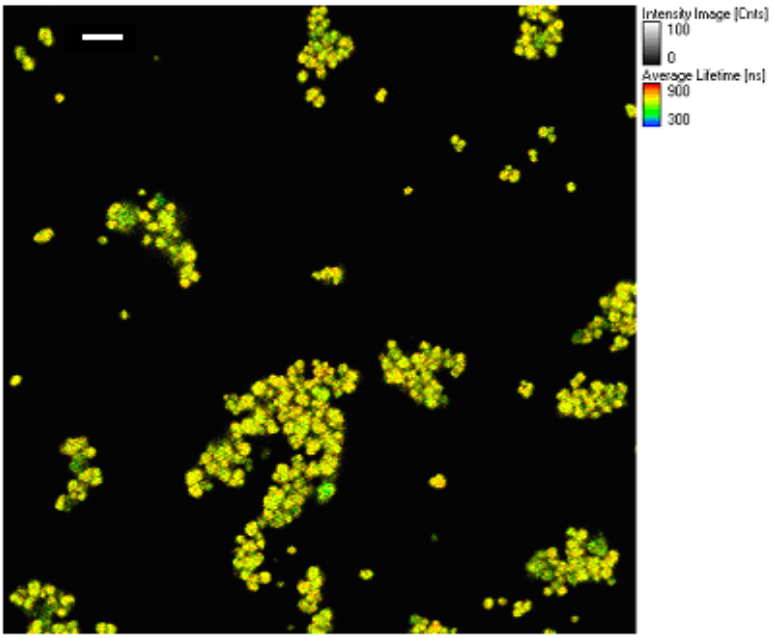

Figure 4.24: Fluorescence lifetime imaging map of 1:7 Z-$[Ir(tpy)_2]^{3+}$, Scale bar is 5 μm, excitation 448 nm.

Figures 4.24 and 4.25 are fluorescence lifetime images of the 1:7 Z-$[Ir(tpy)_2]^{3+}$. The actual lifetimes shown must be interpreted only with respect to changes in the lifetime across a particle rather than the actual lifetime of the species present. Excited state lifetime studies performed on the materials (*vide infra*) yielded lifetimes in excess of the instruments operating range so care must be taken with their interpretation. In broad terms however, there appears to be a slight decrease in the lifetimes at the outer edges of the zeolite particles, indicated by the green colour as compared to the centre of the particle that has the yellow colour (Figure 4.25). Figure 4.26 shows a global selection of zeolite crystals and indicates that the lifetime distribution is not as homogeneous as was expected. Figure 4.27 shows individual particles of 1:30 Z-$[Ir(tpy)_2]^{3+}$. Some whole crystals rather than portions of crystals display a shorter lifetime distribution that is indicated by the green areas.

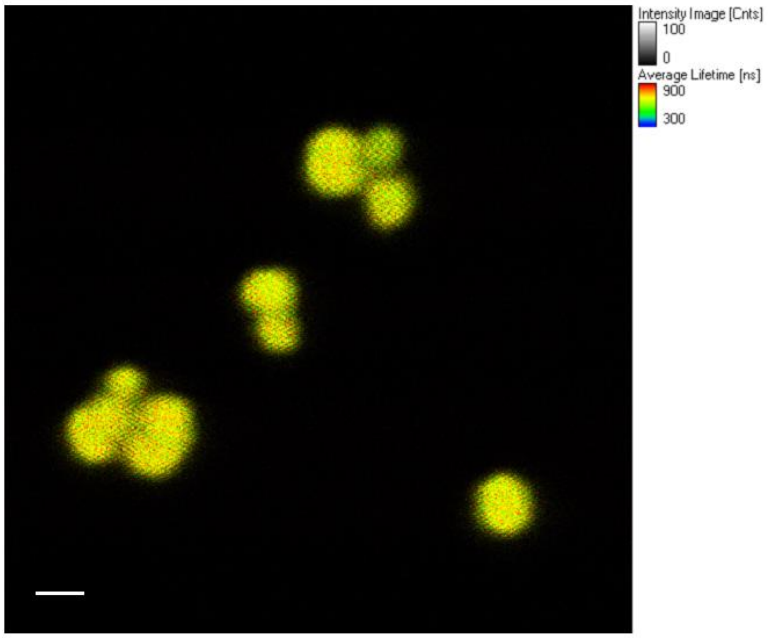

Figure 4.25: Fluorescence lifetime imaging maps of 1:7 Z-$[Ir(tpy)_2]^{3+}$. Excitation at 448 nm and scale bar 1 μm.

These broad trends are reproduced with the lower concentration sample 1:30 Z-$[Ir(tpy)_2]^{3+}$. The appearance of a shorter lifetime distribution at the edge of the crystal is reproduced in these samples, as is the non-unifomity in the global samples. It must be reiterated however, that these values only represent lifetime changes rather than the actual excited state lifetime.

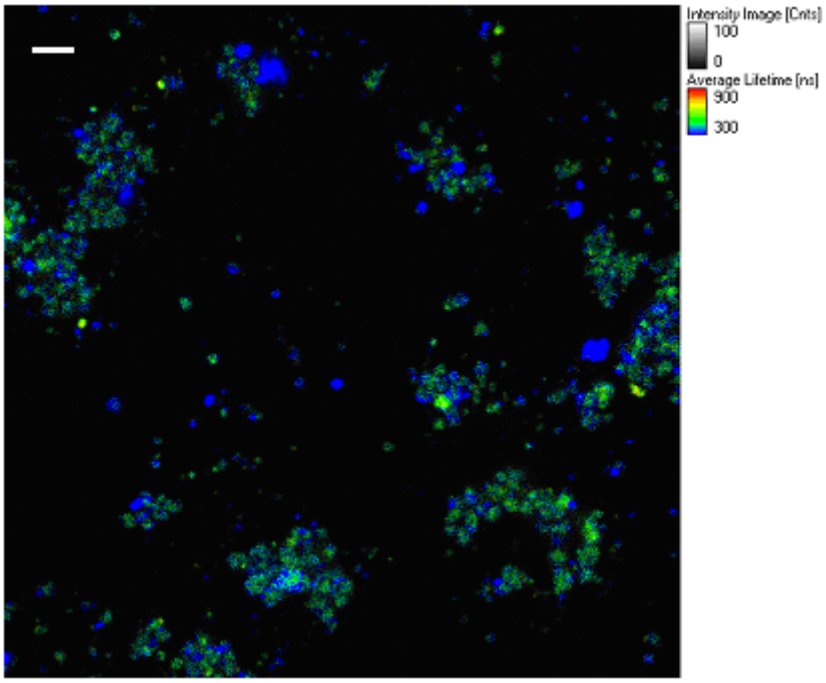

Figure 4.26: Fluorescence lifetime imaging maps of 1:30 Z-$[Ir(tpy)_2]^{3+}$. Scale bar 5 μm. Excitation at 448 nm.

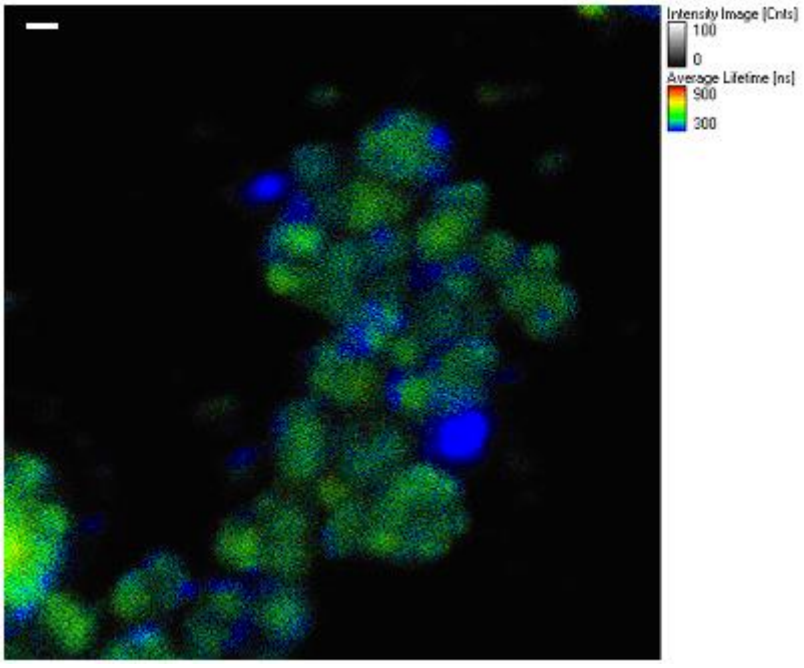

Figure 4.27: Fluorescence lifetime imaging maps of 1:30 Z-$[Ir(tpy)_2]^{3+}$. Scale bar 1 μm. Excitation at 448 nm.

4.2.2.5 Effect of encapsulation on Z-$[Ir(bpy)_3]^{3+}$ electronic emission

The emission spectra of the zeolite entrapped Z-$[Ir(bpy)_3]^{3+}$ series is shown in Figure 4.28. Three vibrational resolved emission maxima occur at 451 nm, 482 nm and 504 nm. Comparison of the emission profile of the entrapped species to the emission profile of $[Ir(bpy)_3]^{3+}$ in acetonitrile shows substantial blue shifts across all emission maxima (Figure 4.29 and table 4.2).

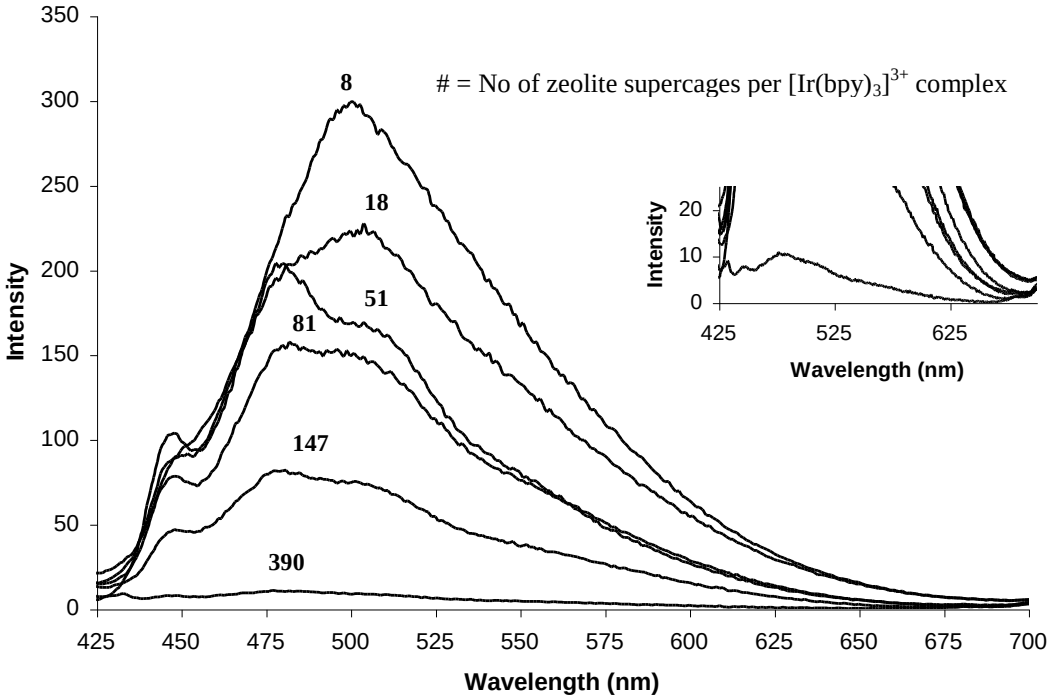

Figure 4.28: Luminescence spectra of Zeolite entrapped $[Ir(bpy)_3]^{3+}$ coated on glass slides. Samples excited at 319 nm, slit width 5 nm. Inset: Expanded section of plot showing spectrum of $[Ir(bpy)_3]^{3+}$ (1 $[Ir(bpy)_3]^{3+}$:390 supercages)

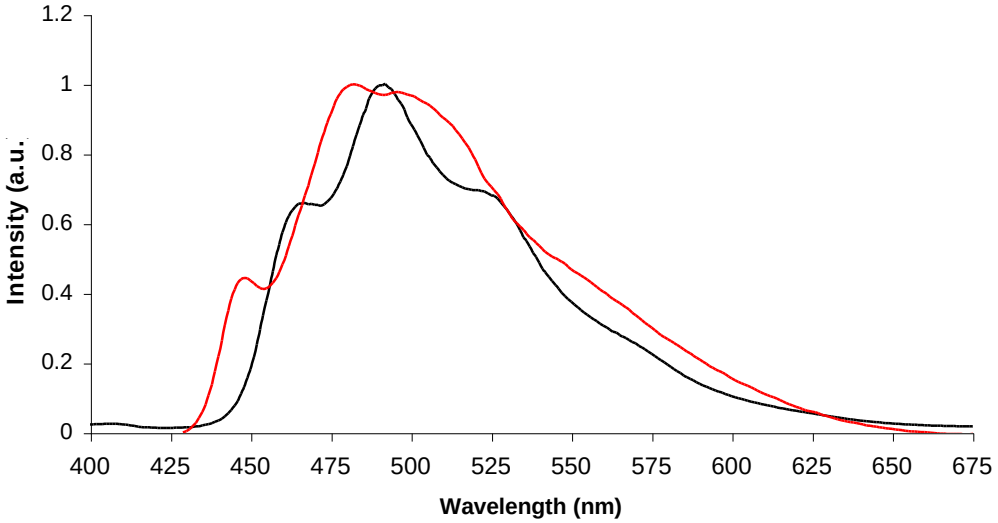

Figure 4.29: Comparison of normalised electronic emission spectra of $[Ir(bpy)_3][PF_6]_3$ (1.14 X 10^{-5} M) in butyronitrile exciting at 319 nm and slit width of 5 nm (black trace) and Z-$[Ir(bpy)_3]^{3+}$ (1 complex per 81 supercages), exciting at 319 nm and slit width 5 nm (red trace). Z-$[Ir(bpy)_3]^{3+}$ spectrum above was Savitzky-Golay smoothed (4%) for clarity of presentation only.

Z-$[Ir(bpy)_3]^{3+}$	$[Ir(bpy)_3]^{3+}$	Shift upon entrapment
451 nm	468 nm	17 nm
482 nm	493 nm	11 nm
504 nm	525 nm	21 nm

Table 4.2: Emission maxima of Z-$[Ir(bpy)_3]^{3+}$ on glass slide and $[Ir(bpy)_3][PF_6]_3$ in acetonitrile (+/- 5 nm). Emission maxima extracted from Figure 4.29.

The large blue shift in the emission maxima upon encapsulation is indicative of a tight, sterically hindered fit within the pore structure resulting in impeded vibrational relaxation and hence higher energy transitions and is reflective of rigidochromism observed for such metal complexes at 77 K (Figure 4.29).[34] The extent of the shifts suggests that the bipyridine complexes are more hindered than the terpyridine analogues. This tight fit may also contribute to the lower than expected loadings of the prepared samples, the combination of

the inherent inertness of the iridium coordination sphere towards ligand substitution coupled with the sterically hindered environment makes high yield, tris-ligated preparations of Ir(III) difficult. The degree and extent of the confined environment is discussed in chapter 5.

4.2.2.6 Concentrations effects on the extent of intercage $[Ir(bpy)_3]^{3+}$ interactions

The trend towards enhanced low energy emissions as seen in the Z-$[Ir(tpy)_2]^{3+}$ materials continues with the Z-$[Ir(bpy)_3]^{3+}$ materials. At the higher concentrations of 1:8 Z-$[Ir(bpy)_3]^{3+}$ and 1:18 Z-$[Ir(bpy)_3]^{3+}$ the lowest energy band of the vibrational progression becomes the most prominent band similar to the trend observed for the Z-$[Ir(tpy)_2]^{3+}$ materials. The emission profile for the lower concentrations (1:390 – 1:51 Z-$[Ir(bpy)_3]^{3+}$) is broadly similar, the only exception is 1:51 Z-$[Ir(bpy)_3]^{3+}$, where the intermediate band displays a slightly higher intensity relative to the other maxima.

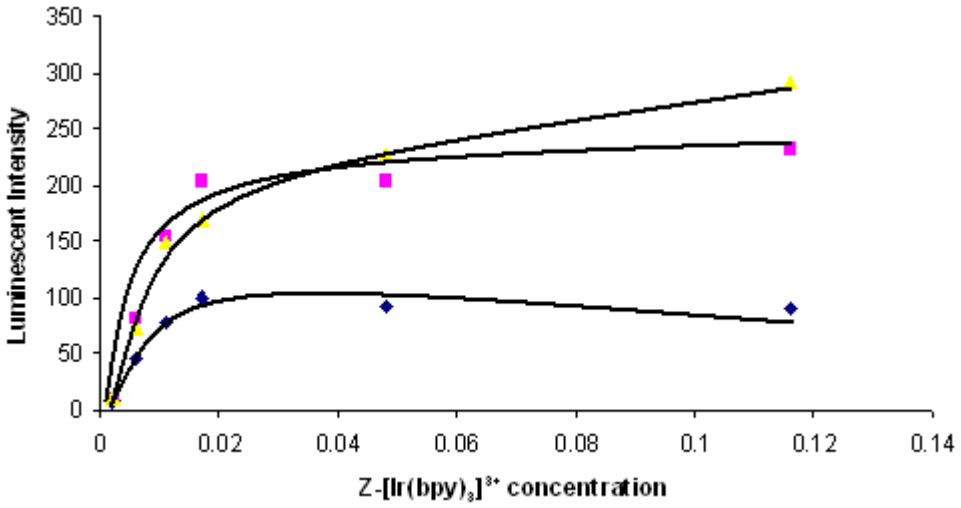

Figure 4.30: Emission intensity at 451 nm (blue dots), 482 nm (purple dots), 504 nm (yellow dots) vs. concentration (mols dm^{-3}). Included trend lines are for clarity of data presentation only.

A plot of the intensity of each band maxima vs. concentration is shown in Figure 4.30. As observed with the Z-$[Ir(tpy)_2]^{3+}$ materials the plots become non-linear after approximately 0.02 M. The relative intensities of the high and

intermediate maxima remain reasonable consistent with increasing complex concentration unlike the Z-$[Ir(tpy)_2]^{3+}$ material, but the low energy component again deviates, and grows in relative intensity with increasing concentration.

In order to confirm that self-absorption was occurring, a dilute $[Ir(bpy)_3][PF_6]_3$ solution (1.6 x 10^{-5} M in acetonitrile) was excited at 454 nm (exciting into the highest energy emission band wavelength) and the emission monitored (Figure 4.31). The solution displayed the same emission profile confirming the large overlap of the absorption and emission spectra.

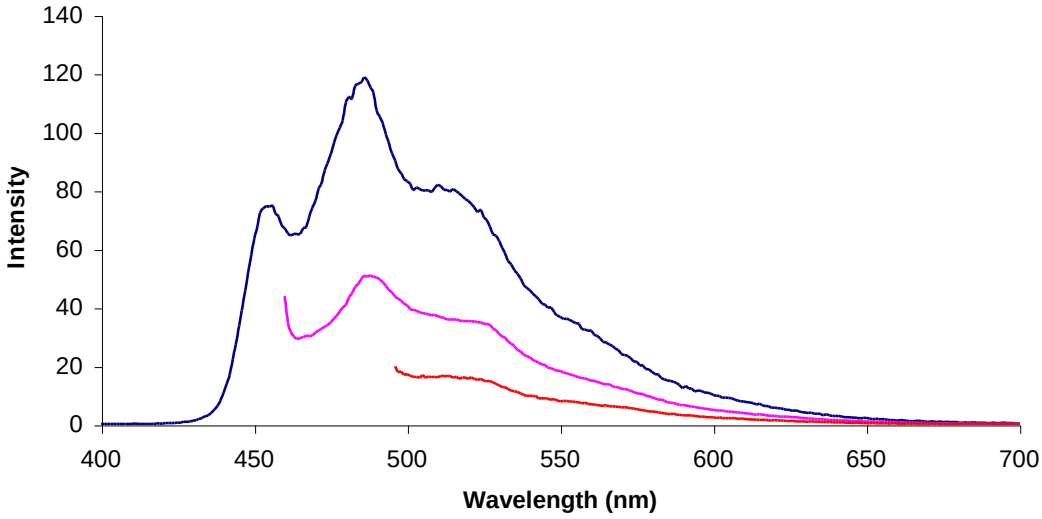

Figure 4.31: Emission spectrum of $[Ir(bpy)_3][PF_6]_3$ (1.6 x 10^{-5} M in acetonitrile) with excitation at 319 nm (blue trace), excitation at 454 nm (magenta trace) and 488 nm (red trace). Slit widths 5 nm for the three experiments.

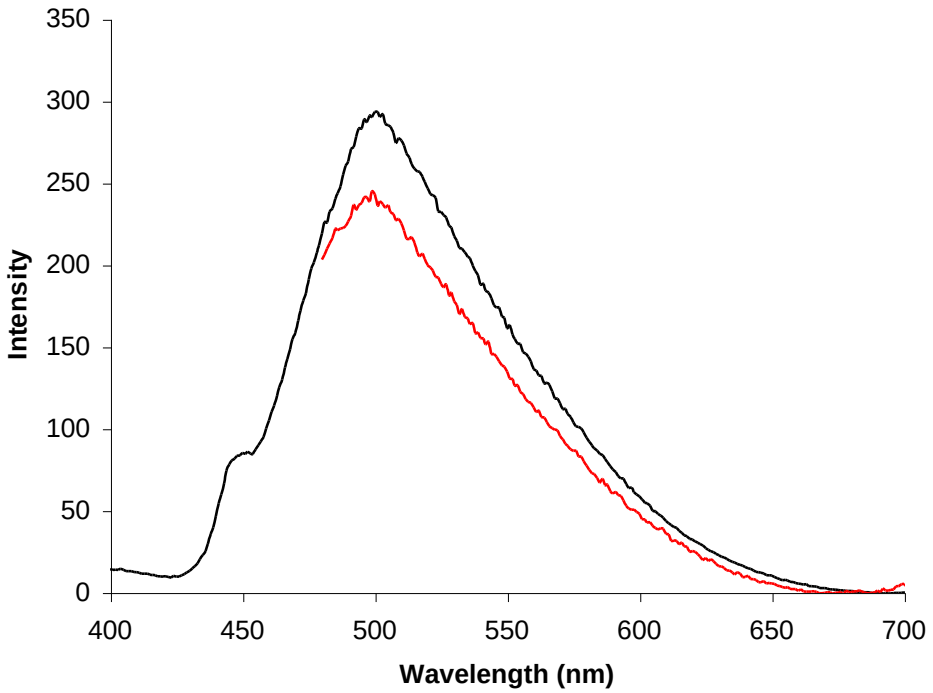

Figure 4.32: Emission spectrum of Z-$[Ir(bpy)_3]^{3+}$ (1:8) excitation at 319 nm (black trace) and emission spectrum of Z-$[Ir(bpy)_3]^{3+}$ (1:8), excitation at 454 nm. Slit width 5 nm for both experiments.

To confirm that self-absorption was operable within the zeolite entrapped materials, Z-$[Ir(bpy)_3]^{3+}$ (1:8) was excited at an emission wavelength (454 nm) and the emssion monitored (Figure 4.32). As expected the structured emission of $[Ir(bpy)_3]^{3+}$ was observed. The self-absorption again explains the observed spectral changes with increasing zeolite concentrations of $[Ir(bpy)_3]^{3+}$. The origin of the self-absorption is tentatively attributed to the same process as outlined in previous section.

4.2.2.7 Aggregation of Iridium polypyridyl complexes

In an attempt to reproduce the spectral changes observed with the zeolite materials containing high complex loadings (Figures 4.15 and 4.28), the solutions $[Ir(tpy)_2][PF_6]_3$ (0.015 M in acetonitrile) and $[Ir(bpy)_3][PF_6]_3$ (0.043 M in acetonitrile) were prepared. Figures 4.33 and 4.35 shows the excitation and emission spectra of the two solutions.

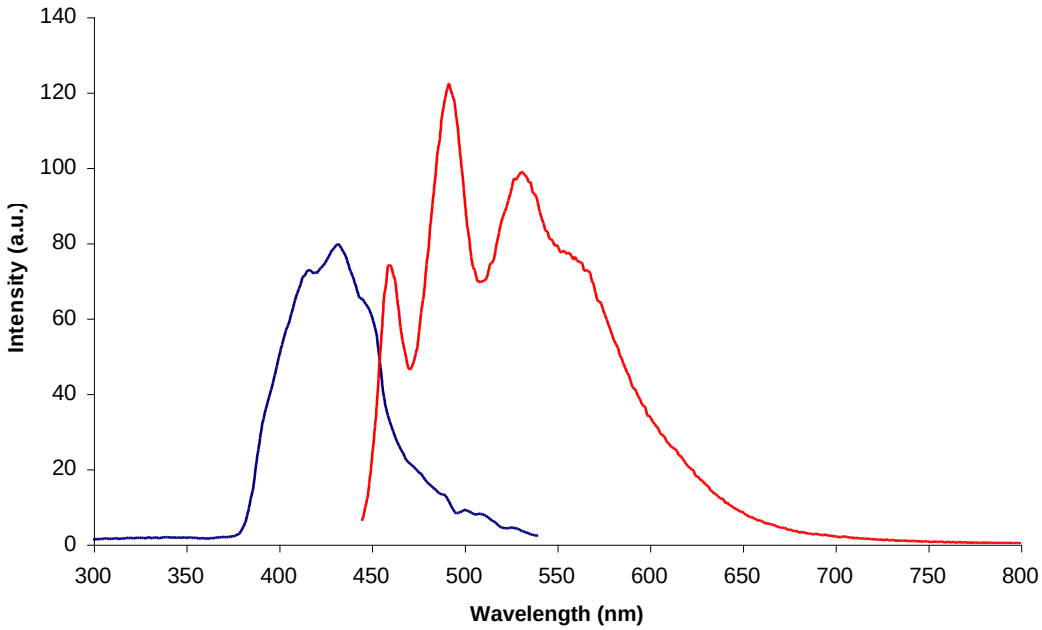

Figure 4.33: Excitation spectrum of $[Ir(tpy)_2][PF_6]_3$ (0.015 M in acetonitrile) monitoring emission at 550 nm (blue trace) and emission spectrum of the same solution, excitation at 432 nm. Slit width 5 nm for both measurements.

It appears in both cases that high concentrations of the complexes result in aggregation of the complexes in acetonitrile and substantial changes in the excitation and emission spectra of both materials. The excitation spectrum of $[Ir(tpy)_2][PF_6]_3$ (3.6×10^{-5} M in acetonitrile) is shown in Figure 4.34 for comparison. The excitation maximum is red-shifted from 319 nm in the dilute sample (3.6×10^{-5} M in acetonitrile) to 434 nm in the concentrated sample (0.015 M in acetonitrile). Such large shifts in excitation maxima are typically associated with complex aggregation.

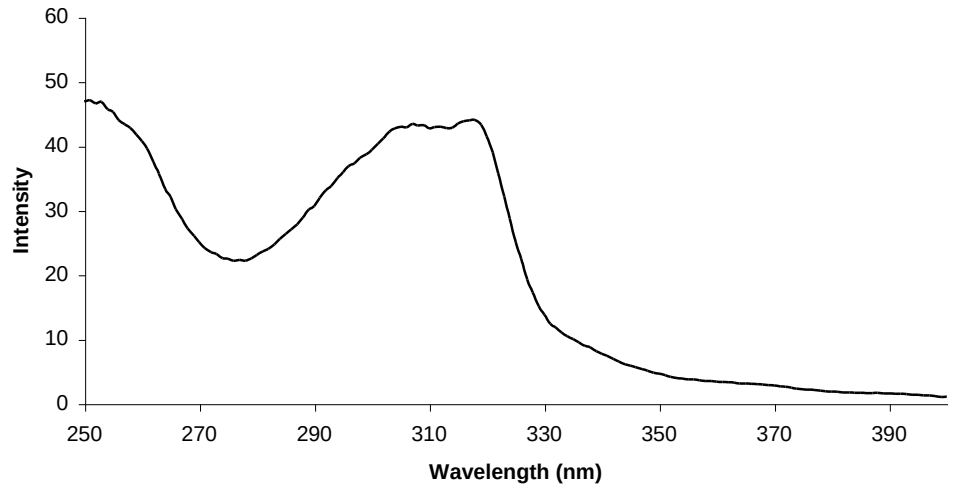

Figure 4.34: Excitation spectrum of $[Ir(tpy)_2][PF_6]_3$ (3.6 x 10^{-5} M in acetonitrile) monitoring the emission at 550 nm. Slit widths 5 nm.

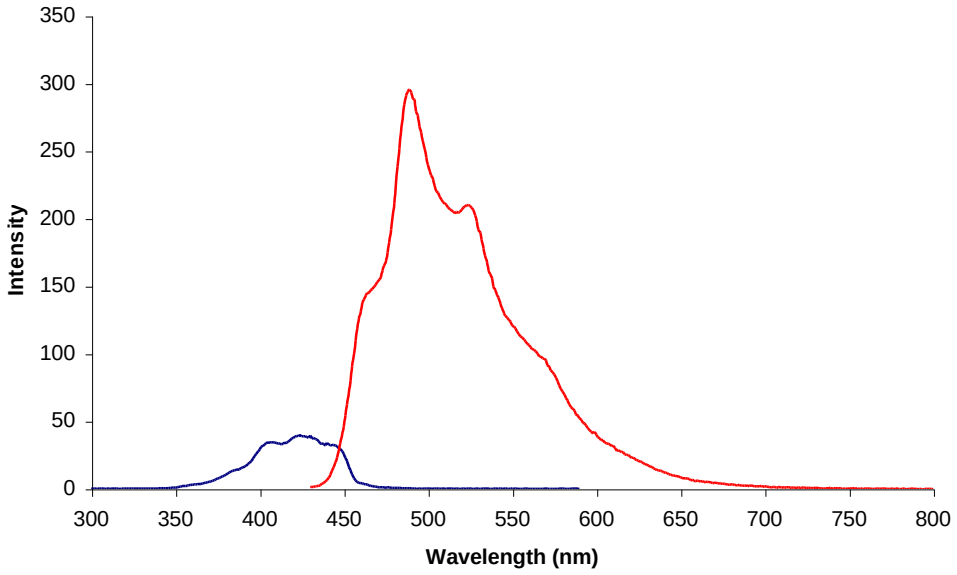

Figure 4.35: Excitation spectrum of $[Ir(bpy)_3][PF_6]_3$ (0.043 M in acetonitrile) monitoring emission at 600 nm (blue trace) and emission spectrum of the same solution, excitation at 424 nm. Slit width 5 nm for both measurements.

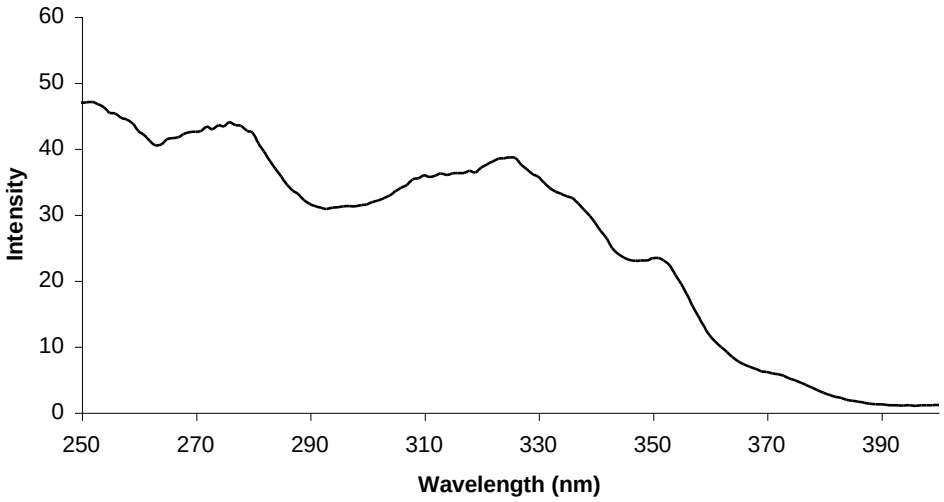

Figure 4.35: Excitation spectrum of $[Ir(bpy)_3][PF_6]_3$ (2.0 x 10^{-5} M in acetonitrile) monitoring the emission at 550 nm. Slit widths 5 nm.

Similar behaviour is observed with the $[Ir(bpy)_3][PF_6]_3$ complex. The excitation maximum of a dilute solution of $[Ir(bpy)_3][PF_6]_3$ (2.0 x 10^{-5} M in acetonitrile) at 328 nm is red-shifted to 430 nm in the concentrated sample (Figure 4.35 and 4.36). Silmilar aggregation behaviour was recently described by Takayasu *et al.* for iridium (III) fac-Tris(2-phenylpyridinato-C^2N) which is the cyclometalled analogue of $[Ir(bpy)_3]^{2+}$ (Figure 4.36).[35]

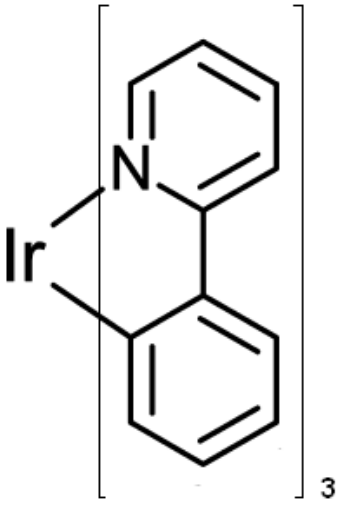

Figure 4.36: iridium (III) fac-Tris(2-phenylpyridinato-C^2N).[35]

4.2.3 Raman Spectroscopy

4.2.3.1 Raman spectroscopy Z-$[Ir(tpy)_2]^{3+}$

Raman spectroscopy of the entrapped complexes was studied in order to glean further information on ground state structural changes accompanying encapsulation. As stated in chapter 3, Raman studies of $[Fe(bpy)_3]^{2+}$ and $[Ru(bpy)_3]^{2+}$ separately encapsulated in zeolite have been reported previously.[36,37] Figure 4.37 shows the Raman spectrum of Z-$[Ir(tpy)_2]^{3+}$ (1:69) and for comparison solid $[Ir(tpy)_2][PF_6]_3$ excited at 633 nm. This excitation wavelength is non-resonant with the ligand-based absorptions. Resonance Raman could not be obtained due to the strong background luminescence of the samples. The noise associated with Raman spectrum for the solid $[Ir(tpy)_2][PF_6]_3$ is due to the very low laser power employed for its measurement as the complex was found to be thermally unstable under intense laser irradiation.

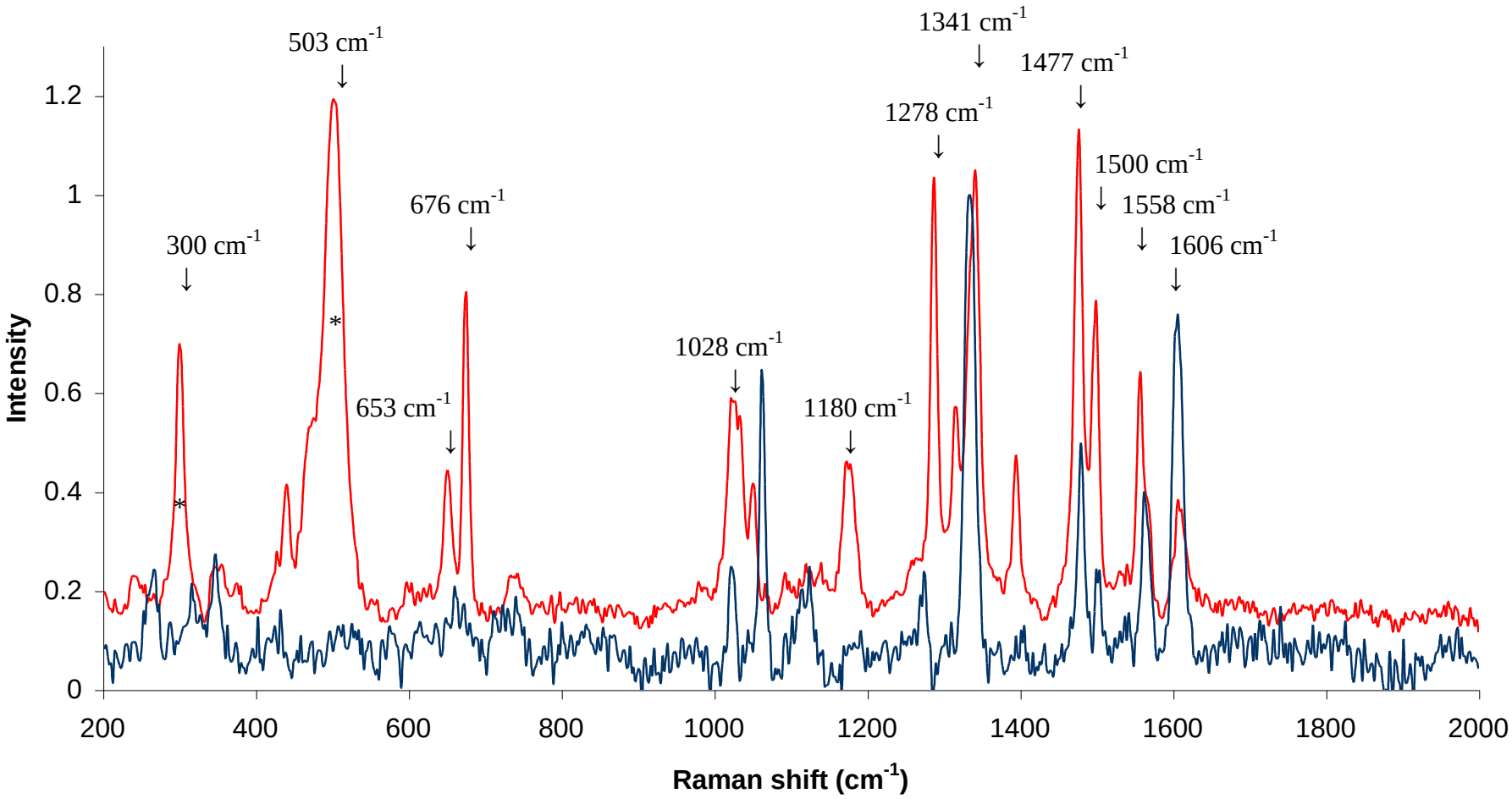

Figure 4.37: Raman Spectroscopy of Z-$[Ir(tpy)_2]^{3+}$ (1:69) powder excited at 633 nm (red upper trace) and solid $[Ir(tpy)_2][PF_6]_3$ excited at 633 nm (blue lower trace). * Indicates zeolite modes

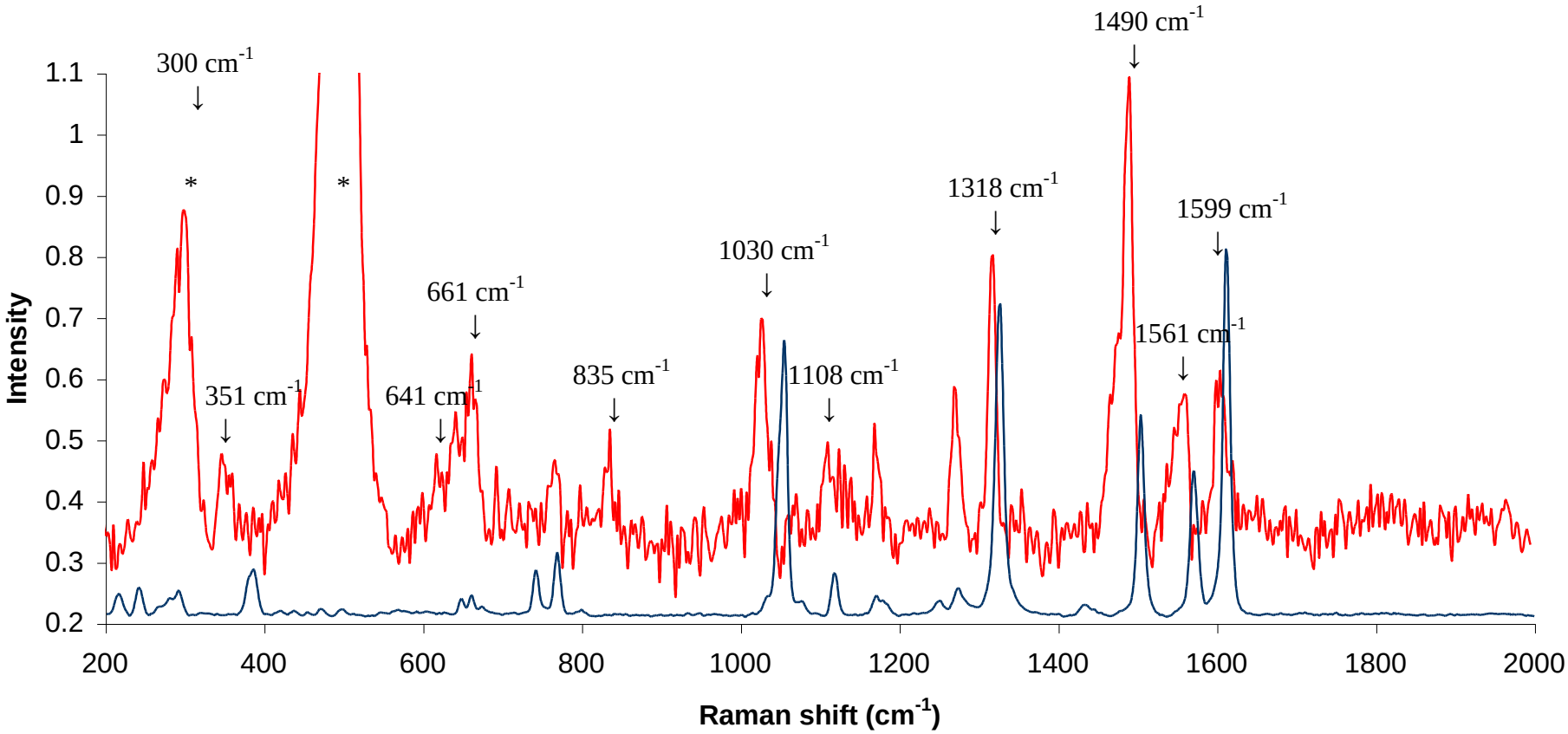

Figure 4.38: Raman Spectroscopy of Z-$[Ir(bpy)_3]^{3+}$ (1:390) powder excited at 688 nm (grey red trace) and solid $[Ir(bpy)_3][PF_6]_3$ excited at 633 nm (blue lower trace). * Indicates zeolite modes

Examination of the two spectra reveals the same trends as observed for the previously studied zeolite entrapped complexes, mainly broadening of the Raman features of the complex within the zeolite due to the local heterogeneous microenvironment and blue shifts towards higher vibrational frequencies for many of the modes of the entrapped complex compared to the solid material. Unexpectedly, certain modes of the solid $[Ir(tpy)_2][PF_6]_3$ were actually blue shifted with respect to the zeolite material, a phenomenon not previously observed with transition metal polypyridyl complexes entrapped within zeolite materials. This is unusual as vibrational frequencies are typically higher in zeolite due to the sterically hindered internal environment restricting bond elongation.

Burger *et al.*[38] and Jenson *et al.*[39,40] previously carried out solution phase structural studies on $[Ir(tpy)_2][ClO_4]_3$ and $[Ru(tpy)_2][PF_6]_2$ respectively. These studies were exploited for the band assignments presented here. The intense peaks at 300 cm^{-1} and 503 cm^{-1} are zeolite based modes and are assigned to bending modes of either Si-O-Si or Al-O-Al.[41,42,43] Assignments of individual bands for the iridium complexes is more difficult than the previous complexes studied as the excitation laser is off resonance which increases the complexity of the spectra. The band observed at 347 cm^{-1} with the solid complex is associated with Ir-N stretching and appears broadened with the zeolite samples. It is difficult to determine the extent of any shift in this peak compared to the solid. The ring deformation mode associated with the middle tpy ring undergoes a modest blue shift from 673 cm^{-1} to 676 cm^{-1} upon encapsulation, not indicative of any large degree of distortion. The ring stretch at 1024 cm^{-1} is blue shifted 4 cm^{-1} after entrapment. The intense mode observed at 1180 cm^{-1} for the zeolite-entrapped species is very weak in the corresponding solid material and is associated with C-H bends. The peak at 1334 cm^{-1} is blue shifted to 1341 cm^{-1} upon encapsulation and is attributed to ring stretches for the non-central pyridine rings. The modes at 1479 cm^{-1}, 1504 cm^{-1}, and 1562 cm^{-1} are red shifted in the zeolite material to 1477 cm^{-1}, 1500 cm^{-1}, and 1558 cm^{-1} with the peak at 1606 cm^{-1} remaining unchanged.

All of the above shifts relate to CC ring stretches modes. The source of these red shifts is unclear considering the confined environment within the zeolite interior, but indicates that the intrazeolite environment affects the peripheral ligands. A red shift in a Raman mode implies bond lengthening that is generally unexpected in zeolite guest molecules. However as shown in chapter 5, the iridium polypyridyl complexes appear to be more mobile and less hindered within the pore structure than their ruthenium analogues, which may explain this behaviour.

4.2.3.2 Raman spectroscopy Z-$[Ir(bpy)_3]^{3+}$

Figure 4.38 shows the Raman spectrum of Z-$[Ir(bpy)_3]^{3+}$ (1:69) and solid $[Ir(bpy)_3][PF_6]_3$ excited at 633 nm. As for the previous sample the laser excitation wavelength is off resonance. The low concentration sample was selected due to the strong background luminescence signal from the concentrated materials. Comparison of the two spectra reveals a trend towards lower energy vibrations with quite dramatic red shifts observed for some modes when encapsulated within the zeolite matrix compared to the solid complex. Strommen *et al.* previously carried out solution phase structural studies on $[Ru(bpy)_3]^{2+}$.[44] This study is exploited for the band assignments presented here. Similar to the previous sample the zeolite the intense Si-O-Si bands are observed at 300 cm^{-1} and 503 cm^{-1}. These can be used as an internal standard as they do shift from sample to sample. The band observed at 389 cm^{-1} with the solid complex is associated with Ir-N stretching vibrations and is substantially red-shifted 38 cm^{-1} to 351 cm^{-1} after encapsulation. This implies large changes in the iridium-bipyridine bond length upon entrapment. This trend towards lower energy transitions is repeated across the Raman spectrum. The CCC bending modes observed at 655 cm^{-1} and 666 cm^{-1} in the solid are red shifted 14 cm^{-1} and 5 cm^{-1} to 641 cm^{-1} and 661 cm^{-1} in the zeolite material. These modes are also associated with Ir-N stretching vibrations but to a lesser extent than the 389 cm^{-1} band. A new band is observed at 835 cm^{-1} with the zeolite sample and is likely associated with peripheral C-C stretching vibrations. The most dramatic shift is at 1055 cm^{-1} for the solid material, shifting to 1030 cm^{-1} after encapsulation.

This band is assigned to C-C stretching vibrations prodominantly located at the 4 and 5 positions (Figure 4.39), indicative of changes in the local environment of the outer portion of the ligand. The CCH bend at 1122 cm^{-1} for the solid is red shifted 14 cm^{-1} to 1122 cm^{-1} in zeolite, again a dramatic decrease in energy upon encarceration of the complex. Red shifts to stretching vibrations are not just confined to the periphery of the ligand. A 7 cm^{-1} red shift in band at 1278 cm^{-1} in the solid to 1271 cm^{-1} in the zeolite is strongly associated with C_2-N stretching vibrations.

The ring stretch C-C at 1327 cm^{-1} in the solid is associated with the two carbons bridging the two pyridyl rings. This is red shifted 11 cm^{-1} to 1316 cm^{-1} within the zeolite. It is also interesting to note the large red shift at 1504 cm^{-1} in solid to 1490 cm^{-1} within zeolite. This band is assigned to ring stretches at the five and six positions of the bipyridine ring, so based on this and the observed stretch at 1327 cm^{-1} noted above, there appears to be substantial distortion down this axis. The bands at 1504 cm^{-1}, 1571 cm^{-1} and 1613 cm^{-1} are red shifted 14 cm^{-1}, 10 cm^{-1}, and 14 cm^{-1} to 1490 cm^{-1} 1561 cm^{-1} and 1599 cm^{-1} in the zeolite material. These are all attributed to predominantly C-C stretching vibrations on the outer bipyridine carbons. Similar to the iridium bis-terpyridine, the majority of bands are red shifted upon inclusion and is attributed to the same relatively unhindered fit of the complex within zeolite Y compared to ruthenium polypyridyl analogues.

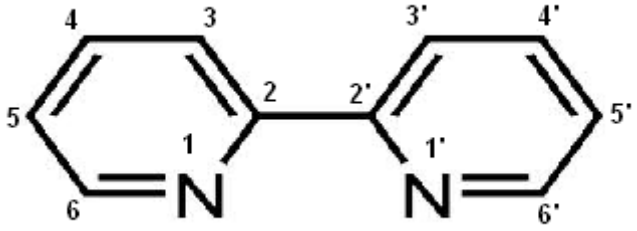

Figure 4.39: Numbering system for 2,2'-bipyridine used for Raman assignments.

4.2.4 Excited state lifetimes of zeolite entrapped Iridium complexes

The lifetimes of zeolite entrapped species are shown in tables 4.3 and 4.4.

4.2.4.1 Excited state lifetimes of Z-$[Ir(tpy)_2]^{3+}$

The apparent lifetimes of the Z-$[Ir(tpy)_2]^{3+}$ materials increase with increasing concentration of complex within the zeolite. This is not unexpected considering the self-absorption observed in the emission spectroscopic measurements. Self-absorption becomes more prevalent at higher concentrations and this is demonstrated with the fitted lifetime decays of the material. For the all but the two lowest concentrations of $[Ir(tpy)_2]^{3+}$ loaded material a three exponential decay was required to fit the experimental data. The short lifetime component (4 ns – 5 ns) is comparable to the instrument response function (IRF) recorded using LUDOX colloidal solution and is therefore attributed to scatter. The lifetime measurements were complicated by the large amount of scattering associated with the measurement of zeolite suspensions. This was mitigated somewhat by carrying out acquisitions using a high numbers of counts. Even with counts as high as 50,000, the errors associated with the decays were relatively large (up to 11 %), but unfortunately could not be improved upon but should not interfere with the conclusions drawn from the data.

There appears to be two broad categories associated with the lifetimes of the $[Ir(tpy)_2]^{3+}$ materials (Table 4.4). For the two lowest concentrations of Z-$[Ir(tpy)_2]^{3+}$ at 0.016 M and 0.018 M, single lifetimes of 1080 ns ± 95 and 1042 ns ± 109 were recorded. They represent a loading of 1 $[Ir(tpy)_2]^{3+}$ per 47 and 57 supercages. The lifetime of $[Ir(tpy)_2][PF_6]_3$ found to be 374 ns +/- 19 ns in aerated acetonitrile, so it seems that upon encapsulation the lifetimes are comparable to those found for degassed acetonitrile (1.2 μs)[18] at the lower concentrations of zeolite loading even under the aerated conditions of the dmso suspension. The remainder of the lifetimes required a three exponential fit, yielding two lifetimes, the third being attributed to scatter as stated earlier. These lifetimes within experimental error are the same ~2330 ns. There is

also a second shorter lifetime of 334 ns presentating around 10 % of the overall decay. Again this is the same value within experimental error for all the short compoments with exception of the 0.126 M Z-$[Ir(tpy)_2]^{3+}$ sample which has a shorter 206 ns lifetime. These longer lifetimes are attributed to a self-absorption process whereby emitted photons are reabsorbed and subsequently emitted etc. resulting in *apparently* longer lifetimes when in fact both K_r and K_{nr} have remained unchanged. This process is not commonly observed with transition metal complexes but is observed with organic dyes and dye loaded zeolite-L.[29,45]

What is unclear is the origin of the shorter 330 ns lifetime at the higher concentrations of complex. It seems unlikely to be due to adjacent cage interactions, as the % lifetime contribution of the component remains low in spite of concentrations that would guarantee a large degree of adjacent cage occupation. For example at the concentrations of Z-$[Ir(tpy)_2]^{3+}$ of 0.178 M, 0.126 M and 0.029 M it means that 59 %, 46 % and 13 % of the $[Ir(tpy)_2]^{3+}$ complexes are expected to be adjacent to another $[Ir(tpy)_2]^{3+}$ complex at each concentration respectively. Since the short lifetime remains invariant with concentration (at the four higher concentrations), it is likely associated with the self-absorption process.

4.2.4.2 Excited state lifetimes of Z-$[Ir(bpy)_3]^{3+}$

All the decays were fit to biexponential decay kinetics, with one lifetime being attributed to scatter as described for Z-$[Ir(tpy)_2]^{3+}$ (Table 4.5). The observed lifetime is also considerably longer than the 345 ns +/- 11 ns we observed in aerated acetonitrile. The lifetimes of Z-$[Ir(bpy)_3]^{3+}$ were found to remain mainly static with increasing concentration of complex. At the four lowest loadings of Z-$[Ir(bpy)_3]^{3+}$, the excited state lifetimes are, within experimental error the same. The two higher concentrations of Z-$[Ir(bpy)_3]^{3+}$ (0.048 M and 0.116 M) were also found to have the same excited state lifetime within experimental error. The decrease in the lifetime at the two highest concentrations may be indicative of adjacent cage interactions, since the change only becomes apparent at relatively high complex concentrations, implying a far greater

chance that an $[Ir(bpy)_3]^{3+}$ complex is adjacent to another $[Ir(bpy)_3]^{3+}$, as shown in table 4.3. The likelihood of the two higher concentration samples even having two or more adjacent cages occupied is also substantially greater than the other samples. However, adjacent cage interactions would be expected to yield at least two lifetimes across the entire range of concentrations as observed in the previous chapter whereas the Z-$[Ir(bpy)_3]^{3+}$ decays were all fit by a double exponential model which yielded one excited state lifetime (the second being scatter). The source of the concentration dependence of the decay remains as yet unclear.

Conc. $[Ir(bpy)_3]^{3+}$	% of adjacent cages occupied by another $[Ir(bpy)_3]^{3+}$
0.116	41
0.048	20
0.017	8
0.011	5
0.006	3
0.002	1

Table 4.3: % of $[Ir(bpy)_3]^{3+}$ complexes which are adjacent to at least one other $[Ir(bpy)_3]^{3+}$ complex.

Conc $[Ir(tpy)_2]^{3+}$ (Mol dm^{-3})[a]	τ_1/ns	A[b]	τ_2/ns	B[b]	τ_2/ns	C[b]
0.178	2313 ± 113	87	339 ± 54	12	4	1
0.126	2316 ± 85	81	206 ± 41	13	4	6
0.029	2389 ± 77	90	334 ± 43	9	5	1
0.025	2356 ± 102	90	326 ± 38	9	5	1
0.018	1042 ± 109	96	4 ± 1	4	-	-
0.016	1080 ± 95	95	13 ± 2	6	-	-

Table 4.4: [a]Concentration of co-encapsulated $[Ir(tpy)_2]^{3+}$ within zeolite Y. [b]Percent contribution of each individual lifetime decay fit to the appropriate exponential model. Lifetimes were recorded as a suspension in dimethyl sulphoxide (aerated). All lifetime decay fits had X^2 values between 1 and 1.3.

Conc $[Ir(bpy)_3]^{3+}$ (Mol dm^{-3})[a]	τ_1/ns	A[b]	τ_2/ns	B[b]
0.116	747 ± 43	98	9	2
0.048	894 ± 89	98	12	2
0.017	1037 ± 79	98	15	2
0.011	1110 ± 85	75	8	25
0.006	1132 ± 93	99	5	1
0.002	1290 ± 63	100	-	-

Table 4.5: [a]Concentration of co-encapsulated $[Ir(bpy)_3]^{3+}$ within zeolite Y. [b]Percent contribution of each individual lifetime decay fit to the appropriate exponential model. Lifetimes were recorded as a suspension in dimethyl sulphoxide (aerated). All lifetime decay fits had X^2 values between 1 and 1.3.

4.3 Conclusions

For the first time both $[Ir(tpy)_2]^{3+}$ and $[Ir(bpy)_3]^{3+}$ were successfully entrapped within the pore structure of zeolite-Y. It was found that both complexes were formed in low yields due to the inertness of the Ir (III) ion coupled with the sterically hindered intra-pore environment.

The Z-$[Ir(tpy)_2]^{3+}$ luminescence spectrum was moderately blue shifted compared to the solution phase complex reflective of the polar zeolite interior. The effect of increasing concentration of the complex was also studied in order to ascertain the extent of interpore interactions. It was found that the complex undergoes self-absorption, with substantial distortion of the luminescence spectra at the highest concentration as well as an increase in the apparent lifetime of the material. The lack of significant shifts in the emission maxima with increased loading suggests little or no inter-cage interactions even at the highest concentrations.

The Z-$[Ir(bpy)_3]^{3+}$ luminescence spectrum was substantially altered after zeolite entrapment. Blue shifts of up to 21 nm were observed indicative of a sterically confined polar environment. The effect of increasing concentration of the complex within the zeolite was also examined. This material also displayed strong self-absorption but without any increase in the apparent lifetime of the material. The lifetimes displayed a modest drop at the highest loadings of complex, which may be due to adjacent complexes but the overall nature of any interaction is as yet unclear.

Raman spectroscopy of both materials also confirmed zeolite encarceration, with substantial changes to the spectra noted for both complexes after zeolite entrapment. It was found that many of the modes associated with the outer portion of the polyimine rings were shifted or had disappeared completely, further demonstrating interactions of the complexes with the zeolite framework.

4.4 References

[1] Flamigni, L.; Barbieri,. A.; Sabatini, C.; Ventura, B.; Barigelletti, F. *Top Curr. Chem*. **2007**, 281, 143.

[2] Wunschel, K.R. Ohnesorge, W.E. *J.am .Chem. Soc.* **1967,** *89*, 2777.

[3] Sullivan, B.P.; Meyer, T.J. *J. Chem. Soc., Chem. Commun.* **1984,** 403.

[4] Williams, J.A.G.; Wilkinson, A.J.; Whittle, V.L. *Dalton Trans.*, **2008**, 2081.

[5] DeRosa, M.C.; Hodgson, D.J.; Enright, G.D.; Dawson, B.; Evans, C.E.B.; Crutchley, R.J. *J. Am. Chem. Soc.* **2004**, *126*, 7619.

[6] Xiong, Y.; Ye, Z.; Xu, J.;Zhu, Y.;Chen, C.; Guan Y. *Analyst*, **2013**, *138*, 1819.

[7] Ulbricht, C.; Beyer, B.; Friebe, C.; Winter, A.; Schubert, U.S. *Adv. Mater.* **2009**, *21*, 4418 and references therein.

[8] Collin, J.-P.; Dixon, I. M.; Sauvage, J.-P.; Williams, J. A. G.; Barigelletti, F.; Flamigni, L. *J. Am. Chem. Soc.* **1999**, *121*, 5009.

[9] Leslie, W.; Batsanov, A. S.; Howard, J. A. K.; Williams, J. A. G. *Dalton Trans.* **2004**, 623.

[10] Flamigni, L.; Ventura, B.; Barigelletti, F.; Baranoff, E.; Collin, J.P.; Sauvage, J.P. *Eur. J. Inorg. Chem.* **2005**, 1312.

[11] Ayala, N. P.; Flynn, C.M.; Sacksteder, L.; Demas J.N.; DeGraff, B. A. *J. Am. Chem. Soc.* **1990**, *112*, 3837.

[12] Leslie, W.; Batsanov, J.A.; Howard, K.; Williams, J.A.G. *Dalton Trans.* **2004**, *4*, 623.

[13] Dixon, I.M.; Collin, J.-P.; Sauvage, J.-P.; Flamigni, L.; Encinas, S.; Barigelletti,F. *Chem. Soc. Rev.,* **2000** , *29*, 385 and references therein.

[14] Martin, B.; Waind, G.M. *J. Chem. Soc.*, **1958**, 4282.

[15] Flynn, C. M. Demas, Jr.; Demas, J. N. *J. Am. Chem. Soc.*, **1974**, *96*, 1959.

[16] Sullivan, B. P.; Meyer, T.J. *J. Chem. Soc. Chem. Commun.*, **1984**, 403.

[17] R. J. Watts, *Comments Inorg. Chem.* **1991**, *11*, 303.

[18] Demas, J. N.; Harris, E. W.; Flynn, C. M. Jr.; Diemente, D. *J. Am.*

Chem. Soc., **1975**, *97*, 3838.

[19] Wittmann, H.F.; Friend R.H.; Khan, M.S.; Lewis, J. *J. Chem. Phys.* **1994**, *101*, 2693.

[20] Marin, V.; Holder, E.; Hoogenboom, R.; Schubert, U.S. *Chem. Soc. Rev.*, **2007**, *36*, 618 and references therein.

[21] Rothe, C.; King, S.; Monkman, A. *Nat. Mater.* **2006**, *5*, 463.

[22] Kawi, S.; Gates, B.C. *J. Phys. Chem.* **1995**, *99*, 8824.

[23] Li, F.; Gates, B.C. *J. Phys. Chem. B*. **2004**, *108*, 11259.

[24] Xu, C.; Mochizuki, D.; Hashimoto, Y.; Honda, T.; Tsukahara, Y.; Yamauchi, T.; Wada, Y. *Eur. J. Inorg.* **2012**, 3113.

[25] Xu, Y.; Langford, C.H. *J. Phys. Chem. B.* **1997**, *101*, 3115.

[26] Breck, D. W. *Zeolite Molecular Sieves: Structure Chemistry and Use*; John Wiley and sons: New York, **1974**.

[27] Weitcamp, J.; Karge, H. G.; Pfeifer, H.; Holderich, W. Eds. *Zeolites and Related Materials*: State of the Art; Elsevier: Amsterdam, **1994**.

[28] Gagliardi,L.G.; Castells ,C.B.; Ràfols, C. Rosés,M.; Bosch, E. *J. Chem. Eng. Data* **2007**, *52*, 1103.

[29] Dhami, S.; De Mello, A.J.; Rumbles, G.; Bishop, S.M.; Philips, D.; Beeby, A. Photochem. Photobio, **1995**, *61* , 341.

[30] Hammond, P.R. *J. Chem. Phys.* **1979**, *70*, 3884.

[31] Decurtins,S.; Felix, F. Ferguson, J.; Güdel, H.U.; Ludila, A. *J. Am. Chem. Soc.* **1980**, *102*, 4102.

[32] Montalti, M.; Credi, A.;Prodi, L.; Gandolfi, M.T. Handbook of Photochemistry, CRC Press, Boca Ration, FL, **2006**.

[33] Goodman, B. A.; Raynor, J. B. *Adv. Inorg. Chem. Radiochem.* **1970**, *13*, 192. (b) Hill, N. J. *J. Chem. Soc., Faraday Trans.* **1972**, *68*, 427.

[34] Krausz, E. Higgins, J. Riesen, H. *Inorg. Chem.* **1993**, *32,* 4053.

[35] Takayasu, S.; Suzuki, T.; Shinozaki, K. *J. Phys. Chem. B* **2013**, *117*, 9449.

[36] Incavo, J. A.; Dutta, P. K. *J. Phys.Chem.* **1990**, *94*, 3075.

[37] Dutta, P. K.; Incavo, J. A. *J. Phys.Chem.* **1987**, *91*, 4443.

[38] Burger, K.; Wagner, F.E.; Vértes, A; Bencze, É.; Mink, J.; Labádi, I.; Nemes-Vetéssy, Z.S. *J. Phys. Chem. Solids* **2001**, *62*, 2059.

[39] Jensen, P. W.; Jørgensen, L. B. *J. Mol. Struct.* **1982**, *79*, 87.

[40] Hansen, P. W.; Jensen, P. W. *Spectrochim.Acta Part A* **1994**, *50*, 169.

[41] Yu, Y; Xiong, G.; Li, C.; Xiao, F.S. *Microporous Mesoporous Mater.* **2001**, *46*, 23.

[42] Dutta, P.K.; Shieh, D.C.; Puri, M. *J. Phys. Chem.* **1987**, *91*, 2332.

[43] Dutta, P.K.; Shieh, D.C. *J. Phys. Chem.* **1986**, *90*, 2331.

[44] Strommen, D.P.; Mallick, P.K.; Danzer, G.D.; Lumpkin, R.S.; Kincaid, J.R. *J. Phys. Chem.* **1990**, *94,* 1357.

[45] Devaux, A.; Calzaferri, G.; Miletto, I. Cao, P.; Belser, P.; Brühwiler, D. Khorev, O.; Häner, R.; Kunzmann, A *J. Phys. Chem. C* **2013**, *117*, 23034.

Chapter 5

Huang-Rhys analysis of the Effect of Zeolite-Y confinement on the excited state Structure of selected ruthenium and iridium polypyridyl complexes

5.0 Introduction

As outlined in previous chapters there is strong evidence for the distortion of octahedral iridium and ruthenium polypyridyl complexes encapsulated in zeolite systems from spectroscopic data presented here and this also been considered in theoretical calculations.[1]

In order to better understand the extent of the imposed distortion in molecular structure upon ship in a bottle introduced guest molecules within the tightly confined zeolite structure, this chapter looks to quantify the degree of distortion. Franck-Condon analysis of emission profiles yields parameters related to the nuclear displacement of excited state molecules. The most important of these is the Huang-Rhys value, which allows for comparison of geometric distortion between ground and excited state along bonds important in relaxation between different steric environments.[2]

The potential sources of geometric distortion in the ligand environment when octahedral complexes are included in zeolite matrices, are two fold; firstly the sterically restrictive inter-pore environment and secondly interaction of guest molecules with the anionic framework wall resulting in distortion due to electrostatic rather than steric effects. It is primarily the former parameter this chapter will explore, but some reference to the later is important to explain some of the changes to the complexes emissive properties observed.

A dramatic example of excited state distortion by zeolite-Y on the photophysics of a transition metal luminophore is the comparison between solution phase non-emissive species $[Ru(tpy)_2]^{2+}$ and its zeolite entrapped analogue (where tpy is 2,2';6',2''-terpyridine).[3] The complex emits strongly at room temperature when encapsulated within the pores of zeolite-Y, yielding an increase in excited state lifetime from 250 ps to 140 ns but is practically non-emissive in solution at room temperature. This effect was attributed to destabilisation of the ligand field state that previously led to efficient excited

state thermal deactivation. The destabilisation was caused by the restricted intra-pore configuration the species encounters.

The aim of this chapter is to establish the extent of excited state distortion of various entrapped Iridium and ruthenium polypyridyl complexes, in order to better understand the zeolite-Y intra-pore environment and its effect on large guest molecules. In understanding the influence of the zeolite environment on the ground and excited state geometries of encapsulated guests we should be able to better control the luminescent properties of such guests and tune their properties in for example, sensing or photovoltaics applications.

5.0.1 Excited state distortion of complexes

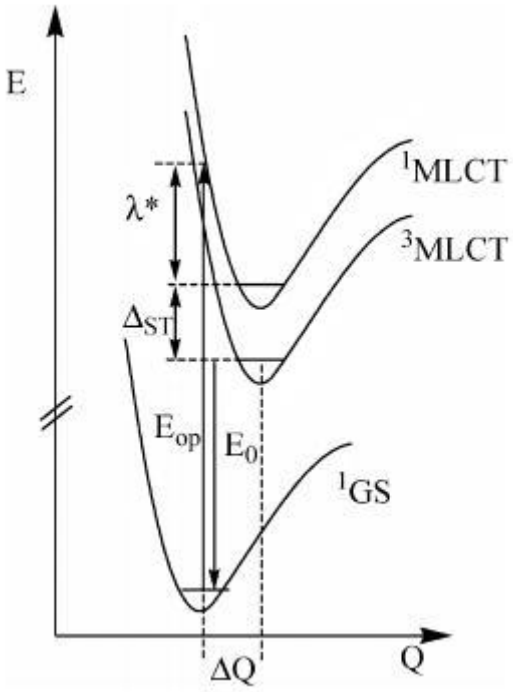

Figure 5.1: Potential energy surfaces for ground state, singlet and triplet excited state processes (McClure *et al. J. Am. Chem. Soc.*, **2010**, *132*, 5428).[4]

Before discussing the calculation of the Huang-Rhys factor, Figure 5.1 needs to be considered.

In principle, the full width half maximum (fwhm) of a given single absorption band in the absence of inhomogeneous broadening is proportional to the degree of nuclear displacement between the ground state molecule and the initially formed singlet excited state.[4] This displacement is represented in Figure 5.1 by the quantity ΔQ. The value λ* is the re-organisational energy, that is the energy required to attain the new excited state nuclear equilibrium configuration and includes contributions from solvent, intra-ligand and ligand-metal interactions. The re-organisational value is proportional to the fwhm squared.[4] The spin state-triplet state energy difference is denoted by ΔST and the optical absorption energy required for electron promotion to singlet excited state is labelled $E_{op.}$ The zero-zero energy is $E_{0,}$ the difference between the absorption energy and the zero point energy is a good indicator of the degree of distortion between ground and excited state geometry a species undergoes.

5.0.2 Vibrational overlap and excited state distortion

A molecule that undergoes an electronic transition, has available new vibrational degrees of freedom as a result of the new distribution of charge associated with the transition. The width of absorption bands can be related the vibrational structure of the molecule undergoing the transition.[5] The vibrational structure of an electronic transition can be understood by consideration of the Franck-Condon principle:

'Because nuclei being much more massive than electrons, electronic transitions take place much faster then nuclei can respond.'[5]

The physical significance of this statement is that electronic transitions between energy levels occur with effectively stationary nuclei. Electron charge accumulates during a transition and the equilibrium position of the nuclei change by vibration to a new equilibrium position, typically at a greater equilibrium distance. This is due to excited state molecules typically possessing more anti-bonding character compared to the ground state leading to longer bond lengths. The initial inter-nuclear separation is similar

for the ground and excited state molecules and represents a turning point for the nuclei, in effect they are stationary (Figures 5.2 and 5.3). This can be considered in terms of the classical pendulum model. If it swings about an equilibrium point r_0 (Figure 5.2), its velocity decreases to zero only at the turning points during its cycle, therefore, the pendulum probability of residing at these turning points is greatest and hence the larger area of the associated vibrational wavefunction at this particular inter-nuclear separation and increased overlap between initial and final states. Figure 5.2 shows these vibrational wavefunctions of a polyatomic molecule, with the associated increase in wavefunction area at the turning points.

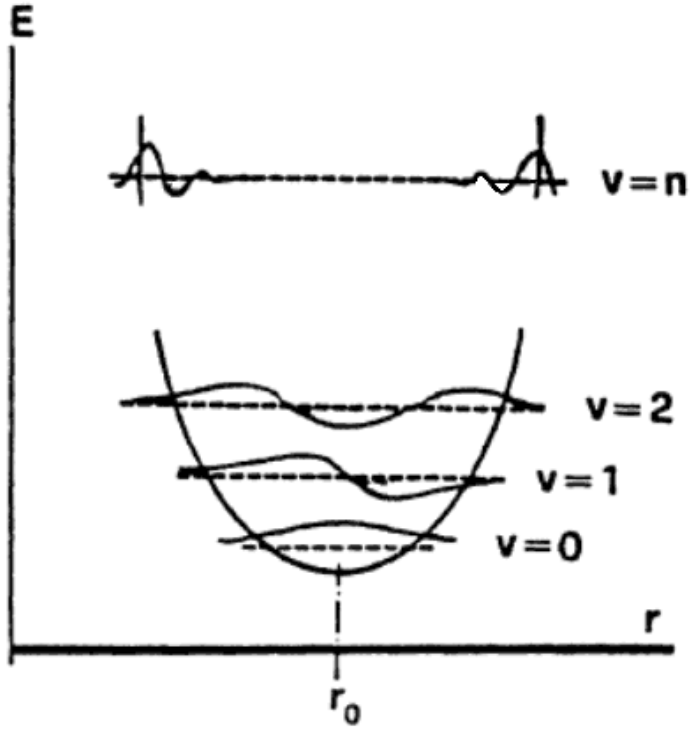

Figure 5.2: Vibrational wavefunctions of a diatomic molecule (Suppan, P. *Chemistry and Light;* Royal Society of Chemisty, 1994).[6]

Figure 5.3 demonstrates coupling of ground and excited state vibrational wavefunctions. Line A represents a transition from the lowest energy level of the ground state molecule to that of an upper vibrational energy levels of the first excited electronic state. Line B shows the vibrational coupling of an upper excited state with a lower vibrational wavefunction. The vibrational wavefunctions for some representative v_n states are shown and ΔQ is the

nuclear displacement. It is clear from diagram B that further displacement of the upper excited state potential energy surface would result in increased vibrational coupling between the upper 0-0 state and a new lower state energy level.

Non-radiative electronic transitions occur most efficiently between vibrational wavefunctions that most closely resemble the originating vibrational wavefunction. Figure 5.3 below gives a more realistic representation of upper vibrational wavefunctions. The extent of vibronic coupling between two potential energy surfaces can be estimated by the Huang-Rhys factor, which is discussed below.

When considering excited state distortion of MLCT states it is useful to consider the nature of the distortion. A MLCT transition involves a transfer of an electron from a metals d orbital to an anti-bonding orbital of an appended ligand. Changes in the ligand environment can influence the energetics of unoccupied orbitals and hence have an impact on the overall excited state properties of a molecule.[7]

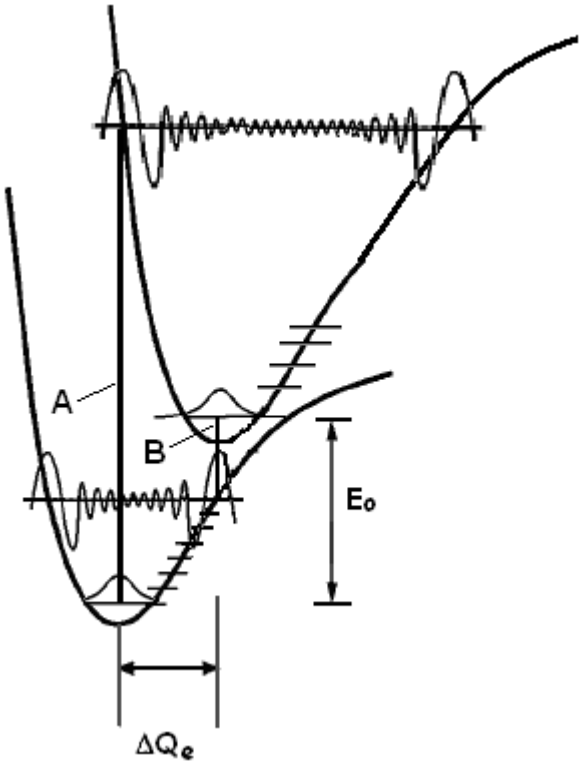

Figure 5.3: Graphical representation of two potential energy surfaces and examples of associated vibrational wave functions for each surface (Damrauer *et al.*, *J. Am. Chem. Soc.* **1997**, *119,* 8253).[7] The quantities ΔQ_e is the relative nuclear displacement between states and E_0 is the energy gap.

5.0.3 Huang-Rhys analysis of emission spectra

The degree of excited state distortion can be approximated by examination of the emission spectra of the complex. The emission spectrum, most typically for metal complexes, are collected at 77 K because of improved resolution of vibrational progression due to attenuation of inhomogeneous band broadening at low temperatures. These vibrational progressions are modelled by the summation of the individual contributing vibronic Franck-Condon transitions. Each of these transitions is associated with vibrational wavefunctions that are coupled in the ensuing transition. Each individual emission envelope therefore corresponds to at least one or more vibrational modes, the energy of which can be determined and the identity of the vibrational modes made. Generally for polypyridyl transition metal complexes, two average vibrational modes are sufficient to accurately model the emission

profile, a medium energy component for the ligand stretching modes as well as a low energy component to include metal-nitrogen stretching modes.

Equation 5.1:

$$I(\nu) = \sum_{\upsilon_m=0}^{n} \left[\left(\frac{E_{00} - \upsilon_m \hbar\omega_m}{E_{00}} \right)^3 \frac{S_m^{\upsilon_m}}{\upsilon_m !} \times \exp\left(-4\ln(2) \times \left(\frac{\nu - E_{00} + \upsilon_m \hbar\omega_m}{\Delta\nu_{0,1/2}} \right)^2 \right) \right]$$

Equation 1 describes the emission intensity of a given transition at a given energy I(v) with one Huang-Rhys parameter, where $\Delta v_{0,1/2}$ is FWHM of the vibronic band and υ_m is the number of ground state vibrational levels of $\hbar\omega_M$ that are final vibronic states and S_m is the Huang-Rhys parameter. Equation 5.1 above calculates the Huang-Rhys factor for one frequency mode only. For polypyridyl complexes whose emission characteristics are due totally, or in part to MLCT transitions, a two-mode model is often required to accurately model excited state distortions at low temperature (*vide infra*).[8] This is due to contribution from elongation of the metal-nitrogen bond upon formation of the excited state anionic diphenyl ligand,[9,10] however other low frequency modes can also be associated including purely internal polypyridyl based vibrations (low energy ring deformations for example). Generally care must be taken in absolute frequency mode assignments as the low and medium frequency modes can actually represent an average of a variety of differing vibrational modes.

The coupling of a particular vibrational mode is described by $\hbar\omega_{M.}$ This is the average energy of the vibrational mode coupled to an upper and lower state. The ring stretch modes for di-imine ligands involved in MLCT transitions being one common example at 1350 cm^{-1}.

Equation 5.2:

$$S_M = \frac{1}{2}\left(\frac{M\omega_M}{\hbar}\right)\left(\Delta Q_e\right)^2$$

Equation 5.2 describes the Huang-Rhys factor or the degree of distortion (S_m) associated with a particular transition, mapping the relative positions of the ground and excited state energy surfaces along a given reaction coordinate, where M is the reduced mass of the oscillator, ω_M is the oscillator fundamental frequency which equates to the vibrational mode associated with a given reaction coordinate, ħ is the reduced Planck constant and ΔQ_e is the difference between ground and excited state equilibria associated with a particular vibrational coordinate (Figure 5.3). Information garnered from spectral fitting to Equation 5.1 is used to estimate S_m and in turn ΔQ_e.

5.0.3.1 Two-mode Huang-Rhys Analysis

Equation 5.3 was used for calculation of the two-mode Huang-Rhys factor:

Equation 5.3

$$I(\nu) = \sum_{\upsilon_M=0}^{5}\sum_{\upsilon_L=0}^{5}\left(\frac{E_{00}-\upsilon_M\hbar\omega_M-\upsilon_L\hbar\omega_L}{E_{00}}\right)^3\left(\frac{S_M^{\upsilon_M}}{\upsilon_M!}\right)\left(\frac{S_L^{\upsilon_L}}{\upsilon_L!}\right)\times\exp\left\{-4\ln 2\left(\frac{\nu-E_{00}+\upsilon_M\hbar\omega_M+\upsilon_L\hbar\omega_L}{\Delta\nu_{1/2}}\right)^2\right\}$$

where S_L and S_M are the Huang-Rhys Factors for the low and medium frequency modes ħω_L and ħω_M. Figure 5.4 shows the relationship of some of the above terms to the emission envelopes of a deconvolution of Z-$[Ru(bpy)_3]^{2+}$. The terms υ_m and υ_L are the vibrational quantum number of the ground state stretching vibrations of the ligands which contribute substantially to the emission spectrum whilst S_M is the dimensionless fractional displacement of the normal mode between the ground and excited state.[11] In d_6 polypyridyl complexes, the medium frequency mode is associated with di-imine ring C-C ring stretches at around 1350 cm^{-1} and the low frequency modes at around 300 - 500 cm^{-1} contain dominant contributions from Ru-N

stretching vibrations.[12,13] Both Equations 5.2 and 5.3 neglect any contribution from thermal population of higher energy excited states, therefore any conclusions drawn utilising the equations for room temperature spectral fitting must be interpreted with regard to the absence of these contributions.[14]

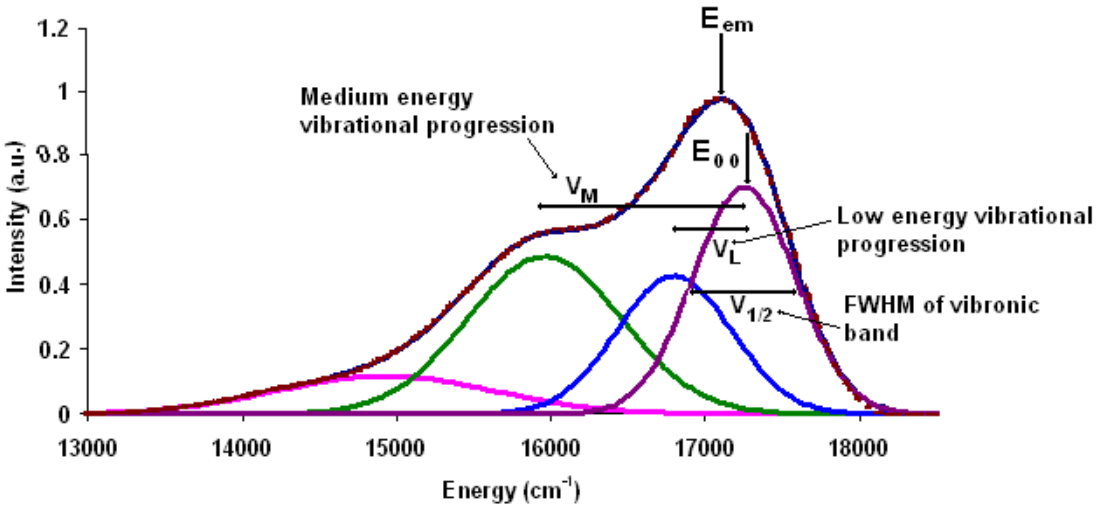

Figure 5.4: A diagram demonstrating an emission envelope fitting profile for Z-$[Ru(bpy)_3]^{2+}$. The various parameters required for the Huang-Rhys analysis are shown. The dashed line is the experimental data and the continuous line is the fit based on the Gaussian curves.

5.1 Experimental

Hexaammineruthenium(III) chloride, ruthenium trichloride, 2,2'-bipyridine, 2,2':6',2"-terpyridine, Iridium trichloride trihydrate, potassium hexafluorophosphate, ammonium hexafluorophosphate, trifluoromethane sulphonic acid (TFMS) and all solvents were purchased from Sigma Aldrich and used without further purification. All solvents used for photophysical measurements were spectroscopic grade. Water was purified to greater than 18 MΩ.cm utilising a 'MilliQ' water purification system.

Sodium Zeolite Y was purchased from Sigma Aldrich and calcined in air at 600 °C for six hours, extensively washed with 10% NaCl solution and finally washed with deionised water until no chloride could be detected with silver nitrate solution (0.1 M). The preparation of the zeolite-entrapped species is

explained in detail in previous chapters. All complexes were synthesized according to literature methods and were characterized by NMR. Their purity was assessed by either TLC or HPLC using a cation exchange column.

Low temperature measurements (77 K) were carried out in butyronitrile either as a suspension or solution. Emission spectral fitting was carried out using two software packages IGOR Pro and Peakfit, which are commercially available technical graphing, and analysis software packages. For the purposes of calculations, the Equations 5.2 and 5.3 were used in IGOR, with the variables allowed to float as necessary to obtain a fit. The data was normalized and was fit ultilising iterative data fitting using the Levenberg-Marquardt algorithm to search for the minimum value of chi-squared. The curve fit terminated after 40 passes in searching for the best fit or after nine if there was no enhancement in the chi-squared value after nine passes in a row. Any variable that were kept static are noted in the text. For the peak deconvolution, a minimum number of peaks was used to reproduce the fit all with similar initial FWHM. The area of these was allowed to float in order to model the data while the bandwidth was restricted. Whilst no parameters are extracted from the deconvoluted spectra, it was found useful to be able to visualise individual emission contributions to overall spectra.

5.1.1 Preparation of $[Ir(tpy)_2][PF_6]_3$

1. $Ir(tpy)Cl_3$

$IrCl_3.3H_2O$ (0.199 g, 5.64 X 10^{-4} moles) was dissolved in ethylene glycol (10 cm^3) and degassed under N_2 for twenty minutes. To this was added an equimolar quantity of 2,2':6',2"-terpyridine (0.132 g, 5.65 X 10^{-4} moles) and he solution heated at 160 °C for 15 minutes. This yielded $Ir(tpy)Cl_3$ in a 39% yield (0.117 g) as a dark red precipitate that was washed with ethanol (25 cm^3), deionised water (25 cm^3) and finally diethyl ether (25 cm^3).

2. $[Ir(tpy)_2][PF_6]_3$

$Ir(tpy)Cl_3$ (0.117 g, 2.199 X 10^{-4} moles) was dispersed in ethylene glycol (9 cm^3) and an equimolar quantity of 2,2':6',2"-terpyridine (0.051 g, 2.186 X 10^{-4} moles) was added. This was degassed under N_2 and brought to reflux for 15 minutes. The solution was then cooled and the product precipitated with a saturated aqueous KPF_6 solution yielding crude $[Ir(tpy)_2][PF_6]_3$ in a yield of 60% (0.144 g). This was then purified via semi-preparative HPLC utilizing the method outlined above.

5.1.2 Preparation of $[Ir(bpy)_3][PF_6]_3$

1. $[Ir(bpy)_2Cl_2]Cl$

$IrCl_3.3H_2O$ (0.204 g, 5.78 X 10^{-4} moles) was dissolved in ethylene glycol (2 cm^3) and a 2-fold molar excess of 2,2'-bipyridine was added (0.180 g, 1.152 X 10^{-4} moles). The solution was degassed for 20 minutes under N_2 and brought to 180 °C for 2 hours during which time the solution turned an orange colour. After cooling de-ionised water (4 cm^3) was added and the solution was left at 4 °C overnight. The dark yellow precipitate was collected by filtration and washed with 3 portions of diethyl ether (3 x 20 cm^3) in order to remove any excess ligand giving $[Ir(bpy)_2Cl_2]Cl$ in a 39% yield (0.140 g).

2. $[Ir(bpy)_2Cl_2][TFMS]$

$[Ir(bpy)_2Cl_2]Cl$ (0.140 g, 2.291 X 10^{-4} moles) was suspended with magnetic stirring in acetonitrile (30 cm^3) and trifluoromethane sulphonic acid (TFMS, 99.9 %) (10 drops) was added. The suspended solid went immediately into solution and was left for 40 minutes. The solution was filtered to remove insoluble impurities and the orange product in a yield of 78% (0.130 g) was recovered by addition to a large volume of vigorously stirred diethyl ether (150 cm^3) and subsequent filtration.

3. $[Ir(bpy)_2(TFMS)_2][TFMS]$

$[Ir(bpy)_2Cl_2][TFMS]$ (0.130 g, 1.79 x 10^{-4} moles) was suspended in degassed 1,2- dichlorobenzene. TFMS (10 drops) was added and the solution brought to reflux under N_2 for 1 hour. The solution was then cooled and a further quantity of TFMS was added (10 drops) and the solution put under reflux for another two hours during which time the solution went from orange-yellow to a brown yellow colour. After cooling the product was collected by addition to a large volume of diethyl ether (150 cm^3). This was dissolved in acetonitrile and filtered in order to remove a black impurity and recollected by addition to diethyl ether giving a finely divided light yellow material in a yield of 58% (0.100 g).

4. $[Ir(bpy)_3][PF_6]_3$

$[Ir(bpy)_2(TFMS)_2][TFMS]$ (0.100 g, 1.047 X 10^{-4} moles) was dispersed in ethylene glycol (10 cm^3) and a 20 fold molar excess of 2,2'-bipyridine (0.325 g) was added. The solution was degassed for 20 minutes and brought to reflux under N_2 for 10 hours. The solution was cooled and aqueous ammonium hexafluorophosphate (20 cm^3) added yielding a pink precipitate. This cooled at 4°C for 6 hours, filtered and washed with de-ionised water (25 cm^3), dichloromethane (25 cm^3) and finally diethyl ether (3 x 20 cm^3): yield 55% (0.063 g). This compound was then purified by ion exchange HPLC as detailed above.

5.1.3 Preparation of $[Ru(tpy)_2][PF_6]_2$

The complex was prepared by the method described by Constable.[15] $RuCl_3.3H_20$ (0.128 g, 4.89 X 10^{-4} moles) was dissolved in ethanol (40 cm^3) and heated to reflux for 1 hour during which time the solution turned green. 2,2':6',2"-terpyridine (0.230 g, 9.85 X 10^{-4} moles) was added and the solution refluxed for 2 hours. The resulting solution was filtered to remove partially reacted $[Ru(tpy)Cl_3]$. The product was isolated by addition of an aqueous

ammonium hexafluorophosphate solution (2 cm^3). The red crystalline $[Ru(tpy)_2][PF_6]_2$ was washed with 2 portions of diethyl ether to remove unreacted ligand and was obtained in a yield of 18% (0.078 g)

5.1.4 Preparation of Z-$[Ru(tpy)_2]^{2+}$

The zeolite material was prepared in an analogous manner to the Z-$[Ru(bpy)_3]$ material outlined in previous chapters. Briefly, the zeolite material was ion-exchanged with a ruthenium salt and subsequently reacted with 2,2':6',2"-terpyridine to yield the structurally entrapped complex. This was followed with the rigorous washing and purification steps as performed with the other zeolite based materials studied.

5.2 Results and Discussion

All the complexes above were prepared according to literature methods and were characterised by NMR. Their purity was assessed by either HPLC or TLC. The photophysical characteristics of the complexes under examination have been outlined in previous chapters. The results of the 77 K and 298 K spectral fitting of the zeolite entrapped and solution phase species are outlined in tables 5.1 and 5.2 below. The details of the formulae used and the conditions of the experiment are outlined in the experimental section above. All data was fit to both a one-mode and two-mode model to assess which was more appropriate based on the reproduction of the experimental data by the model. Tables 5.3 and 5.4 are the band assignments for the key modes as calculated. In order to assist interpretation of the spectral bands Figure 5.5 shows the numbering system and anticipated distortion of $(H_2bpy)^{2+}$ resulting from photoexcitation into the lowest π^* orbital.[16] The arrows represent the expected general changes in the framework of the ligand.

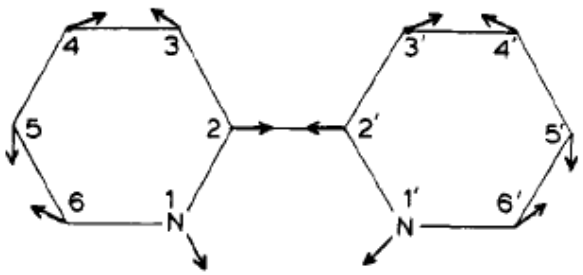

Figure 5.5: Semi-quantitative predicted distortion of (H_2bpy^{2+}) after excitation into the lowest π^* orbital (Kober *et al.*, *Inorg. Chem.* **1985**, *24*, 106).[16]

This is based on computer modelling of the expected distortion of bipyridine after excitation to the lowest π^* orbital. If two neighbouring atoms have the same phase contribution to the π^* orbital there will be enhanced bonding between them and decreased bond length. If they have opposite phase contributions the bond length will increase.

5.2.1 Huang-Rhys analysis 77 K of ruthenium polypyridyl complexes

5.2.1.1 $Ru(bpy)_3][PF_6]_2$ and Z-$[Ru(bpy)_3]^{2+}$

The results of spectral fitting of the spectra of frozen matrix and zeolite entrapped $[Ru(bpy)_3]^{2+}$ to the Huang-Rhys equation (Equation 5.3) is shown in Figure 5.6 and 5.7 below.

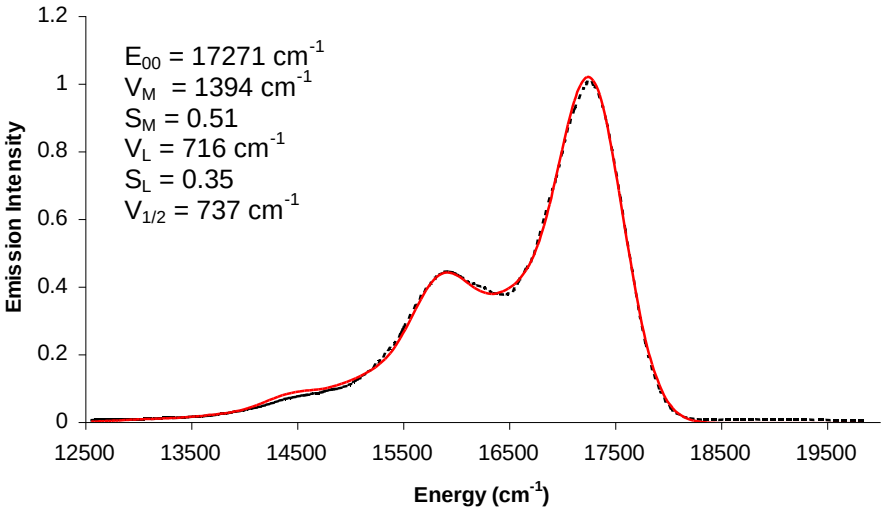

Figure 5.6: Spectral two mode fitting results of $[Ru(bpy)_3]Cl_3$ (1.1×10^{-5} M) at 77 K in butyronitrile. Experimental spectrum (- - -), calculated (—). Excitation 452 nm and slit width 5 nm.

Complex	E_{00} cm^{-1}	ν_M cm^{-1}	S_M	ν_L cm^{-1}	S_L	$\nu_{1/2}$ cm^{-1}
$[Ru(bpy)_3]^{2+}$	17271 ± 3	1394 ± 5	0.51 ± 0.05	716 ± 11	0.35 ± 0.04	737± 5
Z-$[Ru(bpy)_3]^{2+}$	17118 ± 7	1412 ± 37	0.36 ± 0.01	907± 38	0.5 ± 0.01	930 ± 14
$[Ru(tpy)_2]^{2+}$	16491 ± 3	1256 ± 9	0.33 ± 0.01	627± 8	0.46 ± 0.02	673 ± 6
Z-$[Ru(tpy)_2]^{2+}$	16378 ± 5	1370 ± 19	0.37 ± 0.02	767 ± 18	0.54 ± 0.01	814 ± 11
$[Ir(bpy)_3]^{3+}$	21833 ± 0[a]	1508 ± 10	1.03 ± 0.03	1000 ± 0[a]	0.67 ± 0.03	600 ± 0[a]
Z-$[Ir(bpy)_3]^{3+}$ [b]	22302 ± 36	1324 ± 21	1.82 ± 0.08	-675 ± 58	-0.88 ± 0.04	1502 ± 28
$[Ir(tpy)_2]^{3+}$	21772 ± 7	1496 ± 8	1.13 ± 0.02	999 ± 13	0.62 ± 0.02	457 ± 9
Z-$[Ir(tpy)_2]^{3+}$	22055 ± 8	1560 ± 10	1.05 ± 0.03	1050 ± 0[a]	0.76 ± 0.03	631 ± 13

Table 5.1: Two mode-fitting results for ruthenium and iridium polypyridyl complexes and materials at 77 K.

[a] This value was fixed during fitting to enhance fit quality.[b] See text for discussion of erroneous results. Luminescence spectra were recorded in as either a solution or suspension in butyronitrile. The concentrations of $[Ru(bpy)_3]^{2+}$ and $[Ru(tpy)_2]^{2+}$ were 1.1 x 10^{-5} M and 1.2 x 10^{-5} M and their zeolite entrapped analogues Z-$[Ru(bpy)_3]^{2+}$ and Z-$[Ru(tpy)_2]^{2+}$ were 1 complex per 22 supercages and 1 complex per 20 supercages respectively. The concentrations of $[Ir(tpy)_2]^{3+}$ and $[Ir(bpy)_3]^{3+}$ were 1.25 x 10^{-5} M and 1.1 x 10^{-5} M and their zeolite entrapped analogues Z-$[Ir(tpy)_2]^{2+}$ and Z-$[Ir(bpy)_3]^{2+}$ were 1 $[Ir(tpy)_2]^{3+}$ per 36 supercages and 1 $[Ir(bpy)_3]^{3+}$ per 18 supercages.

Complex	E_{00} cm^{-1}	ν_M cm^{-1}	S_M	ν_L cm^{-1}	S_L	$\nu_{1/2}$ cm^{-1}
$[Ru(bpy)_3]^{2+}$	16641 ± 8	1523 ± 22	0.39 ± 0.01	N/A	N/A	1805 ± 18
Z-$[Ru(bpy)_3]^{2+}$	16249 ± 7	1571 ± 23	0.37 ± 0.01	N/A	N/A	1829 ± 16
[a]$[Ru(tpy)_2]^{2+}$						
Z-$[Ru(tpy)_2]^{2+}$	15973 ± 18	1474 ± 36	0.52 ± 0.03	N/A	N/A	1823 ± 42
[b]$[Ir(bpy)_3]^{3+}$	21528 ± 10	1520 ± 23	0.80 ± 0.04	955 ± 17	1.06 ± 0.04	731 ± 16
[c]Z-$[Ir(bpy)_3]^{3+}$	22625 ± 7	2605 ± 32	0.95 ± 0.02	1553 ± 24	1.93 ± 0.04	1543 ± 31
$[Ir(tpy)_2]^{3+}$	21751 ± 7	1558 ± 15	1.06 ± 0.04	1028 ± 21	0.79 ± 0.04	733 ± 12
Z-$[Ir(tpy)_2]^{3+}$	22011 ± 6	1595 ± 11	1.13 ± 0.03	1033 ± 13	0.89 ± 0.02	704 ± 10

Table 5.2: One and two mode-fitting results for ruthenium and iridium polypyridyl complexes and materials at 298 K. [a] This complex was not fit as it has no room temperature luminescence spectrum. Luminescence spectra were recorded in as either a solution or suspension in butyronitrile. The concentrations of $[Ru(bpy)_3]^{2+}$ and $[Ru(tpy)_2]^{2+}$ were 1.1 x 10^{-5} M and 1.2 x 10^{-5} M and their zeolite entrapped analogues Z-$[Ru(bpy)_3]^{2+}$ and Z-$[Ru(tpy)_2]^{2+}$ were 1 complex per 22 supercages and 1 complex per 20 supercages respectively. The concentrations of $[Ir(tpy)_2]^{3+}$ and $[Ir(bpy)_3]^{3+}$ were 1.25 x 10^{-5} M and 1.1 x 10^{-5} M and their zeolite entrapped analogues Z-$[Ir(tpy)_2]^{2+}$ and Z-$[Ir(bpy)_3]^{2+}$ were 1 $[Ir(tpy)_2]^{3+}$ per 36 supercages and 1 $[Ir(bpy)_3]^{3+}$ per 18 supercages.

Complex	ν_M cm^{-1}	Associated vibrational modes	ν_L cm^{-1}	Associated vibrational modes
$[Ru(bpy)_3]^{2+}$	1394 ± 5	σ (C_5C_6H), σ (CCH), ν (C_3-C_4), ν (C_6-N)	716 ± 11	σ (CCC), σ (CCH), ν (C_2-N)
Z-$[Ru(bpy)_3]^{2+}$	1412 ± 37	σ (C_5C_6H), σ (CCH), ν (C_3-C_4), ν (C_6-N)	907± 38	σ (CCC), ν (C_5-C_6), ν (C_4-C_5), ν (C_3-C_4)
$[Ru(tpy)_2]^{2+}$	1256 ± 9	ν (CCN) Ring str.	627± 8	σ (CCC)
Z-$[Ru(tpy)_2]^{2+}$	1370 ± 19	(CH) Deformation	767 ± 18	ν (CCC)
$[Ir(bpy)_3]^{3+}$	1508 ± 10	ν (C_4-C_5), ν (C_2-C_3), σ (CCH)	1000 ± 0[a]	ν (C_4-C_5), ν (C_2-N), σ (CCC), σ (C_2C_3H), σ (C_5C_6H)
Z-$[Ir(bpy)_3]^{3+}$ [b]	1324 ± 21	ν (C_2-$C_{2'}$), σ (C_2C_3H), σ (CCH)	-675 ± 58	
$[Ir(tpy)_2]^{3+}$	1496 ± 8	ν (CC) Ring str.	999 ± 13	ν (CC) Ring str.
Z-$[Ir(tpy)_2]^{3+}$	1560 ± 10	ν (CC) Ring str.	1050 ± 0[a]	ν (CC) Ring str.

Table 5.3: 77 K calculated frequencies and band assignments of ruthenium and iridium polypyridyl complexes.[17,18]

Complex	ν_M cm^{-1}	Associated vibrational modes	$\nu_L$cm^{-1}	Associated vibrational modes
$[Ru(bpy)_3]^{2+}$	1523 ± 22	ν (C_3-C_4), ν (C_5-C_6) ν (C_6-N) σ (C_5C_6H) σ (CCH)	N/A	N/A
Z-$[Ru(bpy)_3]^{2+}$	1571 ± 23	ν (C_3-C_4), ν (C_5-C_6) ν (C_6-N) σ (C_5C_6H) σ (CCH)	N/A	N/A
[a]$[Ru(tpy)_2]^{2+}$	N/A		N/A	N/A
Z-$[Ru(tpy)_2]^{2+}$	1474 ± 36	ν (CC) Ring str.	N/A	N/A
[b]$[Ir(bpy)_3]^{3+}$	1520 ± 23	ν (C_5-C_6), ν (C_3-C_4), ν (C_2-C_3), σ (CCH)	955 ± 17	ν (C_5-C_6), ν (C_4-C_5) ν (C_3-C_4) σ (CCC)
[c]Z-$[Ir(bpy)_3]^{3+}$	2605 ± 32		1553 ± 24	ν (C_5-C_6), ν (C_3-C_4), ν (C_2-C_3), σ (CCH)
$[Ir(tpy)_2]^{3+}$	1558 ± 15	ν (CC) Ring str.	1028 ± 21	ν (CC) Ring str
Z-$[Ir(tpy)_2]^{3+}$	1595 ± 11	ν (CC) Ring str.	1033 ± 13	ν (CC) Ring str

Table 5.4: 298 K calculated frequencies and band assignments of ruthenium and iridium polypyridyl complexes.[17,18]

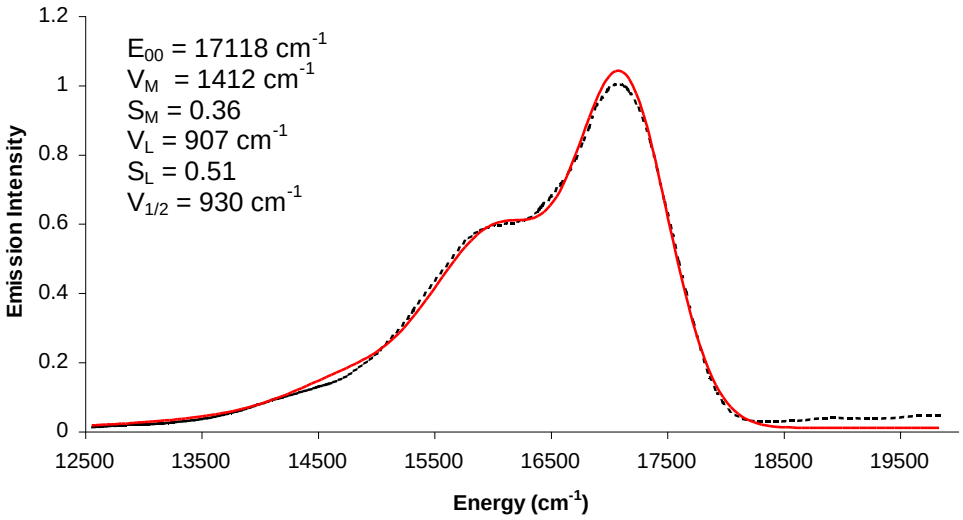

Figure 5.7: Spectral two mode fitting results of Z-$[Ru(bpy)_3]^{2+}$ (1 $[Ru(bpy)_3]^{2+}$ per 22 supercages) at 77 K dispersed in butyronitrile. Experimental spectrum (- - -), calculated (—). Excitation 452 nm, slit width 5 nm.

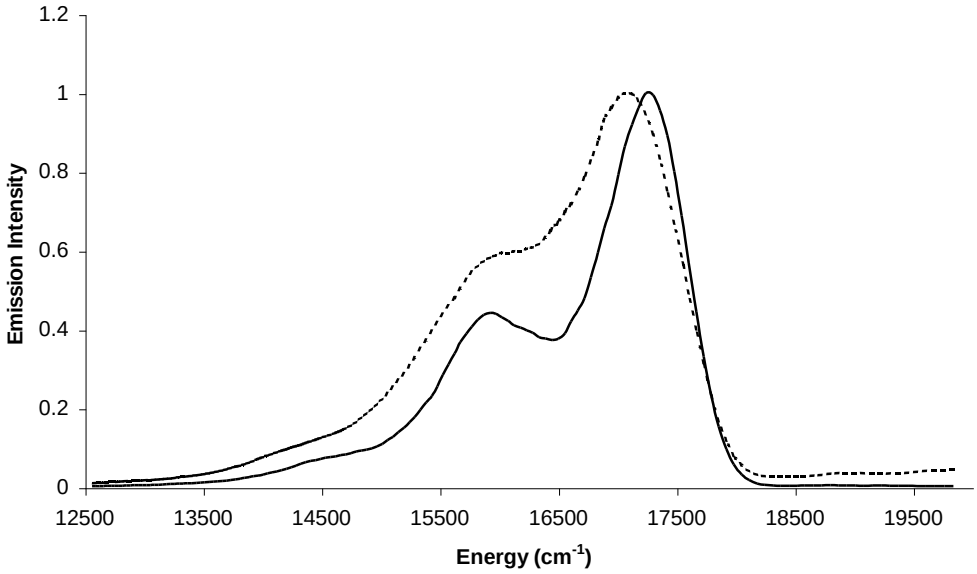

Figure 5.8: Emission spectrum comparison of $[Ru(bpy)_3]Cl_2$ (1.1 x 10^{-5} M) (—) and Z-$Ru(bpy)_3^{2+}$ (1 $[Ru(bpy)_3]^{2+}$ per 22 supercages) (- - -) at 77 K in butyronitrile. Excitation 452 nm and slit width 5 nm for both samples.

Comparison of the zeolite entrapped and non-entrapped $[Ru(bpy)_3]Cl_2$ reveals a red-shift in the emission λ_{max} upon zeolite entrapment (~143 cm^{-1}). Also apparent is the less well defined vibrational progression and larger emission

envelope of the low energy band of the zeolite species. The relative intensity of the vibrational progression changes significantly, making the source of these differences likely to orginate in the degree of distortion the excited state molecule is experiencing. The heterogeneity of the intra-zeolite environment may also contribute to the observed broadening. Therefore the Huang-Rhys factor (S) was expected to be revealing. For the medium energy mode within the frozen matrix S_M was calculated as 0.51 for $[Ru(bpy)_3]^{2+}$ and 0.36 for Z-$[Ru(bpy)_3]^{2+}$. The greater value of S_M outside of the zeolite matrix is indicative of greater excited state distortion along this coordinate. The calculated fit models the experimental data well at all points and reproduces excellently the expected peak separation and relative ratios. This indicates that the zeolite framework limits the degree of distortion the excited state molecule can achieve along this coordinate relative to the frozen matrix. As stated earlier, the C-C stretching and C-C-H bending modes at 1394 cm^{-1} and 1412 cm^{-1} are implicated in relaxation of the free and entrapped species respectively. With reference to table 5.1 and Figure 5.5, $\nu(C_3\text{-}C_4)$ stretching modes which lie on the outer edge of the bipyridine ligand are implicated in these modes, hence this distortion is attributed to medium energy vibration modes that most likely reside close to the framework wall, thus providing a degree of buffering to the entrapped species along these vibrational coordinates. Interestingly, the S_L values associated with the low energy vibrational modes exhibit opposing behaviour, the zeolite causes an enhanced distortion relative to the frozen matrix. The decrease of the E_{00} energy discussed earlier may provide a clue to the source of this seeming anomaly. The absence of frozen solvent molecules in the plane towards the zeolite window may allow for greater Ru-N bond lengths than are possible where a frozen matrix exists around the entire molecule, providing a less sterically hindered environment and therefore greater opportunity for distortion. The associated low energy modes are mainly bending modes for the $[Ru(bpy)_3]^{2+}$ complex with contributions from $\nu(C_2\text{-}N)$. The Z-$[Ru(bpy)_3]^{2+}$ low energy deactivational modes involve predominantly C-C stretching modes suggestive of a differing molecular mobility along coordinates not available to the frozen $[Ru(bpy)_3]^{2+}$.

The question remains as to whether the zeolite environment causes more excited state distortion at 77 K than a frozen matrix. This is difficult to determine definitively from the extracted data. Examination of the emission spectra comparison does however suggest enhanced distortion within the framework along metal ligand and bond bending coordinates but reduced distortion along ligand aromatic stretch coordinates. The relative intensity of the high-energy band compared to the lower one yields information on excited state geometry. An increase in the intensity of the low energy band relative to the higher one implies a greater population of a higher vibrational sublevel, i.e. a decrease in the population of the E_{00} level, suggestive of distortion of the excited state (with no displacement of the upper excited state manifold the 0-0 transition is expected to be the most likely transition). The increase in $v_{1/2}$ from 737 cm^{-1} to 930 cm^{-1} upon zeolite inclusion is suggestive of a change in the vibrational mode, with contributions from higher energy vibrations contributing more to the overall progression. This however does not necessarily imply the absence of lower frequency modes, since the progressions represent the average of a selection of modes, its possible their contribution to the overall averaged mode has decreased.

5.2.1.1 $[Ru(tpy)_2][PF_6]_2$ and Z-$[Ru(tpy)_2]^{2+}$

The dramatic effect of the zeolite matrix on the photophysics of Z-$[Ru(tpy)_2]^{2+}$ was described earlier and indicate strongly that the zeolite reduces k_{nr} dramatically. It was expected also that this would be reflected in the Huang Rhys analysis of the complex in solution versus Zeolite. The complex has no room temperature luminescence, so the comparison can only be made to the frozen matrix to assess the extent of excited state distortion. Here, the ruthenium bis-terpyridine species was examined at 77 K within a frozen butyronitrile matrix and a 77 K zeolite-entrapped environment and the fits and comparison are shown in Figures 5.9 and 5.10 below.

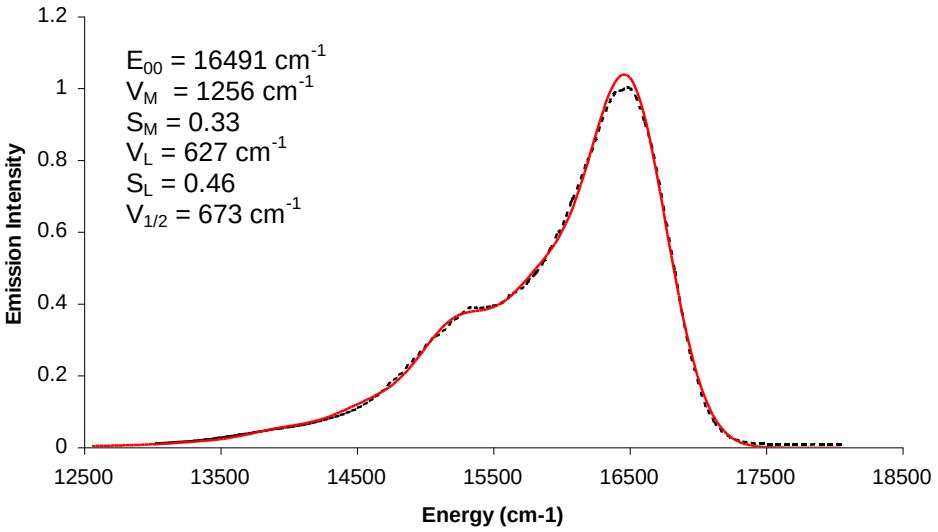

Figure 5.9: Spectral two mode fitting results of $[Ru(tpy)_2][PF_6]_2$ (1.2 x 10^{-5} M) at 77 K in butyronitrile. Experimental spectrum (- - -), calculated (—). Excitation 458 nm and Slit width 5 nm.

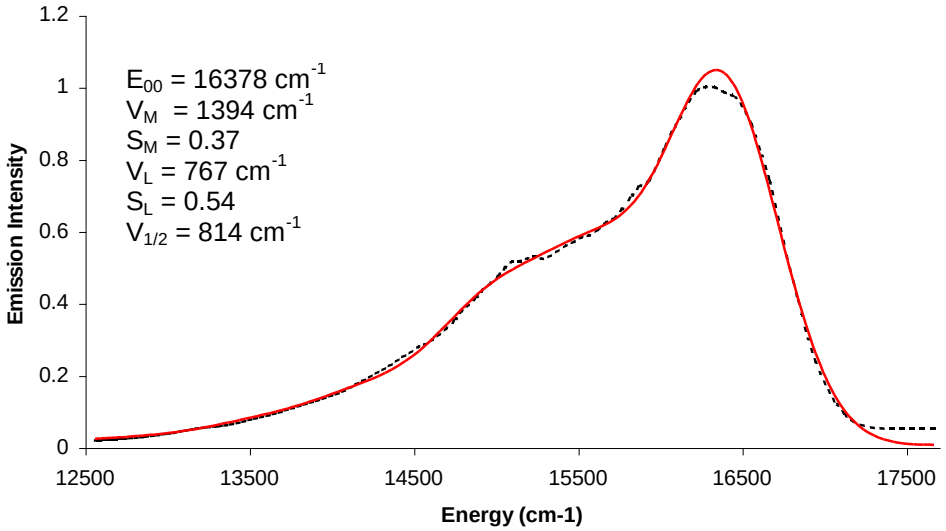

Figure 5.10: Spectral two mode fitting results of Z-$[Ru(tpy)_2]^{2+}$ (1 $[Ru(tpy)_2]^{2+}$ per 20 supercages) at 77 K dispersed in butyronitrile. Experimental spectrum (- - -), calculated (—). Excitation 458 nm and Slit width 5 nm.

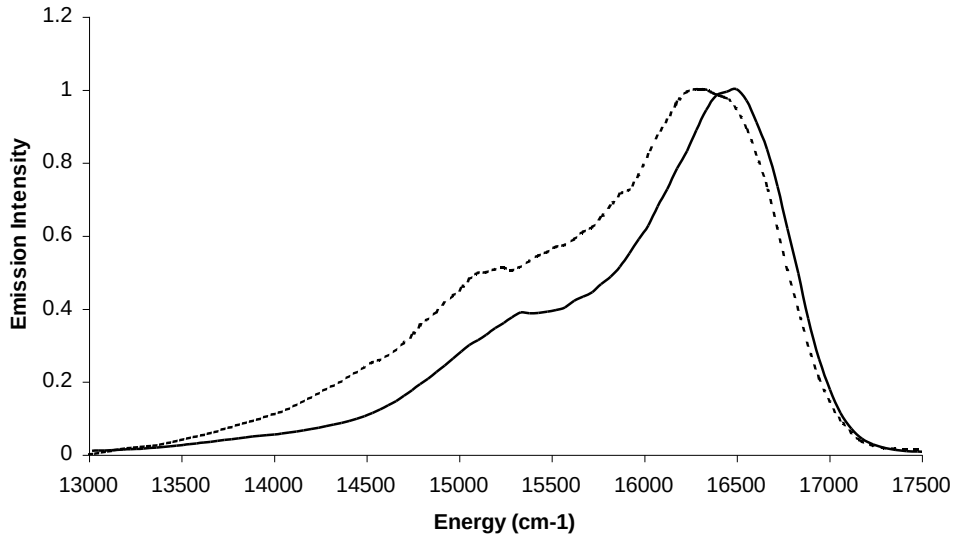

Figure 5.11: Emission spectrum comparison of $[Ru(tpy)_2][PF_6]_2$ (—) (1.2×10^{-5} M) and Z-$[Ru(tpy)_2]^{2+}$ (1 $[Ru(tpy)_2]^{2+}$ per 20 supercages) (- - -) at 77 K in butyronitrile. Excitation was 458 nm for both samples. Slit width 5 nm.

The model slightly overestimates the intensity at the emission maxima but overall the relative intensities and peak separation are well reproduced by the fits. Once again a red-shift in the emission λ_{max} is evident (~113 cm^{-1}) on zeolite encapsulation. The excited state is MLCT based so the effect of solvent reorganisation/ionic environment is expected to play a part in excited state stabilisation. The actual degree of distortion of the entrapped species versus the frozen matrix appears to be quite small according to the calculated values.

For the medium frequency modes (S_m) the difference is 0.01, whilst the difference for the low energy contribution (S_L) is 0.05, these being markedly smaller than the distortions of the bipyridine analogue. These results are attributed to the different fit of the bis-terpyridine molecule within the zeolite cage as well as the effect of greater delocalisation of excited state electron density, over three pyridyl rings as opposed to two. Greater delocalisation of electron density leads to a decrease in bond displacement and hence to a decrease in S_m (Equation 5.2).[19] The molecular volume of $[Ru(bpy)_3][PF_6]_2$ was estimated at 4722 $Å^3$ whilst the volume of $[Ir(tpy)_2][PF_6]_2.2C_2H_3N$

(diacetonitrile solvate was essential for the maintenance of crystal structure during measurement) was estimated at 7544 Å^3.[20,21] Even without factoring in the contribution to the volume from the acetonitrile (acetonitrile has a molecular volume of around 87 Å) it is obvious there is a more than modest difference in molecular volumes between the two complexes and likely between the two ruthenium cationic species, suggesting a tighter fit for the terpyridine species within the zeolite pore. This fit would also account for the observed decrease in the population of the ligand field state with Z-$[Ru(tpy)_2]^{2+}$.[3] The ligand field state is expected to possess longer Ru-N bonds than the ground state complex, so hindrance to this elongation effectively destabilises the ligand field state and increases the ^{3}MLCT –^{3}dd energy gap from ~2300 cm^{-1} for the free complex to ~4000 cm^{-1} to the zeolite entrapped species.[22]

The calculated Huang-Rhys values are in good quantitative agreement with Huang-Rhys values calculated by Amini *et al.*[23] They examined the emission spectrum of $[Ru(tpy)_2]^{2+}$ over a wide temperature range and calculated the Huang-Rhys factors at each temperature point (Figure 5.12). They observed a precipitous drop in the excited state lifetime of the complex at temperatures above 140 K. They used a 4-state model to explain the lifetimes, where the lowest triplet state interacts with two other triplet states (one of which is presumed to be the ^{3}dd state) and the ground state. They calculated S_m = 0.43 at 77 K for $[Ru(tpy)_2]^{2+}$ compared to our measured S_m = 0.33 and S_L = 0.46. They stated that a low energy progression term was included in calculations before 140 K to enhance fit quality, however no S_L was calculated.

Based on the parameters extracted our data indicates that the zeolite-entrapped complex is more distorted than the frozen matrix, suggestive of greater vibrational mobility of the complex within an intrazeolitic cage than in a frozen matrix. Comparison of the excited state lifetimes of the zeolite entrapped Z-$[Ru(tpy)_2]^{2+}$ (140 ns)[3] and frozen glass $[Ru(tpy)_2]^{2+}$ (10.4 μs)[23] is entirely consistant with this view.

Temperature/K	Φ_{LUM}	τ_{LUM}/ns[a]	τ_T/ns[b]	E_T/cm^{-1}	λ_T/cm^{-1}	S	$h\omega_M$/cm^{-1}
77	0.42	10400	NA	17095	580	0.43	1,380
90	0.42	10210		17140	610	0.41	1,370
100	0.40	9,790		17075	590	0.41	1,360
110	0.36	8,910		17070	600	0.36	1,370
120	0.29	7,025		17010	605	0.37	1,380
130	0.165	4,100		17000	610	0.41	1,350
140	0.072	1,750		17000	590	0.41	1,370
150	0.025	660		16960	620	0.50	1,390
160	0.010	255		16920	625	0.55	1,370
170	0.0045	107		16940	640	0.61	1,360
180	0.002	48		16960	710	0.75	1,390
190	0.0010	24		16930	715	0.72	1,380
200	0.00052	12.5		16910	710	0.74	1,390
210	0.00022	7.0	7.0	16940	715	0.69	1,380
220	0.00012	4.1	4.0	16900	740	0.70	1,360
230	0.00008	2.2	2.5	16910	720	0.72	1,340
240	0.00005	1.0	1.6	16910	720	0.72	1,350
250	<0.00002		1.1				
260	<0.00002		0.75				
270	<0.00002		0.52				
280	<0.00002		0.38				
290	<0.00002		0.21				

[a] Measured by time-resolved emission spectroscopy. [b] Measured by transient absorption spectroscopy.

Figure 5.12: Low temperature study of $[Ru(tpy)_2]^{2+}$ in butyronitrile carried out by Amini *et al.*[23] The luminescence quantum yield Φ_{LUM}, triplet state energy E_T the total reorganisational energy of the triplet state λ_T, average medium-frequency vibrational mode $h\omega_M$ and Huang-Rhys factors S are also noted

There is a moderate increase in the calculated value for the Z-$[Ru(tpy)_2]^{2+}$ medium frequency progression 1394 cm^{-1} versus 1256 cm^{-1} for the frozen sample. Kincaid *et al.* examined the resonance raman of $[Ru(tpy)_2]^{2+}$ and Z-$[Ru(tpy)_2]^{2+}$. They noted the largest hypsochromic rR shifts upon encapsulation at frequency modes thought to involve the central pyridine fragment, making it likely that this portion of the molecule is involved in the hindrance of certain deactivational modes.[3] The modes at 1471 cm^{-1}, 1018 cm^{-1} and 729 cm^{-1} were shifted 6 cm^{-1}, 7 cm^{-1} and 5 cm^{-1} respectively. This data further indicates the importance of the contribution of higher frequency modes to the overall low energy progression.

From the data obtained it appears zeolite-entrapped material at 77 K provides broadly the same degree of restriction as the frozen matrix at 77 K. Comparison of the emission spectra (Figure 5.11), suggests a small degree of distortion exists by virtue of the relative first and second peak heights and the moderate broadening of the peaks.

5.2.2 Huang-Rhys analysis 77 K of iridium polypyridyl complexes

5.2.2.1 $[Ir(tpy)_2][PF_6]_3$ and Z-$[Ir(tpy)_2]^{3+}$

Huang-Rhys analysis of Iridium bis-terpyridine and its zeolite-entrapped analogue were next examined at 77 K, both measured as either a solution or suspension in butyronitrile. The spectra were fitted using a combination of IGOR commercial graphing software and Peakfit peak separation and analysis software, due to the complexity of the spectra

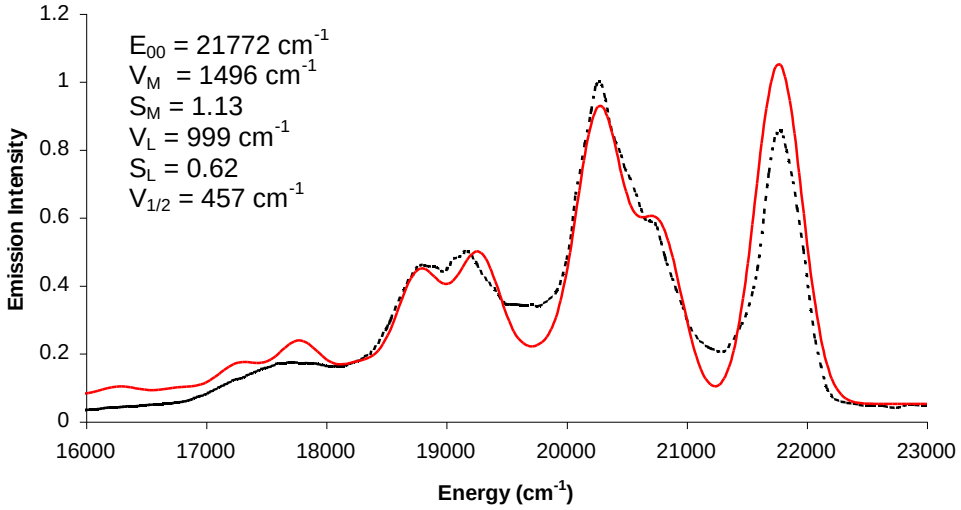

Figure 5.13: Spectral two mode fitting results of $[Ir(tpy)_2][PF_6]_3$ (1.25 x 10^{-4} M) at 77 K in butyronitrile. Experimental spectrum (- - -), calculated (—). Excitation 350 nm and slit width 5 nm.

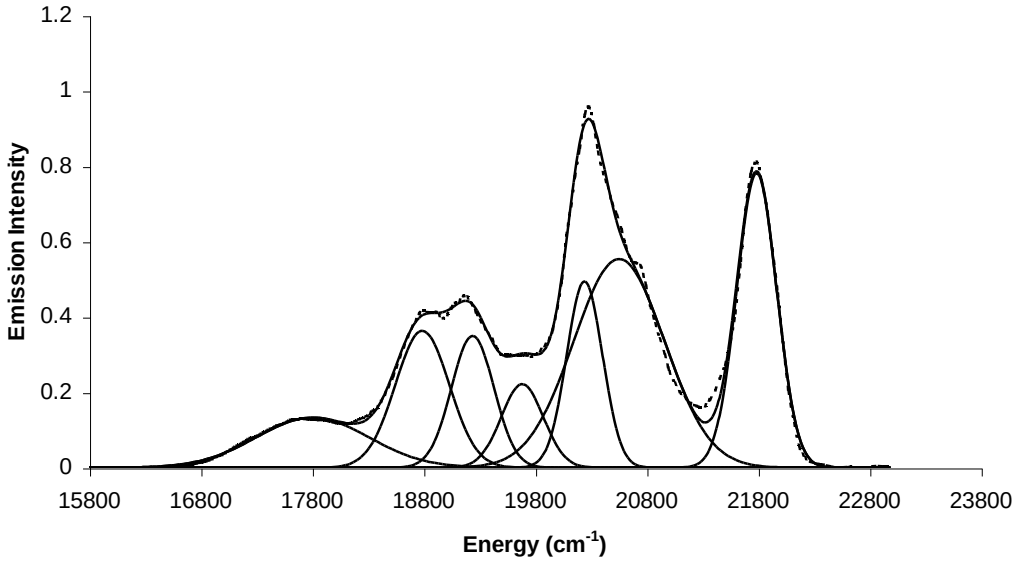

Figure 5.14: Spectral deconvolution of $[Ir(tpy)_2][PF_6]_2$ (1.25 x 10^{-5} M) emission profile at 77 K in butytronitrile. Experimental spectrum (- - -), calculated (—). Excitation 350 nm and slit width 5 nm.

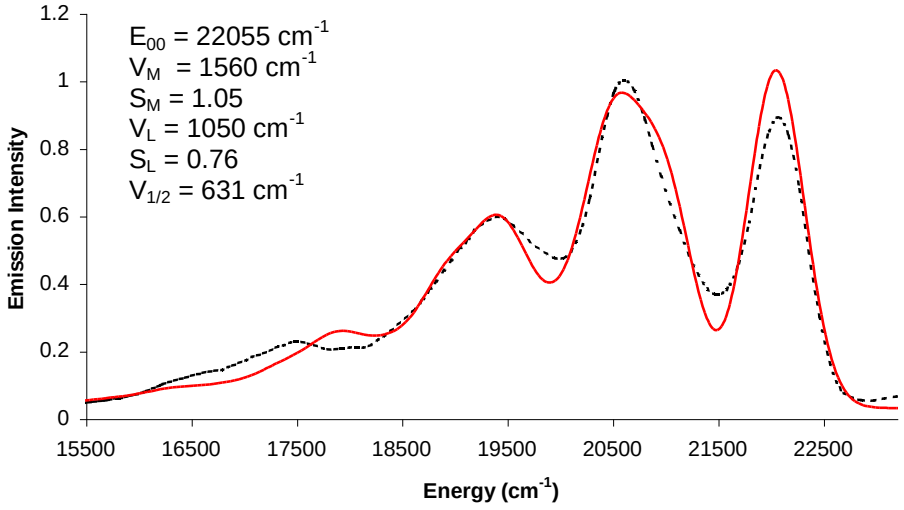

Figure 5.15: Spectral two mode fitting results of Z-$[Ir(tpy)_2]^{3+}$ (1 $[Ir(tpy)_2]^{3+}$ per 36 supercages) suspension at 77 K in butyronitrile. Experimental spectrum (- - -), calculated (—). Excitation 330 nm and slit width 5 nm.

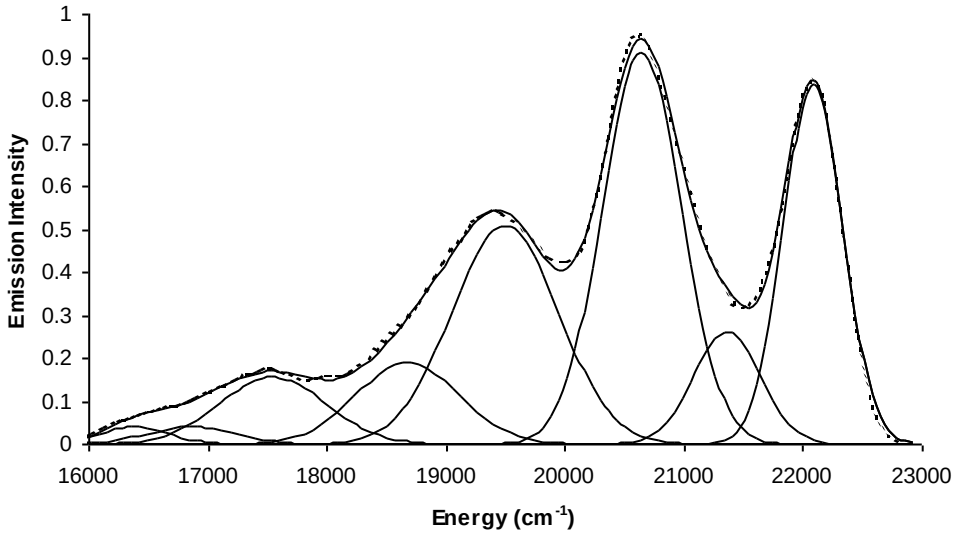

Figure 5.16: Spectral deconvolution of Z-$[Ir(tpy)_2]^{3+}$ (1 $[Ir(tpy)_2]^{3+}$ per 36 supercages) emission profile at 77 K dispersed in butyronitrile. Experimental spectrum (- - -), calculated (—). Excitation 330 nm and slit width 5 nm.

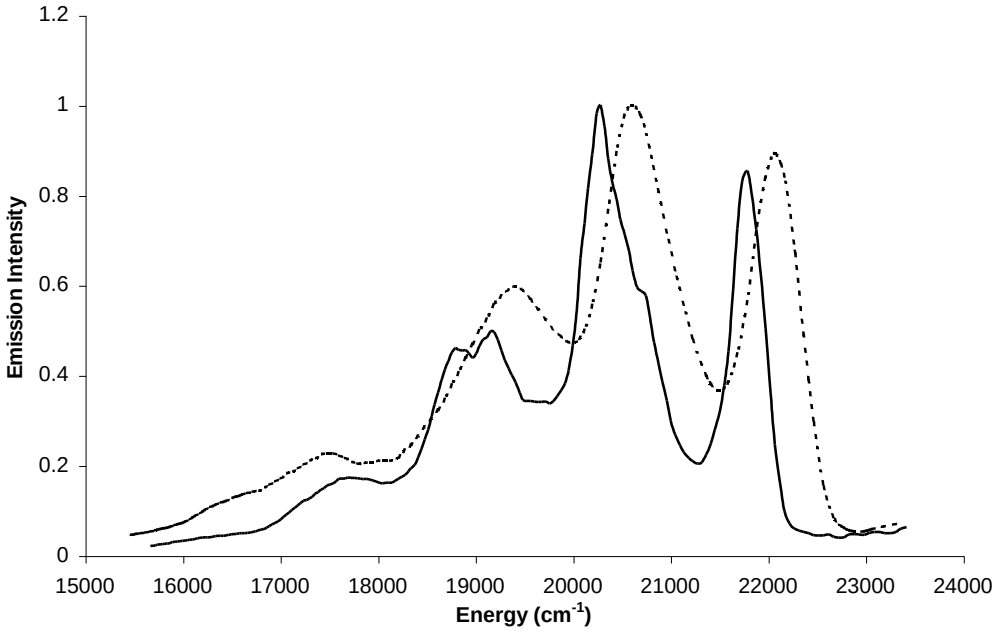

Figure 5.17: Emission spectrum comparison of $[Ir(tpy)_2][PF_6]_3$ (1.25×10^{-5} M) (—), excitation 350 nm and Z-$[Ir(tpy)_2]^{3+}$ (1 $[Ir(tpy)_2]^{3+}$ per 36 supercages), excitation 330 nm (- - -) at 77 K in butyronitrile. Slit width for both experiments 5 nm.

Comparison of the 77 K emission spectra of the frozen matrix and zeolite-entrapped $[Ir(tpy)_2]^{3+}$ species (Figure 5.17) shows a blue shift in the emission energy upon encapsulation, the highest energy band is blue-shifted 284 cm^{-1}, the second band 370 cm^{-1} and the third by 258 cm^{-1} all with respect to the frozen matrix sample. This shift is opposite to hyposchromic shifts observed for the ruthenium polypyridyl species. The excited state for iridium polypyridyl complex is thought have significant ^{3}LC character rather than ^{3}MLCT due to the high oxidation potential of the Ir(III) ion, 2.4 eV vs. SCE.[24] Since the excited state is ligand centred, the origin of the emission λ_{max} blue shift is attributed to the high dielectric intrazeolitic environment. The ligand based excited state is less polar than the ground state equivalent due to electron delocalisation and is less stabilised in a polar environment leading to increased excited state energy. A study by Uppili *et al.* using organic dye probes to measure intrazeolite polarity suggested that the intracage environment of Na-Zeolite-Y was even more polar than water.[25] Based on the solvatochromism study on the iridium polypyridyls carried out in Chapter 4, its

reasonable to attribute the substantial blue shift to this property of local zeolite environment.

The two-mode fit for the Iridium terpyridine complexes reproduced the experimental data reasonably well. The peak separation was well fitted and the intensities were well matched with the exception of a small overestimation of the intensity of the highest energy transition to a small extent and deviating from the lower frequency progressions below 18,000 cm^{-1}. The spectrum of $[Ir(tpy)_2][PF_6]_3$ (Figure 5.13) is substantially more complex than the corresponding ruthenium complexes, which implies that a more sophisticated model may be required in order to best fit the experimental data. However, attempts to apply a three and four mode model were unsuccessful as the added number of parameters resulted in excessive calculation times. The spectrum of the zeolite entrapped $[Ir(tpy)_2]^{3+}$ (Figure 5.15) was found interestingly to be less complex than the corresponding $[Ir(tpy)_2][PF_6]_3$ spectrum and was well fit by the model.

The experimental data was also examined using software allowing for deconvolution of individual emission envelopes, in order to better illustrate the number of emission envelopes required and provide qualitative data only (Figures 5.14 and 5.16).

In terms of the quality of the fit to experimental data, some caution is required due to the quality of the two mode fitting results at the lower frequency progressions (below 18000 cm^{-1}), however the observed fits are reasonably good for the higher energy portion of the spectrum. Overall, the fits (Figure 5.13 and 5.15), to the two-component model are likely to yield an underestimate of the degree of distortion. This is evident from the differing ratio of the first and second high-energy peaks. The intensity is erroneously reversed in the fit, so the deconvoluted models likely provide a more realistic appraisal of the actual emission envelopes (Figure 5.14 and 5.16). These demonstrate enhanced vibrational overlap of ground-state potential energy surfaces with displaced upper ones (reduction in 0-0 transition intensity).

However, even though the difference in distortion between the frozen and zeolite Huang-Rhys factors cannot be deduced from this data, it would appear by reference to Figure 5.17 quite small. The limited difference in distortion as judged by the Huang-Rhys values obtained for the medium energy (S_m = 1.13 and S_m = 1.05) and low energy (S_L = 0.62 and S_L = 0.76) progressions for the frozen and zeolite samples respectively implies greater distortion associated with the low energy progressions of the zeolite material. Both the medium and low energy progressions are comprised primarily of ν(CC) ring stretch modes, so its difficult to definitively attribute the particular modes implicated in the progression.

Comparison of the deconvoluted spectra of both the frozen matrix and the zeolite material shows a complicated emission spectrum associated with the frozen matrix and a relatively simple one in comparison to the zeolite. The greater access of the complex to 'non-frozen' solvent molecules within the zeolite cage might account for the band broadening, compared to the globally rigid molecular environment expected for the 77 K butyronitrile matrix, however contributions from additional vibrational modes may also lead to FWHM broadening.

5.2.2.2 $[Ir(bpy)_3][PF_6]_3$ and Z-$[Ir(bpy)_3]^{3+}$

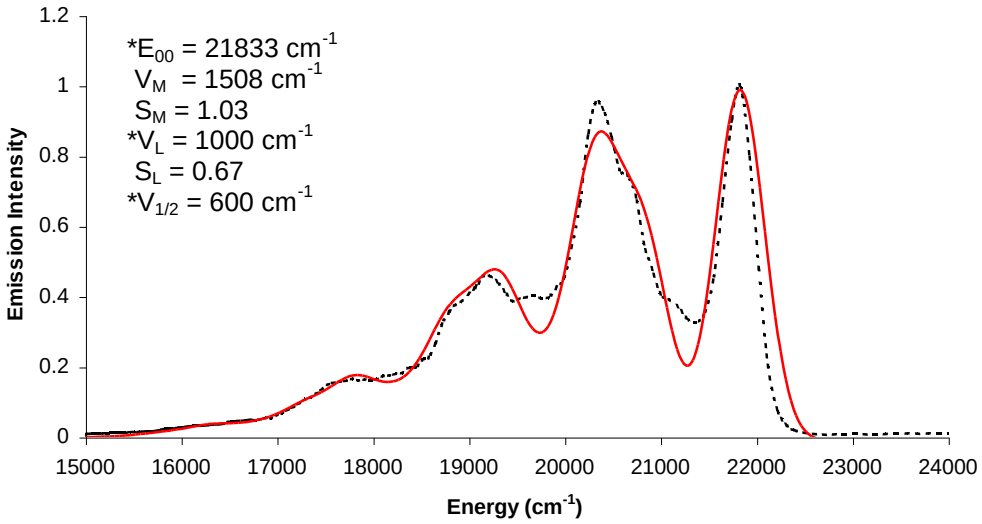

Figure 5.18: Spectral two mode fitting results of $[Ir(bpy)_3][PF_6]_3$ (1.1×10^{-5} M) at 77 K in butyronitrile, excitation 319 nm and slit width 5 nm. Experimental spectrum (- - -), calculated (—). *Parameters were fixed during fitting iterations.

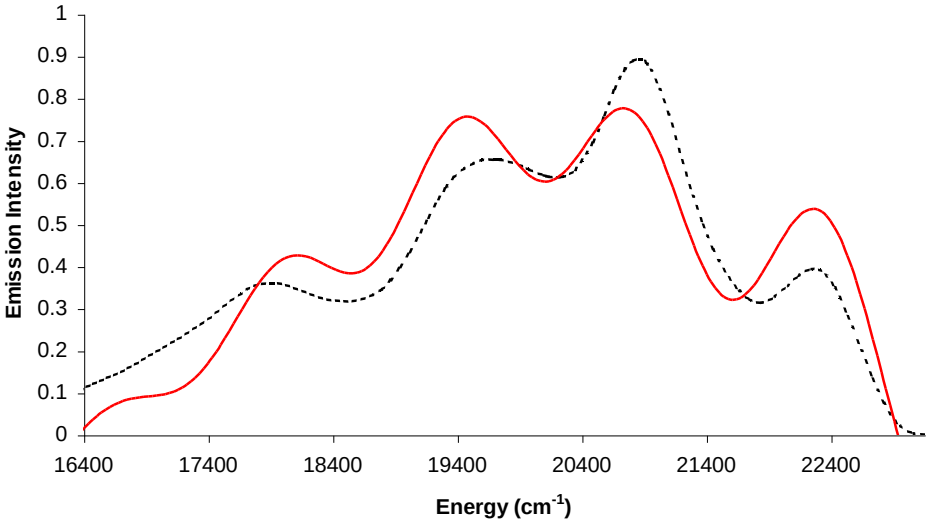

Figure 5.19: Spectral two mode fitting results of Z-$[Ir(bpy)_3]^{2+}$ (1 $[Ir(bpy)_3]^{2+}$ per 18 supercages) at 77 K dispersed in butyronitrile, excitation at 319 nm and slit width 5 nm. Experimental spectrum (- - -), calculated (—).

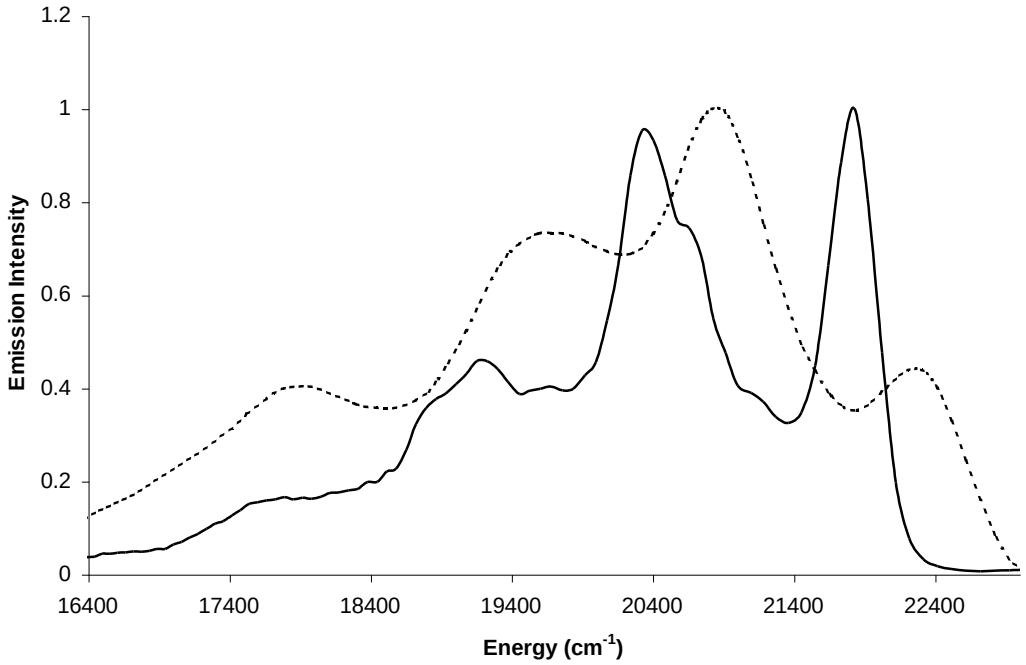

Figure 5.20: Emission spectrum comparison of $[Ir(bpy)_3][PF_6]_3$ (1.1 $x10^{-5}$ M) (—) and Z-$[Ir(bpy)_3]^{3+}$ (1 $[Ir(bpy)_3]^{2+}$ per 18 supercages) (- - -) at 77 K in butyronitrile. Excitation 319 nm and slit width 5 nm for both samples

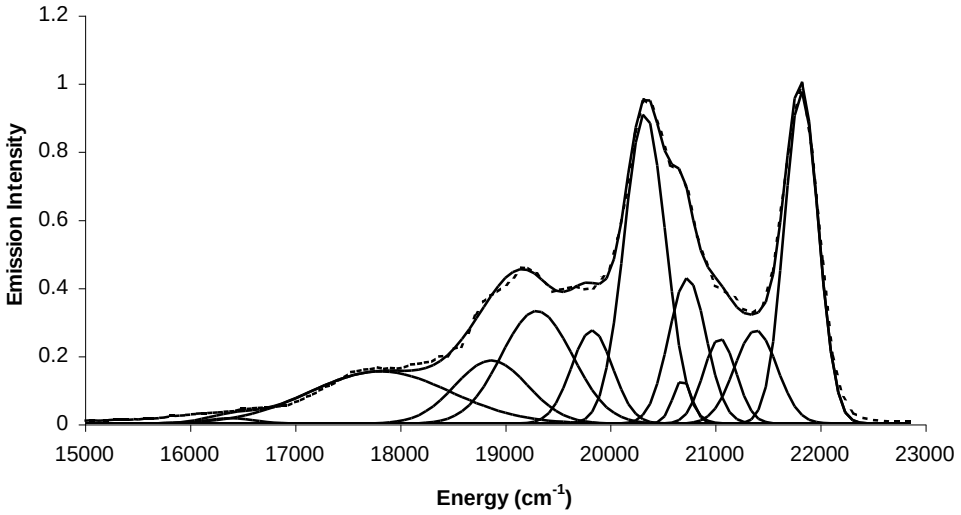

Figure 5.21: Spectral deconvolution of $[Ir(bpy)_3][PF_6]_2$ (1.1 x 10^{-5} M) emission profile at 77 K in butyronitrile, excitation 319 nm and slit width 5 nm. Experimental spectrum (- - -), calculated (—).

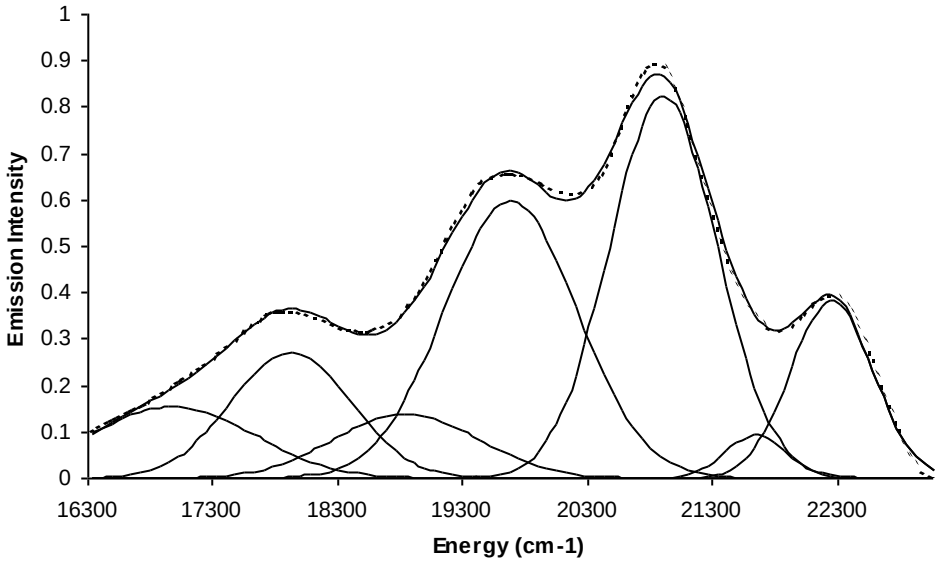

Figure 5.22: Spectral deconvolution of Z-$[Ir(bpy)_3]^{3+}$ (1 $[Ir(bpy)_3]^{2+}$ per 18 supercages) emission profile at 77 K in butyronitrile. Experimental spectrum (- - -), calculated (—). Excitation 319 nm and slit width 5 nm.

The Huang-Rhys analysis on the iridium tris bipyridine samples using the two mode-fit equation was more complex than the preceding terpyridine complex. The fit for the frozen $[Ir(bpy)_3][PF_6]_3$ was reasonably good, but the model slightly underestimates the second peak of the progression (Figure 5.18). To model the experimental data for $[Ir(bpy)_3][PF_6]_3$, half the floating variables had to be fixed to yield a reasonable fit. Attempts to model sections of the spectra to reduce the complexity and garner data for the medium progression vibrational modes did not lead to further insights. The low temperature emission spectrum appears to require a greater number of modes to properly fit the data that is apparent from the deconvoluted spectrum (Figure 5.21). It demonstrates that a large number of Gaussian curves of varying spectral separation (and hence vibrational progressions) are needed to replicate the spectrum. The two component $[Ir(bpy)_3][PF_6]_3$ Huang-Rhys model fit for the Z-$[Ir(bpy)_3]^{3+}$ (Figure 5.19) is not ideal, particularly at 22400 cm^{-1} and 21000 cm^{-1} where intensity is not fit well, although the peak separation appears to model the data fairly well. The non-ideal fit is somewhat surprising given the relative simplicity of the deconvoluted spectra (Figure 5.22) that once again yielded a greatly simplified emission profile similar to the terpyridine analogue. This

again is tentatively attributed to the absence of a rigid solvent cage within the porous material compared to the fine structure apparent with the frozen butyronitrile. This is likely due to the lack of space available for the formation of a solvent cage within the zeolite pore.

Comparison of the 77 K emission spectra of the frozen and encapsulated complex indicates dramatic differences in the excited state geometries (Figure 5.20). There is a substantial blue shift of emission λ_{max} of the Z-$[Ir(bpy)_3]^{3+}$ compared to frozen $[Ir(bpy)_3][PF_6]_3$. The hypsochromic shifts for the first three vibrational progressions were 392 cm^{-1}, 507 cm^{-1} and 373 cm^{-1} compared with solvent. As for the $[Ir(tpy)_2]^{3+}$ complex the excited state of $[Ir(bpy)_3]^{3+}$ is thought to be ^{3}LC based in nature due to the high oxidation potential of the Ir(III) cation. The source of this blue shift is once again mainly attributed to the polar zeolite environment and the effective destablisation of the excited state. Contributions to the blue shift may also derive from the sterically hindered ligand environment within the zeolite pore. In terms of nuclear distortion, Z-$[Ir(bpy)_3]^{3+}$ undergoes substantial excited state geometry changes. The Huang-Rhys factors S_m = 1.03 and S_L = 0.67 are large relative to the ruthenium polypyridyls. The dominant vibrational modes for the medium energy progression are ascribed to mainly outer-ring $\nu(C_4\text{-}C_5)$, $\nu(C_2\text{-}C_3)$ stretching modes and the low energy progression to a mixture of stretching and ring bend modes. The highest energy band of Z-$[Ir(bpy)_3]^{3+}$ decreases in relative intensity to the same band in the frozen glass by greater than 50% upon encapsulation, suggesting that distortion is greater in this complex than $[Ru(bpy)_3]^{2+}$ but bonds involved in relaxation are similar.

There are several broad trends to note from the data in table 5.1. For the ruthenium based polypyridyl species E_{00} red-shifts upon encapsulation in the zeolite matrix. The emission λ_{max} of $[Ru(bpy)_3]^{2+}$ in low temperature glasses is typically blue shifted with respect to solution phase emission. The source of the blue shift is believed to lie with the inability of solvent molecules to re-orient and properly solvate the highly polar MLCT excited state, as would occur rapidly in solution.[26] The decrease in E_{00} upon encapsulation is therefore not an unexpected result and is most likely due to the relative

paucity of space available to water molecules co-entrapped with the complexes

Within the zeolite cage, the formation of a solvent cage surrounding the complex is unlikely to be complete given the size constraints, however translational motion of individual water molecules may provide limited stabilisation of the excited state molecule. As proposed by Dutta *et al.* rotational motion of $[Ru(bpy)_3]^{2+}$ at 77 K is possible and the molecule is most likely to orient its excited state anionic ligands towards a zeolitic window rather than towards the highly electronegative walls of the cage.[27] This would increase the probability of water/solvent molecule infiltration from adjacent cages, where it is more plentiful (assuming the adjacent cage does not contain another complex) towards the excited state species that may aid in its stabilisation.[28] Another possibility is stabilisation of the excited state not by water but by the highly polar environment caused by the extremely high local concentration of sodium ions within the zeolite cage.[29] This trend of decreasing excited state energy is reversed for the $[Ir(tpy)_2]^{3+}$ entrapped species which is good evidence for the difference in excited states of the iridium complexes which have significant ^{3}LC character.

The second trend is the notable increase in the energy of low frequency modes in the fit parameters for the ruthenium polypyridyl complexes. This implies an overall increase in the average energy of the low energy vibrational modes involved in relaxation. It must be remembered that the low energy mode represents the average of a number of possible vibrational deactivation pathways available to a molecule, indicating that either previously poorly deactivating modes are now important, or the frequency of the original deactivating vibrations become more important or possibly a mixture of both. Many of the modes proposed to be responsible for excited state deactivation lie on the outer sections of the polypyridyl ligands (see Chapter 3 Raman data on Z-$[Fe(tpy)_2]^{2+}$) , which lie directly adjacent to the zeolite wall. This proximity of these oscillators to the rigid framework wall could certainly account for the increase in the observed vibrational frequency.

5.2.3 Huang-Rhys analysis 298 K

The data in table 5.2 is composed of one and two mode fitting data for the zeolite and free complexes at room temperature (298 K). As discussed earlier, only one mode is required to fit the ruthenium polypyridyl complexes at room temperature, as low energy vibrations are less important contributors towards excited state deactivation at room temperature.[30,31]

Attempts to use two mode fits increased the quality of the fit, but yielded extremely large vibrational frequencies and negative Huang-Rhys distortion values, clearly a case of over-parameterisation of the data. The iridium complexes required a two mode fit to model the experimental data, however in the case of the zeolite entrapped Z-$[Ir(bpy)_3]^{2+}$, even this was insufficient to completely model the data.

5.2.3.1 Huang-Rhys analysis 298 K $[Ru(bpy)_3][PF_6]_2$ and Z-$[Ru(bpy)_3]^{2+}$

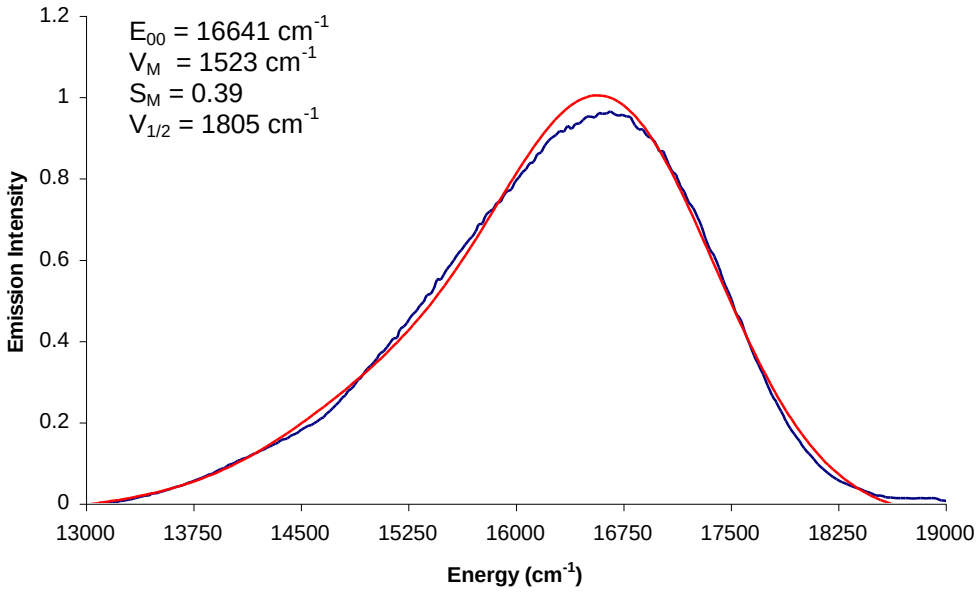

Figure 5.23: Spectral two mode fitting results of $[Ru(bpy)_3]Cl_3$ (1.1×10^{-5} M) at 298 K in butyronitrile. Experimental spectrum (Blue trace), calculated (Red trace). Excitation 452 nm and Slit width 5 nm.

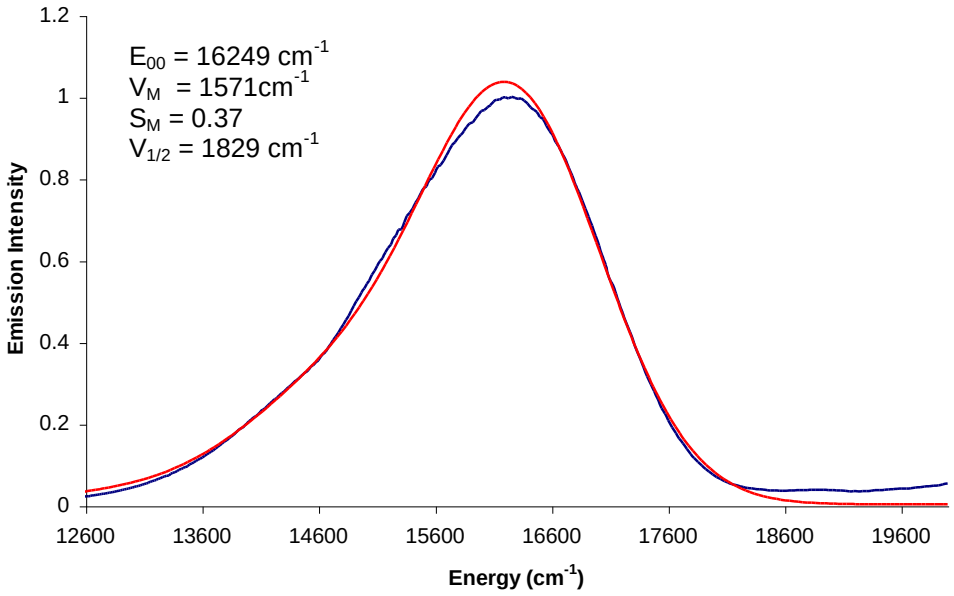

Figure 5.24: Spectral one mode fitting results of Z-$[Ru(bpy)_3]^{2+}$ (1 $[Ru(bpy)_3]^{2+}$ per 22 supercages) at 298 K dispersed in butyronitrile. Experimental spectrum (Blue trace), calculated (Red trace). Excitation 452 nm, Slit width 5 nm.

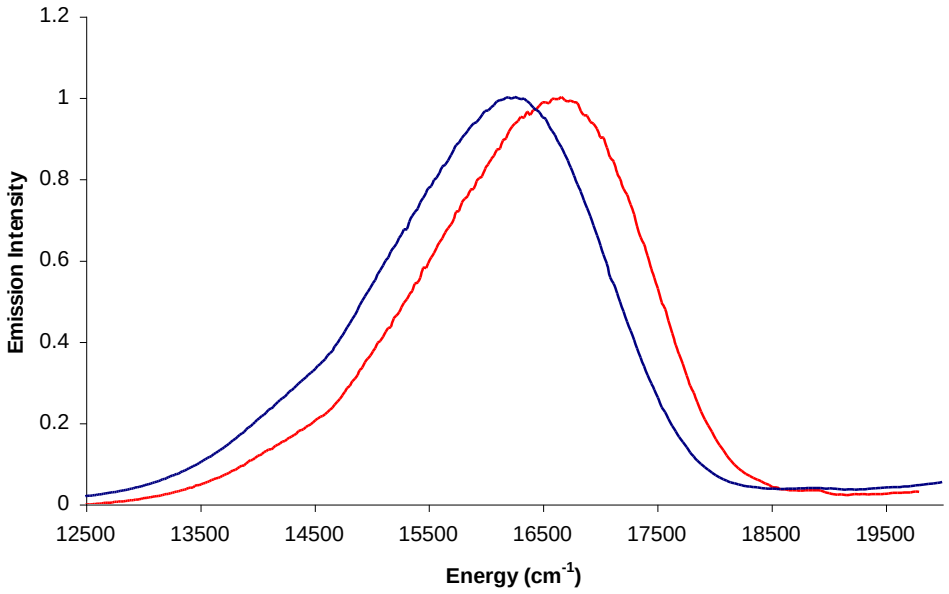

Figure 5.25: Emission spectrum comparison of $[Ru(bpy)_3]Cl_3$ (1.1 x 10^{-5} M) (Red trace) and Z-$Ru(bpy)_3^{2+}$ (1 $[Ru(bpy)_3]^{2+}$ per 22 supercages) (Blue trace) at 298 K in butyronitrile. Excitation 452 nm and slit width 5 nm for both samples.

A one-mode fit was used to model the experimental emission spectra of both zeolite entrapped $[Ru(bpy)_3]^{2+}$ and dissolved $[Ru(bpy)_3]^{2+}$ complexes (Figure 5.23 and 5.24). Comparison of the extracted data suggests a very similar degree of excited state distortion upon encapsulation, both possess the same S_m within experimental error. The only evidence of host-guest interaction is the small red shift in emission λ_{max} of the encapsulated complex. This likely results from either intrazeolitic H_2O stabilisation of the excited state (the water is present during the synthesis and the material is conditioned in a non-dessicating environment) or interaction of the anionic portion of the excited state complex with the charge balancing sodium cations present on the zeolite framework structure.[29] Given the dielectric constant of water is 80.4 and butyronitrile is 20.7 it is unsurprising the red shift is observed as more polar solvents tend to stablise the $[Ru(bpy)_3]^{2+}$ excited state (as well as the polarity effects of the cage itself). Dutta *et al.* performed a limited 298 K Franck-Condon analysis on zeolite entrapped $[Ru(bpy)_3]^{2+}$.[28] The aim of their examination was to study the effect of introduction of tetraethyl ammonium (TEA) to the zeolite entrapped ruthenium complex, (TEA was used to mimic the steric effects of a bipyridinium ion but without quenching the luminescence). They noted a very modest increase in nuclear displacement after introduction of TEA, due to the added bulkiness of these molecules compared to H_2O. Their results indicated a larger displacement than our calculated values, yielding a S_m value of 0.94 compared to our S_m = 0.37. The Z-$[Ru(bpy)_3]^{2+}$ they used was 1 $[Ru(bpy)_3]^{2+}$ per 30 supercages, however they used a modified Franck-Condon equation that may account for the difference as it included a term to account for the anharmonicity of the Morse potential of the excited and ground states.[8] We also carried out the measurement in butyronitrile as opposed to the non-suspended solid-state material measured by Dutta *et al.* that could also yield a differing distortion value. Given the good fit of our experimental data to the model used, it is unclear why such a large difference exists between the two S_m values.

5.2.3.2 Huang-Rhys analysis 298 K Z-$[Ru(tpy)_2]^{2+}$

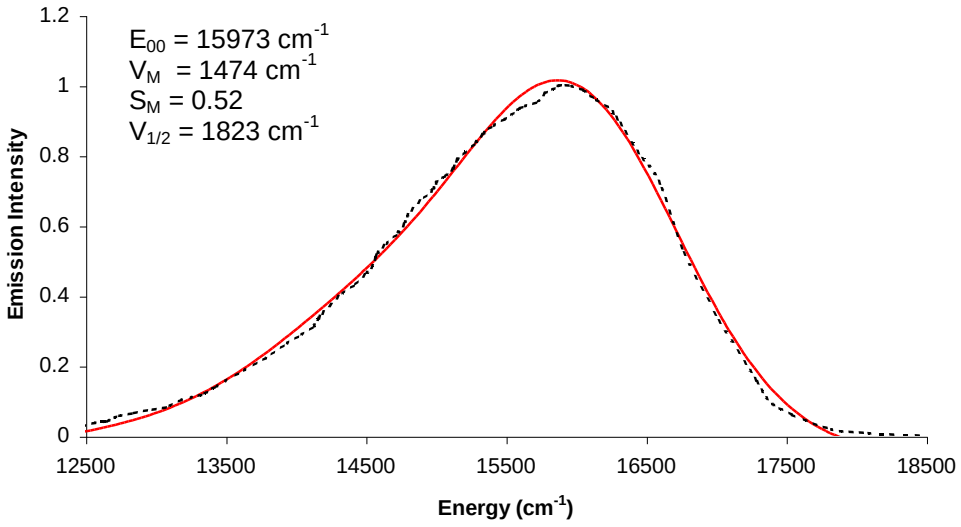

Figure 5.26: Spectral one mode fitting results of Z-$[Ru(tpy)_2]^{2+}$ (1 $[Ru(tpy)_2]^{2+}$ per 20 supercages) at 298 K dispersed in butyronitrile. Experimental spectrum (- - -), calculated (—). Excitation 458 nm and Slit width 5 nm.

The Huang-Rhys factors were also calculated for zeolite entrapped $[Ru(tpy)_2]^{2+}$ (Figure 5.26). The model reproduced the date excellently. The calculated S_m indicates that the molecule undergoes reasonably modest excited state distortion within the zeolite structure as expected from the spectroscopic data discussed earlier, $S_m = 0.37$ and $S_L = 0.54$ for the complex at 77 K. Since the complex is non-emissive at room temperature, there are no parent complex distortion values with which to compare it. The best comparison available is to the study by Amini *et al.*[23] The highest temperature spectrum they analysed was at 240 K and yielded a Huang-Rhys value of 0.72, suggesting a large distortion would be expected at RT (Figure 5.12), which causes k_{nr} to eliminate emission (thermal population of ^{3}dd state). However, it seems likely less distorted (from an ideal octahedral geometry) within the confines of the zeolite than in solution, hence its room temperature luminescence.

Its interesting to note that Amini *et al.* measured recorded a lifetime of 255 ns for $[Ru(tpy)_2]^{2+}$ at 160 K in butyronitrile and calculated an associated Huang-

Rhys factor of S = 0.55 at that temperature.[23] Bhuiyan *et al.* recorded a room temperature lifetime of 140 ns using Z-$[Ru(tpy)_2]^{2+}$ material substantively the same as that used for our Huang-Rhys analysis (the excited state lifetime recorded for our material was 99 ns +/- 22 ns in aerated dmso).[3] The 298 K Huang-Rhys factor calculated for our material is S = 0.53 ± 0.03, a remarkable similarity in lifetime and Huang-Rhys distortion given the four orders of magnitude across their excited state lifetimes.

5.2.3.3 Huang-Rhys analysis 298 K $[Ir(bpy)_3][PF_6]_3$ and Z-$[Ir(bpy)_3]^{3+}$

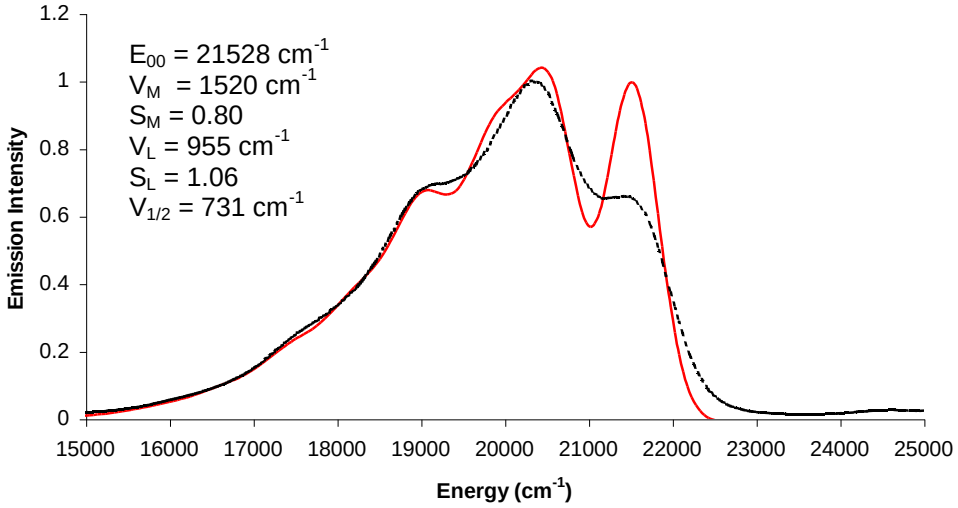

Figure 5.27: Spectral two mode fitting results of $[Ir(bpy)_3][PF_6]_3$ (1.1×10^{-5} M) at 298 K dissolved in butyronitrile. Experimental spectrum (- - -), calculated (—). Excitation 319 nm and slit width 5 nm.

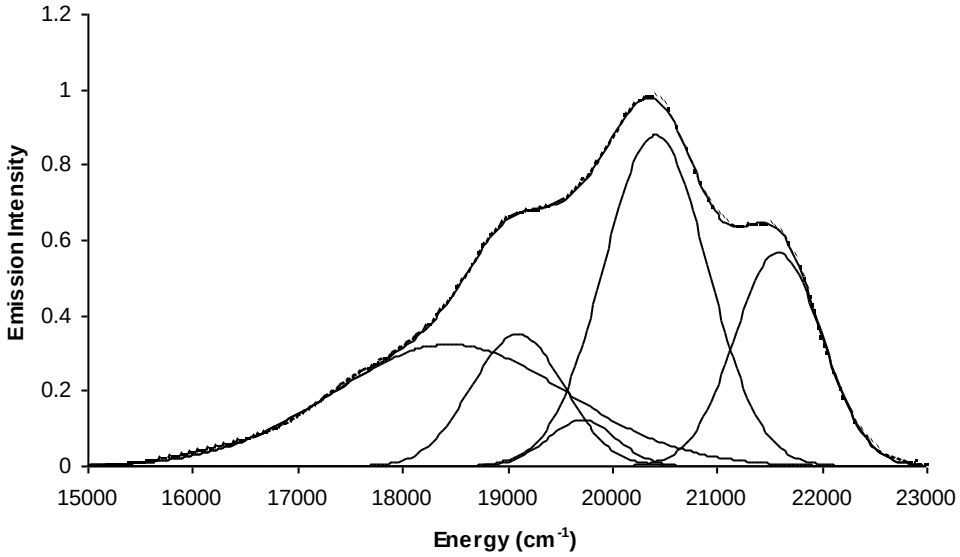

Figure 5.28: Spectral deconvolution of $[Ir(bpy)_3][PF_6]_3$ (1.1×10^{-5} M) emission profile at 298 K in butyronitrile. Experimental spectrum (- - -), calculated (—). Excitation 319 nm and Slit width 5 nm.

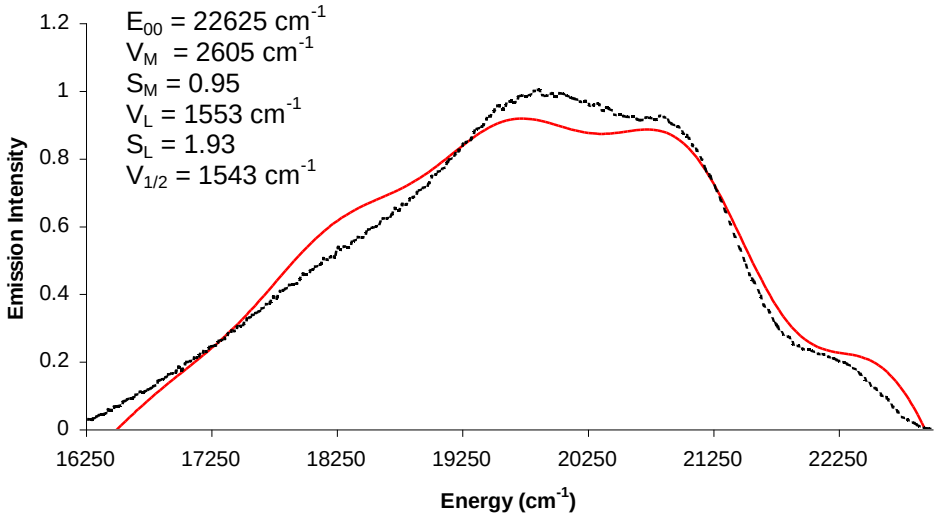

Figure 5.29: Spectral two mode fitting results of Z-$[Ir(bpy)_3]^{3+}$ (1 $[Ir(bpy)_3]^{3+}$ per 18 supercages) at 298 K dispersed in butyronitrile. Experimental spectrum (- - -), calculated (—). Excitation 319 nm and Slit width 5 nm.

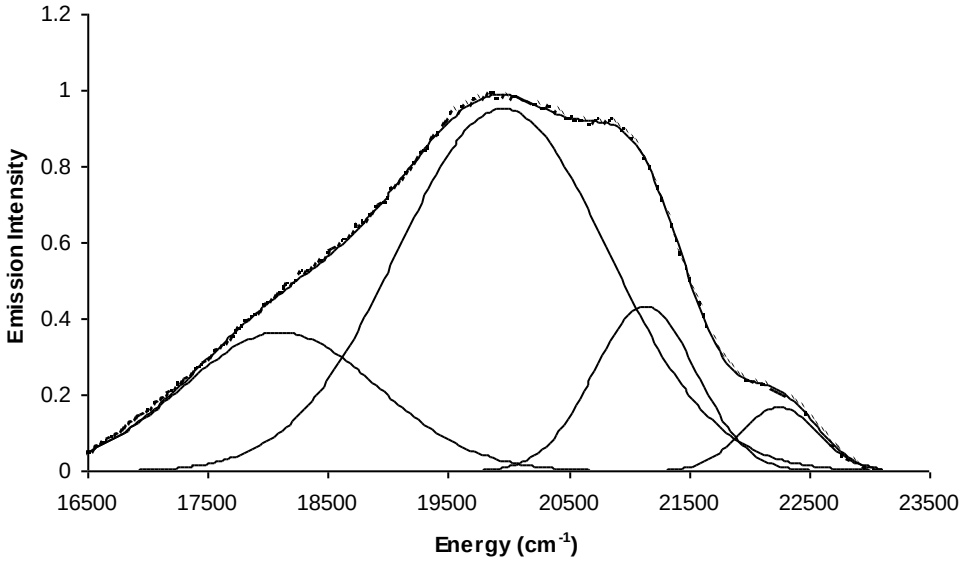

Figure 5.30: Spectral deconvolution of Z-$[Ir(bpy)_3]^{3+}$ (1 $[Ir(bpy)_3]^{2+}$ per 18 supercages) emission profile at 298 K dispersed in butyronitrile. Experimental spectrum (- - -), calculated (—). Excitation 319 nm and slit width 5 nm.

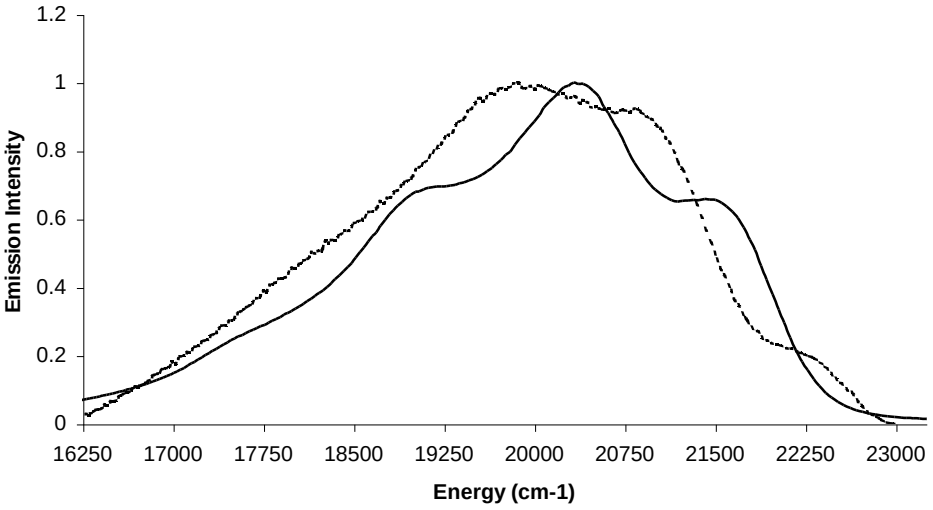

Figure 5.31: Emission spectrum comparison of solution phase $[Ir(bpy)_3][PF_6]_3$ (1.1 x10^{-5} M) (—) and Z-$[Ir(bpy)_3]^{3+}$ (1 $[Ir(bpy)_3]^{2+}$ per 18 supercages) at 298 K dispersed (- - -) in butyronitrile. Excitation 319 nm and slit width 5 nm for both samples.

Ideal fitting of the iridium polypyridyl luminescence data once again proved difficult. The spectra of both of the complexes studied, in contrast to the

ruthenium materials, exhibit vibrational progressions at room temperature. The fit for the Z-$[Ir(bpy)_3]^{3+}$ material follows the peak separation and relative intensities reasonably well at shorter wavelengths but deviates at around 19000 cm^{-1}. The two-mode fit for the $[Ir(bpy)_3][PF_6]_3$ (Figure 5.27) appears to underestimate the degree of distortion of the molecule, so care must be taken in reference to the extracted parameters. What can be safely concluded is the FWHM going from solution phase to zeolite entrapped is substantially broadened, nearly doubling in value. Although the fit is imperfect, by inspection of the deconvoluted spectral profile (Figure 5.28 and Figure 5.30), a much wider Gaussian distribution appears crucial and appropriate to model the data. Additional contributions to vibronic progression could also broaden the FWHM or indeed the broadening may reflect the heterogeneity of the environment with respect to the orientation of the complex within the cage. With Z-$Ir(bpy)_3^{2+}$ the highest energy band is drastically reduced in intensity whilst the low and mid energy resolved progressions are enhanced. Comparison of the deconvoluted spectra (Figure 5.28 and 5.30) also demonstrates pronounced changes in the emission envelopes.

Comparing the emission spectra of the entrapped and free $[Ir(bpy)_3][PF_6]_3$, the zeolite-entrapped materials are blue shifted as reported for the 77 K measurements, with differences between the progressions of 18 nm, 14 nm and 19 nm going from high to low energy (Figure 5.27). The nature of blue shift is attributed to interactions with the zeolites polar nanocavity as discussed previously, the excited state being more diffuse in $[Ir(bpy)_3]^{3+}$ and less well stabilised in polar environments (*vide supra*). The excited state lifetime of the zeolite entrapped $[Ir(bpy)_3]^{3+}$ was ~1030 ns in aerated dmso compared to 345 ns in aerated acetonitrile. This increase in excited state lifetime is likely due to a reduction in k_{nr} due to the tight steric fit of the zeolite pore and is further evidence of the decrease in excited state distortion imposed by the zeolite.

5.2.3.4 Huang-Rhys analysis 298 K $[Ir(tpy)_2][PF_6]_3$ and Z-$[Ir(tpy)_2]^{3+}$

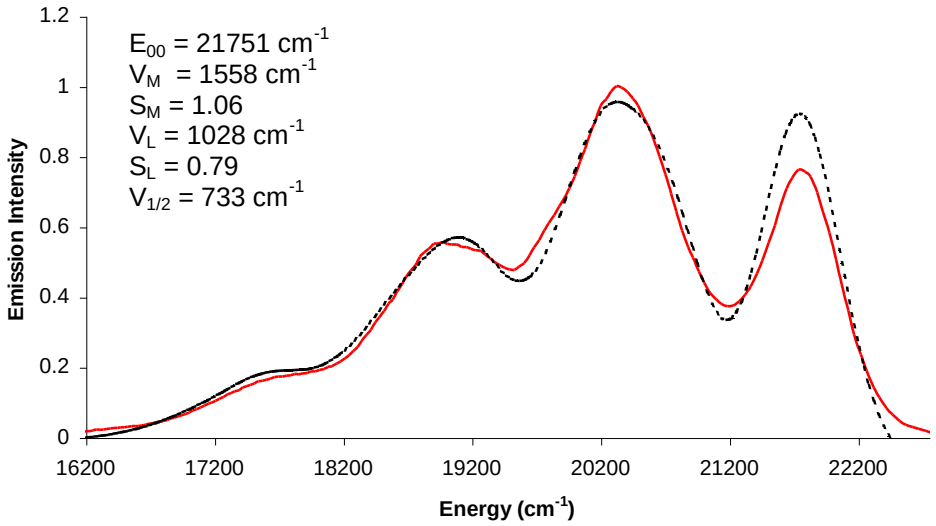

Figure 5.30: Spectral two mode fitting results of $[Ir(tpy)_2][PF_6]_3$ (1.25×10^{-5} M) at 298 K dissolved in butyronitrile. Experimental spectrum (- - -), calculated (—). Slit width 5 nm and excitation at 350 nm.

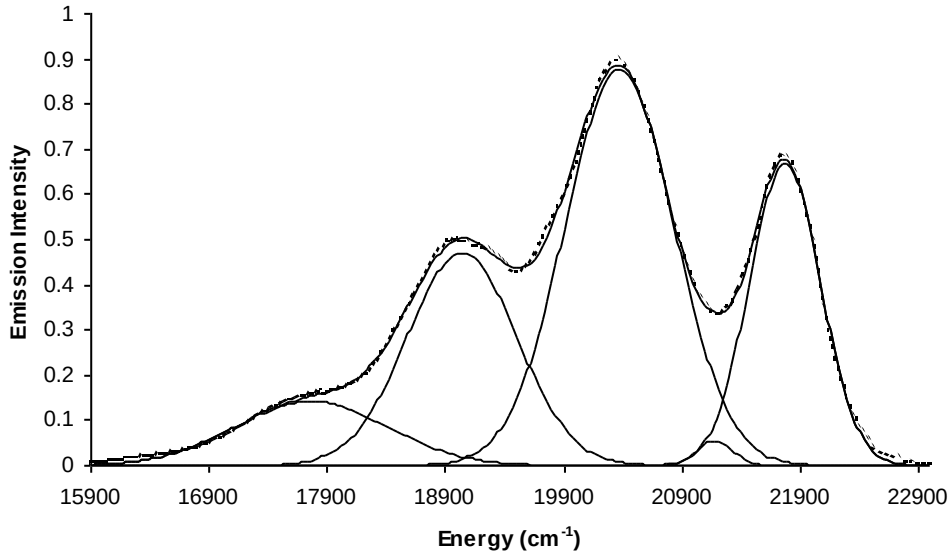

Figure 5.31: Spectral deconvolution of $[Ir(tpy)_2][PF_6]_3$ (1.25×10^{-5} M) emission profile at 298 K in butyronitrile. Experimental spectrum (- - -), calculated (—). Slit width 5 nm and excitation at 350 nm.

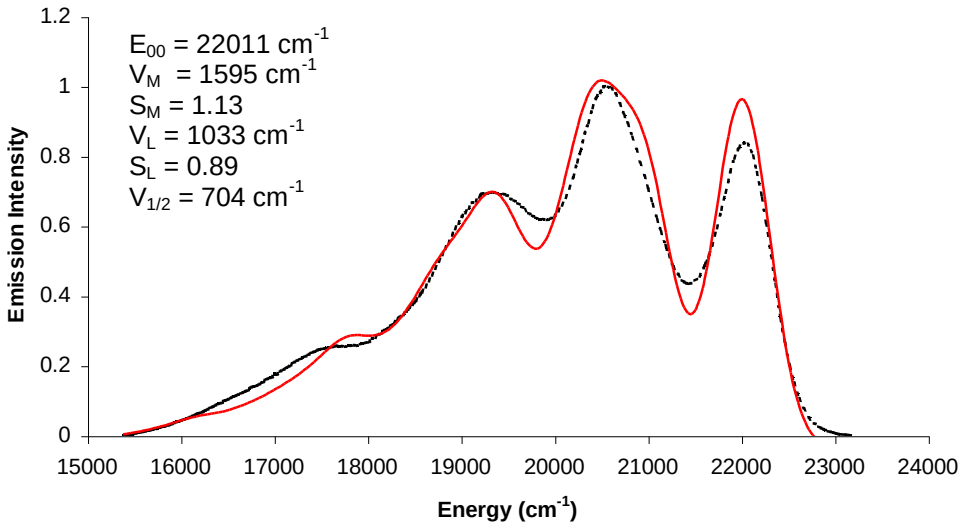

Figure 5.32: Spectral two-mode fitting results of Z-$[Ir(tpy)_2]^{3+}$ (1 $[Ir(tpy)_2]^{3+}$ per 36 supercages) at 298 K dispersed in butyronitrile. Experimental spectrum (- - -), calculated (—). Slit width 5 nm and excitation 330 nm.

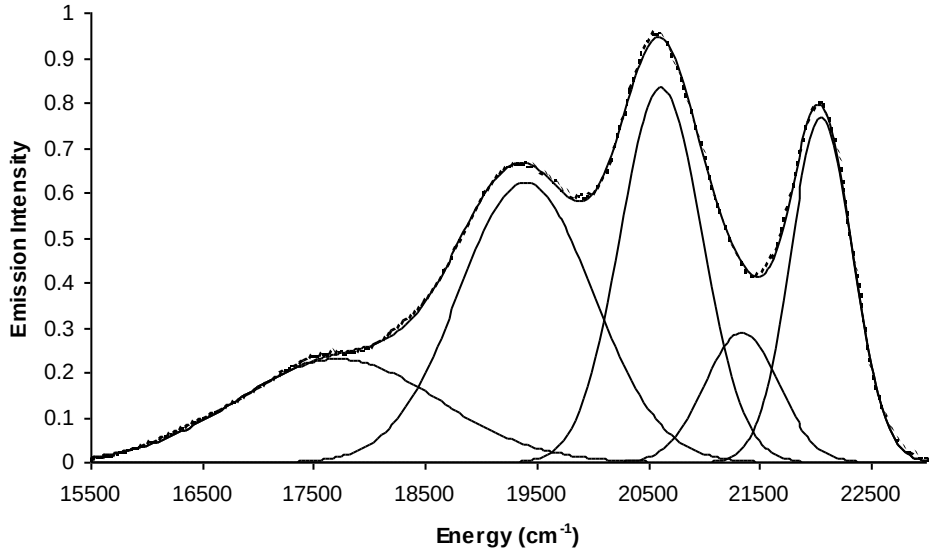

Figure 5.33: Spectral deconvolution of Z-$[Ir(tpy)_2]^{3+}$ (1 $[Ir(tpy)_2]^{3+}$ per 36 supercages) emission profile at 298 K in butyronitrile. Experimental spectrum (- - -), calculated (—). Excitation 330 nm and slit width 5 nm.

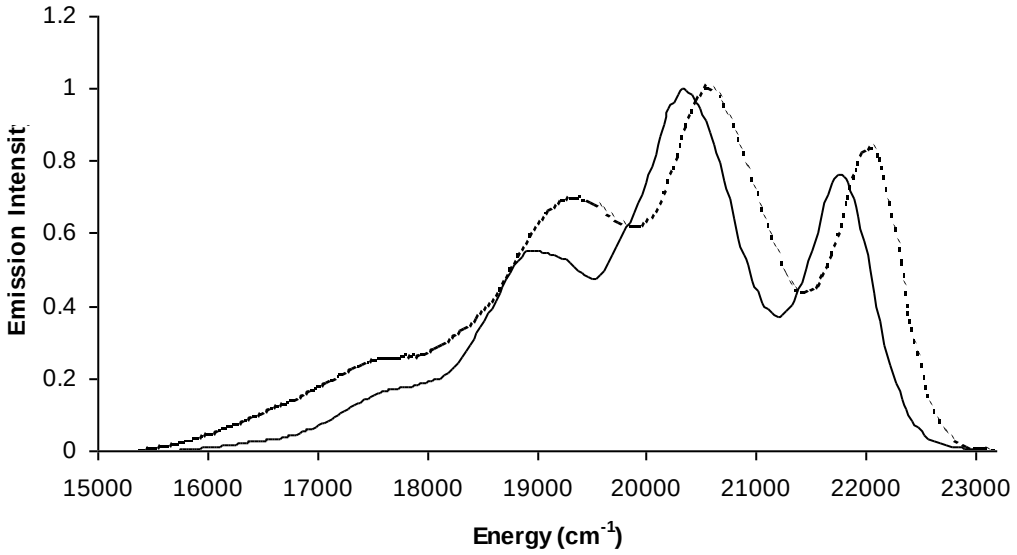

Figure 5.34: Emission spectrum comparison of solution phase $[Ir(tpy)_2][PF_6]_3$ (1.25×10^{-5} M) (—) and Z-$[Ir(tpy)_2]^{3+}$ (1 $[Ir(tpy)_2]^{3+}$ per 36 supercages) at 298 K dispersed (- - -) in butyronitrile. Excitation at 350 nm and 330 nm respectively and slit width was 5 nm for both samples.

Finally the iridium bis-terpyridine complexes $[Ir(tpy)_2][PF_6]_3$ and Z-$[Ir(tpy)_2]^{3+}$ were examined. The fitting model again proved to be somewhat deficient in fully describing the experimental data, underestimating the degree of distortion of the Z-$[Ir(tpy)_2]^{3+}$ and overestimating it in the case of $[Ir(tpy)_2][PF_6]_3$ based on the two highest energy peak intensities of the fitting results (Figure 5.30 and 5.32). However based on the FWHM peak widths and the ratios of the vibrational progressions for the comparison of the two spectra (Figure 5.34) it appears that the Z-$[Ir(tpy)_2]^{3+}$ is less distorted than $[Ir(tpy)_2][PF_6]_3$ on the basis of the ratio of the first two high energies peaks. The blue shifted emission is evident again and is attributed to the same phenomenon as previously described. Based on the calculated Huang-Rhys factor $S_M = 1.06$ and $S_M = 1.13$ and $S_L = 0.79$ and $S_L = 0.89$ for $[Ir(tpy)_2][PF_6]_3$ and Z-$[Ir(tpy)_2]^{3+}$ respectively it appears that they are equally distorted in their excited state. However the model overestimates the degree of distortion of $[Ir(tpy)_2][PF_6]_3$ so care must be exercised in interpreting the extracted factors. It does appear however that the zeolite material undergoes less excited state distortion then in solution. Comparison of the excited state lifetimes is also suggestive of

decreased excited state distortion. The lifetime of Z-$[Ir(tpy)_2]^{3+}$ in aerated dmso is ~1000 ns compared to an aerated acetonitrile solution of $[Ir(tpy)_2][PF_6]_3$ at 379 ns +/- 19 ns. The increase in the lifetime upon entrapment is likely a result of a decrease in k_{nr} as a result of the restricted vibrational motion available to the excited state complex within the zeolite pore.

Referring to table 5.1 and 5.2 it is apparent that compared to the medium energy modes, the low frequency modes are less distorted overall. This is expected in the context of the importance of C-C and CH coupled modes in excited state deactivation. Ru-N stretching modes did not appear to contribute much to overall deactivation with the low frequency progressions observed to be substantially higher than the ~400 cm^{-1} typically associated with these vibrations. However they may still be contributing to deactivation processes in zeolite but their relative weighing obscures their contribution. The source of the higher energy modes within the low energy progressions may be due to changes in relative importance of different vibrational modes upon inclusion. Dominant relaxation is through higher energy modes in solvent however in zeolite, lower energy modes that induce smaller changes in molecular volume may feature more prominently in deactivation processes.

5.3 Conclusions

Huang-Rhys analysis was performed on selected iridium and ruthenium polypyridyl species both entrapped in the pores of zeolite-Y and in solution in order to assess the impact of zeolite on the excited state distortion of guest transition metal complexes.

Excited state iridium and ruthenium polypyridyl complexes undergo deformation from their ground state equivalent. It was expected that the sterically tight zeolite cage coupled with the polar intrapore environment would result in less scope for molecular deformation as compared to solution phase. To assess this, the zeolite-entrapped material was compared to a 77 K glass (a very constrained environment) and to complexes in solution (a very unrestrained environment). From the 77 K analysis of $[Ru(bpy)_3][PF_6]_2$ and Z-$[Ru(bpy)_3]^{2+}$ it appears that the zeolite cage prevents excited state distortion to a greater degree than a frozen 77 K butyronitrile matrix along ligand aromatic stretch coordinates but possible enhanced distortion along bond bending coordinates.

The 77 K analysis of $[Ru(tpy)_2][PF_6]_2$ and Z-$[Ru(tpy)_2]^{2+}$ noted a similar degree of restriction as the frozen glass. This is indicative of a tighter intracage fit of the terpyridine species compared to the bipyridine analogues. This was not unexpected since previous studies by other groups outlined substantial changes in the photophysics of the complex upon encapsulation.

The low temperature of studies of Z-$[Ir(tpy)_2]^{3+}$ revealed a similar pattern. Although the fits were not as good, it strongly suggests intracage distortion similar in magnitude to the frozen matrix as found with the ruthenium terpyridine complex. The 77 K analysis of $[Ir(bpy)_3][PF_6]_3$ and Z-$[Ir(bpy)_3]^{3+}$ suggests strong excited state distortion along aromatic stretching coordinates when encapsulated implying a higher degree of mobility of the complex within the zeolite matrix as opposed to the 77 K glass where limited excited state distortion appears to occur.

The room temperature Huang-Rhys analysis of $[Ru(bpy)_3][PF_6]_2$ and Z-$[Ru(bpy)_3]^{2+}$ demonstrate no greater excited state distortion compared to solution phase. This was not unexpected considering the lack of spectral changes apparent upon encapsulation. Z-$[Ru(tpy)_2]^{2+}$ could not be directly compared to the parent complex as its non-luminescent at room temperature. However comparison to 77 K measurements demonstrates greater room temperature distortion of the complex within zeolite-Y compared to a frozen glass.

The room temperature Huang-Rhys analysis of $[Ir(bpy)_3][PF_6]_3$ and Z-$[Ir(bpy)_3]^{3+}$ initially implies a large distortion of the zeolite encapsulated complex compared to the solution phase. This result is unexpected, as the zeolite would be expected to limit distortion rather than promote it. The change in the relative intensities of progression peaks may lie with the inhomogeneity of the system resulting in the enhancement of differing vibrational modes compared to solution measurements, which do not necessarily result from excited state displacement. The room temperature results for $[Ir(tpy)_2][PF_6]_3$ and Z-$[Ir(tpy)_2]^{3+}$ materials are less certain. Apparent decreases in k_{nr} based on excited state lifetimes upon encapsulation certainly suggest a sterically hindered environment. The modelling of the emission spectra was non-ideal but from the data extracted it appears that the degree of distortion is similar to solution studies which would be quite unexpected (kinetic diameter of $[Ir(tpy)_2]^{3+}$ should be comparable to $[Ru(tpy)_2]^{2+}$), however similar to Z-$[Ir(bpy)_3]^{3+}$ the contribution from new lower energy vibrational modes may account for this unexpected result and highlights possible limitations of Huang-Rhys analysis on certain systems. In general the complexes studied undergo greater excited state distortion in solvent than within a zeolite host.

5.4 References

[1] Vargas,A.; Hauser, A.; Daku, L.M.L. *J. Chem. Theory Comput.* **2009**, *5,* 97–115.

[2] Huang, K.; Rhys, A. *Proc. R. Soc. Lond. A* , **1950**, *204*, 406-423.

[3] Bhuiyan, A.A.; Kincaid, J.R. *Inorg. Chem.* **1998**, *37,* 2525-2530.

[4] McClure, B.A.; Abrams, E.R.; Rack, J.J. *J. Am. Chem. Soc.*, **2010**, *132*, 5428–5436.

[5] Atkins, P.W. Physical Chemistry, 6th Edition, **1998**, Oxford University Press.

[6] Suppan, P. *Chemistry and Light;* Royal Society of Chemisty, **1994**.

[7] Damrauer, N.H.; Boussie, T.R.; Devenney, M; McCusker, J.K. *J. Am. Chem. Soc.* **1997**, *119,* 8253-8268.

[8] Hartmann, P.; Leiner, M.J.P.; Sonja, D.; Lippitsch, M.E. Chemical Physics **1996**, *207*, 137-146.

[9] Caspar, J.V.; Meyer, T.J. Inorg. Chem. **1983**, *22*, 2444.

[10] Caspar, J. V.; Westmoreland, T. D.; Allen, G. H.; Bradley, P. G.;Meyer, T. J.; Woodruff, W. H. *J. Am. Chem. Soc.* **1984**, *106*, 3492–3500.

[11] Hartmann, P.;Leiner, M.J.P.; Lippitsch, M.E. *J. Fluoresc.* **1995**, *5* ,179.

[12] Dressick, W. J.; Cline, J.; Demas, J.N.; DeGraff, B.A. *J. Am. Chem. Soc.* **1986**, *108*, 7567-7574.

[13] (a) Caspar, J. V.; Meyer, T. J. *J. Am. Chem. Soc.* **1983,** *105,* 5583.
(b) Caspar, J. V.; Sullivan, B. P.; Meyer, T. J. *Chem. Phys. Lett.* **1982,** *91*,91.
(c) Meyer, T. J. *Pure Appl. Chem.* **1986,** *58,* 1193.
(d) Kober, E. M.;Caspar, J. V.; Lumpkin, R. S.; Meyer, T. J. *J. Phys. Chem.* **1986,** *90*,3722.
(e) Barqawi, K. R.; Murtaza, Z.; Meyer, T. J. *J. Phys. Chem.* **1991,** *95*,47.

[14] Campagna, S.; Puntoriero, F.; Nastasi, F.; Bergamini, G.; Balzani, V. *Top. Curr. Chem.* **2007**, *280*, 117-214.

[15] Constable, E. *J. Chem. Soc. Dalton Trans.* **1985**, *12*, 2687.

[16] Kober, E.M.; Meyer, T.J. *Inorg. Chem.* **1985**, *24*, 106.

[17] Strommen, D.P.; Mallick, P.K.; Danzer, G.D.; Lumpkin, R.S.; Kincaid, J.R. *J. Phys. Chem.* **1990**, *94,* 1357.

[18] Burger, K.; Wagner, F.E.; Vértes, A; Bencze, É.; Mink, J.; Labádi, I.; Nemes-Vetéssy, Z.S. *J. Phys. Chem. Solids* 2001, *62*, 2059.

[19] Coe, B.J.; Thompson, D.W.;Christopher C.T.; Schoonover, J.R.; Meyer T.J. *Inorg. Chem.* **1995***, 34,* 3385.

[20] Biner, M.; Burgi, H.-B.; Ludi, A.; Röhr C. *J. Am. Chem. Soc.* **1992**, *114*, 5197.

[21] Lashgari, K.; Kritikos, M. Norrestam, R.; Norrby, T. *Acta Cryst.* **1999**, *C55*, 64.

[22] Maruszewski, K.; Kincaid, J.R. *Inorg. Chem.* **1995**, *34*, 2002.

[23] Amini, A.; Anthony Harriman.;A.; Mayeux, A. *Phys. Chem.Chem. Phys.* **2004**, *6*, 1157.

[24] Collin, J.P.; Dixon, I.M.; Sauvage, J.P.; Williams, J. A. G.;Barigelletti, F.; Flamigni, L. *J. Am. Chem. Soc.* **1999**, *121*, 5009–5016.

[25] Uppili, S.; Thomas, K.J. Crompton, E.M.; Ramamurthy, V. Langmuir **2000**, *16*, 265.

[26] Milder, S. J.; Gold, J. S.; Kliger, D. S. *J. Phys. Chem.* **1986**, *90*, 548.

[27] Vitale, M.; Castagnola, N. B.; Ortins, N. J.; Brooke, J. A.; Vaidyalingam, A.; Dutta, P. K. *J. Phys. Chem. B.* **1999**, *103*, 2408.

[28] Coutant, M.A.; Le, T.; Castagnola, N.; Dutta, P.K. *J. Phys. Chem. B.* **2000**, *104,* 10783-10788.

[29] Turbeville, W.; Robins, D.S.; Dutta, P.K. *J. Phys. Chem.* **1992**, *96,* 5024-5029.

[30] Caspar, J.V.;Westmoreland, T.D.; Allen, G.H.; Bradley, P.G.;Meyer, T.J.; Woodruff, W. H. J. Am. Chem. Soc. 1984, 106, 3492.

[31] Caspar, J.V.; Meyer,T.J. Inorg. Chem. 1983, 22, 2444.

Chapter 6

Interactions and energy transfer between selected iridium polypyridyl complexes and europium bis-bipyridine

6.0 Introduction

Lanthanide luminescence has attracted considerable attention due to its wide variety of applications across organic light emitting diodes,[1,2] sensors,[3,4] immunoassays and complexes for luminescent imaging.[5,6,7,8] Many lanthanide ions exhibit useful f-f line emission spectra from the visible to the near infrared.[9] The f-f transitions are Laporte forbidden resulting in long lived excited states, up to milliseconds for terbium and europium ions. The Laporte forbidden character of their transitions means they have very poor absorption coefficients. The f electrons are shielded by outer core 5s and 5p electrons and generally are not involved in bonding. However when lanthanides are bound to suitable light absorbing organic ligands, energy transfer from the ligand triplet state to the emissive levels of the ligated lanthanide ion can occur (ligation is not always necessary however). Figure 6.1 shows an energy level diagram for such sensitisation of europium by an organic ligand.

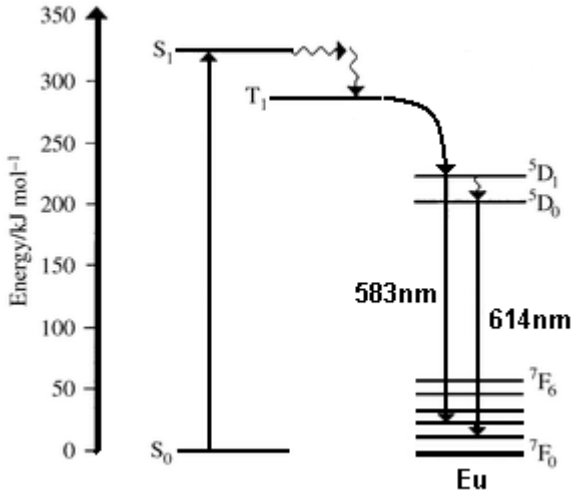

Figure 6.1: Energy diagram showing the energy levels of the organic ligand and the energy accepting lanthanide, europium (Andrew *et al. J. Chem. Soc. Perkin Trans. 2* **2000**, *7*, 1281).[10]

The luminescence emission profile of the lanthanides are narrow and have well defined wavelengths as a result of their unfilled 4f orbitals, with only certain energy levels emissive in nature. This leads to readily observable fine structure (Figure 6.3) and considering the forbidden nature of the f-f

transitions, long-lived excited state lifetimes are typically observed.[11] The choice of ligand for inducing luminescence in a trivalent cation depends on the energy of the emissive state of the lanthanide (the energy of the triplet excited state of the appended phosphor must lie above the lanthanide emissive state) and ability of the ligand to coordinate to the lanthanide to help exclude inner sphere water molecules, which are very effective quenchers of lanthanide luminescence. Figure 6.2 shows the energy levels of various lanthanides, with the emissive levels noted by the black dots.[11]

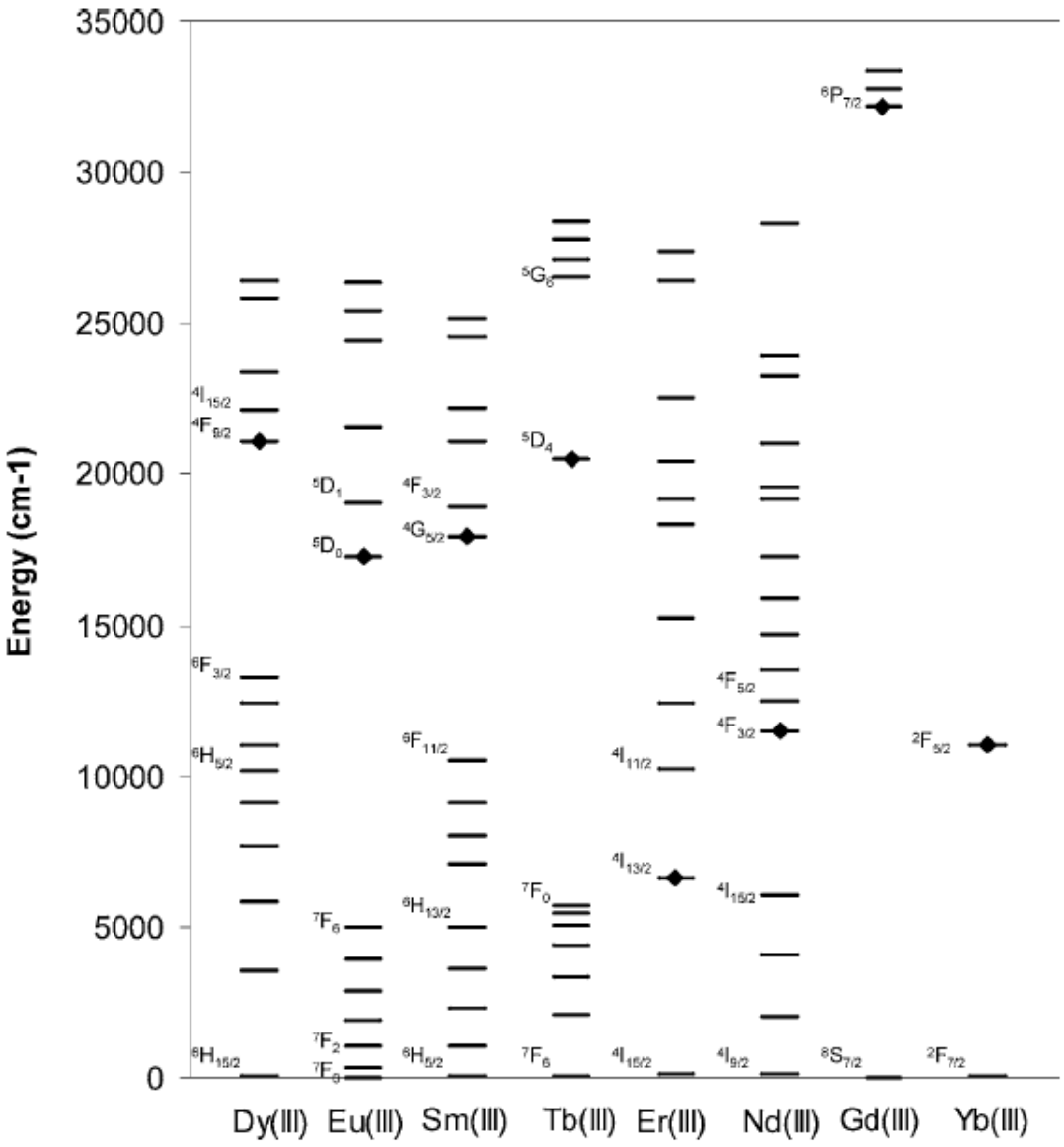

Figure 6.2: Energy levels for selected luminescent lanthanides (Hamila *et al.*. *J. Fluoresc*. **2005**, *4*, 529).[11] The emissive levels are indicated by black dots.

6.0.1 Lanthanide sensitisation with organic complexes

As stated earlier in order to effectively populate the lanthanide f-f states and take advantage of the luminescence properties of the lanthanide ions, they are typically attached to an 'antenna' which harvests light and transfers the energy to the metal ion primarily via a Dexter type mechanism. Organic ligands bound to the ion are one of the simplest antenna systems (Figure 6.3). The π-π* transitions absorb strongly in the UV and usually transfer their energy in one of two ways. The energy of the excited state ligand can be transferred to the central ion in the singlet state, or more commonly in the triplet state following intersystem crossing induced by the heavy atom effect of the proximal metal centre. The transferred energy can then be lost by the lanthanide via a radiative process if the energy transferred is above the emissive state of the lanthanide or may be lost non-radiatively if it lies below the emissive levels.

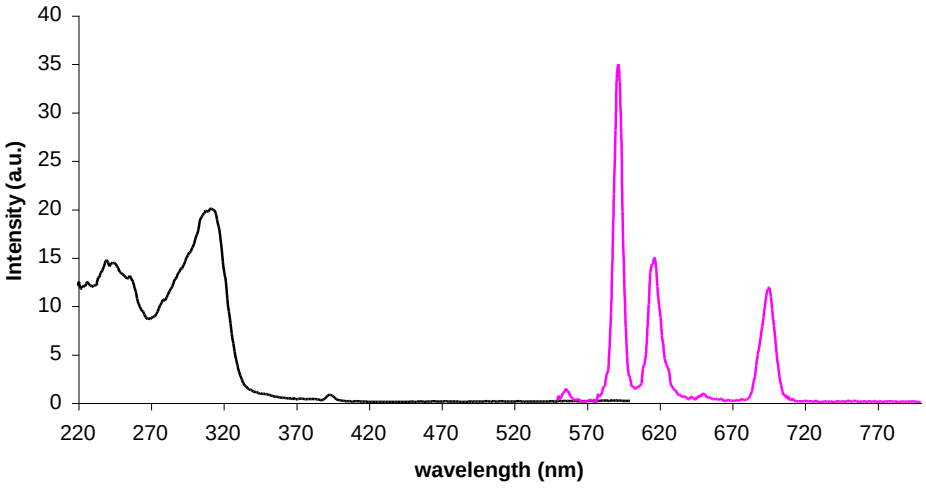

Figure 6.3: Excitation spectra of Z-$[Eu(bpy)_2]^{3+}$ (1 $[Eu(bpy)_2]^{3+}$ per 2 supercages) monitoring at 615 nm, slit width 5 nm (black trace) and emission spectra of Z-$[Eu(bpy)_2]^{3+}$ (1 $[Eu(bpy)_2]^{3+}$ per 2 supercages), excitation wavelength 319 nm, slit width 5 nm (magenta trace).

For many biological applications, sensitisation of lanthanides by visible irradiation rather than UV is desirable. One method is to modify the organic antenna in order to red shift its absorbance enabling visible excitation. Van Deun *et al.* reacted europium with 9-hydroxyphenal-1-one to form the complex shown in Figure 6.4.[12] They found this complex facilitated sensitisation of emissive europium levels at excitation wavelengths up to 475 nm. The absorption, excitation and emission profile of the complex is shown in Figure 6.5. They found that the complex had a quantum efficiency of only 0.5%. This was attributed to back energy transfer due to the similar energy levels of the sensitiser and acceptor. They later examined Nd (III), Yb (III) and Er (III) complexed with the same ligand and found the quantum efficiency to be enhanced relative to Eu (III), again attributing this to the lower emissive states of those lanthanide ions relative to the ligand excited state.[13]

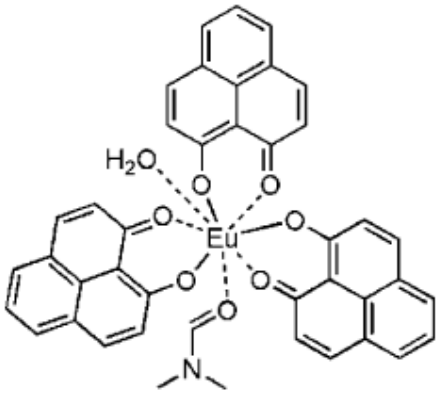

Figure 6.4: Europium 9-hydroxyphenal-1-one complex synthesized by Van Deun *et al. (Chem. Commun* **2005,** 590).[12]

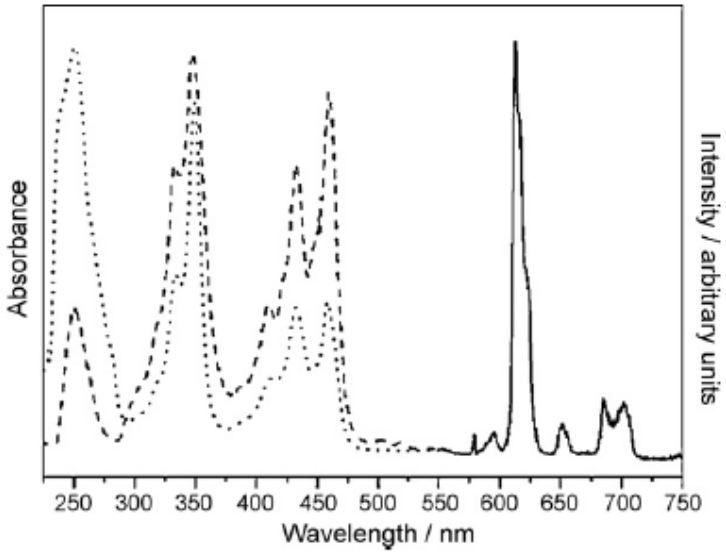

Figure 6.5: Absorption spectrum (dotted line), excitation spectrum (dashed line) and emission spectrum (solid line) of the Europium 9-hydroxyphenal-1-one complex in THF at room temperature (Van Deun *et al. Chem. Commun* **2005,** 590).[12]

Fu *et al.* synthesised the europium complex shown in Figure 6.6.[14] They found that the complex had a quantum efficiency of greater than 50% and could be excited at 800 nm via a two-photon process, albeit with laser excitation required.

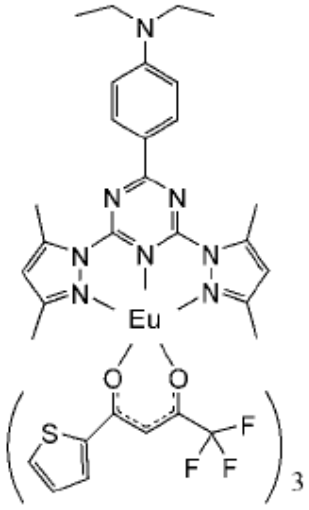

Figure 6.6: Europium complex capable of two-photon 800 nm excitation studied by Fu *et al.* (*Angew. Chem. Int. Ed.* **2005**, *44*, 747).[14]

6.0.2 Lanthanide sensitisation with d-block complexes.

The quest for visible sensitisation of lanthanides led to the study of d-block transition metal complexes as energy donors. The obvious starting point was the extensively studied $[Ru(bpy)_3]^{2+}$ due to its strong visible absorption and low lying triplet state.[15] The photophysical pathway of such a sensitisation of a lanthanide by a complex such as $[Ru(bpy)_3]^{2+}$ is shown in Figure 6.7. The rate of decay of the donor triplet luminescence should match rate of increase in emission of the acceptor species if the donor is acting as an antenna.

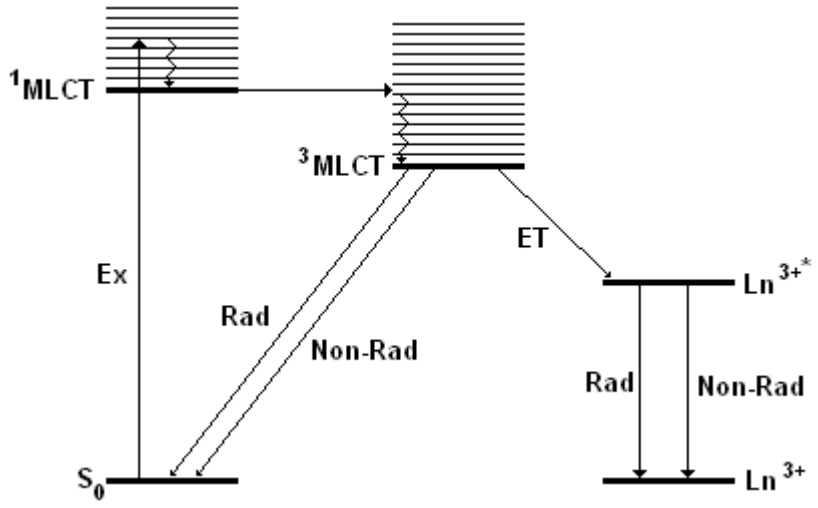

Figure 6.7: Schematic showing the pathway for a transition metal complex acting as an antenna to a luminescent lanthanide ion.

Van Veggel *et al.* used $[Ru(bpy)_3]^{2+}$ as an antenna for the NIR emitting lanthanide ions Nd (III) and Yb (III).[16] They synthesised the complex shown in Figure 6.9 and demonstrated successful sensitisation of the lanthanides. Figure 6.8 (top) shows the luminescence spectrum of both the $[(Nd_2\text{-}Ru)]^{2+}$ complex and $[(Yb_2\text{-}Ru)]^{2+}$ in DMSO, while bottom shows the excitation spectrum of $[(Nd_2\text{-}Ru)]^{2+}$ while monitoring the emission at 1060 nm (solid line) and the absorption spectrum of $[(Nd_2\text{-}Ru)]^{2+}$ (dashed line).

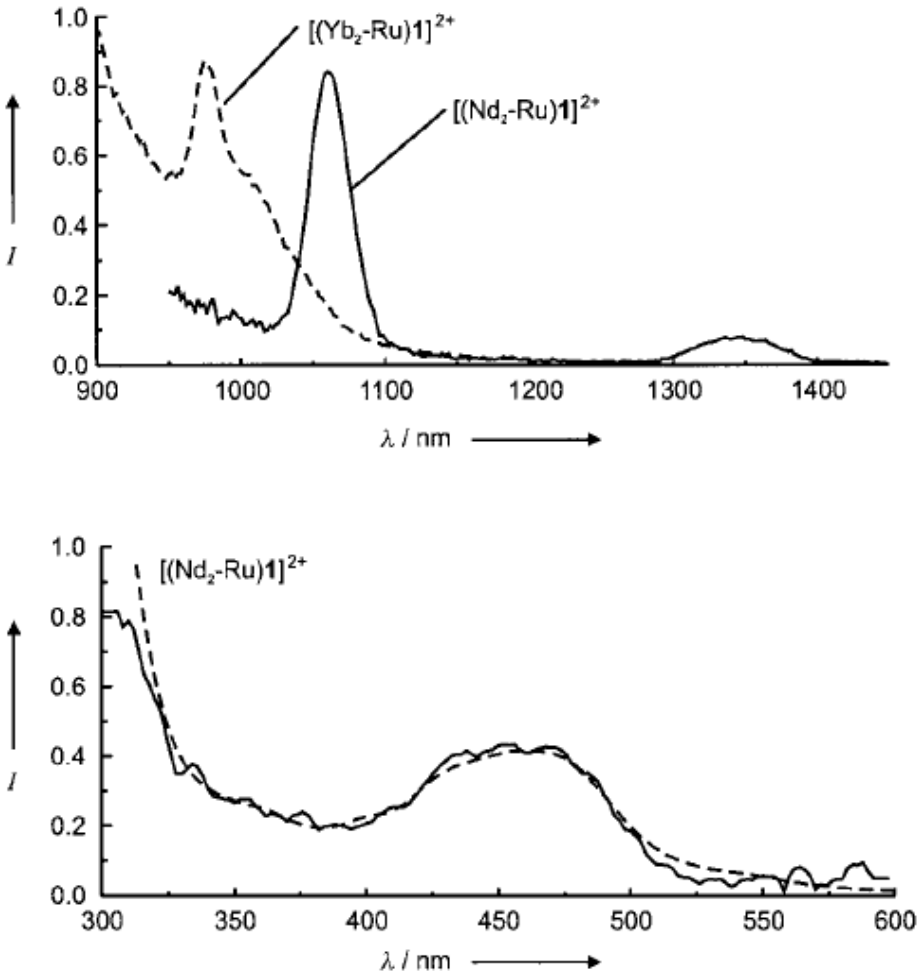

Figure 6.8: NIR luminescence spectrum of both the $[(Nd_2\text{-}Ru)]^{2+}$ complex and $[(Yb_2\text{-}Ru)]^{2+}$ in DMSO (10^{-5} M), while the bottom shows the excitation spectrum of $[(Nd_2\text{-}Ru)]^{2+}$ while monitoring the emission at 1060 nm (solid line) and the absorption spectrum of $[(Nd_2\text{-}Ru)]^{2+}$ (dashed line), (van Veggel *et al. Angew. Chem. Int. Ed*. **2000**, *39*, 4319).[16]

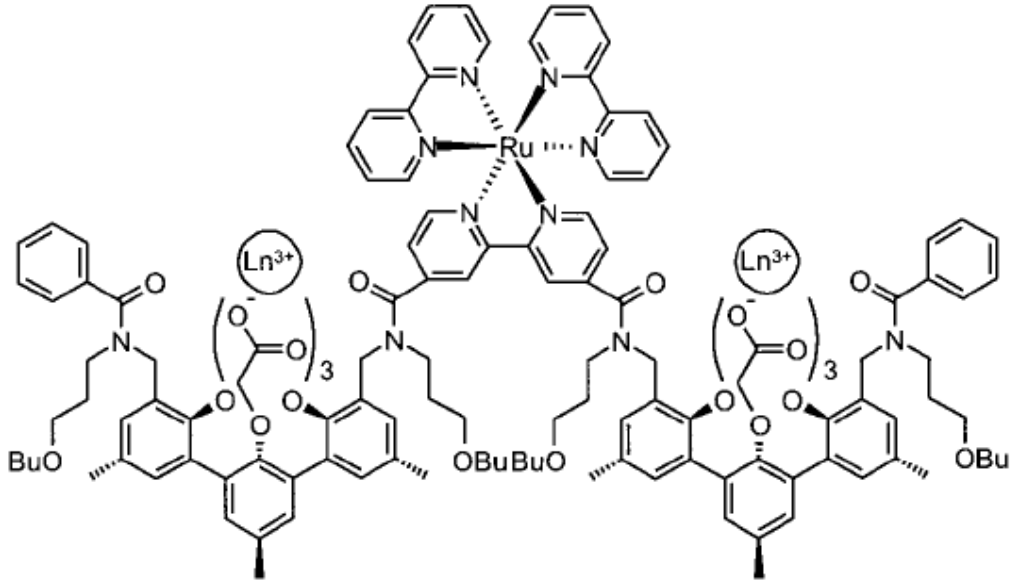

Figure 6.9: Bimetallic transition metal-lanthanide complex synthesised by Veggel *et al.* The Ln^{3+} ion was either Nd (III) or Yb (III), (*Angew. Chem. Int. Ed*. **2000**, *39*, 4319).[16]

Since then a large variety of different transition metals have been studied to assess their suitability as sensitisers to various lanthanide ions, including complexes of osmium,[17] platinum,[18] palladium,[19] gold,[20] rhenium, [21] chromium,[22] cobalt,[23] and zinc.[24] Complexes of iridium have also been used to sensitise lanthanide emission and will be considered in more detail due to their use in this work.

6.0.3 Europium sensitisation with Iridium complexes

De Cola *et al.* prepared the first iridium based transition metal antenna for europium excitation.[25] They reasoned that iridium complexes should possess sufficiently high triplet energy to enable europium luminescence after energy transfer. They prepared an iridium complex with two difluorophenyl ligands and one carboxylic acid functionalised triazole-pyridine bridging ligand to coordinate to a europium complex. The scheme for this reaction is shown in Figure 6.10. They found that partial energy transfer from the iridium centres to the europium occurred, with the white light emission observed for the sample upon excitation at 400 nm. The white light observed was due to a

combination of the residual emission from the blue-green iridium complex coupled with the red emission of the europium (Figure 6.11). The excited state lifetime of the lone iridium complex dropped from 1.4 μs to 0.48 μs in deuterated methanol after reaction with the europium complex. The energy transfer efficiency was determined to be 38%.

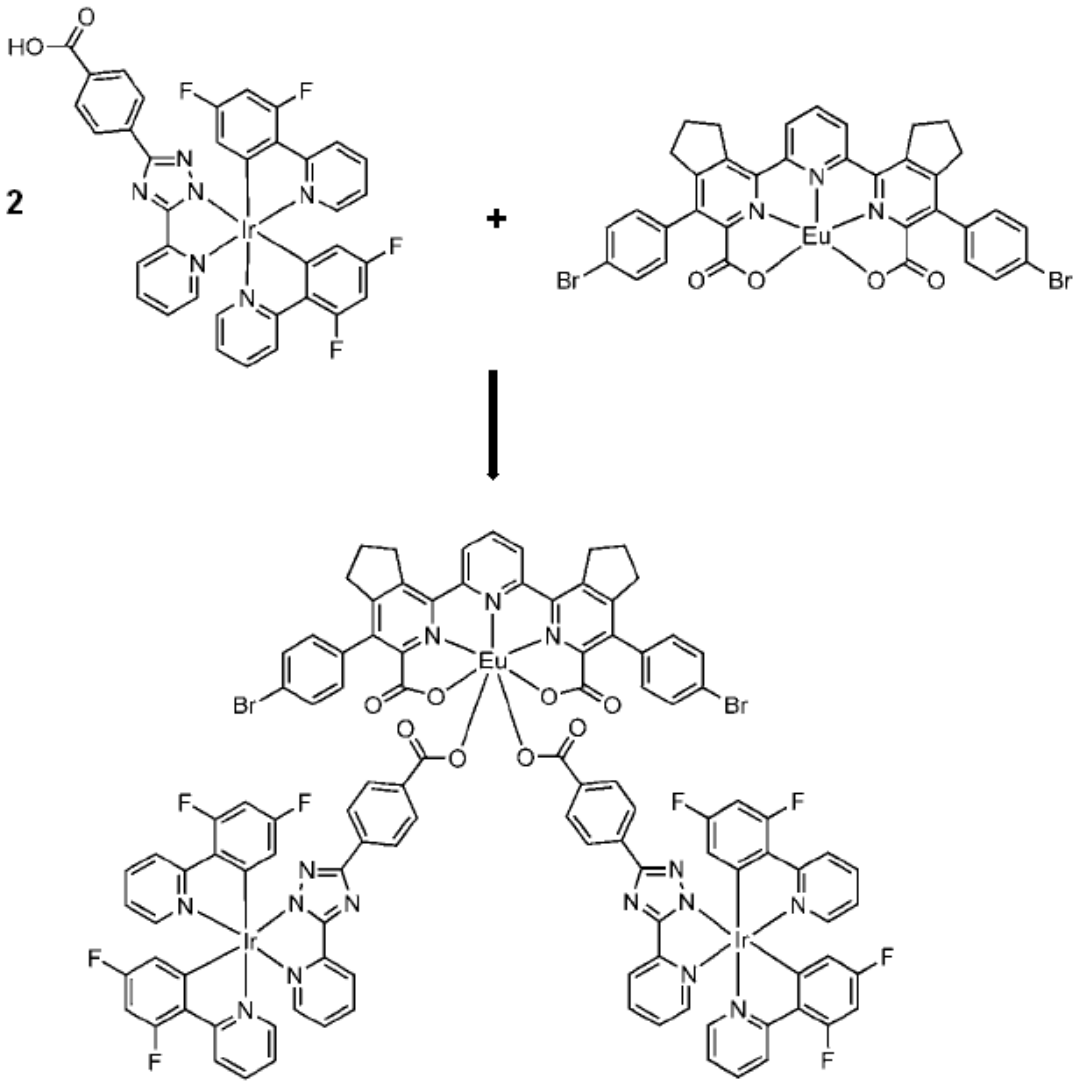

Figure 6.10: Reaction scheme for the white light emitting species bimetallic complex prepared by De Cola *et al.* (*Angew. Chem.Int. Ed.* **2005**, *44*, 1806).[25]

Chen *et al*. sought to enhance both the efficacy of energy transfer leading to emission from only the acceptor and to extend the excitation window of the sensitiser.[26] To this end they prepared the complex shown in Figure 6.12,

which has a central oxygen bound europium species surrounded by three iridium sensitisers. The calculated distance between the bimetallic centres was calculated to be around 6 Å in all cases. They found that MLCT energy transfer from the outer iridium complexes to the europium centre occurred at wavelengths up to 530 nm, demonstrating that the complex could emit red light under solar irradiation.

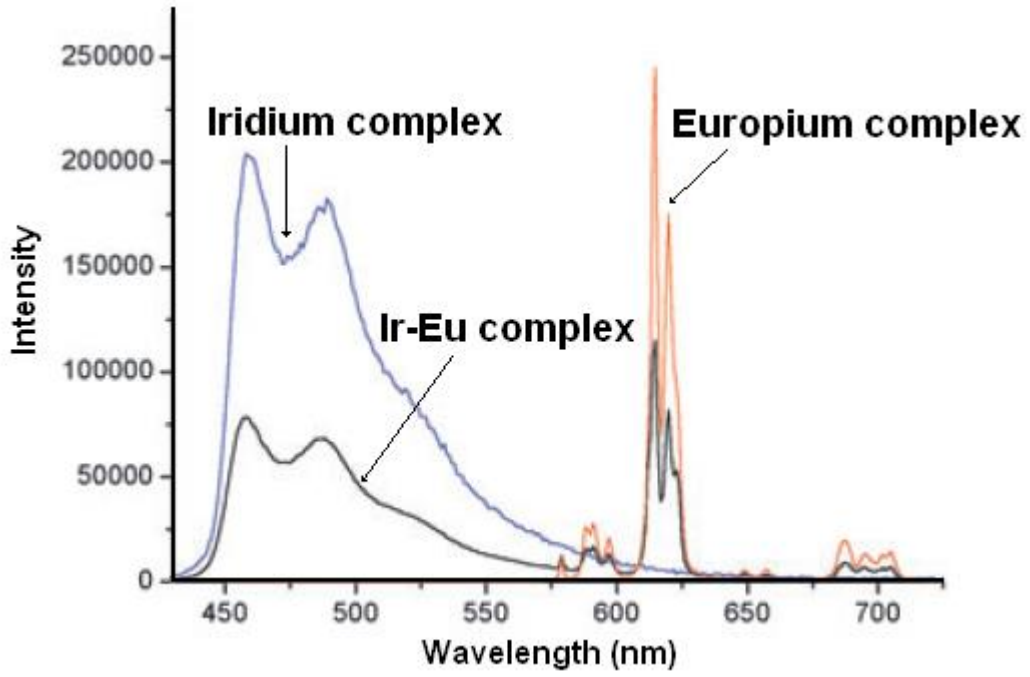

Figure 6.11: Steady state emission spectra of the complexes prepared by De Cola *et al.* The solo iridium complex was excited at 400 nm and the solo europium complex was excited at 350 nm. The bimetallic species was excited at 400 nm. Measurements were recorded in deuterated methanol. (De Cola *et al.*, *Angew. Chem.Int. Ed.* **2005**, *44*, 1806).[25]

The same group was interested in assessing the influence of triplet energy levels of bridging ligands on the efficiency of energy transfer processes in bimetallic Ir-Eu complexes.[27] They synthesised a diazole bridging ligand, and selectively functionalised it to alter its triplet energy levels (Figure 6.13). They found that as the triplet energy level of the bridging ligand decreased, the emission from the iridium moiety also decreased with concomitant increase in emission from the europium. Complete ET was only achieved when the triplet

energy level of the bridging ligand was lower than the triplet MLCT energy level of the donor iridium moiety. In the other cases where the energy levels were higher or even close to that of the bridging ligand incomplete ET was observed.

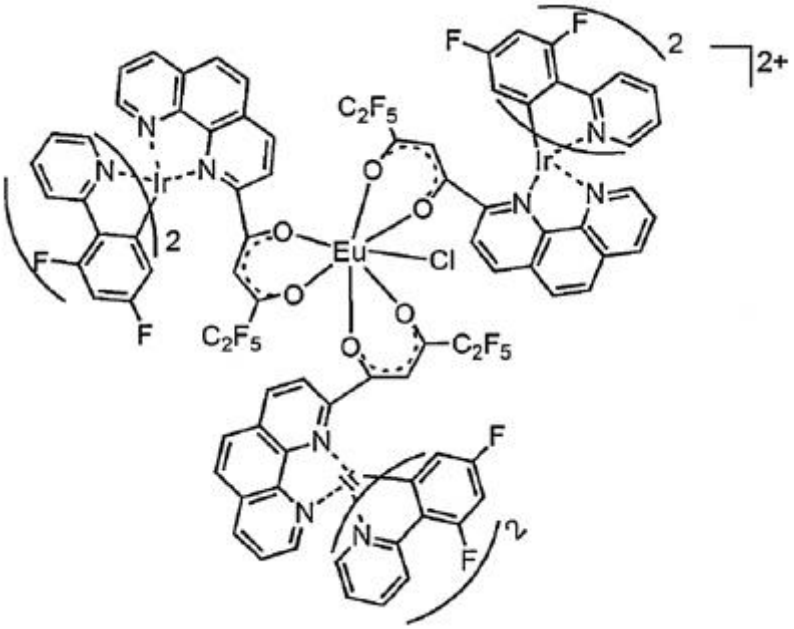

Figure 6.12: Bimetallic complex prepared by Chen *et al.* (*Inorg. Chem.* **2008**, *47*, 2507).[26]

The exact nature of lanthanide sensitisation processes is still a matter of much debate. Studies carried out by Ward *et al.* demonstrated sensitisation of lanthanides by at least three different mechanisms, namely Förster-type, Dexter-type and redox mediated energy transfer.[28] The last mechanism is peculiar to Eu(III) or Yb(III) acceptors and involves photoinduced electron transfer from an excited state donor molecule to a lanthanide ion producing a charge separated state D^{*+}-Ln(II). Rapid back electron transfer can generate sufficient energy to leave the Ln(III) in an excited state which subsequently relaxes by emission. There is no dependence on spectral overlap due to the state being generated by electron transfer.

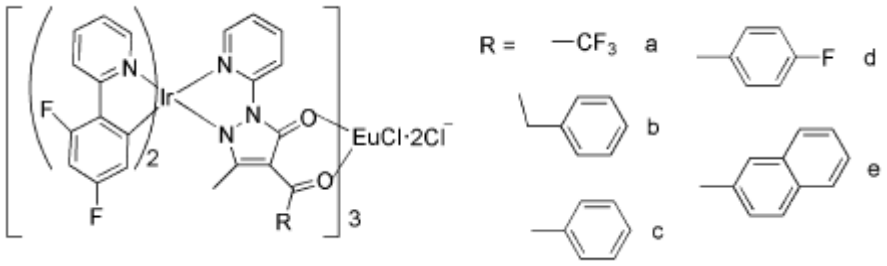

Figure 6.13: Complexes synthesised by Jiang *et al*. (*Dalton Trans*, **2011**, *40*, 11410).[27]

6.0.4 Zeolites as hosts for lanthanides

The porous structure and ion-exchange capability of zeolite materials makes them an attractive host material for lanthanide materials. The materials can be ion-exchanged with a wide variety of lanthanide cations and can be subsequently sequestered via the 'ship in a bottle synthesis' similar to the materials studied in earlier chapters. The ligand, similar to solution studies can act not only as a sensitiser but also to protect the ion from intrazeolitic water. The zeolite framework has low vibrational quanta which limits the degree of non-radiative deactivation available to the guest materials.[29]

6.0.5 Luminescence from europium exchanged zeolites

Luminescence can be observed from europium-exchanged zeolite even in the absence of ligands. Alvaro *et al.* noted emission from Z-Eu^{3+} even when the zeolite material was fully hydrated.[30] They attributed this to the different possible locations that a Eu^{3+} ion can occupy within the zeolite framework and reasoned that the ions located in the large cage would be coordinated to water whilst the cations located in the small sodalite cage could not due to steric constraints. The emission from these isolated ions is typically weak (laser excitation was employed) due to the greater propensity of the ion-exchange to take place in the larger pore rather than in the sodalite cages. The degree of sodalite exchange can be enhanced however, by calcination at

high temperatures.[31] The luminescent emission is greatly enhanced in the presence of suitable ligands.

Rosa *et al.* first examined the luminescence properties of $[Eu(bpy)_2]^{3+}$ supported *on* Zeolite-Y (rather than *in* Zeolite-Y).[32] They noted enhanced emission when $[Eu(bpy)_2]Cl_3$ was deposited on the zeolite material, but it was not clear what the cause of the enhancement was. It may have been due to the $[Eu(bpy)_2]^{3+}$ residing in larger outer irregular cavities resulting in partial exclusion of deactivating water, but this was unclear.

A comprehensive study of zeolite encapsulated europium complexed to a number of ligands was carried out by Alvaro *et al.*[30] (Figure 6.14).

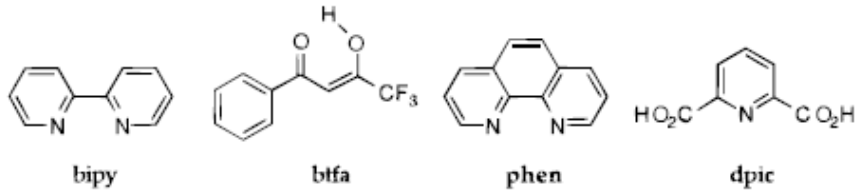

Figure 6.14: Ligands utilised by Alvaro *et al.* for study of zeolite entrapped europium complexes. (*J. Phys. Chem. B* **1998,** *102,* 8744).[30]

They prepared batches of europium-exchanged zeolite-Y of increasing concentration, then reacted the material with various ligands varying quantities from less than equi-molar with respect to the Eu^{3+} to three equivalents of ligand to Eu^{3+}. They noted the appearance of a medium intensity absorbance band at 500 nm in the diffuse reflectance spectra of the complexes formed (Figure 6.16). They attributed the band to hypersensitive transitions, their name deriving from the sensitivity of their intensity with respect to the local environment. In solution these bands are very weak, possessing extinctions coefficients of around 1-2 M^{-1} cm^{-1} (Figure 6.15).[33] These hypersensitive transitions correspond to $^5D_1 \leftarrow {}^7F_1$ and $^5D_2 \leftarrow {}^7F_0$ absorptions (both reside at higher energy than the main emissive level $^5D_0$).

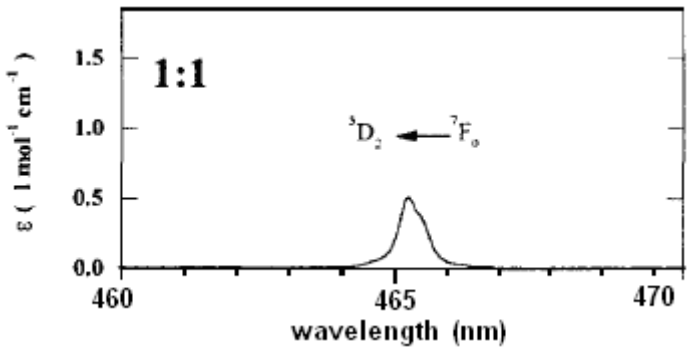

Figure 6.15: Room temperature absorption spectrum of the hypersensitive transition $^5D_2 \leftarrow {}^7F_0$ in $Eu(dpic)^+$ observed by Binnemans *et al.* (*Chem. Phys. Lett.* **1997**, *266*, 297).[33]

They hypothesized that with the dimensions of the cage little larger than the included species, large distortions in symmetry arise resulting in the observed band. They also found that the complexes excited state lifetime was longer in zeolite than in solution (up to 10-fold) and that the lifetime increased with increased loading of ligand. They believe that this increase is due to the steric crowding of the species within a pore making the complex more rigid effectively slowing the decay rate.

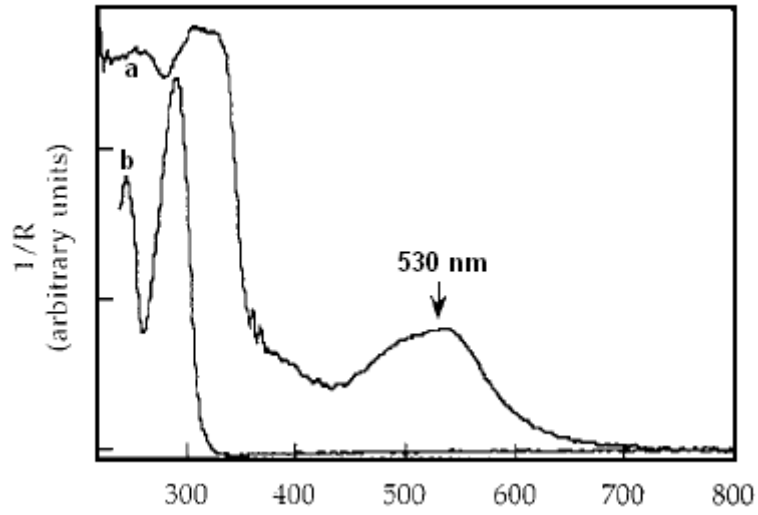

Figure 6.16: Diffuse reflectance spectrum of Z-$[Eu(bpy)_2]^{3+}$ material prepared by Alvaro *et al.*(Curve A) and UV-vis absorption spectrum of 2,2'-bipyridine in CH_2Cl_2 (curve B), (*J. Phys. Chem. B* **1998,** *102,* 8744).[30]

Given the evidence for intercage energy transfer between ruthenium and iron polypyridyl guest species, this chapter looked to establish if intercage energy transfer from entrapped iridium polypyridyl complexes to co-entrapped europium complexes was possible and to assess the efficiency of the process. To this end Z-$[Ir(bpy)_3]^{3+}$ and Z-$[Ir(tpy)^2]^{3+}$ were ion-exchanged with the same concentration of europium and the material treated with bipyridine in order to form the co-entrapped materials Z-$[Ir(tpy)_2]^{3+}[Eu(bpy)_2]^{3+}$ and Z-$[Ir(bpy)_3]^{3+}[Eu(bpy)_2]^{3+}$.

The acceptor complex $[Eu(bpy)_2]^{3+}$ was selected for inclusion based on two criteria. Firstly the bis-bipyridine complex is sufficiently large to be encapsulated and immobilised within the pore structure and secondly to determine if exploitation of the enhanced hypersensitive transition absorptivity for the purpose of europium excitation is feasible. The requirement of spectral overlap for energy transfer should be adequately met by the emission wavelengths of the iridium polypyridyl complexes under investigation. To our knowledge this is the first example of europium sensitisation using a transition metal complex within a zeolite matrix.

6.1 Experimental

6.1.1 Physical measurements

Luminescence measurements were carried out in both fluorescence and phosphorescence mode, and were performed in the same manner as previous experiments. The emission spectra represent the average of four separate emission intensity measurements. Excited state lifetimes were conducted in the same manner as previous outlined.

6.1.2 Preparation of materials

Z-$[Eu(bpy)_2]^{3+}$

Calcined Na-Y zeolite (11.91 g) was suspended in cold degassed deionised water at room temperature. The pH of this suspension was adjusted to pH 5.4 $\pm$ 0.1 using HCl (0.1 M). To this was added an aliquot of europium nitrate of desired concentration that was previous dissolved in pH adjusted deionised water (pH 3). This was stirred overnight, filtered and washed with deionised water until no Cl^- could be detected using silver nitrate solution (0.1 M). The Z-Eu^{3+} was dried, dispersed in ethanol and the required mass of 2,2'-bipyridine was added. This was refluxed overnight, filtered and washed with copious volumes of warm ethanol in order to remove excess ligand. This was then stirred in NaCl (10 % w/v) for one hour to remove any surface bound species and finally washed with deionised water until free of Cl^- ions, and dried in air.

Preparation of codoped Z-$[Ir(tpy)_2]^{3+}[Eu(bpy)_2]^{3+}$ and Z-$[Ir(bpy)_3]^{3+}[Eu(bpy)_2]^{3+}$

These were prepared in the exact manner as above only substituting previously prepared Z-$[Ir(tpy)_2]^{3+}$ (1 $[Ir(tpy)_2]^{3+}$ per 20 supercages) and Z-$[Ir(bpy)_3]^{3+}$ (1 $[Ir(bpy)_3]^{3+}$ per 26 supercages) for the zeolite-Y.

6.2 Results and discussion

6.2.1 Photophysical characterisation of undoped materials

6.2.1.1 Z-$[Eu(bpy)_2]^{3+}$

The phosphorescent excitation and emission spectra of Z-$[Eu(bpy)_2]^{3+}$ are shown in Figure 6.17. Upon excitation at the absorption λ_{max} of 319 nm, the typical structured europium emission was observed. The excitation spectrum yields a broad band at 319 nm typical of encapsulation of $[Eu(bpy)_2]^{3+}$.[30] Three major emission bands are observed at 592 nm, 612 nm and 700 nm corresponding to the transitions $^5D_0 \rightarrow {}^7F_1$, $^5D_0 \rightarrow {}^7F_2$, and $^5D_0 \rightarrow {}^7F_4$. The concentration of Z-$[Eu(bpy)_2]^{3+}$ was set high (1 $[Eu(bpy)_2]^{3+}$ per 2 supercages, 50% occupation) in order to ensure that most of the iridium polypyridyl complexes present are adjacent to an $[Eu(bpy)_2]^{3+}$ complex. This was to ensure that even inefficient energy transfer processes might be observed. The excitation spectrum was recorded in lieu of diffuse reflectance due to the persistent Fe impurities with large extinction coefficients occluding the spectral region of interest. The reason for the absence of the hypersensitive transition in the excitation spectrum is unclear, instrument conditions may play a part due to the use of phosphorescence settings utilising specific time windows, as excitation to $^5D_1$ and $^5D_2$ may also result in emission from these states (more common to observe emission from these upper states in non-aqueous media [34]) which are difficult to detect due to their weakness and differing decay times to $^5D_0$ emissions. Adjustment of the temporal conditions for the acquisitions did not remedy the problem. However, there is no reason to believe that the materials produced are radically different from those produced by Alvaro *et al.* as our emission spectra recorded correspond very well with the values they obtained and our method of material preparation was identical.

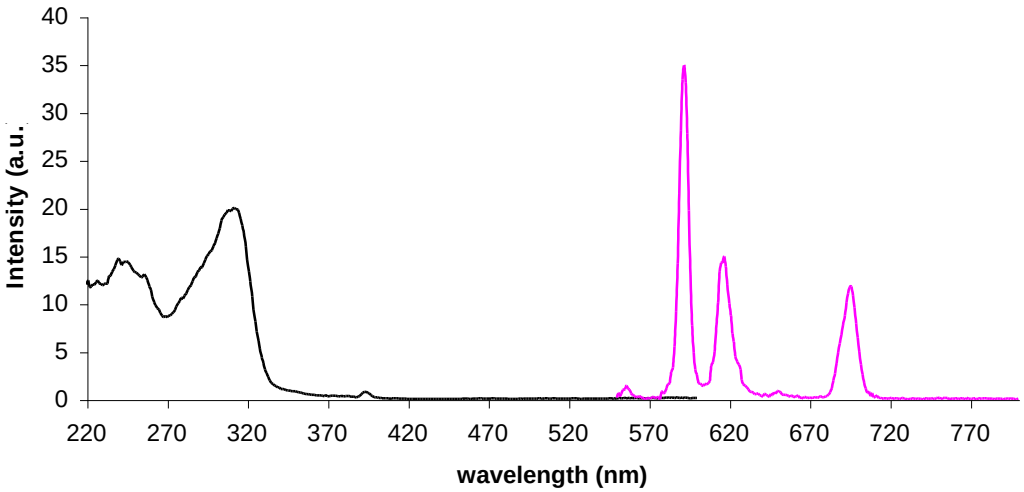

Figure 6.17: Excitation spectra of Z-$[Eu(bpy)_2]^{3+}$ (1 $[Eu(bpy)_2]^{3+}$ per 2 supercages) monitoring at 615 nm, slit width 5 nm (black trace) and emission spectra of Z-$[Eu(bpy)_2]^{3+}$ (1 $[Eu(bpy)_2]^{3+}$ per 2 supercages), excitation wavelength 319 nm, slit width 5 nm (magenta trace)

6.2.2 Photophysical characterisation of Z-$[Ir(tpy)_2]^{3+}[Eu(bpy)_2]^{3+}$ and Z-$[Ir(bpy)_3]^{3+}[Eu(bpy)_2]^{3+}$

6.2.2.1 Iridium polypyridyl luminescence

The photophysical characteristics of the iridium polypyridyls were described previously in chapter 4. In order to assess if energy transfer from the Iridium donor to the Europium acceptor is occurring the luminescence intensity of both Z-$[Ir(tpy)_2]^{3+}$ and Z-$[Ir(bpy)_3]^{3+}$ were compared before and after doping with $[Eu(bpy)_2]^{3+}$ (Figures 6.18 and 6.19). The Z-$[Ir(tpy)_2]^{3+}$ and Z-$[Ir(bpy)_3]^{3+}$ used for the doped and undoped samples were from the same synthetic batch. A modest drop in the emission intensity (~ 8 %) of Z-$[Ir(tpy)_2]^{3+}$ was observed upon doping with $[Eu(bpy)_2]^{3+}$. However the Z-$[Ir(bpy)_3]^{3+}$ material showed minimal changes in emission profile, a very small reduction in the emission on the blue edge of the spectrum, not strongly suggestive of any energy transfer processes.

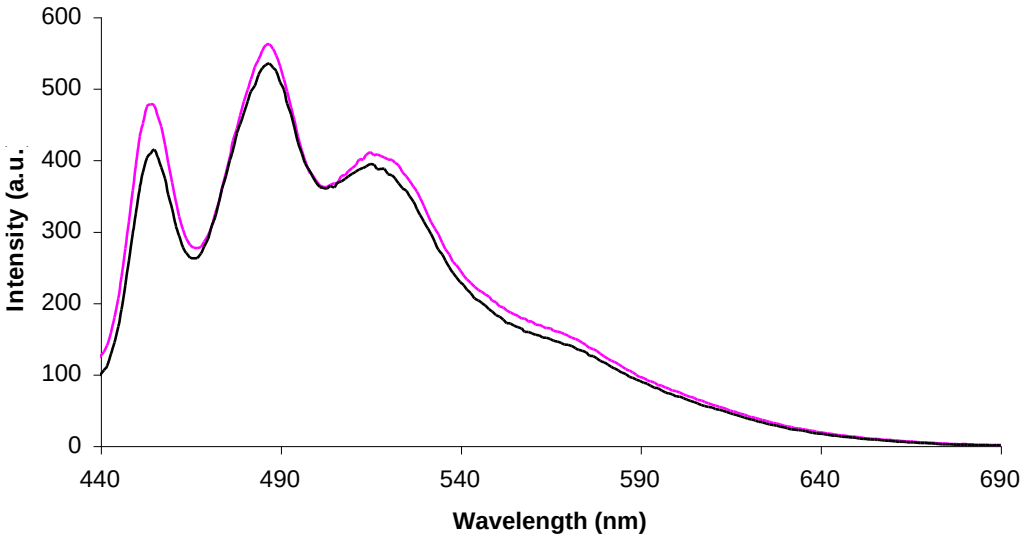

Figure 6.18: Emission spectra of Z-$[Ir(tpy)_2]^{2+}$ (1 $[Ir(tpy)_2]^{3+}$ per 20 supercages) excited at 330 nm and slit widths 5 nm (magenta trace) and Z-$[Ir(tpy)_2]^{3+}[Eu(bpy)_2]^{3+}$ material, (1 $[Ir(bpy)_3]^{3+}$ per 20 supercages and 1 $[Eu(bpy)_2]^{3+}$ per 2 supercages) excited at 330 nm.

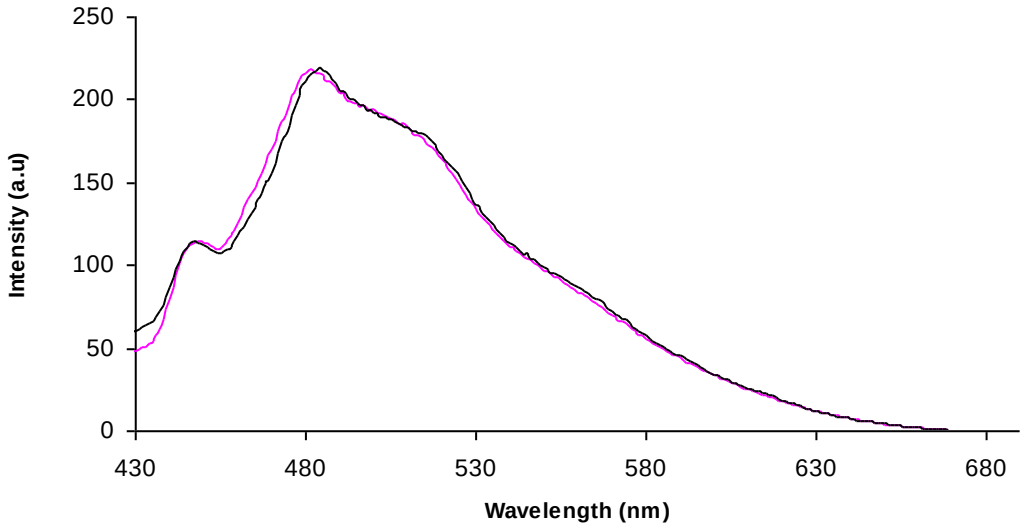

Figure 6.19: Emission spectra of Z-$[Ir(bpy)_3]^{2+}$ (1 $[Ir(bpy)_3]^{3+}$ per 26 supercages) excited at 319 nm and slit widths 5 nm (magenta trace) and Z-$[Ir(bpy)_3]^{3+}[Eu(bpy)_2]^{3+}$ material, (1 $[Ir(bpy)_3]^{3+}$ per 26 supercages and 1 $[Eu(bpy)_2]^{3+}$ per 2 supercages) excited at 319 nm and slit width 5 nm (black trace). and slit width 5 nm (black trace).

6.2.2.2 Excitation and phosphorescent emission

The excitation spectra of each co-doped material was examined for any spectral changes that may point to energy transfer to the europium acceptor. Figure 6.20 shows the excitation spectra of (A) Z-$[Eu(bpy)_2]^{3+}$ (B) Z-$[Ir(tpy)_2]^{3+}[Eu(bpy)_2]^{3+}$ material and (C) Z-$[Ir(tpy)_2]^{3+}$ monitoring the emission at 617 nm. Spectrum (C) was recorded in order to rule out any possible contribution and contamination of the phosphorescent excitation spectra from the Z-$[Ir(tpy)_2]^{3+}$ material itself and that any excitation response observed is related only to europium emission. Spectrum (A) is the excitation spectrum of a sample of Z-$[Eu(bpy)_2]^{3+}$ of comparable concentration to the doped sample. Spectrum (B) shows the excitation spectrum of the co-doped Z-$[Ir(tpy)_2]^{3+}[Eu(bpy)_2]^{3+}$ material. A shoulder next to the main excitation peak is apparent at 345 nm, indicative of a new photophysical process at work.

To assess this the co-doped material was excited at various different wavelengths ranging from 300 nm to 360 nm to gauge the effect on emission intensity from the co-included Z-$[Eu(bpy)_2]^{3+}$ (Figure 6.21).

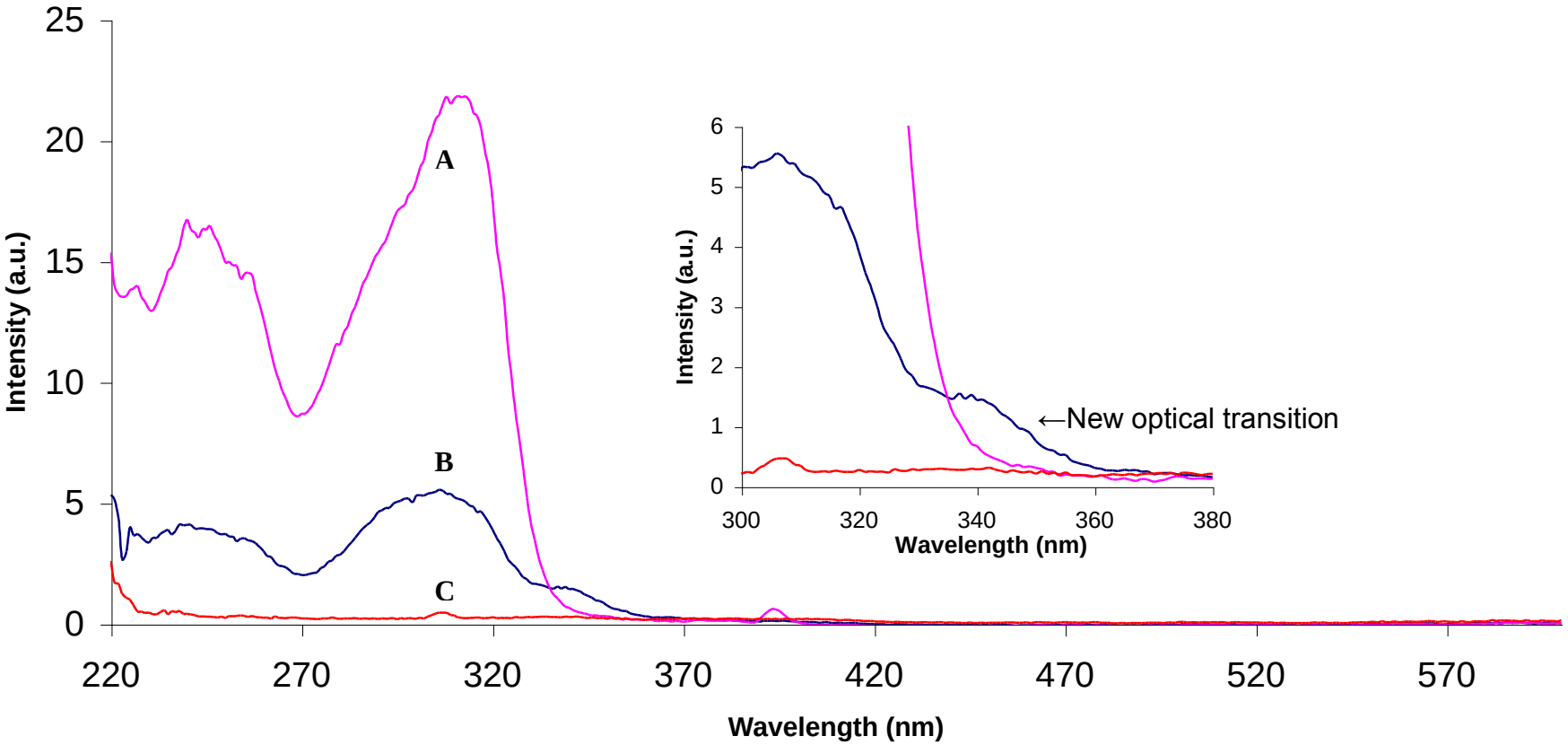

Figure 6.20: Excitation spectra, slit width 5 nm, monitoring emission at 615 nm of (A) Z-$[Eu(bpy)_2]^{3+}$ (1 $[Eu(bpy)_2]^{3+}$ per 2 supercages), (B) Z-$[Ir(tpy)_2]^{3+}[Eu(bpy)_2]^{3+}$ material, (1 $[Ir(tpy)_2]^{3+}$ per 20 supercages and 1 $[Eu(bpy)_2]^{3+}$ per 2 supercages), (C) Z-$[Ir(tpy)_2]^{3+}$ (1 $[Ir(tpy)_2]^{3+}$ per 20 supercages). Inset: Expanded section showing spectral region 300 nm to 370 nm.

As expected, the strongest emission is evident at the absorption maximum at 300 nm and 310 nm and decreases as excitation goes to longer wavelengths. Crucially, excitation into the shoulder at 350 nm results in emission that is more intense than the comparable emission when exciting the Z-$[Eu(bpy)_2]^{3+}$ material at 350 nm, indicative of energy transfer from the iridium complex to the europium acceptor. The difference between the intensity of the two main peaks is around 50 % and is shown in Figure 6.22.

Figure 6.23 shows the excitation spectra of (A) Z-$[Eu(bpy)_2]^{3+}$ (B) Z-$[Ir(bpy)_3]^{3+}[Eu(bpy)_2]^{3+}$ material and (C) Z-$[Ir(bpy)_3]^{3+}$ monitoring the emission at 617 nm. As before, Spectrum (C) was recorded in order to rule out any possible contribution of the phosphorescent excitation spectra from the Z-$[Ir(bpy)_3]^{3+}$ material itself and that any excitation response observed is related only to europium emission. Spectrum (A) is the excitation spectrum of a sample of Z-$[Eu(bpy)_2]^{3+}$ of comparable concentration to the doped sample. Spectrum (B) shows the excitation spectrum of the co-doped Z-$[Ir(bpy)_3]^{3+}[Eu(bpy)_2]^{3+}$ material. There appears to be a very modest increase in the excitation intensity at ~340 nm to ~380 nm and appears to have the same profile as the Z-$[Eu(bpy)_2]^{3+}$ material. In order to assess if there is communication between the iridium and europium complexes the material was excited at a range of wavelengths (Figure 6.24).

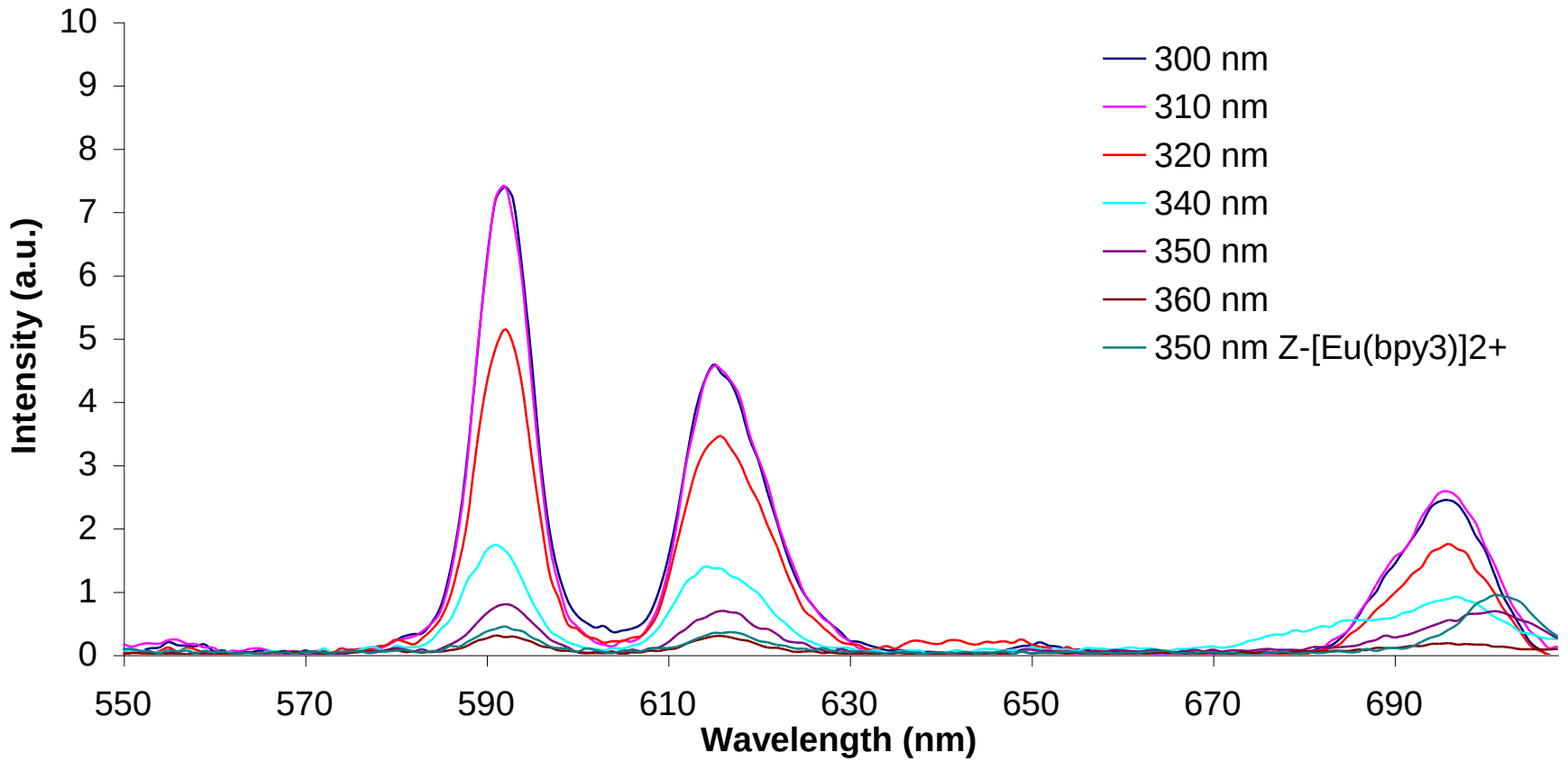

Figure 6.21: Emission spectra of Z-$[Ir(tpy)_2]^{3+}[Eu(bpy)_2]^{3+}$ material, (1 $[Ir(tpy)_2]^{3+}$ per 20 supercages and 1 $[Eu(bpy)_2]^{3+}$ per 2 supercages) excited at 300, 310, 320, 340, 350 and 360 nm with slit width 5 nm and Z-$[Eu(bpy)_3]^{2+}$ (1 $[Eu(bpy)_3]^{3+}$ per 2 supercages) excited at 350 nm and slit width 5 nm.

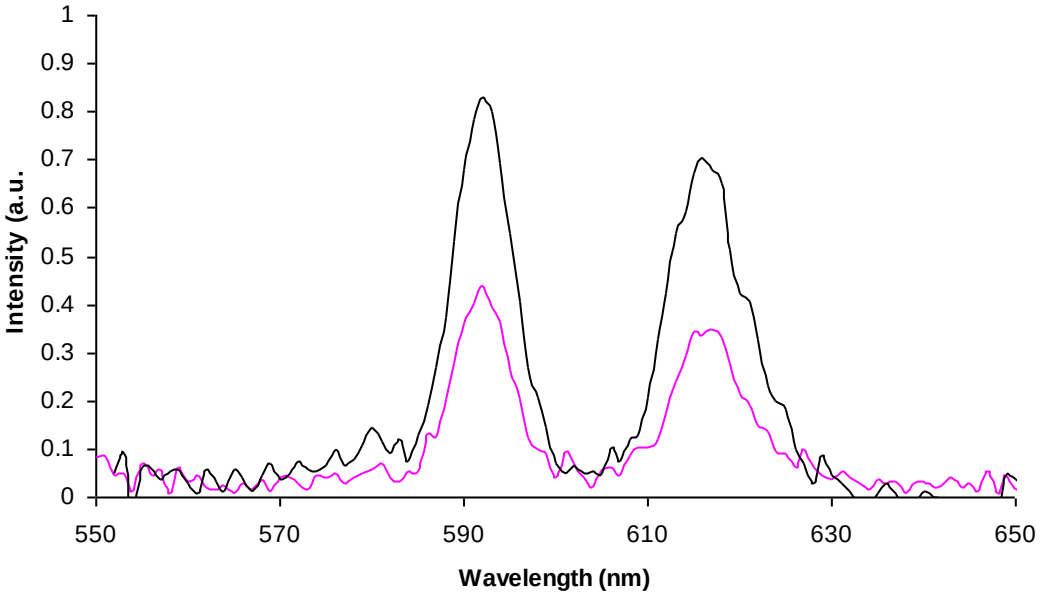

Figure 6.22: Emission spectra of Z-$[Eu(bpy)_3]^{2+}$ (1 $[Ir(bpy)_3]^{3+}$ per 2 supercages) excited at 350 nm and slit widths 5 nm (magenta trace) and Z-$[Ir(tpy)_2]^{3+}[Eu(bpy)_2]^{3+}$ material, (1 $[Ir(tpy)_2]^{3+}$ per 20 supercages and 1 $[Eu(bpy)_2]^{3+}$ per 2 supercages) excited at 350 nm and slit width 5 nm (black trace).

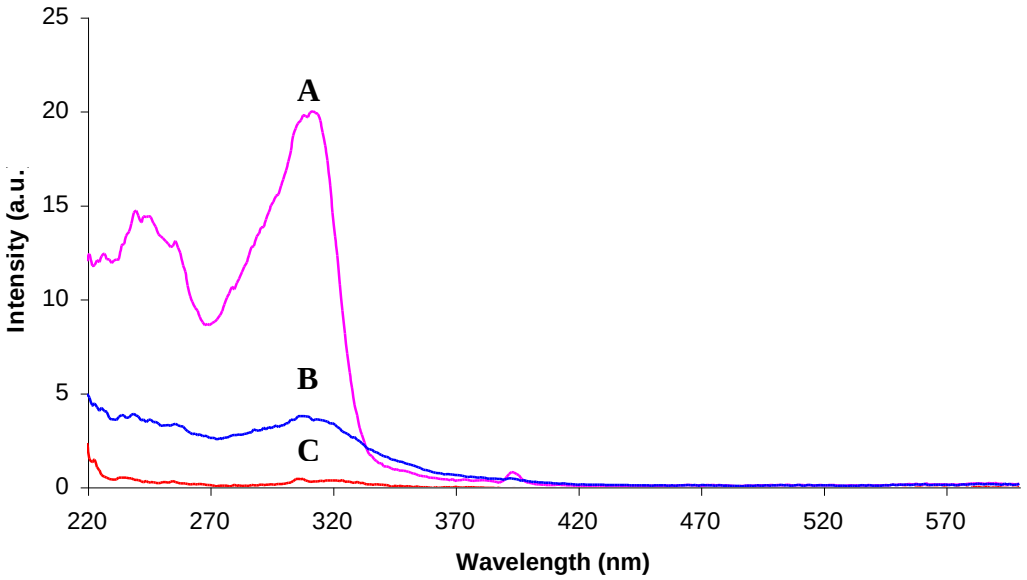

Figure 6.23: Excitation spectra, slit width 5 nm, monitoring emission at 615 nm of (A) Z-$[Eu(bpy)_2]^{3+}$ (1 $[Eu(bpy)_2]^{3+}$ per 2 supercages), (B) Z-$[Ir(bpy)_3]^{3+}[Eu(bpy)_2]^{3+}$ material, (1 $[Ir(bpy)_3]^{3+}$ per 26 supercages and 1 $[Eu(bpy)_2]^{3+}$ per 2 supercages), (C) Z-$[Ir(bpy)_3]^{3+}$ (1 $[Ir(bpy)_3]^{3+}$ per 26 supercages).

The material was excited at 350 nm to coincide with the largest difference between the intensities of the two-excitation profiles noted in Figure 6.23. No substantial changes in the intensity of emission was noted for the undoped Z-$[Eu(bpy)_2]^{3+}$ ruling out any strong communication between $[Ir(bpy)_3]^{3+}$ and $[Eu(bpy)_2]^{3+}$ complexes.

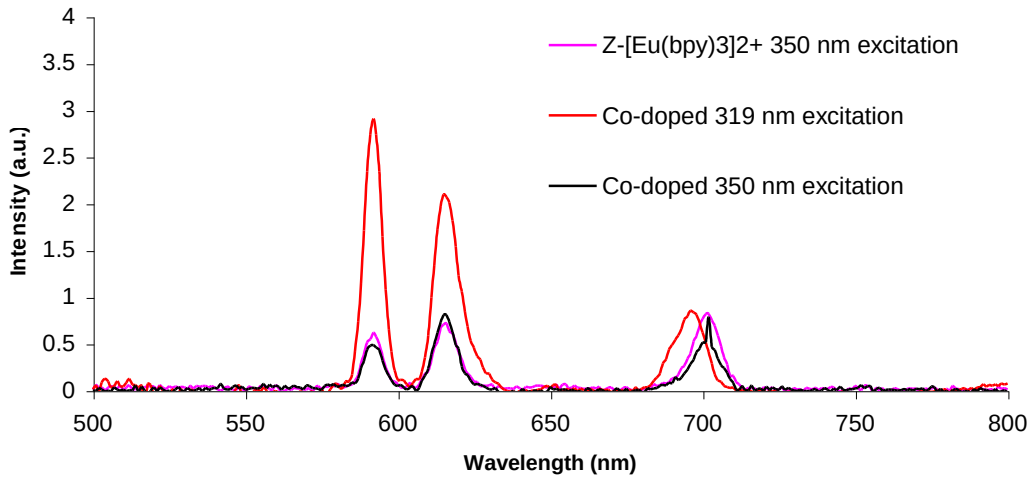

Figure 6.24: Emission spectra of Z-$[Ir(bpy)_3]^{3+}[Eu(bpy)_2]^{3+}$ material, (1 $[Ir(bpy)_3]^{3+}$ per 26 supercages and 1 $[Eu(bpy)_2]^{3+}$ per 2 supercages) excited at 319 nm and 350 nm with slit width 5 nm (red and black trace) and Z-$[Eu(bpy)_3]^{2+}$ (1 $[Eu(bpy)_2]^{3+}$ per 2 supercages) excited at 350 nm and slit width 5 nm (magenta trace).

6.2.2.3 Excited state lifetimes

The lifetimes of both Z-$[Ir(tpy)_2]^{3+}$ and Z-$[Ir(bpy)_3]^{3+}$ and Z-$[Ir(tpy)_2]^{3+}[Eu(bpy)_2]^{3+}$ and Z-$[Ir(bpy)_3]^{3+}[Eu(bpy)_2]^{3+}$ were examined to confirm the existence of new photophysical processes (Table 6.1). As discussed in chapter 4, scattering was a problem when measuring excited state lifetimes in suspension and this is again reflected in the rather large error associated with the lifetimes obtained.

The Z-$[Ir(tpy)_2]^{3+}$ material showed a decrease in the excited state lifetime of its longest lived component of around 550 ns after doping with $[Eu(bpy)_2]^{3+}$. The rate of energy transfer was calculated by:

$$k_{en} = \frac{1}{\tau_{Ir/Eu}} - \frac{1}{\tau_{Ir}} \qquad \textbf{Equation 6.1}$$

and the energy transfer efficiency was calculated by:

$$E = 1 - \frac{\tau_{Ir/Eu}}{\tau_{Ir}}$$ **Equation 6.2**

The rate of energy transfer was determined to be 1.31 x 10^5 s^{-1} and the efficiency of the process was 0.24. This value is reasonably good considering the value of 0.38 achieved for a bimetallic ligand bridged complex described earlier in the chapter. The donor-accepter pairs in zeolite are spatially separated over two supercages, with a centre-to-centre distance of ~1.3 nm and are not bridged in any way. Based on the appearance of a new optical transition (Figure 6.20) along with the change in lifetime the energy transfer process is attributed to a Dexter type mechanism.

The lifetimes for the Z-$[Ir(bpy)_3]^{3+}$ and Z-$[Ir(bpy)_3]^{3+}[Eu(bpy)_2]^{3+}$ material show, within experimental error no change. It would appear that energy transfer from the $[Ir(bpy)_3]^{3+}$ to $[Eu(bpy)_2]^{3+}$ is non-existent or of very low efficiency indeed.

The reason for the differing behaviour of the two iridium polypyridyl complexes is unclear. The two complexes excited states are very close in energy ruling out any enhanced thermodynamic driving force of either of the complexes. The intra-cage orientation of the terpyridine complex relative to the bipyridine may promote the observed process. The excited state terpyridine ligand could lie in closer proximity to the acceptor and with an orientation better disposed towards Dexter energy transfer than the equivalent bipyridine complex.

Zeolite Material	τ_1 (ns)	A	τ_1 (ns)	B	χ^2
Z-$[Ir(tpy)_2]^{3+}$	2329 ± 128	94	180 ± 53	6	1.060
Z-$[Ir(tpy)_2]^{3+}[Eu(bpy)_2]^{3+}$	1782 ± 76	92	197 ± 36	8	1.074
Z-$[Ir(bpy)_3]^{3+}$	977 ± 121	100			1.026
Z-$[Ir(bpy)_3]^{3+}[Eu(bpy)_2]^{3+}$	916 ± 112	100			1.129

Table 6.1: Excited state lifetimes of both $[Eu(bpy)_2]^{3+}$ doped and undoped Z-$[Ir(tpy)_2]^{3+}$ and Z-$[Ir(bpy)_3]^{3+}$. A and B refer to percent contribution of each individual lifetime decay fit to the appropriate exponential model. Concentrations of Z-$[Ir(tpy)_2]^{3+}[Eu(bpy)_2]^{3+}$ material, (1 $[Ir(tpy)_2]^{3+}$ per 20 supercages and 1 $[Eu(bpy)_2]^{3+}$ per 2 supercages) and Z-$[Eu(bpy)_3]^{2+}$ (1 $[Eu(bpy)_3]^{3+}$ per 2 supercages). Concentrations of Z-$[Ir(bpy)_3]^{3+}[Eu(bpy)_2]^{3+}$ material (1 $[Ir(bpy)_3]^{3+}$ per 26 supercages and 1 $[Eu(bpy)_2]^{3+}$ per 2 supercages) and Z-$[Eu(bpy)_3]^{2+}$ (1 $[Eu(bpy)_2]^{3+}$ per 2 supercages).

6.3 Conclusions

For the first time, sensitisation of a zeolite included europium acceptor by a co-included iridium polypyridyl complex has been observed. Energy transfer from the donor complex Z-$[Ir(tpy)_2]^{3+}$ to co-included Z-$[Eu(bpy)_2]^{3+}$ was confirmed by changes in the phosphorescent excitation spectrum of the material as well as by changes in the excited state lifetime. The efficiency of the process, based on the intensity decrease of the doped $[Ir(tpy)_2]^{3+}$ versus undoped material suggests that the efficiency of the process is rather low. A similar system of Z-$[Ir(bpy)_3]^{3+}[Eu(bpy)_2]^{3+}$ showed no new photophysical processes. The reason for the differing behaviour of the two materials is as yet unclear but may be the need for orbital overlap in the materials if energy transfer occurs by a Dexter type mechanism.

6.4 References

[1] Kido, J.; Okamoto, Y. *Chem. Rev.* **2002,** *102*, , 2357.

[2] Jüstel, T.; Nikol, H.; Ronda, C. *Angew. Chem. Int. Ed.* **1998,** *37*, , 3084.

[3] Motson, G.R.; fleming J.S.; Brooker, S. *Adv. Inorg. Chem.* **2004**, *55*, 361.

[4] Chen, Y.; Guo, W.;Zhiqiang Ye, Z.;Wanga, G Yuan, J. *Chem. Commun.* **2011**,*47*, 6266.

[5] Bünzli, J.C.G.; Piguet, C. *Chem Soc. Rev.* **2005**, *34*, 1048.

[6] Yuan, J.L.; Wang, G.L., *TRAC-Trends Anal. Chem.* **2006**, *25*, 490.

[7] Bünzli, J.C.G. *Acc. Chem. Res.* **2006**, *39*, 53.

[8] Santos dos, C.M.G.; Harte, A.J.; Quinn, S.J.; Gunnlaugsson, T. *Coord. Chem. Rev.* **2008**, *252*, 2512.

[9] D'Aléo, A.; Pointillart, F.; Ouahab, L.; Chantal Andraud, C.; Maury O. Coord. *Chem. Rev.* **2012**, *256*, 1604.

[10] Andrew, B.; Bushby, L.M.; Maffeo, D.; Williams, J.A.G. *J. Chem. Soc. Perkin Trans. 2* **2000**, *7*, 1281.

[11] Hemmila, I.; Laitala, V. *J. Fluores*c. **2005**, *4*, 529-542.

[12] Van Deun, R.; Nockemann, P.; Fias, P.; Van Hecke, K.; Van Meervelt, L.; Binnemans, K. *Chem. Commun* **2005,** 590.

[13] Van Deun, R.; Nockemann, P.; Fias, P.; Van Hecke, K.; Van Meervelt, L.; Binnemans, K. *Inorg. Chem.* **2006**, *45*, 10416.

[14] Fu, L.M.; Wen, X.F.; Ai, X.C.; Sun, Y.; Wu, Y.S.; Zhang, J.P.; Wang, Y. *Angew. Chem. Int. Ed.* **2005**, *44*, 747.

[15] Chen, F.F.;Chen, Z.Q.; Bian, Z.Q.; Huang, C.H. *Coord. Chem. Rev.* **2010**, *254*, 991.

[16] Klink, S.I.; Keizer, H.; van Veggel, F.C.J.M. *Angew. Chem. Int. Ed*. **2000**, *39*, 4319.

[17] Pope, S.J.A.; Coe, B.J.; Faulkner, S.; Bichenkova, E.V.; Yu, X.; Douglas, K.T. *J. Am.Chem. Soc.* **2004**, *126*, 9490.

[18] Shavaleev, N.M.; Moorcraft, L.P.; Pope, S.J.A.; Bell, Z.R.; Faulkner, S.; Ward, M.D. *Chem. Commun.* **2003**, 1134.

[19] Beeby, A.; Dickins, R.S.; FitzGerald, S.; Govenlock, L.J.; Maupin, C.L.; Parker, D.; Riehl, J.P.; Siligardi, G.; Williams, J.A.G *Chem. Commun.* **2000** 1183.

[20] Xu, H.B.; Zhang, L.Y.; Ni, J.; Chao, H.Y.; Chen, Z.N. *Inorg. Chem.* **2008**, *47*, 10744.

[21] Shavaleev, N.M.; Bell, Z.R.; Ward, M.D. *J. Chem. Soc. Dalton Trans.* **2002**, 3925.

[22] Sanada, T.; Suzuki, T.; Yoshida, T.; Kaizaki, S. *Inorg. Chem.* **1998**, *37*, 4712.

[23] Brayshaw, P.A.; Bünzli, J.C.G.; Froidevaux, P.; Harrowfield, J.M.; Kim, Y.; Sobolev, A.N. *Inorg. Chem.* **1995**, *34*, 2068.

[24] Wong, W.K.; Liang, H.Z.; Wong, W.Y.; Cai, Z.W.; Li, K.F.; Cheah, K.W. *New J. Chem.* **2002**, *26*, 275.

[25] Coppo, P.; Duati, M.; Kozhevnikov, V.N.; Hofstraat, J.W.; De Cola, L. *Angew. Chem.Int. Ed.* **2005**, *44*, 1806.

[26] Chen, F. F.; Bian, Z.Q.; Liu, Z.W.; Nie, D.B.; Chen, Z.Q.; Huang, C.H.; *Inorg. Chem.* **2008**, *47*, 2507.

[27] Jiang, W.; Lou, B.; Wang, J.; Lv, H.; Bian, Z.; Huang, C. *Dalton Trans*, **2011**, *40*, 11410.

[28] Ward, M.D. *Coord. Chem. Rev.* **2010,** *254*, 2634.

[29] Maas, H.; Currao, A.; Calzaferri, G. *Angew. Chem. Int.* Ed. **2002**, *41*, 2495.

[30] Alvaro, M.; Fornes, V.; Garcıa, S. Garcıa, H,.; Scaiano, J.C. *J. Phys. Chem. B* **1998,** *102,* 8744.

[31] Lee, E. F. T.; Rees, L. V. C. *Zeolites* **1987**, *7*, 143-147.

[32] Rosa, I.L.V.; Serra, O.A.; Nassar, E.J. *J. Lumin.* **1997**, *72-74*, 532.

[33] Binnemans , K.; Herck, K. Van.; Görller-Walrand, C. *Chem. Phys. Lett.* **1997**, *266*, 297.

[34] Richardson F.S. *Chem. Rev.* **1982**, *82*, 541.

Chapter 7

Conclusions and Future Work

7.0 Conclusions and Future Work

This thesis focussed on the study of the properties of zeolite-Y as a platform to support luminescent metal complex donor-acceptor species and to assess its ability to alter their individual photophysical properties and support photophysical processes between them. The rationale for this study is that zeolite host systems have the potential for future use in nanoscale opto-electronic devices because of their capacity for molecular organisation. However, their capacity to accommodate energy transfer and the origin of their influence on the photophysical properties of luminescent coordination compounds is not fully understood.

The ability of zeolite-Y to accommodate excited state energy transfer was established in chapter 3. The use of an entrapped ruthenium polypyridyl luminophore co-doped with an iron polypyridyl proved that long-range Förster energy transfer between co-entrapped complexes was possible. Preparation of various concentrations of the materials allowed for the estimation of the effective distance that energy transfer was operable over. The novel Z-$[Fe(tpy)_2]^{2+}$ demonstrated very well the unusual and oft-times unexpected results that zeolite systems can produce. The 'turning on' of quenching via an enhanced acceptor mode induced by the intrazeolitic environment, offers an interesting example of how the structural and electronic properties of encapsulated complexes can be altered to enhance or mitigate certain photophysical characteristics. Chapter 3 also offered evidence of some of the limitations of zeolite use. The complex lifetime profile of the materials offered insights into the multiple different configurations a complex may find itself when considering long range Förster energy transfer, even when the donor-acceptor pairs were separated by an intercage distance of only three supercages. Future work to emerge from this work will focus on further detailed examination of the ability of zeolite enhanced acceptor modes of $[Fe(tpy)_2]^{2+}$ to quench $[Ru(bpy)_3]^{2+}$ emission within the zeolite but not in solution.

Chapter 4 examined for the first time the incorporation of the iridium polypyridyl complexes $[Ir(tpy)_2]^{3+}$ and $[Ir(bpy)_3]^{3+}$ complexes within zeolite-Y. It was found that they successfully formed complexes within the zeolite pores and that the emission characteristics of the entrapped species were strongly affected. Large blue shifts in emission maxima were observed and well as alteration in the relative band intensities of the vibrationally resolved emission spectra. The source of these shifts was attributed to the highly polar environment within the zeolite cages and the ^{3}LC character of the Ir excited state which is relatively non-polar. These emission shifts also demonstrated the zeolites non-innocent participation in the host-guest systems studied. Self-absorption of the complex as evidenced by strong emission upon excitation at complexes emission λ_{max} was also observed and effects of this on the excited state lifetimes and emission characteristics of the zeolite materials were examined. Future work on the iridium polypyridyl materials will focus on improving the synthetic processes for production of iridium based materials. The careful control of temperature and possibly the use of microwave synthesis may provide a route to enhancement of yields.

Chapter 5 sought to assess the impact of zeolite rigidity and the polar cage environment on the degree of distortion experienced by excited state molecules. The purpose of the chapter was to establish the consequences of entrapment upon the geometry of a complex after excitation to an upper energy state as its foreseen that much of the future of zeolite-based material in the field of nano-electronics will involve luminescent molecules. Huang-Rhys modelling of the 77 K and 298 K emission spectra of ruthenium and novel iridium polypyridyl complexes allowed evaluation of the extent of inhibition of excited state distortion. Examination of the emission spectra and application of the Rhys-Huang model provided both quantitative and qualitative information on the extent that the zeolite inhibits the distortion of excited state molecules. It was found that the excited state ruthenium complexes underwent less distortion within the zeolite compared to solution phase studies.

Initially, the excited state iridium polypyridyl complexes appeared to be strongly affected by the zeolite matrix based on the results of Huang-Rhys analysis. However consideration of the possible enhanced contribution of lower frequency modes towards the observed vibrational progressions cast doubt on the analysis results and allowed for a qualitative interpretation of the distortion imposed by the zeolite material. A useful continuation of the work in chapter five would involve refinement of the Huang-Rhys model, to assess if incorporation of multimode (three plus) spectral fits would better model the experimental data obtained.

Chapter 6 looked to establish if intercage energy transfer from entrapped iridium polypyridyl complexes to co-entrapped europium complexes was possible and to assess the efficiency of the process. For the first time, sensitisation of a zeolite included europium acceptor by a co-included transition metal complex was observed. The sensitisation was observed only with the iridium bis-terpyridine complex and not with the analogous iridium tris-bipyridine complex. The energy transfer process was found to be quite inefficient and was consistent with Dexter energy transfer rather than Förster as observed in chapter 3. This is also consistent with literature explanation of the type of energy transfer that occurs between europium and other donor species. Enhancement of the rather low energy transfer efficiency observed between iridium and europium zeolite entrapped donor-acceptor pairs will be examined in future work. The ratio of donor to acceptor complexes will first be increased, and then the feasibility of introducing intercage bridging ligands between the complexes to increase the rate of Dexter energy transfer will be studied.

Overall, we demonstrate that zeolite-Y supports strong luminescence from metal complexes by restricting k_{nr} via limited distortion of the excited state, consistent with, but less rigid than observed in rigidochromism at 77 K. We also demonstrate that Förster energy transfer is allowed in Zeolite, but the distances imposed by the intercage distances limit the capacity for Dexter energy transfer. Zeolites therefore hold significant potential for photonic devices and continued vigorous research in nanotechnology and

nanomaterials will undoubtedly lead to useful applications across opto-electronics, sensors and other luminescence applications.

Appendix A

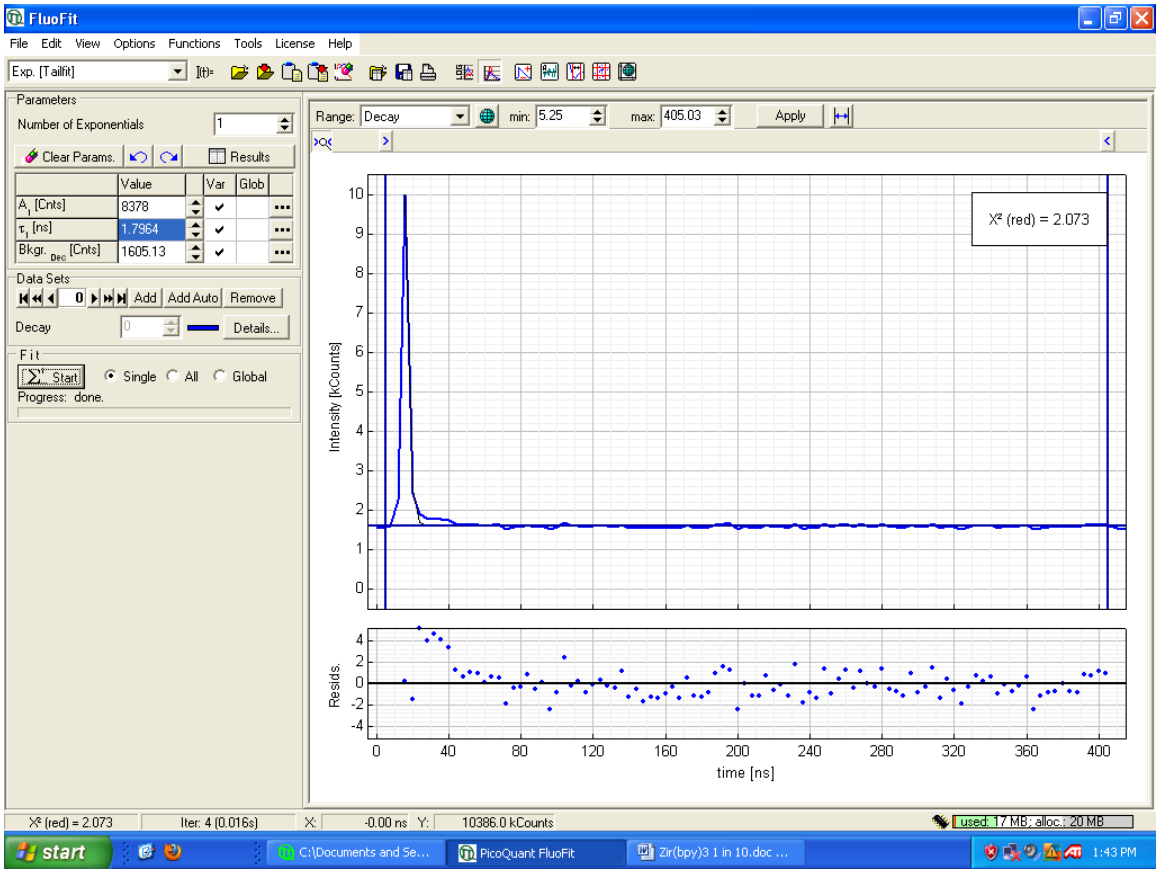

LUDOX Instrument response signal

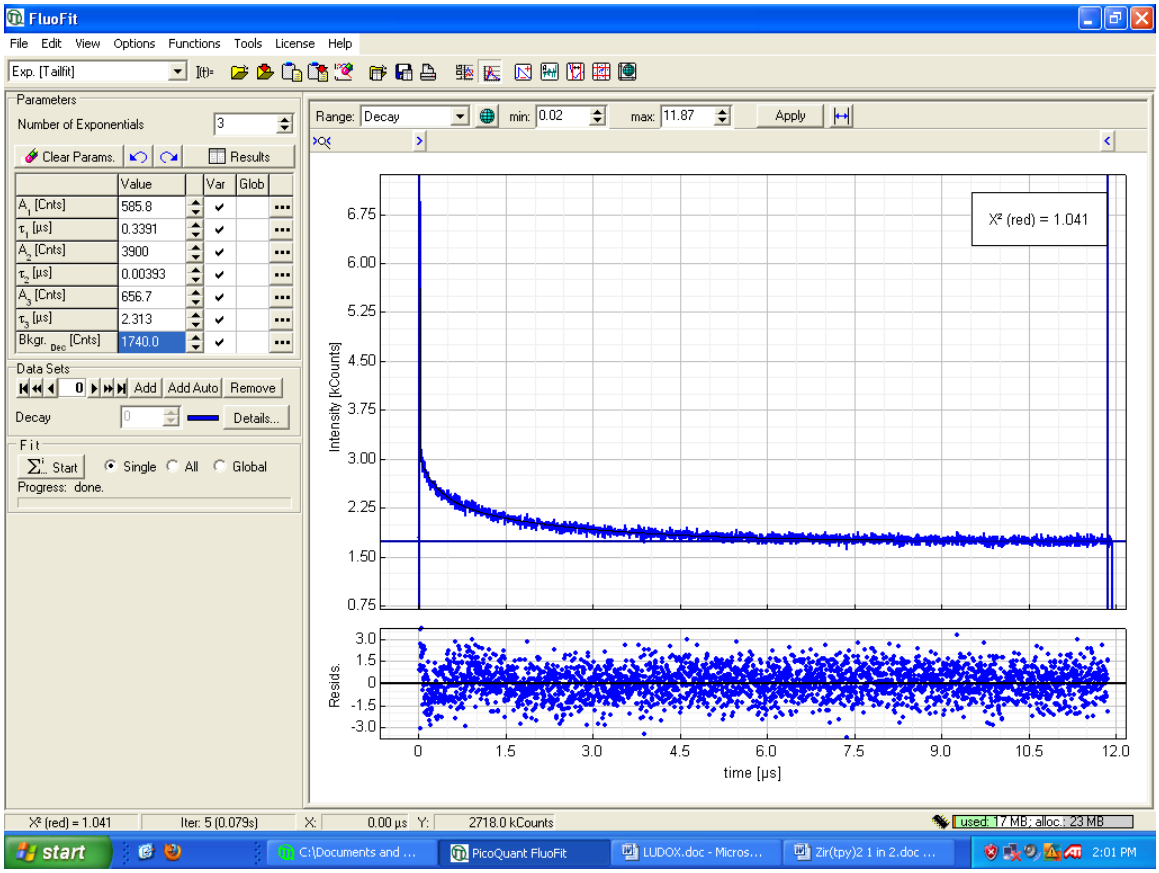

Z-$[Ir(tpy)_2]^{3+}$ (0.178 M) in aerated DMSO

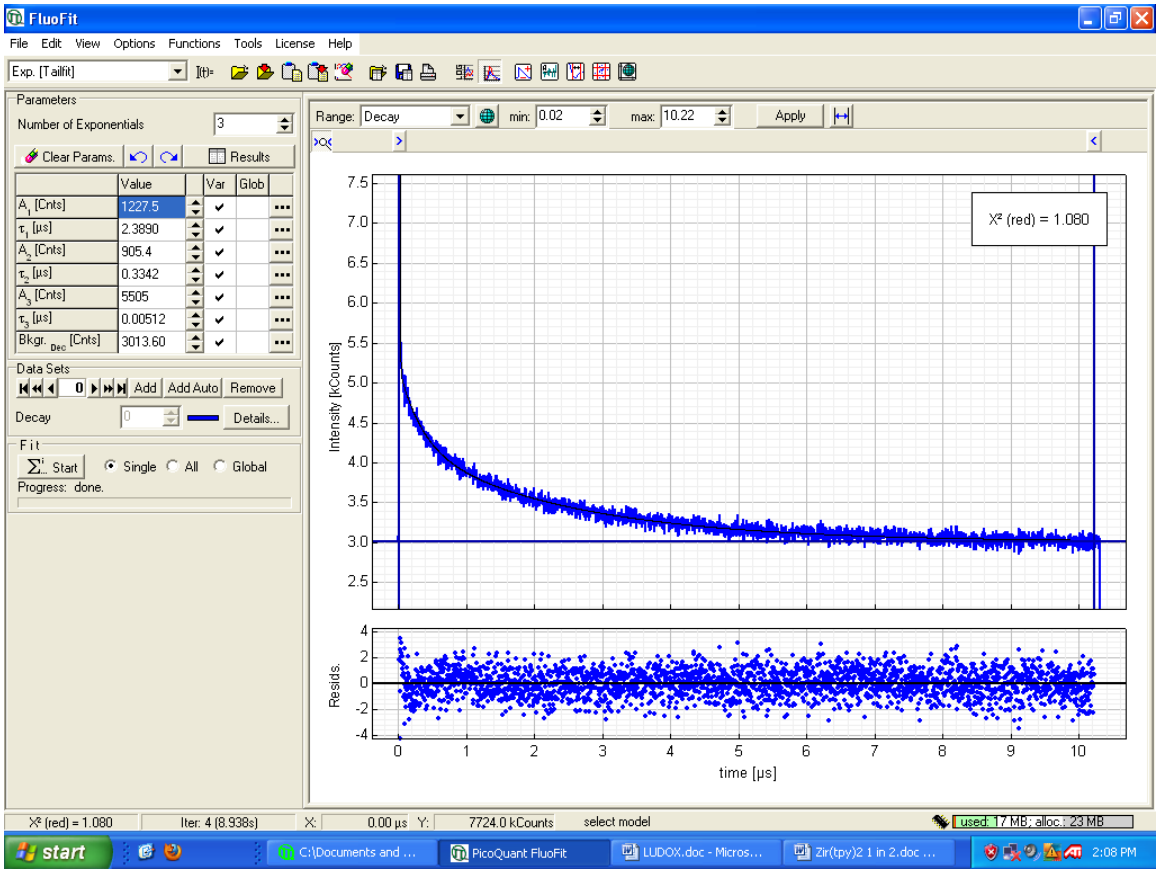

Z-$[Ir(tpy)_2]^{3+}$ (0.029 M) in aerated DMSO

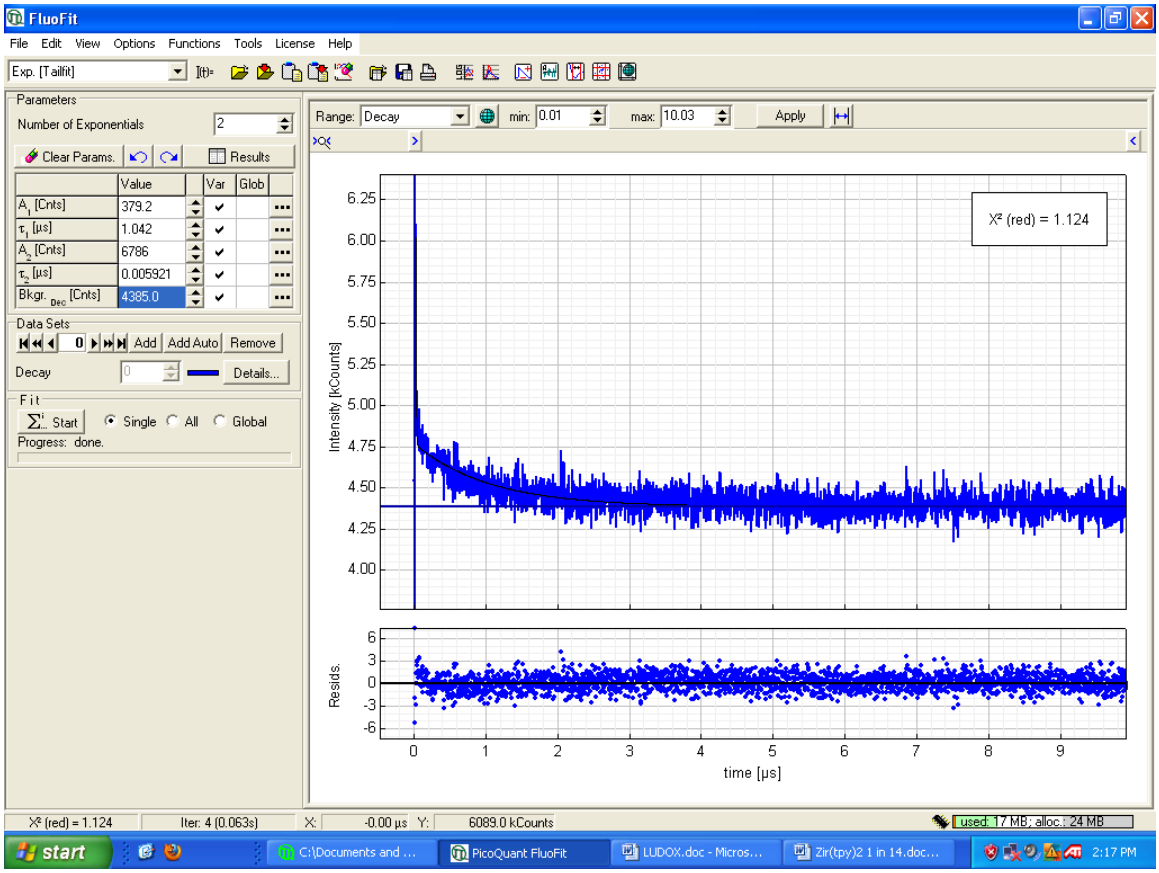

Z-$[Ir(tpy)_2]^{3+}$ (0.018 M) in aerated DMSO

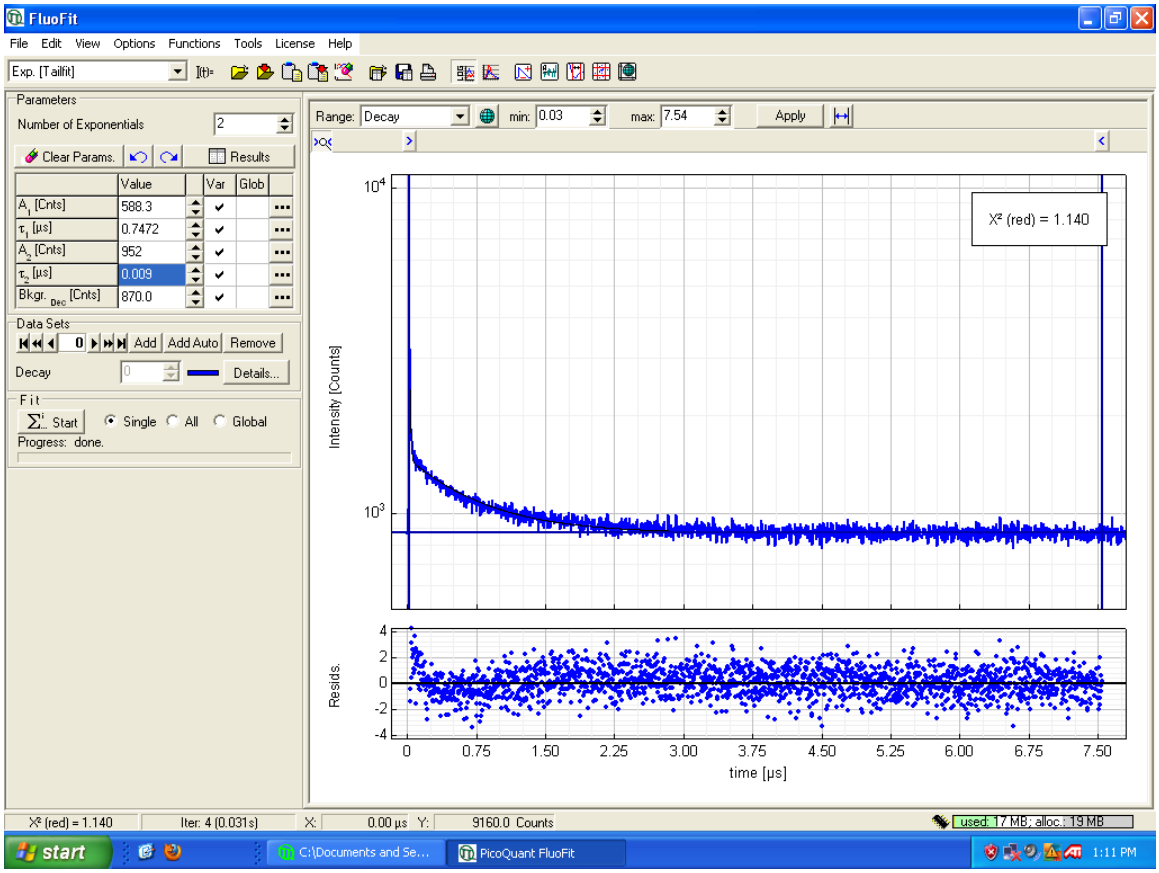

Z-$[Ir(bpy)_3]^{3+}$ (0.116 M) in aerated DMSO

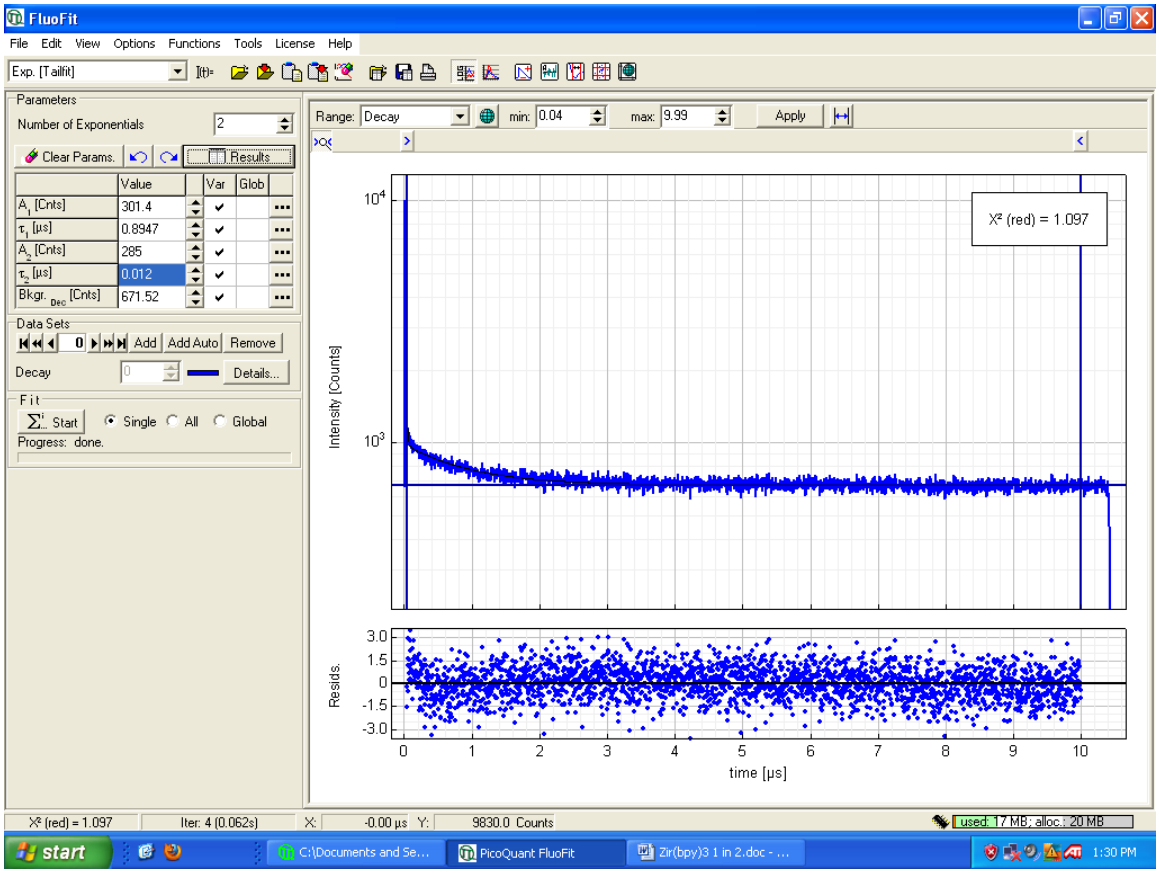

Z-$[Ir(bpy)_3]^{3+}$ (0.048 M) in aerated DMSO

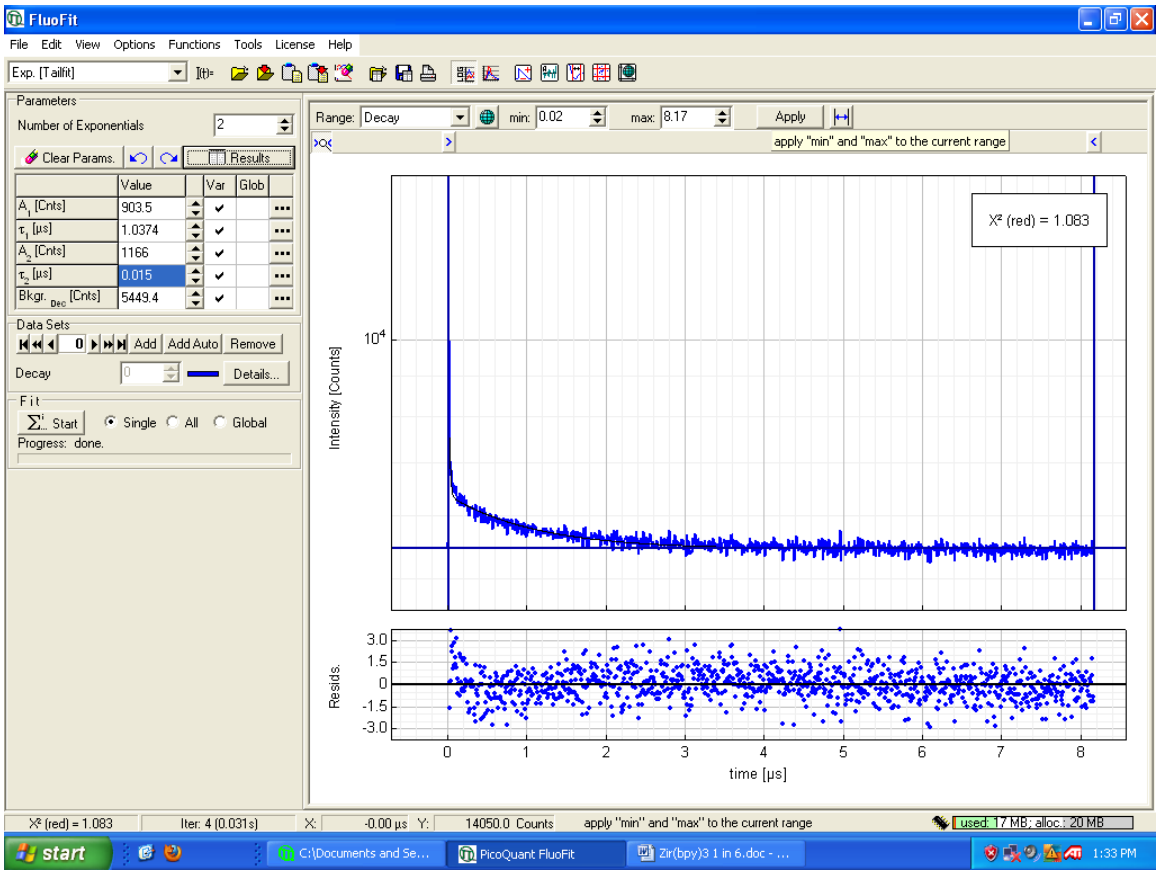

Z-[Ir(bpy)$_3$]$^{3+}$ (0.017 M) in aerated DMSO

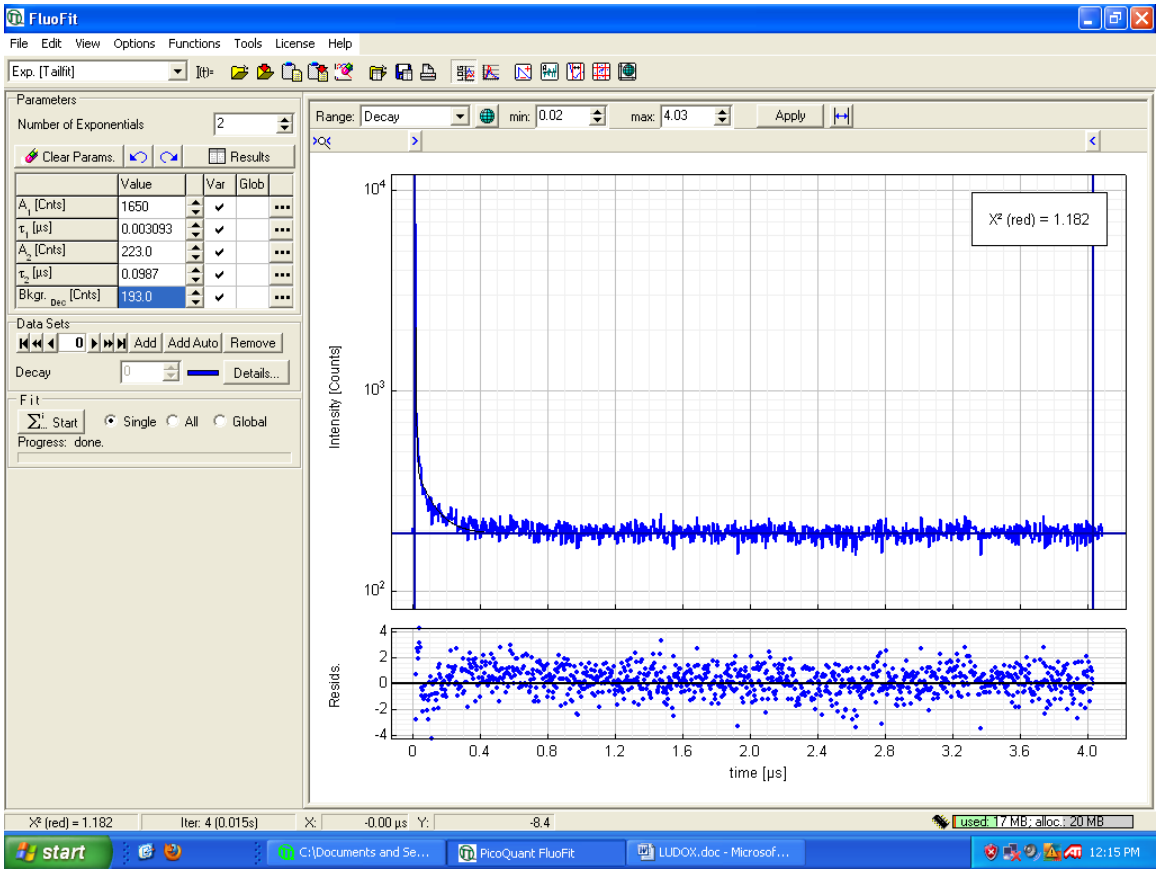

Z-[Ru(tpy)$_2$]$^{2+}$ (1 complex per 15 supercages) in aerated DMSO

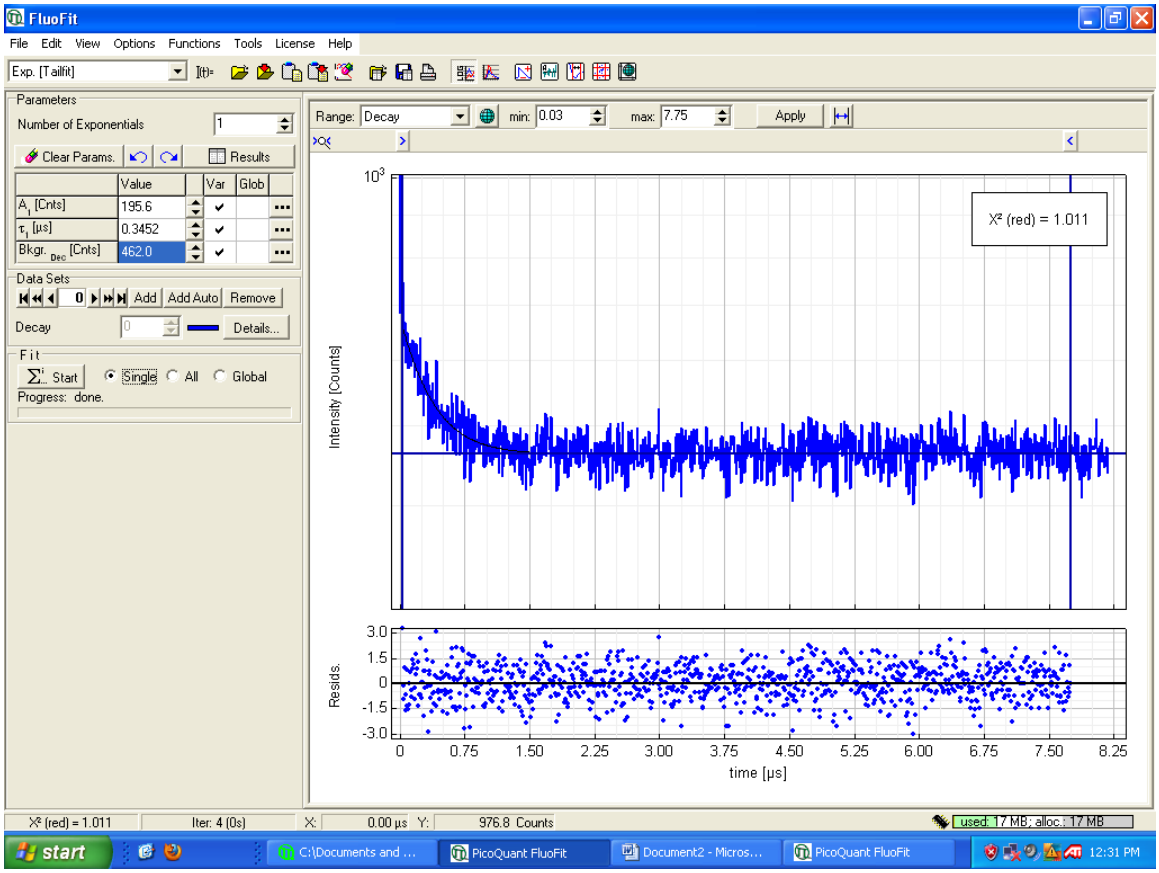

Excited state decay fit $[Ir(bpy)_3][PF_6]_2$ (2.0×10^{-5} M) Aerated

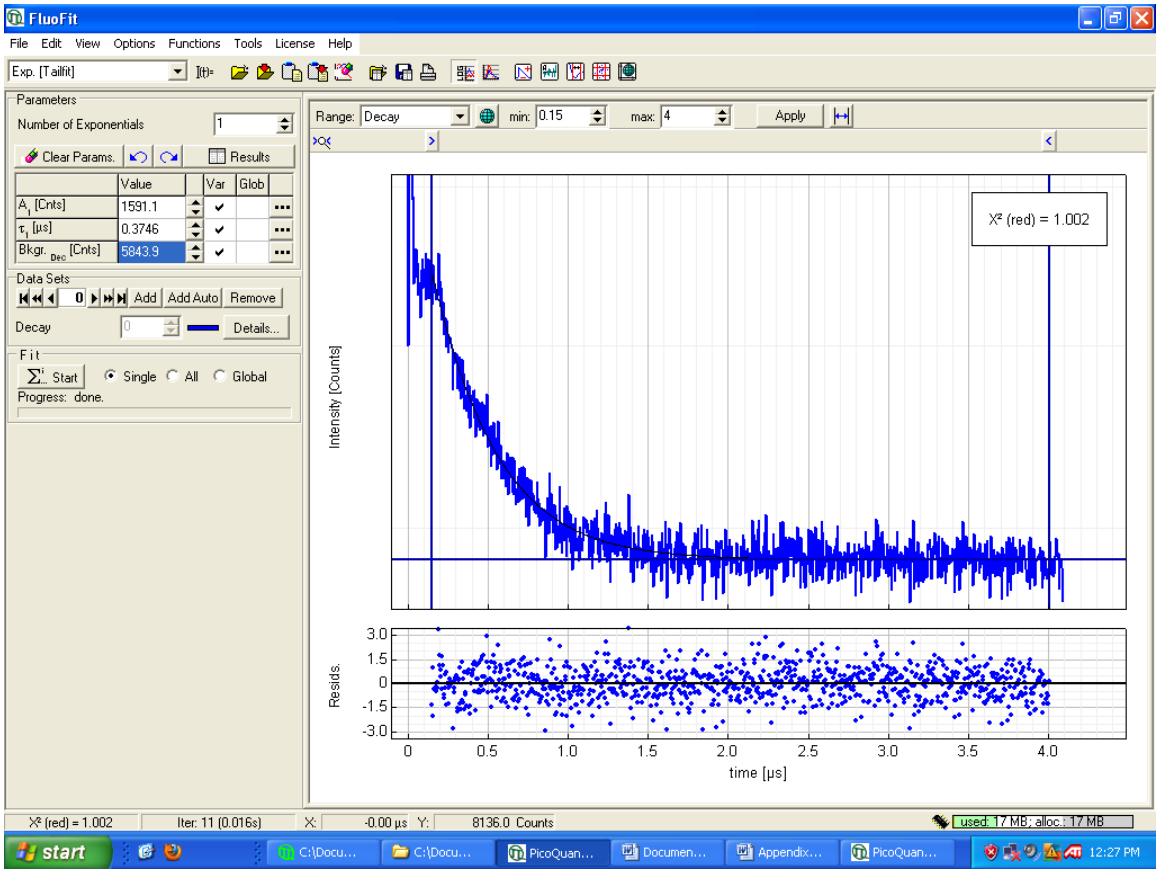

Excited state decay fit $[Ir(tpy)_2][PF_6]_2$ (2.0×10^{-5} M) Aerated